Tracing Star Formation Around Quasars With Polycyclic Aromatic Hydrocarbons

Thesis

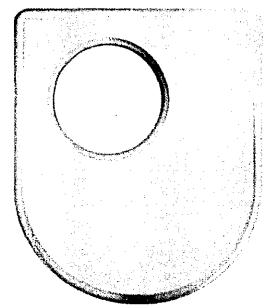

The Open University

Tracing Star Formation around Quasars with Polycyclic Aromatic Hydrocarbons

A Thesis submitted for the degree of Master of Philosophy in Astronomy

Lawrence E. Bilton BSc (Hons) (Open)

Department of Physical Sciences

The Open University

Submitted 20 May 2016

AWARDED 23 SEPTEMBER 2016

ProQuest LLC.
789 East Eisenhower Parkway
P.O. Box 1346
Ann Arbor, MI 48106 – 1346

ACKNOWLEDGEMENTS

It gives me great pleasure to express many, many thanks to both of my supervisors, Jeronimo Bernard-Salas and Stephen Serjeant. Their continued professional support and insight from both of their two different fields of Astronomy have helped my understanding and progression immensely throughout this M.Phil. Teaching me that there is always a delightful (and delicious) spread of information in your data. This is extended to my fellow astronomy students: to Calum and Jonathan for allowing me to be in the meat of your sandwich with endless puns keeping us sane, Dan for the countless conversations on funny American politics against the depressing British variety, George (Jimmy) for putting up with my constant moaning and random rambles as well as living with me, Paul for his upbeat and incredible enthusiasm for his RR Lyrae stars and the Blazkho effect, Ashley for being a constant source of enlightenment and providing good thrilling tales worthy of any epic fantasy, Helen for spreading her love of Star Wars and Thunderbirds to us all in the office and last, but by no means least, to Pam for being the motherly voice of reason to everyone in the office. A thank you to everyone in the Astrochemistry group for your help, advice and friendship. Especially to fellow students Catherine, Natalia and Olivier who've helped kept me grounded; reminding me that I am a human being on the planet earth. A massive thank you to everyone who has helped me in the department; I've met and worked with so many new beautiful people. Finally, a special thank you to my close friends and family: to the League (Simon, Yjan, Sarah, Coral, Phil, Duncan, Vicki, Nick, Steve, Stuart, Jodie, James, Tesca and Colin) for perpetuating silly Physics nonsense "Glory to the almighty members of the league, I greet you, for you shine science upon me.", my brothers James and Andrew for their continued humorous demonstrations of endearment and of course my lovely and wonderful parents for their love and support who made this venture become a reality.

ABSTRACT

The feedback processes linking quasar activity to galaxy stellar mass growth are not well understood. If star formation is closely causally linked to black hole accretion, one may expect star formation confined to nuclear regions rather than extended over several kpc scales. Since Polycyclic Aromatic Hydrocarbon (PAH) emission features are widely used as tracers of stellar formation, it is, therefore, possible to use PAH emission detected around QSOs to help resolve this question. PAH data from a sample of 63 QSOs procured from the Spitzer Space Telescope's Infrared Spectrograph (IRS) is used, employing the Spectroscopic Modelling Analysis and Reduction Tool's (SMART) Advanced Optimal (AdOpt) extraction routines. A composite spectrum was also produced to help determine the average conditions and compositions of star forming regions. It is found, from our high redshift ($z > 1$) sample of QSOs, there is a marginally significant extended star formation on average of 34 kpc scales. At low redshift, the median extension after deconvolving the instrumental point spread function is 3.2 kpc, potentially showing evolutionary variations in star formation activity. However, limitations of the spatial resolving power constrain the ability to make any absolute conclusive remarks. It is also found that the QSO/AGN composite has more neutral PAHs than the starbursting and the main sequence galaxies, consistent with the AGN having no contribution to heating the PAH emission, and also consistent with the average PAH emission found on kpc scales (i.e. not confined to the nuclear regions). A tentative detection of water vapour emission from the gravitationally lensed Einstein Cross quasar, QSO J2237+0305, is also presented suggesting a strong molecular outflow possibly driven by the active nucleus.

LIST OF FIGURES AND TABLES

FIGURES

TABLES

CONTENTS

Chapter 1

INTRODUCTION

It was Carl Seyfert in 1943 who brought to the attention of the astronomical community an unusual selection of spiral galaxies showing highly luminous and variable active nuclei in 1943; unbeknownst to Dr Seyfert this opened the door to a whole new field of astronomical study adding yet another complex layer to the formation, structure and evolution of galaxies. These galaxies presented characteristic high ionisation energy spectra, and were later coined 'Seyfert Galaxies'. Sadly, the field did not come into prominence until after he tragically died in 1960. It was not until the discovery of the first 'quasar' in 1963 with their optical spectra seemingly analogous to that of Seyferts that the new study of 'active nuclei' grew in significance. Quasars, from the term 'quasi-stellar object (QSO)' meaning point-like, were believed to be wholly unique objects of their own until in the early 1980s it was shown they were components to a host galaxy. This discovery ultimately led to the reclassifying of quasars under the umbrella term, 'Active Galactic Nuclei' (AGN).

AGN are one of the most energetic, yet mysterious, sources of radiation in the known Universe. Currently, a great deal is still not known with regards to the apparent mechanisms of AGN: what's the physical mechanism behind the tight correlation between AGN activity and stellar mass growth? Could star formation and AGN activity be causally linked? The answers to these questions impact our understanding of the formation and evolution of the host galaxies, including our now 'dormant' Milky Way. The current scientific consensus towards the physics behind AGN implies a supermassive accreting black hole, with the highly luminous emission originating from the said accretion disc within a tiny region of up to $\sim 10\ AUs$ (see Figure 1.1). If it is assumed that this is the physics, however, then this disc needs to be fed with a supply of gas and dust. Is this the same supply of material that fuels star formation? This question leads

back to the earlier statements on a feedback mechanism: could star formation and AGN activity be causally linked?

One possibility for testing this causal link could be measuring the spatial extent of the star-forming regions in quasars. As it has been already alluded to, the processes that link this stellar mass growth and quasar activity are not well understood. However, if star formation is closely causally linked to black hole accretion, we may expect star formation confined to nuclear regions rather than extended over several *kpc* scales.

The aim main of this thesis is to use a known tracer of star formation to measure the extension of the star formation from the active nucleus of the most luminous quasars, in the attempt to better understand the origin of the variable feedback activity. A composite spectrum consisting of the best signal-noise spectra of the sample will also be presented, which will act as a template for their chemical composition and physical nature of the quasar environment. Finally, star formation rate values will also be determined.

Presented within this Chapter, is a discussion towards the background of AGN and the star formation processes in these extragalactic objects.

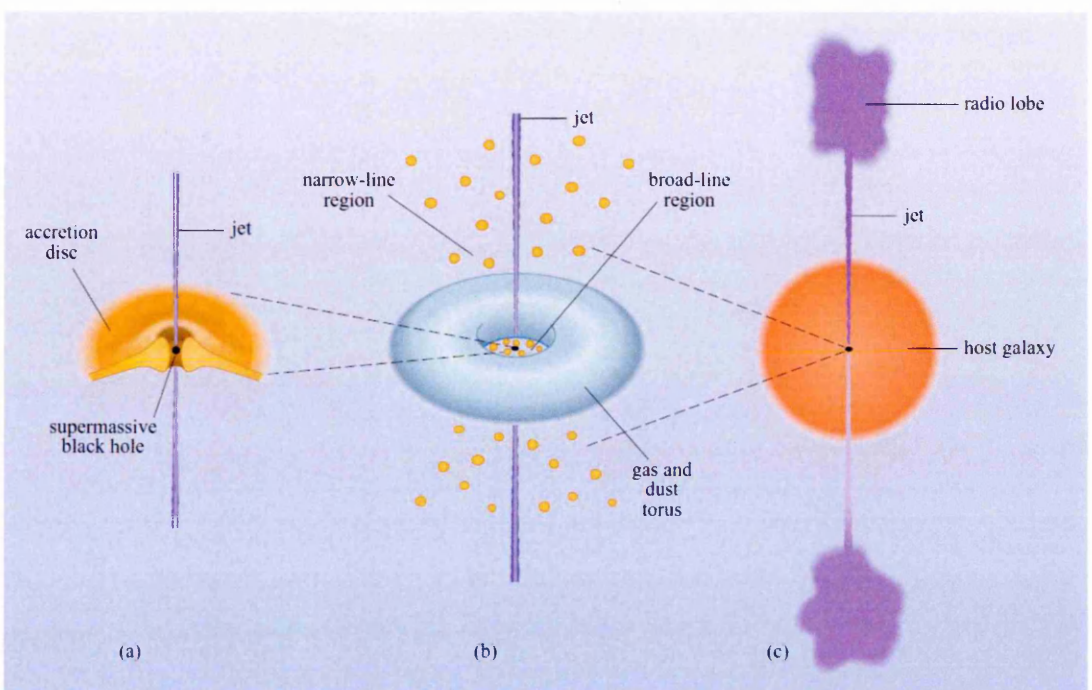

Figure 1.1. This represents the typical supermassive black hole model of AGN; (a) shows the supermassive black hole as the driving source of emission from the accretion disk within ~10 *AUs*; (b) shows the surrounding dusty torus with the different emission regions (as Figure 1.2); (c) shows the resultant relativistic jet with radio lobes. Taken from Jones & Lambourne (2004).

1.1 THE FLAVOURS OF ACTIVE GALACTIC NUCLEI

AGN currently are classified into four broad groups: Quasars (the focus of this work), Seyferts, Blazars and Radio Galaxies. These can be split even further into smaller categories (e.g. Seyfert 1 and Seyfert 2 galaxies). These objects are all currently believed to be all one of the same, with their distinctions determined by the observer's line of sight, and therefore dependence on the orientation of the objects themselves (Phillipps, 2005; Kutner, 2003). This consequence leads to the 'unified model' of AGN, with two types of AGN unification: radio loud and radio quiet. These will be discussed later, the idea behind a unified model of AGN is shown in Figure 1.2. However, the precise nature of such classifications are not so 'cut and dried', especially when distinguishing between type 1 and type 2 Seyferts. Also, the classification can be based on numerous differing parameters (e.g. luminosity) that can be arbitrarily defined by the author(s) as discussed in many reviews of the field such as Tadhunter (2008), or Netzer (2015).

1.1.1 Seyfert Galaxies

The studies of Seyfert (1943) highlighted the unusual nature of these Active Nuclei, producing luminosities of $\sim \times 10^{11} L_{\odot}$ with variability on short time scales, indicating that the region of the emission source is very minuscule compared with the rest of host galaxy (Peterson et al., 2004). One of the key characteristics of Seyfert galaxies is their optical spectra. These are shown in Figure 1.3 with two Seyfert galaxy optical spectra from Netzer (1990). The top spectrum of Mkn 290 shows both broad-line emission and narrow-line emission (e.g. $H\beta$ line is doppler broadened due to the 'fast' moving material), whereas the bottom spectrum of Mkn 270 only possesses stronger narrow-line emission. The former highlights an orientation where the observer can see both the 'Broad-Line Region' (BLR) and 'Narrow-Line Region' (NLR) of the Active Nucleus; these are known as Seyfert 1 or Type 1 galaxies. The latter highlights an orientation where the BLR is obscured by a dusty torus, leaving only the NLR visible along our line of sight; these are known as Seyfert 2 or Type 2 galaxies. The typical line widths for the

BLRs and NLRs are $\times 10^3 - \times 10^4 kms^{-1}$ and up to several hundred kms^{-1} respectively. Both of the Mkn 270 optical spectra profiles are ubiquitous within the unified models of AGN, as it will be shown with regards to the other classifications, such as quasars discussed later.

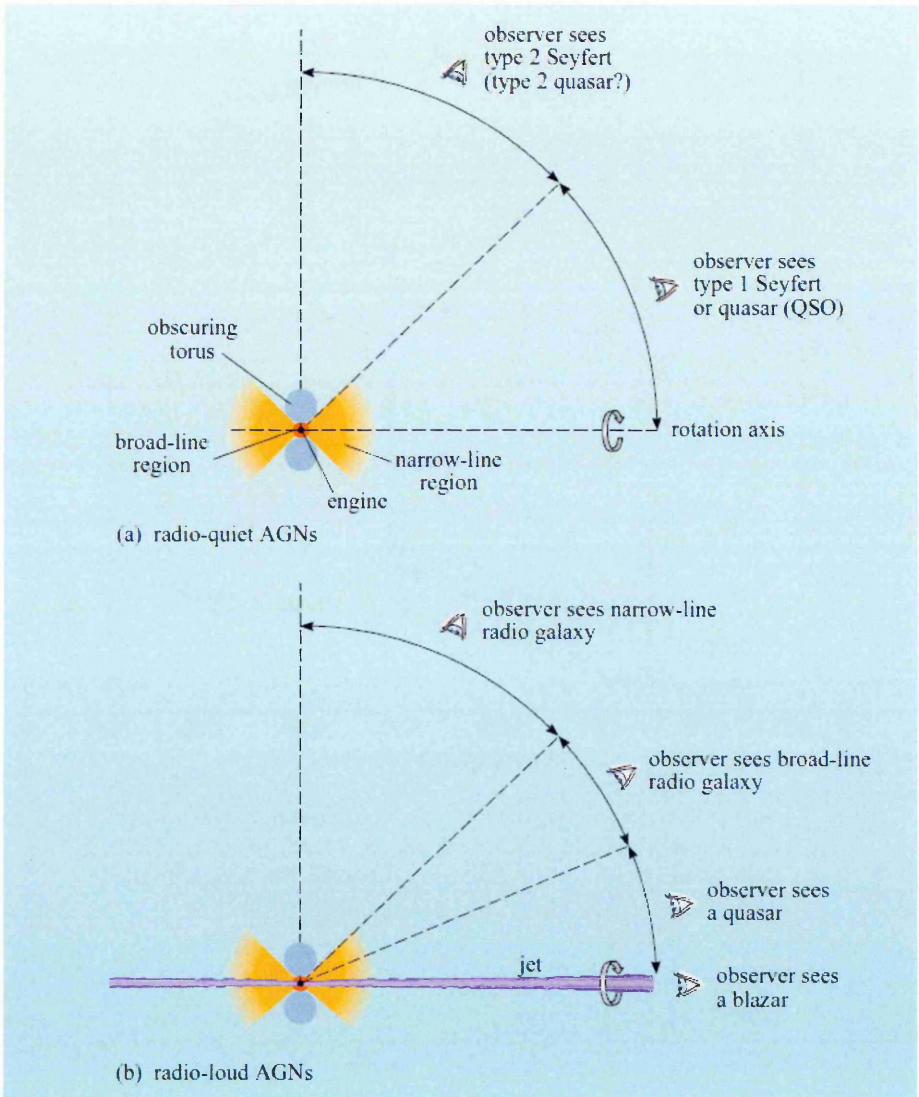

Figure 1.2. This represents a standard unified model of AGN; (a) represents the observations and classifications attributed to radio-quiet AGN; (b) represents the observations and classifications attributed to radio-loud AGN. Taken from Jones & Lambourne (2004).

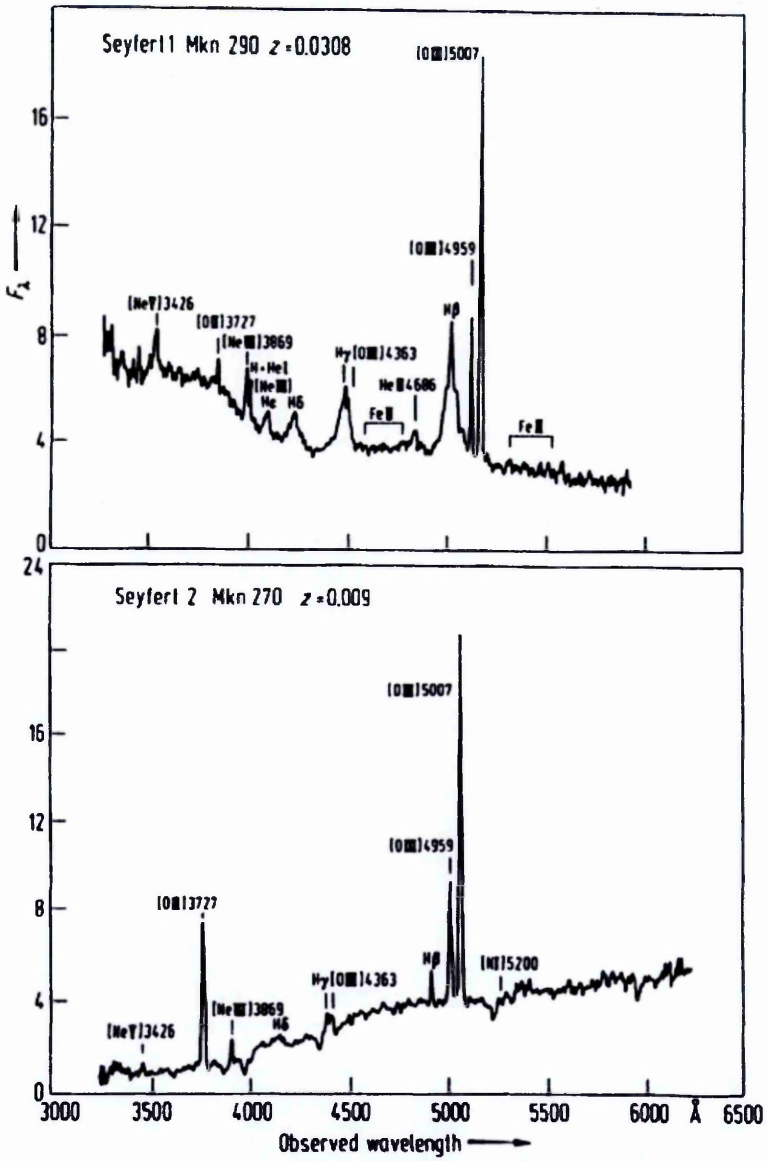

Figure 1.3. Two Seyfert optical spectra; notice the broad features of the top spectrum compared to the absence of these features in the bottom spectrum. This is what defines Seyfert 1 and Seyfert 2 objects respectively. Taken from Netzer (1990).

1.1.2 Quasars

Quasars are extremely similar to Seyfert galaxies, and as such they are both commonly grouped together. The fundamental differences that distinguish quasars from Seyferts, however, are the more apparent point-like nature of quasars due to their great distances, hence the name 'quasar' which is derived from 'quasi-stellar object (QSO)'. Also, the optical spectra of the known lines and features characteristic to Seyferts are also present in quasars but typically lie at greater redshifts. Figure 1.4 highlights the redshifted optical spectra of the first identified quasar 3C 273 by Schmidt (1963) with a luminosity of $\sim \times 10^{14} L_{\odot}$, providing more clarity to

the idea of unified models depicted in Figure 1.2. It should be noted that there is no clear dividing line between the luminosities of Seyferts and Quasars, as they are merely distinguished by the observer's ability to resolve the host galaxy or not respectively.

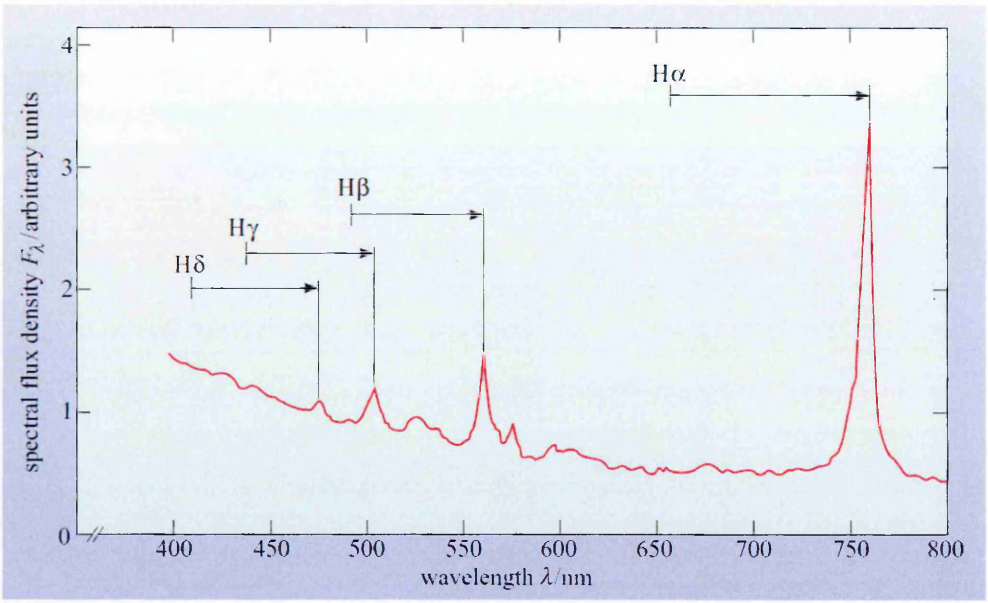

Figure 1.4. Optical spectrum of quasar 3C 273 by Schmidt (1963), notice how it has similar broad features to a Seyfert 1 object. The arrows indicate the amount of redshift that has occurred due to the distant nature of quasars, leading to believe it is an AGN hosting galaxy with point-like emission. Taken from Jones & Lambourne (2004).

1.1.3 Radio Galaxies

Approximately 10% of AGN are known as "radio-loud" (Hooper et al., 1995), which as the name suggests, implies the presence of radio emission. This radio emission is strong and typically presented in the form of prominent radio lobe pairs that emanate from the central nucleus itself (Jones & Lambourne, 2004), commonly with jets, and these features stretch out towards vast distances from $10s - 100s$ of kpc as shown in Cygnus A (Figure 1.5). In Figure 1.2, with regards to the common AGN Unification model, the radio-loud categorisation exhibits more sub-categories than those AGN that are radio-quiet; the Seyfert classification is dropped with the addition of the radio galaxy classification. Heckman & Best (2014) refer to radio AGN being in "jet mode", in reference to the primary AGN feedback emission output caused by the collimated particle driven jets producing the radio-emitting lobes. These radio lobes are caused

by cocoons of optically thin synchrotron emission within the bow shocks from radio jets penetrating the ISM and IGM (see Figure 1.5). Radio-loud AGN can also be further characterised by the presence of 'edge-darkened' or 'edge-brightened' lobes, which are so named Fanaroff-Riley (FR) type I and II respectively.

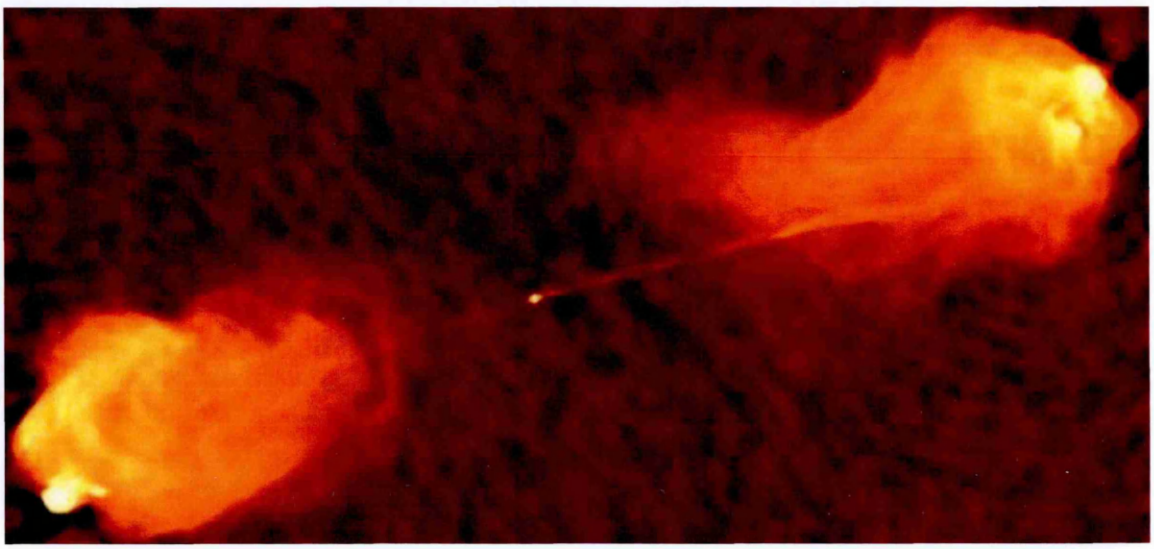

Figure 1.5. This radio image shows Cygnus A; you can clearly see the two lobes representing material being 'blown away' along the tightly constrained jet that transverses from the source AGN at the centre. This jet seemingly appears fainter towards the left lobe, presumably as a result of our line of sight. Perley et al. (1984).

1.1.4 Blazars

Blazars are a classification exclusive to radio-loud AGN that also appear point-like, presented in the unification model of Figure 1.2 as our line of sight looking directly down the jet itself, where the inclination angle is $\sim 0°$. The first object identified as such was BL Lacertae (BL Lac), initially thought to be an irregular variable star (Hoffmeister, 1929) it was later found by Schmitt (1968) that there was a strong radio emission coming from the object. Subsequently Oke & Gunn (1974) observed its redshift to be $z = 0.07$ determined from resolving the host galaxy's absorption spectral lines; making BL Lac too distant and luminous to be an irregular variable star. As a result, these types of objects are known as BL Lacs, where they present a variable continuous spectrum with little to no emission features characteristic of a jet and thus far most of them have been found to have a host elliptical galaxy (see Figure 1.6). Another

category of a blazar is the Optically Violent Variable (OVV), and as the name suggests presents an emission of vastly varying brightness from hours to days (Jones & Lambourne, 2004). OVVs are similar to BL Lacs, with the exception that they have some broad-line emission features, and tend to be present at greater redshifts. It should be noted that the speeds of these relativistic jets cannot be measured directly, meaning a blueshift of these jets cannot be compared well with the redshift of the host galaxy.

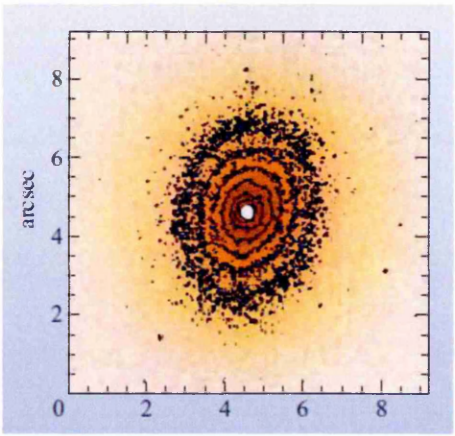

Figure 1.6. An Example of a resolved BL Lac object taken by the Hubble Space Telescope; the isophotes clearly indicate the presence of a host elliptical galaxy (BL Lac 05480-322). Taken from Jones & Lambourne (2004).

1.1.5 Non-Active Starburst Galaxies and ULIRGs

Galaxies are considered 'active' due to the presence of bolometrically-significant supermassive black hole accretion that leads to the great amount of energy released ultimately from the gravitational binding energy, this is what leads to what we know as AGN that harbour tiny regions in the cores of their host galaxies. There are also 'non-active' galaxies that possess dormant nuclei such as our Milky Way. However, there is another type of non-active class of galaxy that is known as a 'starburst galaxy'. As the name suggests a starburst galaxy's principal source of emission comes from intense star formation processes, and can produce infrared (IR) luminosities as a result of their star formation on average of $\sim 10^{8-10} L_{\odot}$ (e.g. Brandl et al., 2006; Kennicut et al., 1998a). These objects do not necessarily contain an active nucleus.

There are however other luminous galactic objects that generate luminosities up to $\sim 10^{12-13} L_{\odot}$ (e.g. Higuera & Ramos, 2013; Farrah et al., 2007) in the infrared; these unusual objects are known as Ultra-Luminous Infrared Galaxies (ULIRGs). There is a lot of confusion and debate on what the actual source of this highly luminous emission that emanates from these galaxies is. However, there is a consensus that the source of this radiation is either from an AGN component or even a heavily starbursting galaxy of greater infrared luminosity. Most studies (e.g. Elbaz et al., 2011; Farrah et al.,2007) compare a sample of varying starbursting and AGN-hosting galaxies by their strength of the star formation with that of the fine structure lines. This information is used to infer the presence and strength of the AGN component (e.g. [OIV] and [NeV]) to determine which candidate is responsible. It is suggested that it could be, in part, a combination of both an AGN and starbursting regions. Possibly as a result of mergers between two galaxies (e.g. Farrah et al., 2007; Dasyra et al., 2006; Clements et al., 1996).

1.1.6 The M-σ Relation

This thesis hopes to ascertain whether or not there is a good correlation between the AGN activity and stellar mass growth in the bulge by using the physical sizes of the star formation regions from the nucleus, however, what is this based on? Magorrian et al. (1998) first noticed from a sample of 36 nearby galaxies that their supermassive black hole masses correlated with their bulge luminosities. In succession Ferrarese & Merritt (2000) analysed parameters of a sample of spiral and elliptical galaxies to find a surprising tightly correlated relation between the mass of the supermassive black holes (typically between $\sim \times 10^{6} - \times 10^{10} M_{\odot}$) and the velocity dispersion of their host bulges. Gebhardt et al. (2000) follows on from this by generating a luminosity-weighted velocity dispersion that represents the stellar kinematics within the bulge, an example of this tight correlation can be seen in Figure 1.7. From these works it was concluded that the mass of the supermassive black hole growth must be in some way dependent on or constrained by the stellar mass growth in the host galaxy's bulge.

Many attempts are now being made to try and understand this correlation. The most commonly sought and widely accepted view is that this relation implies a feedback mechanism

where black hole growth and stellar mass growth in the bulge are somehow regulating or feeding each other. Considering that the same gas could feed star formation and the AGN, there is cause for a possible link between AGN activity and stellar mass growth as they feed off of each other's processes. Therefore, by testing this through constraining the physical size of star formation regions around AGN, perhaps it is possible to indicate whether or not AGN activity and star formation activity are as closely and tightly correlated as $M - \sigma$.

It is worth noting, however, how remarkable that such a tiny region that produces the high power output from AGN (as the scale shows in Figure 1.1) can have such an influence over larger scales throughout its host bulge.

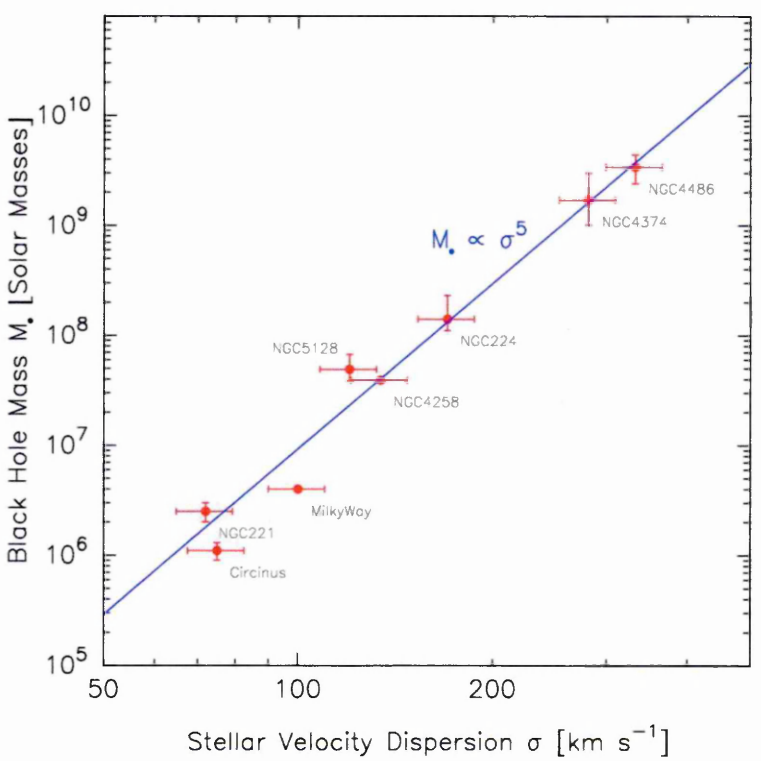

Figure 1.7. A representation of the $M - \sigma$ relation. Here it can be clearly seen that the black hole mass and stellar velocity dispersion of the host bulge have a remarkably tight correlation with errors limited to observational errors. Taken from Wikipedia (2016).

1.2 Star Formation in Extragalactic Objects

Star Formation (SF) can be found ubiquitously in many young galaxies like our own Milky-Way Galaxy. SF, however, is not exclusive to non-active galaxies but is also present within distant quasar hosting galaxies (Serjeant et al., 2010; Lutz et al., 2008; Schweitzer et al., 2006). SF is important in helping us determine the physical and chemical nature of galaxies and their evolution. This knowledge enables us to see how parameters such as metallicity, gas density and varying radiation fields can affect SF and how SF can, in turn, have an impact on the environment it lies within.

Therefore, this section will briefly overview star formation from an extragalactic context, and how this relates to the IR luminosity, PAH emission and quasars that are the focus of this work.

1.2.1 A brief Introduction to Star Formation

The process of SF can be easily thought of as a system that requires an input of 'fuel' to obtain the resultant output of stellar birth. Therefore, the amount of fuel available can determine the rate at which these stars can be formed, with the fuel being the gas in the respective galaxy's interstellar medium. The surface density of Star Formation Rate (SFR) has been found to possess a power-law relationship with the surface density of gas available; this is the so-called 'Schmidt Law' (Schmidt, 1959):

$$\Sigma_{SFR} = A\Sigma_{gas}^{n} \tag{1.1}$$

where Σ_{SFR} is the surface density of star formation, A is a proportionality constant and Σ_{gas}^{n} is the surface gas density. The value of n has been shown by observations to be in the median range between 1 and 2. Kennicutt (1998a) states $n = 1.4$, for example.

However, the means by which one can observe the presence of SF are not direct, and deducing quantitative information such as the SFR requires calibration to what is known from observations of the nearest analogue, the Milky Way. For example, we know from the local Interstellar Medium (ISM) that newly forming O and B stars are found in *HII* regions; the emission of UV photons from the star ionises the surrounding gas (Phillipps, 2005; Kutner, 2003). This process induces Balmer line emission, predominantly with $H\alpha$ lines.

Therefore, the presence of these $H\alpha$ lines can be used to indicate the presence of newly forming stars within other galaxies (Kennicutt & Kent, 1983). This has shown to be a very popular and shared tracer as discussed by Kennicutt & Evans (2012), and this can be extended into determining the SFR of each galaxy in turn if it is assumed that the total $H\alpha$ luminosity is entirely contributed by the UV photons from O and B stars, that an Initial Mass Function is known to determine the number of O and B stars formed and that the star formation has been constant given a significant timescale. This conversion can be then demonstrated by the following formula (Kennicutt, 1998b):

$$SFR(H\alpha)\ (M_{\odot}\ yr^{-1}) = 7.9 \times 10^{-42} L(H\alpha)\ (ergs\ s^{-1}) \qquad (1.2)$$

where $L(H\alpha)$ is the $H\alpha$ luminosity, allowing for an observational estimate of $SFR(H\alpha)$, which is the mass of stars formed per unit time in the units of $M_{\odot}yr^{-1}$.

However, stellar $H\alpha$ emission can underestimate the SFR due to the presence of dust (Lonsdale & Helou, 1987). This deficit is the result of attenuating dust that surrounds the young stars in these nebulous regions. If one knows the extinction of the atomic line due to dust, one can compensate for the effects of dust although this is only possible if the SF regions are themselves resolvable (Dopita et al., 2002). When consideration is taken for distant objects such as distant quasars, any $H\alpha$ emission will often be redshifted out of the optical into the infrared. There is also a risk of the SFR being overestimated from $H\alpha$ emission due to contaminating UV radiation from the nucleus of an active galaxy that would also excite the $H\alpha$ line, an effect that is more

prominent when dealing with an object with a highly luminous AGN component. Using $H\alpha$ emission is an example of one of the key 'classical indicators' of SF. However, SF also produces IR radiation, and therefore IR emission could be used instead to remove the burden of dust attenuation. This absorption no longer becomes a problem in the IR because dust absorbs the stellar optical/UV light and remits it in the IR, therefore, granting greater transparency on determining rates of SF.

1.2.2 Star Formation in the IR and AGN

At the IR end of the spectrum of SF galaxies ($1 - 1000\mu m$), the emission due to the dust that enshrouds these young stars becomes prominent. In turn, this emission is the result of the dust absorbing the energy output of the OB stars that they obscure, leading to the re-radiation of this absorbed energy as thermal emission as suggested by Devereux & Young (1990). This inference relies upon current theories and models of stellar formation itself. Therefore, if IR dust emission is used as an SF tracer its proposed origin should be considered. Massive OB stars are born within their dusty molecular clouds, starting on the main sequence on which they will spend the majority of their lives. They then irradiate the surrounding dusty material. The dust within this material absorbs the UV photons from these young stars and then re-emits the UV photons into the IR and submm continua, giving rise to the IR emission as it expands and cools/relaxes (Alonso-Herrero et al., 2006; Phillipp, 2005). Determining the SFR from the total IR luminosity can be calculated by integrating across the IR emission spectrum to obtain the total IR luminosity $L(IR)$. Therefore, due to the SFR correlating with the $L(IR)$ we can use a proportionality constant similar to equation 1.2 with the same assumptions to give a theoretical value for $SFR(IR)$ (Kennicutt, 1998b):

$$SFR(IR)\ (M_{\odot}\ yr^{-1}) = 4.5 \times 10^{-44} L(IR)\ (ergs\ s^{-1}). \tag{1.3}$$

Observational comparisons between the emission of $H\alpha$ photons and those of the IR continuum have shown that the total IR luminosity correlates with the SFR to a better degree than that of $H\alpha$ (Kennicutt, 1998b). An example of this is shown below in Figures 1.6 and 1.7 taken from Kewley et al. (2002).

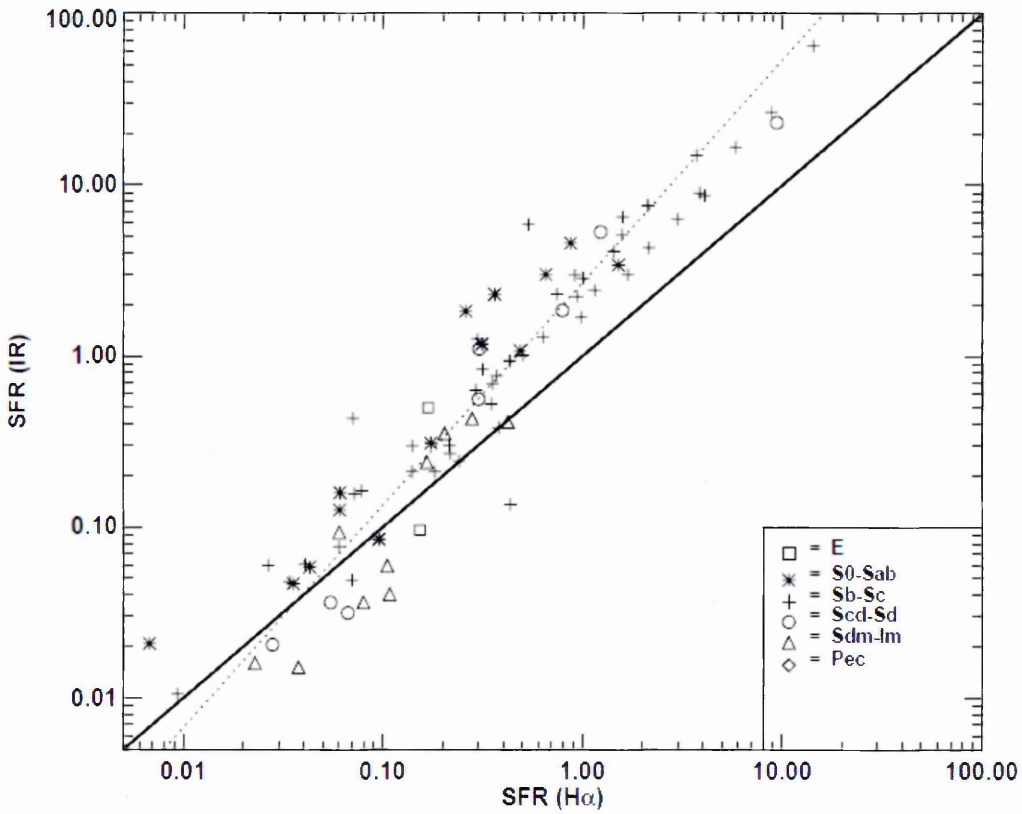

Figure 1.6. A correlation between the IR and uncorrected $H\alpha$ determined SFRs, with the dashed line representing the correlation of the uncorrected $H\alpha$. The solid line represents the trend if directly correlated. Taken from Kewley et al. (2002).

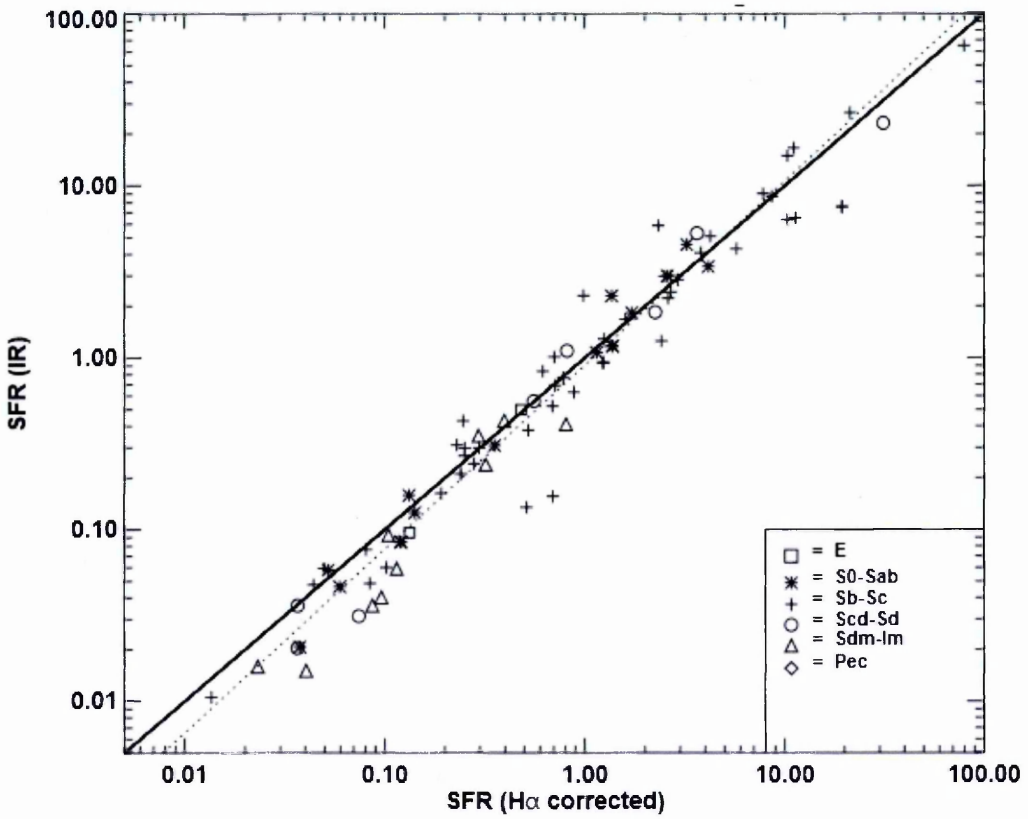

Figure 1.7. As Figure 1.6, a correlation between the IR and the corrected $H\alpha$ determined SFRs. After correction for reddening the IR and $H\alpha$ SFRs show a fairly tight correlation. Taken from Kewley et al. (2002).

In relation to those galaxies with an AGN component, however, studies of ULIRGs (e.g. Farrah et al., 2007) demonstrate that an AGN component can also contribute to the total IR luminosity as well as any IR luminous starbursts. Therefore, trying to analyse or ascertain the SFR from more distant, and thus unresolvable, AGN such as quasars is difficult. This burden is a result of the 'bleeding' of IR emission from the nucleus into its host galaxy of an apparent point-like source, arising from the inability to disentangle the origin of the IR emission spatially.

However, in recent works (e.g. Hernán-Caballero et al., 2015; Alonso-Herrero et al., 2014; Lutz et al., 2008) an alternative tracer of SF and, therefore, the SFR has been exploited. This alternative tracer can potentially solve the problems of AGN contamination, and this tracer is the near-infrared emission of 'Polycyclic Aromatic Hydrocarbons' (discussed further in Chapter 2). Polycyclic Aromatic Hydrocarbons (PAHs) allow the ability to probe the SF within these seemingly hostile environments, and by extension, provide an opportunity to answer the science goals of this thesis.

Chapter 2

POLYCYCLIC AROMATIC HYDROCARBONS (PAHS)

From what was discussed in Chapter 1, star formation cannot be observed and determined accurately through optical indicators such as $H\alpha$ emission. The $H\alpha$ luminosity commonly represents a smaller fraction of the total star formation from extragalactic sources as a result of the $H\alpha$ luminosity being obscured by dust (e.g. Kewley et al., 2002). Moreover, the AGN can contribute to the $H\alpha$ emission, causing an overestimate in SFR values. With this in mind one can turn to the infrared end of the spectrum as discussed in Chapter 1, namely the wavelengths of the Unidentified Infrared (UIR) bands, which are currently attributed to Polycyclic Aromatic Hydrocarbons (PAH) (Allamondola et al., 1985; Léger & Puget, 1984). PAHs are found to be ubiquitous across the Universe, from Young Stellar Objects and Evolved Stars (e.g. AGBs, Planetary Nebulae etc.) to the Interstellar Medium and Galaxies, and have even been detected up to redshifts of $z \sim 2.8$ (Lutz et al., 2008).

Therefore, this Chapter shall explore these PAHs, and how they can be used to trace the Star Formation around AGN.

2.1 INTRODUCTION TO PAHS

PAHs are hydrocarbon compounds. These molecules form because of the flexible bonding nature of carbon atoms. The base of these molecules is made up of 6 carbon atoms and 6 hydrogen atoms bonded together to form a planar hexagonal shape, as shown in Figure 2.1. This structure is held into place by the carbon atoms having 3 localised electrons forming covalent bonds, with the remainder fourth electron forming delocalised double bonds across the ring. This co-location gives us a 'Benzene Ring'. Hydrocarbons arranged into similar shapes and structures such as these are known as 'aromatic' and can form multiple chains bonded together. These can, therefore, form what we know as Polycyclic Aromatic Hydrocarbons, where the carbon-hydrogen (C-H) bonds are substituted with more carbon-carbon (C-C) giving rise to a chain of planar hexagonal rings, again as shown in Figure 2.1 (Peeters, 2002).

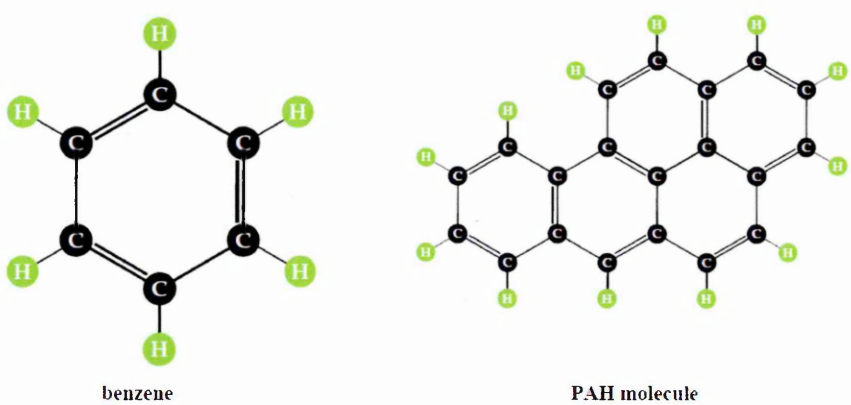

Figure 2.1. On the left we have a typical benzene ring demonstrating the planar hexagonal structure, and on the right an example PAH molecule which shows how the hydrogen atoms are displaced for carbon atoms appropriately depending on the shape and structure of the chain. Taken from Peeters (2002).

2.1.1 PAH Emission

These ubiquitous PAH molecules are detected through characteristic broad emission features in the mid-infrared spectrum that commonly peak at wavelengths 3.3, 6.2, 7.7, 8.6, 11.3 and 12.7μm. The size of the molecules responsible for these features is generally believed to be ~50 – 150 carbon atoms (Peeters, 2002; Tielens et al., 1999). In Figure 2.2 various carbon-

hydrogen (C-H) and carbon-carbon (C-C) vibrational bending and stretching modes are illustrated. These modes give rise to the infrared emission of the broad PAH features that are seen in Figure 2.3.

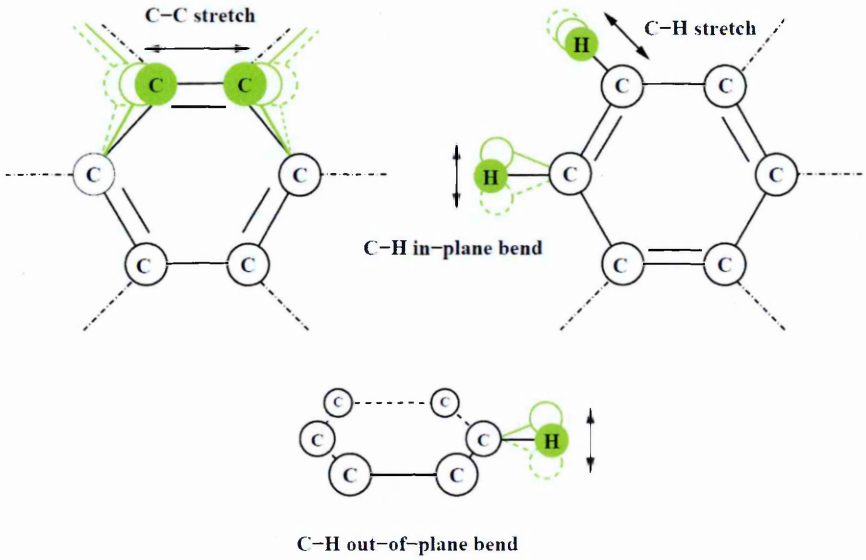

Figure 2.2. Here we can see an illustration of an individual hexagonal ring, and how the different physical stretching and bending modes between C-C and C-H bonds give rise to the emission features we see peaking at their specific wavelengths. Taken from Peeters (2002).

These PAHs reside within interstellar dust. The precise nature of this dust (size, structure and composition) is not clearly known, however, they are believed to be composed of several components, such as carbonaceous and silicate grains frosted onto icy mantles in dense clouds. There are three main types of grain that can be distinguished from their size and properties: The PAHs and amorphous hydrocarbons contain tens to thousands of carbon atoms and have sizes in the range from $0.4 - 1nm$, and these grains are stochastically heated and produce prominent emission bands in the mid-IR region. At mid-IR wavelengths (e.g. in the IRAS 25 and $60\mu m$ bands) the global emission has been attributed to larger carbonaceous grains of sizes about $1 - 10nm$ called Very Small Grains (Desert et al., 1990). Finally, the FIR-mm dust emission ($100\mu m - 1mm$) is attributed to what are called the Big Grains (BG), which are a mixture of $(10 - 100nm)$ amorphous carbon and silicate grains (e.g. Compiegne et al. 2010, Li

& Draine, 2001; Weingartner and Draine, 2001) and these are in thermal equilibrium with the interstellar radiation field.

In the context of these dusty star-forming regions, Chapter 1 highlighted how PAHs can be used to trace stellar formation. Newly forming stars emit predominantly in the UV, however from Chapter 1 we know this UV radiation irradiates the surrounding gas and dust that enshrouds the star forming regions. Thus, the optical SFR become poor tracers due to extinction. Despite this, we also know PAHs are abundant in these regions meaning they too become irradiated by the stellar UV photons. This excites the PAH molecule to a greater energy state and as the molecule relaxes, it does so as prescribed in Figure 2.2 through the bending and stretching of the many C-C and C-H bonds. Producing IR photons as the broad features at the wavelengths shown in Figure 2.3 (Peeters, 2002).

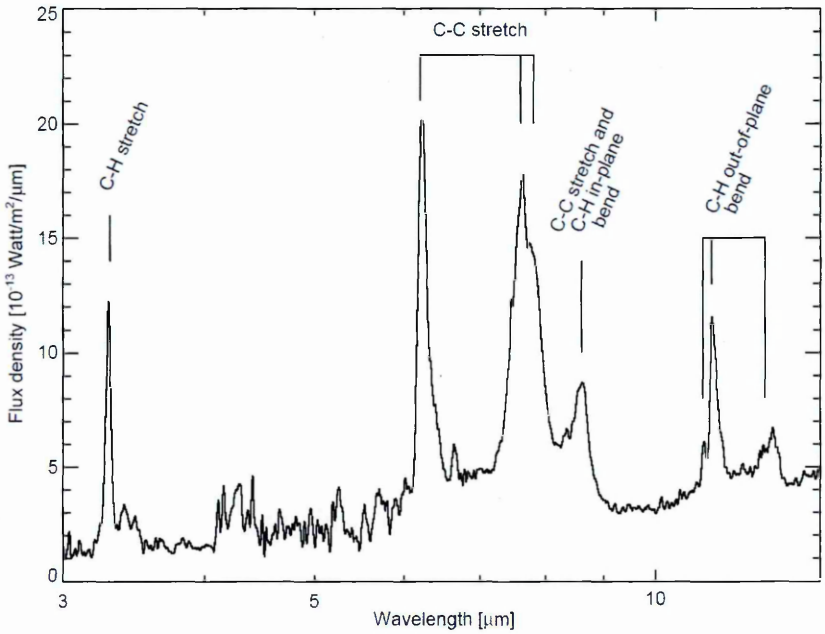

Figure 2.3. This spectrum shows the profiles of the PAH emission features. Each of these features correlates to the stretching and bending modes as depicted in Figure 2.2. Taken from Peeters (2002).

2.1.2 The PAH Profile

The different PAH features depicted in Figure 2.3 are commonly known at their peak wavelengths stated in 2.1.1. However, it was noted in Peeters et al. (2002) that the PAH emission, in particular 6.2, 7.7 and 8.6μm, has slightly varying features: the profile, shape and peak wavelength. Subsequently these PAHs are classified into bands A,B and C of increasing peak wavelength (see Figure 2.4).

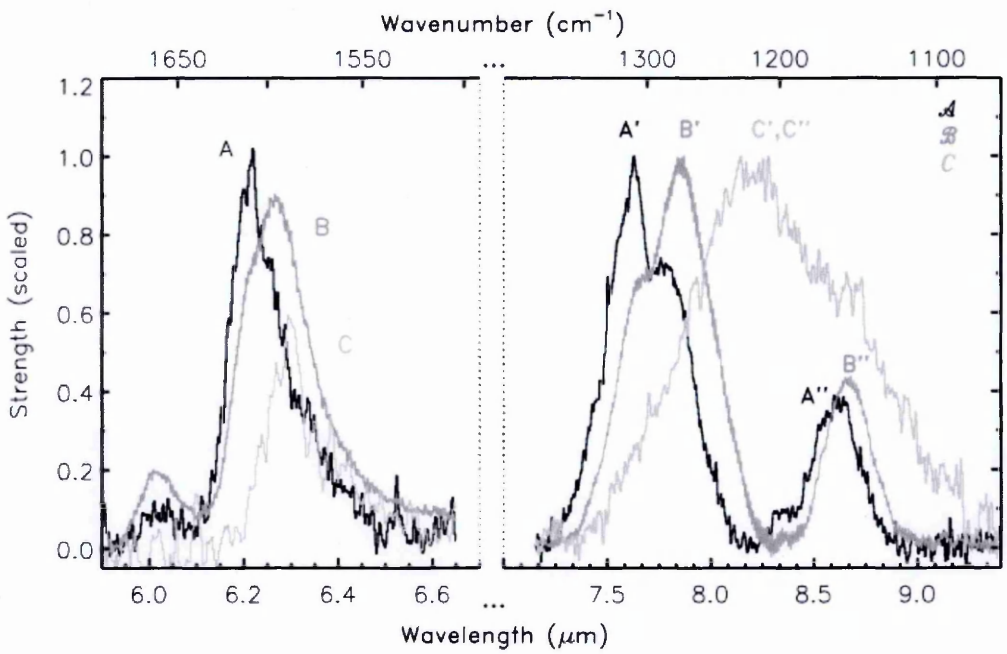

Figure 2.4. The PAH emission features 6.2, 7.7 and 8.6μm and their respective classes A-C. These classes are detailed in table 1. Taken from Peeters et al. (2002).

The current train of thought that highlights the responsible mechanism for these shifted profiles is that they portray greater reprocessing of the carbonaceous dust from classes C-A (Peeters et al., 2002): Class A commonly associated with YSOs and ISM/*HII* regions; Class B with Planetary Nebulae and isolated Herbig AeBe stars; Class C with AGB/Post-AGB/evolved stars (e.g. Sloan et al., 2007). Table 1 below defines each of these classes for each of the PAH features that this is known to affect.

Characteristics					
$6.2\mu m$ PAH		$7.7\mu m$ PAH		$8.6\mu m$ PAH	
Class	λ_{peak}	Class	Component	Class	λ_{peak}
A	~6.22	A'	7.6	A''	~8.6
B	6.24 – 6.28	B'	7.8	B''	> 8.62
C	~6.3	C'	8.22	C''	none

Table 1. The PAH emission features 6.2, 7.7 and $8.6\mu m$ and their respective classes A-C are detailed here. λ_{peak} represents the peak of the PAH class, except for the $7.7\mu m$ which has multiple components of a varying dominant peak between the classes. Reproduced from Peeters et al. (2002).

2.1.3 PAHs and Star Formation in AGN

The PAH emission process, as explained and demonstrated in Figure 2.2 and Figure 2.3, has the useful by-product of being a tracer of SF (Peeters et al, 2004). This concept has been aided by further work of various studies on AGN/quasar host galaxies that also show the presence of star formation. Farrah et al., (2007) show how the $6.2\mu m$ PAH feature tightly correlates with the total IR luminosity and by extension we can, therefore, determine the SFR based upon a simple formula similar to equation 1.3 as shown below:

$$SFR(PAH)\ (M_{\odot}\, yr^{-1}) = 1.18 \times 10^{-41} L_{PAH}\ (ergs\ s^{-1}) \qquad (1.4)$$

The use of PAHs as tracers of star formation is now common practice when it comes assessing many areas of extragalactic astrochemistry, from starburst galaxies to quasars (e.g. Alonso-

Herrero et al., 2014; Bernard-Salas et al., 2009b; Brandl et al., 2006). In particular, PAHs have been found ubiquitously in AGN/quasars up to redshifts of $z \sim 2.8$ using the Spitzer Space Telescope (Lutz et al., 2008). PAHs have even been resolved in local AGN (e.g. Alonso-Herrero et al., 2014), which have 11.3μm PAH detections within their nuclear regions as close as 10pc away from the AGN's harsh radiation fields, indicating a stronger resilience to destruction by the molecule due to the AGN than first thought. This is particularly the case when the PAH molecules are protected from the AGN radiation fields by greater column densities of intervening dust.

2.1.4 PAH Ionisation Fraction

There is a remarkable effect that the ionisation of the PAH molecules has on the overall IR spectral profile, and this effect has been shown in numerous laboratory studies (e.g. Kim et al. 2001; Langhoff 1996). It is evident from these studies that when PAH molecules are in ionising environments, the relative intensities of the PAH emission from 6.2, 7.7 and 8.6μm increases (see Figure 2.5).

From Figure 2.3 the PAH emission at 3.3μm, 11.3μm and 12.7μm are due to the C-H bonds, with the emission from 6.2, 7.7 and 8.6μm due to the C-C bonds. The emission from the C-C bonds is enhanced when the PAHs are ionised compared to the neutral case, as shown in Figure 2.5. This emission process is caused by the increased stretching vibration activity, altering the charge distribution of the molecule and thus creating a stronger oscillating dipole. With the C-H bonds, the opposite is true and the oscillating dipole strength is reduced, causing the intensity to diminish in ionised environments (Peeters et al., 2002). This consequence means an ionisation fraction can be determined by the strength of the ionised PAHs of 6.2, 7.7 and 8.6μm, and that of the neutral cases 3.3μm, 11.3μm and 12.7μm. Strongest of these PAH features are the ones belonging to 6.2, 7.7 and 11.3μm in which can, therefore, be used as a proxy for the stellar radiation field strengths.

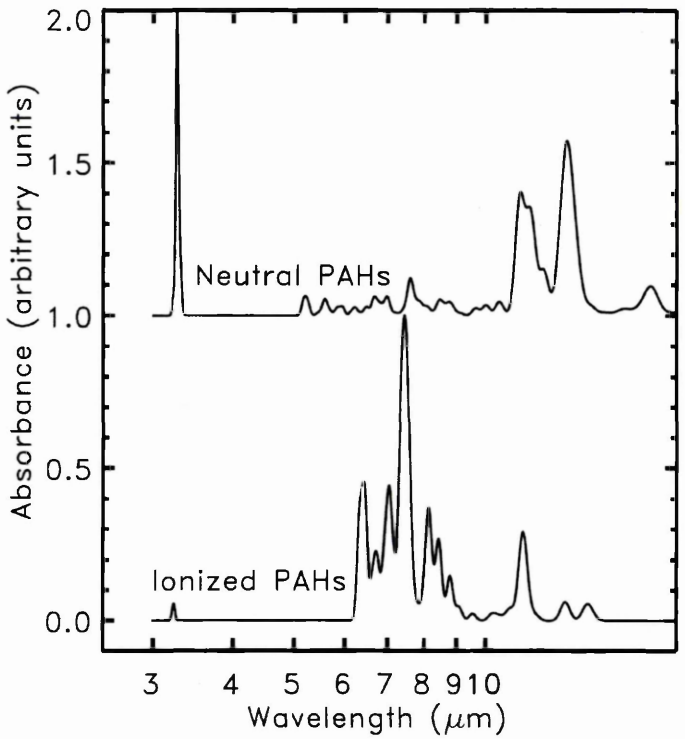

Figure 2.5. This profile shows the response of the PAH molecules when present in ionising environments compared with those that are neutral. The relative intensities of those between $5\mu m - 10\mu m$ have their features enhanced by ionisation and those outside of this range are weakened (Peeters et al., 2002; Allamandola et al., 1999).

2.2 THE SPITZER SPACE TELESCOPE

For this project spectral data from the Spitzer Space Telescope's (SST) on-board Infrared Spectrograph (IRS) has been used.

This sub-section shall now discuss the details of the instrumentation and mission, as well as the direct predecessors that show the evolution of space-based IR spectroscopy.

2.2.1 Previous Missions

In January 1983, the Infrared Astronomical Satellite (IRAS), the first space-based IR telescope, was launched to overcome the restrictions of the narrow wavelength 'windows' as a result of the limiting transparency of Earth's atmosphere on the ground. The filters were centred at four infrared wavelengths of the IR spectrum that cannot be observed from the ground: $12, 25, 60\ and\ 100\mu m$ (Pouw, 1983). The mission lasted for ten months until it ran out of the cryogen. IRAS produced a sensitive, unbiased IR survey of the sky (mapping 96% of the entire sky) with a series of new catalogues, containing point sources, extended sources less than 8′, low-resolution IR spectra from the low-resolution spectrometer and finally an atlas of the absolute surface brightness of the sky itself (Beichman et al., 2002). The mission was also successful in discovering new comets, many extragalactic objects and the discovery of the PAH emission features (Harland, 2015), which supplied its successor space-based telescopes with a plethora of potential observing targets.

One such successor was the European Space Agency's (ESA) Infrared Space Observatory (ISO, Kessler et al., 1996). Launched in November 1995, the mission lasted over two years until the helium cryogen depleted in April 1998. The mission provided a greater focus on spectroscopy with the Short-Wavelength Spectrometer (SWS, de Graauw et al., 1996), and the Long-Wavelength Spectrometer (LWS, Clegg et al., 1996) giving a combined spectral coverage of $2.4 - 196\mu m$. ISO provided instrumentation that was of greater sensitivity and with superior spatial resolution when compared to IRAS, vastly improving the science products. Its

successes include the first discovery of crystalline silicates, the development of quasar evolutionary scenarios and most importantly the discovery that PAHs are ubiquitous (Bernard-Salas, 2015; Salama, 2007).

2.2.2 The Spitzer Space Telescope

The SST (Werner et al., 2004) derives its name from Lyman Spitzer Jr. who was a prolific figure in astronomy for his work on stellar plasma physics, the pioneering of Infrared Spectroscopy, and also known for also suggesting the relatively 'simple' idea of placing into space telescopes that could combat the problems of the atmospheric absorption and aberration.

Initially named the 'Space Infrared Telescope Facility' (SIRTF) the first draft proposal was to have a primary mirror of $1.2m$, roughly double the size of both the IRAS and ISO telescopes with a sensitivity that was to be a thousand times greater with data extraction speeds from its targets that were over a million times faster than any current programme operating at these wavelengths (Bahcall, 1991; Witteborn, 1976). However, due to budget cuts to NASA by the US government, the initial and outlandish brief was never met, reducing its operational and technical specifications. The resultant telescope was still one, however, of greater sensitivity and had a primary mirror at $85cm$ providing greater spectral and spatial resolution than ISO or IRAS. This instrumental power allowed for PAHs to be scrutinised to a level they could never have been before, from a variety of astronomical objects. To prevent the instruments from becoming over saturated, the instrument needed to be kept cool and protected from the Sun; it does this by lagging behind Earth's orbit.

Onboard the SST there are three science instruments: The Infrared Spectrograph (IRS), the Infrared Array Camera (IRAC) and the Multiband Imaging Photometer for Spitzer (MIPS).

The next few subsections will discuss the on-board instrumentation. Such as the IRS instrument, which is the source of the data used within this project.

2.2.2.1 *The Infrared Spectrograph (IRS)*

The IRS (Houck et al., 2004) is the principal on-board spectrograph for the SST. It covers a wavelength range of roughly $5 - 38\mu m$ with two long-slit low-resolution modules and two cross-dispersed high-resolution echelle modules available across the entirety of this wavelength coverage. These modules produce their spectra via diffraction gratings that disperses the light onto $128 \times 128px$ CCD arrays. Each of the modules, their wavelength coverages and resolutions are presented in Table 2 below; spectral resolution is defined as $R = \lambda/\Delta\lambda$, where λ is the wavelength observed and $\Delta\lambda$ being the smallest difference in wavelengths that can be distinguished from the observed wavelength of λ.

Module	Wavelength Coverage (μm)	Resolution
Short-Low (SL)	5.2 – 14.5	60 – 127
Long-Low (LL)	14.0 – 38.0	57 – 126
Short-High (SH)	9.9 – 19.6	~600
Long-High (LH)	18.7 – 37.2	~600

Table 2. A breakdown of the IRS modules, their respective wavelength coverage and spectral resolution.

All of the spectra in this thesis have been observed in 'staring mode'. This mode is for the direct observation of objects where spectra can be obtained from variable exposure times, which is as the name suggests, effectively staring at the chosen target. For both of the low-resolution modules there exists two overlapping sub-slits, known as orders: SL2, SL1, LL2 and LL1 (e.g. where SL2= Short-Low Order 2, see Figure 2.6), with the SH and LH modules possessing ten orders each. These orders represent the incremental increase in wavelength (i.e. SL2 = 5.2 – $7.7\mu m$ and SL1= $7.4 - 14.5\mu m$, see Figure 2.6), and each of the orders in the SL and LL modules observes their targets in two nodding positions or 'nods'; nod 1 and nod 2 (e.g. SL2 nod 2 and SL2 nod 1), each of which lies one-third and two-thirds along the length of the slit. The two pointings for the two nodding positions allows the observer in the data reduction stages to

subtract the background effectively from their data, enhancing any spectral features present and also this redundancy in the data allows to facilitate for the identification and removal of glitches.

During the observation of a target in a low-resolution module, the 'peak-up' cameras on IRS are used to help point and centre the telescope onto the object for the requested module(s) and order(s). The telescope uses two pointings in each order for the two nods when observing a target, the resultant spectra of each nod and order are then recorded for the chosen integration times and number of cycles/images taken. Observations in a high-resolution module only require a single pointing for the entire wavelength coverage thanks to the echelle grating, however, 'off-observations' are made in order to subtract background noise during the reduction stages.

There are various applications and uses for both high and low-resolution modules depending on the target object: the high-resolution modules can disentangle more detail from a target source, its observations are particularly ideal for extracting and analysing atomic line spectra from sources, compared to the low-resolution modules that cannot disentangle the same amount of information from the observations as the high-resolution modules can. The low-resolution modules do possess greater sensitivity than their high-resolution counterparts and are therefore more suitable for performing observations of broad dust features emanating from dim, distant objects such as quasars (Houck et al., 2004). An illustration of the dimensions, the IRS modules and peak-up arrays are shown in Figure 2.6.

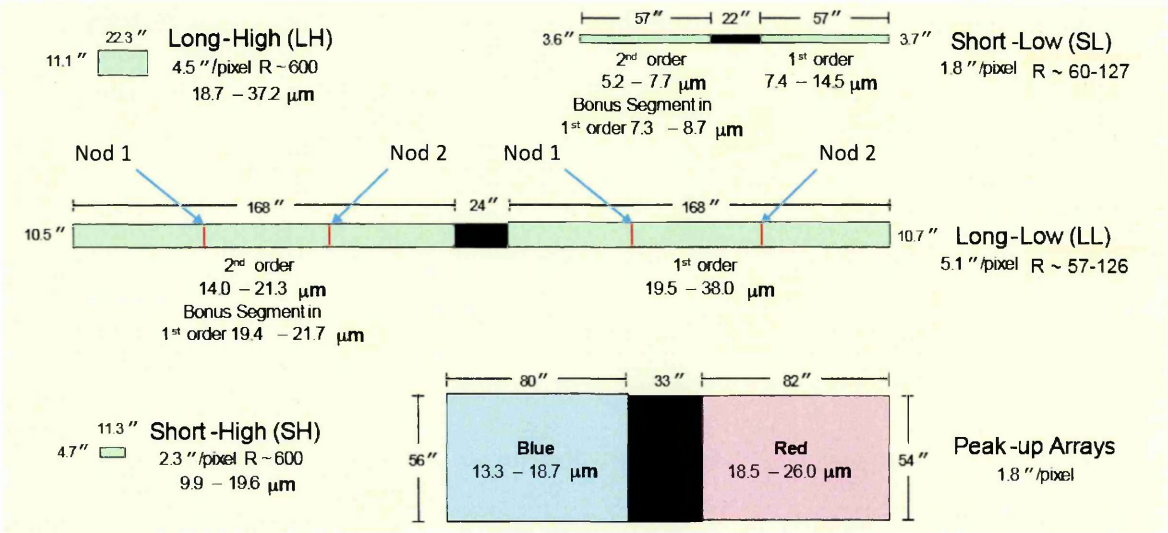

Figure 2.6. Illustration and dimensions of the IRS Modules, Orders, and Peak-up Arrays. Examples of the nodding positions are shown also along with the 'bonus' third orders, which are not used, as they are not well calibrated (Houck et al., 2004).

The wavelength coverage of this instrument is perfectly situated within the range of the PAH emission profiles as discussed earlier, including those quasars that lie at greater redshifts. The description of the data reduction and tools used will be discussed in Chapter 3.

2.2.2.2 The Infrared Array Camera (IRAC)

IRAC (Fazio et al., 2004) is an imager with a $5.2' \times 5.2'$ field of view with four channels at $256px \times 256px$ each that support simultaneous imaging centred at wavelengths $3.6, 4.5, 5.8\ and\ 8.0\mu m$, with the simultaneous imaging operating in pairs ($3.6\mu m$ and $5.8\mu m$; $4.5\mu m$ and $8.0\mu m$). The wide field of view enables the imager to image whole galaxies at redshifts $1 < z < 5$, with the primary goal of imaging the stellar emission that peaks at $\sim 1.6\mu m$ with the channels whose centroids lie at $3.6\mu m\ and\ 4.5\mu m$. With the $5.8\mu m\ and\ 8.0\mu m$ channels being aptly suitable for imaging PAH features (for objects not redshifted), and due to the simultaneous imaging that is enabled in the pairs as described it can actively map these features within the images.

2.2.2.3 The Multiband Imager for Spitzer (MIPS)

The MIPS (Rieke et al., 2004) is an imaging photometer that operates at the centred wavelengths $24\mu m, 70\mu m$ *and* $160\mu m$; it can also perform low-resolution spectroscopy ($R = 15 - 25$) for the purpose of measuring the Spectral Energy Distributions (SEDs) between $52 - 97\mu m$ of extragalactic sources. The $24\mu m$ detector chip has an array of $128px \times 128px$, the $70\mu m$ detector chip has an array of $32px \times 32px$ and finally the $160\mu m$ detector chip possesses a smaller $2px \times 20px$ array. These arrays were used only for imaging photometry.

2.2.3 Current Mission Status

The SST, like its predecessors, had a limited lifespan with its limited supply of helium cryogen which depleted in May 2009. Thus, ended the 'cool-phase' of the mission, where the IRS and MIPS instruments can no longer obtain any viable data due to oversaturation of the sensitive electronics. The SST mission current exists, however, as a "warm-mission" in which the IRAC instrument can still take images with its two remaining channels centred at wavelengths $3.6\mu m$ and $4.5\mu m$.

Since the initial launch of Spitzer, however, a new IR space-based mission has already been launched and has exhausted its cryogen; the ESA's Herschel Space Observatory launched in May 2009. Herschel had a substantially larger primary mirror than Spitzer's at $3.5m$ with instruments operating at greater sensitivity and resolution observing from the far-Infrared to sub-mm wavelengths in the range of $55 - 672\mu m$, Herschel's cryogen depleted in April 2013.

A future mission that is set to continue this work certainly is the James Webb Space Telescope (JWST) due for launch in 2018. It will operate between wavelengths $0.6 - 28.5\mu m$ utilising a $6.5m$ primary mirror, which is set to boast even greater sensitivity and spectral resolution that will better detect and resolve PAH features than the SST. Therefore, JWST can and will help to advance the work done in this thesis and beyond (see Chapter 7).

Chapter 3

CONSTRAINING THE PHYSICAL SIZE OF SF REGIONS

Quasars, as it has been discussed, can be enigmatic objects when it comes to understanding and answering questions about their nature. Quasars possess a highly luminous source of emission across small scales with an apparent correlation between the host galaxy's stellar mass growth and the central black hole mass. This apparent correlation leads to the focus of this Chapter: to constrain whether the SF present in quasars correlates spatially with a quasar's activity, through the measurement of the PAH extent (this will be discussed in detail later in the Chapter).

In order reach the science goals IR spectral data of a selection of quasars must first be obtained. This Chapter will describe the sample and how its objects were selected, how the PAH extent was measured, along with the results.

3.1 METHODOLOGY

This section describes the key methodological steps in how the Spitzer IRS spectra were selected and extracted, along with the subsequent steps involved in measuring the angular sizes of the emission caused by the PAH molecules corresponding to the wavelengths as discussed in Chapter 2.

3.1.1 Sample Selection

The project consists of sample data of 63 quasars, where the data were originally obtained through using the Spitzer IRS instrument from across a variety of different observing programmes. The process by which this data were mined is as follows:

1. Using the Caltech (2015) hosted programme database, keyword terms involving quasars e.g. "Quasar" or "QSO" were searched.
2. Any relevant programmes to these keywords were noted with their Programme ID (PID) number, and using the PID, were subsequently checked in the Cornell Atlas for Spitzer/IRS Sources (CASSIS) (Lebouteiller et al., 2011) to see if the observing programmes contained low-resolution IRS data. The low-resolution data are favoured due to the greater sensitivity of the modules to compensate for the relatively dim nature of quasars, therefore, are better suited to observing the broad spectral features such as those of PAH emission from the continuum.
3. If low-resolution IRS data were present within a programme, the individual object data within each were further analysed by eye for any PAH emission using the built-in CASSIS spectrum viewer. Those objects with PAH emission were noted with their unique Astronomer Observation Request (AOR) keys, as well as noting on the numbers of programmes involved.

This process was repeated for 177 programmes that were identified as having observed quasars. 79 out of the 177 programmes had low-resolution IRS data and 10 out of those 79 programmes contained objects with PAH features, in total leading to the 63 objects in the sample two separate populations at low-z ($z \leq 1$) and the other in high-z ($z > 1$). These two populations are arbitrary, and are merely the result of what data is available in the archive. The resultant sample is detailed in Table 3. The remaining 69 programmes containing quasars lack PAH features due to a sensitivity bias, meaning the lack of PAH features in these programmes is due to the sensitivity/flux limits of the instrumentation. Future telescopes (see Chapter 7) could disentangle more PAH features from a greater number of quasars, such as the ones found in the 69 spitzer programmes, than the sample in this thesis contains.

PID	AOR Key	Object Name	Coordinates[a]		Redshift (z)[ab]	d_A (Mpc)[c]	Spitzer Order/M
			α_{J2000}	δ_{J2000}			
20083	14014464	[VV2006] J171818.2+584905	17h 18m 18.2s	58° 49' 05.00"	0.634	1414	SL1+SL2+LL1+L
	14015744	FLSVLA J171106.7+590436	17h 11m 06.7s	59° 04' 36.00"	0.462	1206	SL1+SL2+LL1+L
	14016256	[VV2010c] J171324.2+585548	17h 13m 24.2s	58° 55' 48.00"	0.610	1389	SL1+SL2+LL1+L
	14017024	[PCE2006] 1404	17h 24m 58.35s	59° 15' 45.80"	0.494	1251	SL1+SL2+LL1+L
49	4163840	2MASS J00070361+1554238	00h 07m 03.61s	15° 54' 23.80"	0.114	426	SL1 +SL2
	4164096	2MASS J01203157+2003278	01h 20m 31.57s	20° 03' 27.80"	0.087	335	SL1 +SL2
	4165632	IRAS F16574+1838	16h 59m 39.77s	18° 34' 36.90"	0.171	601	SL1 +SL2
	4165888	2MASS J17144277+2602485	17h 14m 42.77s	26° 02' 48.50"	0.163	578	SL1 +SL2
	4166400	2MASS J00505570+2933381	00h 50m 55.7s	29° 33' 38.10"	0.136	497	SL1 +SL2
	4166656	2MASS J01083516+2148186	01h 08m 35.16s	21° 48' 18.60"	0.285	886	SL1 +SL2
	4166912	2MASS J01572105+1712484	01h 57m 21.05s	17° 12' 48.40"	0.213	715	SL1 +SL2
	4168192	[VV2000] J125807.5+232922	12h 58m 07.50s	23° 29' 22.00"	0.259	828	SL1 +SL2
	4168448	2MASS J13070066+2338050	13h 07m 00.66s	23° 38' 05.00"	0.275	864	SL1 +SL2
	4168960	2MASS J14533151+1353587	14h 53m 31.51s	13° 53' 58.7.0"	0.139	506	SL1 +SL2
	4169472	2MASS J16370022+2221140	16h 37m 00.22s	22° 21' 14.00"	0.211	709	SL1 +SL2
	4169984	2MASS J22255425+1958372	22h 25m 54.25s	19° 58' 37.20"	0.147	530	SL1 +SL2
30314	18027008	LBQS 0018-0220	00h 21m 27.35s	-02° 03' 33.62"	2.596	1651	LL1 + LL2
	18027264	[VV2000] J023233.1-211726	02h 32m 33.1s	-21° 17' 26"	2.162	1710	LL1 + LL2
	18027520	[VV2006] J041327.2+102743	04h 13m 27.2s	10° 27' 43.00"	2.837	1614	LL1 + LL2
	18027776	QSO J0812+4028	08h 12m 00.49s	40° 28' 14.35"	1.802	1741	LL1 + LL2
	18028032	QSO B0908+0603	09h 11m 27.61s	05° 50' 54.28"	2.793	1621	LL1 + LL2
	18028288	[VV2000] J100517.5+434609	10h 05m 17.44s	43° 46' 09.29"	2.095	1717	LL1 + LL2
	18028800	LBQS 1230+1627B	12h 33m 10.43s	16° 10' 52.90"	2.735	1630	LL1 + LL2
	18029312	QSO J1415+1129	14h 15m 46.25s	11° 29' 43.40"	2.560	1656	LL1 + LL2
	18029568	QSO B1611+4719	16h 12m 39.92s	47° 11' 57.50"	2.396	1679	LL1 + LL2
	18028544	QSO B1104-181	11h 06m 33.39s	-18° 21' 23.80"	2.305	1692	LL1 + LL2
20142	14193408	2MASSI J1118302+402553	11h 18m 30.20s	40° 25' 53.00"	0.154	552	SL1+SL2+LL1+L
	14194432	2E 2584	12h 04m 42.11s	27° 54' 11.70"	0.165	584	SL1+SL2+LL1+L
	14200064	2E 1519.0+2238	15h 21m 14.25s	22° 27' 43.80"	0.136	496	SL1+SL2+LL1+L
	14197504	2MASSI J1417008+445606	14h 17m 00.8s	44° 46' 06.00"	0.114	425	SL1+SL2+LL1+L
	14196224	2XMM J132349+654148	13h 23m 49.49s	65° 41' 48.20"	0.168	592	SL1+SL2+LL1+L
50508	26328320	2MASS J00501008+2806199	00h 50m 10.08s	28° 06' 19.90"	0.277	869	SL1+SL2+LL1+
	26334720	2MASS J22394602+1929549	22h 39m 46.02s	19° 29' 54.90"	0.194	664	SL1+SL2+LL1+
	26334976	2MASS J23030430+1624406	23h 03m 04.3s	16° 24' 40.60"	0.289	895	SL1+SL2+LL1+
	26334208	2MASS J17053665+2101380	17h 05m 36.65s	21° 01' 28.00"	0.271	855	SL1+SL2+LL1+
	26334464	2MASX J22374267+1456143	22h 37m 42.67s	14° 56' 14.30"	0.279	873	SL1+SL2+LL1+
	26330624	2MASS J10012116+2150112	10h 01m 21.16s	21° 50' 11.20"	0.248	802	SL1+SL2+LL1+
	26333440	2MASS J15215105+2251209	15h 21m 51.05s	22° 51' 20.90"	0.287	891	SL1+SL2+LL1+
50558	26413568	LEDA 2822178	00h 25m 49.16s	-26° 02' 12.62"	0.322	963	SL1+SL2+LL1+
	26413824	4C 05.16	03h 49m 46.5s	05° 51' 42.00"	0.339	988	SL1+SL2+LL1+
	26415104	LEDA 2830969	21h 27m 50.04s	-20° 42' 31.50"	0.636	1416	SL1+SL2+LL1+
242	13628416	QSO J0920+4531	09h 20m 14.11s	45° 31' 57.20"	0.402	1112	SL1+LL2
	13628672	[VV2010c] J115718.4+600345	11h 57m 18.4s	60° 03' 45.00"	0.491	1246	SL1+LL2
3231	10497536	2MASS J01051501-2612466	01h 05m 15.01s	-26° 12' 46.60"	0.114	426	SL1+SL2+LL1+
	10496000	2MASS J22023161-5657577	22h 02m 31.61s	-56° 57' 57.70"	0.083	322	SL1+SL2+LL1+
	10495744	2MASS J21573517+0114331	21h 57m 35.17s	01° 14' 33.10"	0.136	497	SL1+SL2+LL1+
	10494464	2MASS J15554606+1532218	15h 55m 46.06s	15° 32' 21.80"	0.131	481	SL1+SL2+LL1+
	10494208	2MASS J02542961+1509122	02h 54m 29.61s	15° 09' 12.20"	0.099	377	SL1+SL2+LL1+
	10491648	2MASS J03574895-1340458	03h 57m 48.95s	-13° 40' 45.80"	0.075	295	SL1+SL2+LL1+
	10491392	2MASS J23080919+0538305	23h 08m 09.19s	05° 38' 30.50"	0.146	527	SL1+SL2+LL1+
	10490624	2MASS J22565483-3649515	22h 56m 54.83s	-36° 49' 51.50"	0.086	333	SL1+SL2+LL1+
	10490368	2MASS J00285431-7726146	00h 28m 54.31s	-77° 26' 14.60"	0.087	336	SL1+SL2+LL1+
40330	22929920	2MASX J11182408+5602074	11h 18m 24.08s	56° 02' 07.40"	0.068	268	SL1+SL2+LL1+LL2
	22930432	LEDA 2600134	11h 33m 00.22s	60° 16' 27.60"	0.065	256	SL1+SL2+LL1+LL2
	22931968	NVSS J110909+455125	11h 09m 09.00s	45° 51' 25.00"	0.064	253	SL1+SL2+LL1+LL2
	23509504	NVSS J103228+121037	10h 32m 28.00s	12° 10' 37.00"	0.033	136	SL1+SL2+LL1+LL2
	23510016	NVSS J15574349+2727530	15h 57m 43.49s	27° 27' 53.00"	0.032	130	SL1+SL2+LL1+LL2
	23510528	2MASX J22385422+1311404	22h 38m 54.22s	13° 11' 40.40"	0.063	249	SL1+SL2+LL1+LL2
	23510784	2MASX J08004768+3743435	08h 00m 47.68s	37° 43' 43.50"	0.042	170	SL1+SL2+LL1+LL2
	23511040	2MASX J09040105+0127294	09h 04m 01.05s	01° 27' 29.40"	0.053	215	SL1+SL2+LL1+LL2
30715	18852608	[BKD2008] WR 525	12h 37m 41.19s	26° 42' 27.50"	0.021	87	SL1+SL2+LL1-
	18852864	Mrk 42	11h 53m 41.77s	46° 12' 42.60"	0.025	102	SL1+SL2+LL1-
	18853120	2MASS J04344153+4014216	04h 34m 41.53s	40° 14' 21.60"	0.020	86	SL1+SL2+LL1-

Table 3. Sample used in this study with the relevant Programme ID and AOR Keys along with the objects themselves and their coordinates. [a] Data were obtained from SIMBAD; [b] Data were obtained from the NED; [c] Values were determined using the 'iCosmos Cosmology Calculator' with a standard cosmology (see section 3.2.2.).

3.1.2 SMART: Data Reduction

After the data had been downloaded and organised appropriately, the data from the accrued sample were then reduced before the extents of the PAH emission features were measured during the extraction process using corresponding empirical Point Spread Functions (PSF). These PSFs represent the intrinsic profile of the optics of the telescope and varies with wavelength. Any source of emission that has a spatial profile smaller than that of the PSF's cannot be resolved as it becomes completely entangled within the PSF.

The reduction process is done by utilising the dedicated extraction routines for Spitzer's spectral data. The collective software package is the Spectroscopic Modelling Analysis and Reduction Tool (SMART) (Higdon et al., 2004). This software also includes the built-in optimal extraction package that was used for the measurement of the PAH emission's extent from the empirical PSF, this package is known as "Advanced Optimal" (AdOpt) extraction (Lebouteiller et al., 2010). Previous extraction methods, such as 'tapered column', rely upon using wide extraction windows that weight each pixel equally. Therefore, this means that the pixels are weighted whether there is a signal present or not in the pixel, meaning a lot of noise contaminates the data leading to a poor Signal-Noise Ratio (SNR). AdOpt enables the use of star-calibrated empirical PSFs for a series of different wavelengths, with the PSF's flux weighted against the source emission profile's flux incrementally pixel by pixel in the dispersion direction. The consequence provides spectra with a greater SNR than was previously possible. These routines are therefore ideal for disentangling information from spatially small and distant objects such as quasars/AGN. It shall also be noted that due to their apparent size and dim nature as a function of their distance, the low-resolution modules of the SST's IRS are adopted for their greater sensitivity, and as a result, no high-resolution data is used due to the lack of data. SMART utilises a Graphical User Interface (GUI), which allows for the reduction of the data, as well as to extract and review the resultant spectrum interactively (see Figure 3.1 for an example).

Starting with the original files generated from Spitzer's BCD pipeline, the so-called "level 1" data (defined below) are distributed into three separate '.fits.' Files: the raw image file, the BCD mask file and the uncertainty file. These three different files complement each other as single frame/exposure (each image frame consists of these three files). The following is a breakdown of the data reduction processes using SMART:

1. Of those quasars with PAH emission, their data were found from the Spitzer Heritage Archive (NASA, 2015) using each of their unique AOR keys to easily find the correct data. "Level 1" data were downloaded from the SHA, where level 1 data represented the "Basic-Calibrated Data" (BCD) sets of a non-reduced Spitzer pipeline, with the "Level 2" data representing the "Post-BCD" (PBCD) sets of already reduced data sets by the pipeline.
2. All of the available low-resolution files for a given object were imported into SMART's GUI. Each image frame was displayed in the window in their three separate files, after which all of the data were then converted into '3-Plane' data; the three separate files were then kept together after being merged into a single image file of each exposure, making data management easier.
3. With the newly combined 3-Plane data, they were then all individually processed through the 'IRSCLEAN' routine package. IRSCLEAN removes 'rogue'/bad pixels (i.e. pixels with significant variations in their responsivity over time) based off BCD mask files made for each observing campaign. IRSCLEAN also uses its own algorithms that determine the 'rogue' pixels from outlying flux values that are > 10 times the median uncertainty in the pixel values (see Figure 3.2). These pixels are substituted by the algorithms determining averages from the neighbouring 'normal' pixels.
4. The cleaned 3-pane data were then passed through a combined/stacked routine according to the Data Collection Event (DCE) of each file; all of the repeated exposures taken from the same nods and modules were then co-added together. Once complete, eight low-res files should remain (SL2, SL1, LL2 and LL1) depending on which orders

and modules were used in the observing run along with a file for each module order and 'nod' position (e.g. LL2 nod 1 and LL2 nod 2 etc.).

5. Finally, to reduce the background noise from each of the cleaned and combined exposure frames, the modules and their orders were passed through simple arithmetic routines present with SMART. These routines used simple subtraction of one nod from another. For example, the module and order LL2 with its two nods will be passed through the formulae $LL2\ nod\ 2 - LL2\ nod\ 1$ and $LL2\ nod\ 1 - LL2\ nod\ 2$. The result produces background removed versions, $LL2\ nod\ 2$ and $LL2\ nod\ 1$ respectively (See Figure 3.3. This subtraction process leads to positive and negative source emission profiles from each of the nods, as shown in Figure 3.4.

The background can also be removed via subtraction by order (i.e. $LL2\ nod\ 2 - LL1\ nod\ 2$). This method is useful if either both or one of the nods contaminate each other due to their proximity to each other on the CCD chip. It is preferred however that the reduction of the background is made via a nod subtraction, simply due to the nods being in closer proximity, meaning the background in each will also be closer, thus minimising any possibility of any large variances in the background compared with the errors induced in repointing between each order.

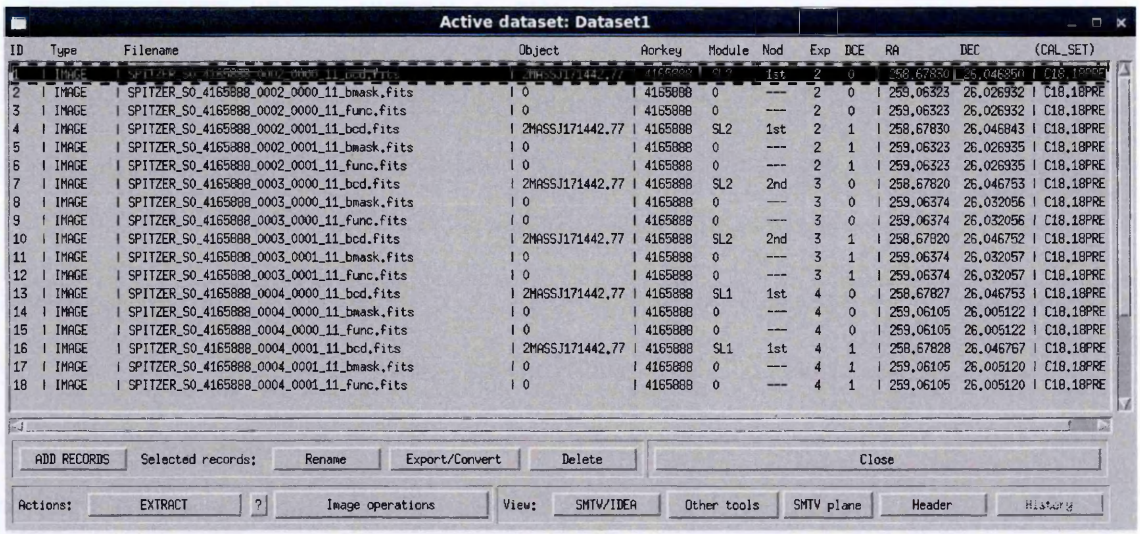

Figure 3.1. Illustration of the SMART GUI. Here the data files are imported ready for reduction and extraction.

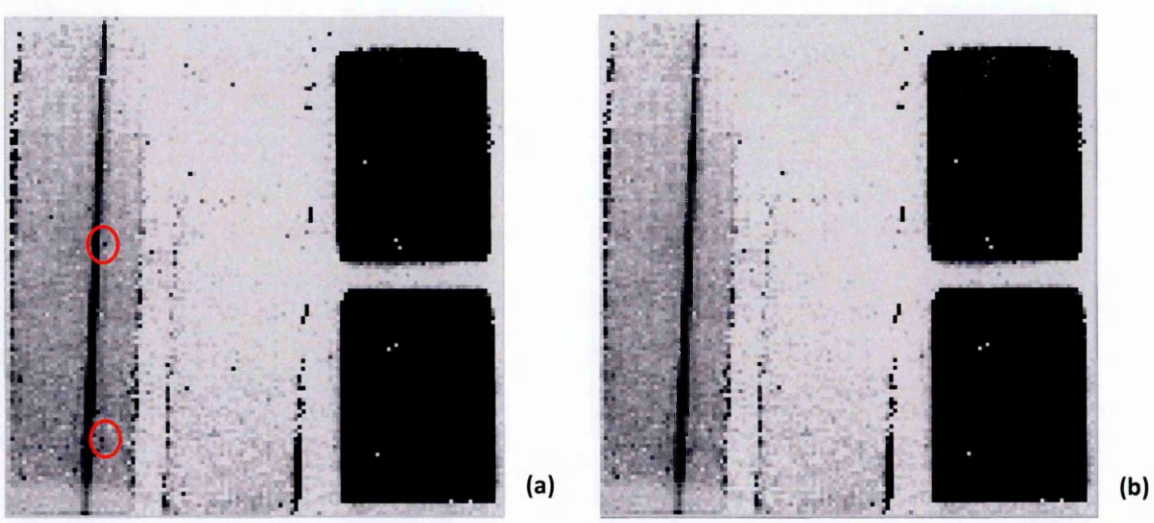

Figure 3.2. An illustration of the IRSCLEAN routine with the SL1 nod 2 CCD frame. In (a) there are some 'rogue' pixels, that are outliers relative to the count level (examples are highlighted in the red circles). In (b) the rogue pixels have been removed. Both images have the same greyscale.

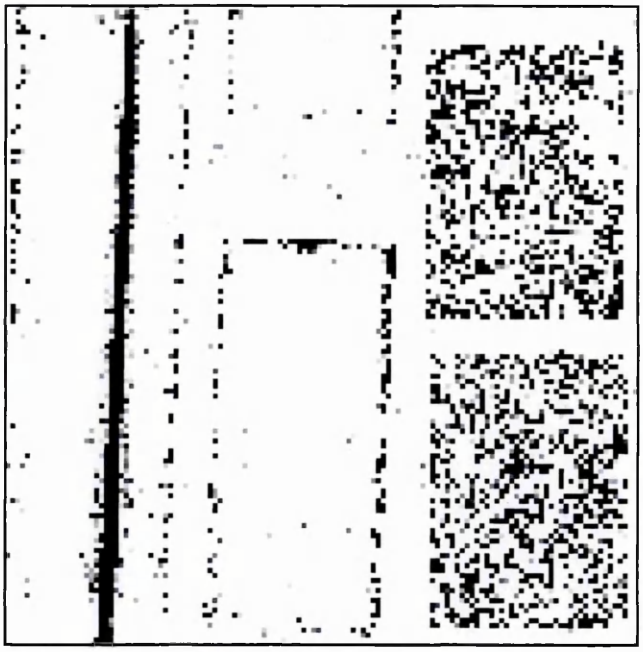

Figure 3.3. An illustration of the simple subtraction arithmetic routine with the $SL1\ nod\ 2 - SL1\ nod\ 1$. The subtraction of nod 1 from nod 2 of SL1 is shown, leaving behind the source signal as a strong black line with a few remaining rouge pixels.

3.1.3 SMART: Data Extraction and PAH Measurement with AdOpt

After the data reduction process, as described above, the built-in optimal extraction routines can now be utilised through the AdOpt package to measure the extension of the PAH emission. SMART in general, however, does possess three different methods of data extraction: Full Aperture, used for high-resolution data where a fixed column measures the full width of the slit; Tapered Column, a column extract that scales along with wavelength to account for the changing FWHM of the PSF; Optimal, an extraction that uses the PSF profile to weigh against the data, which is the primary extraction method used for this project. The process used in this thesis is detailed as follows:

1. For each module and nod, the data were extracted by the desired extraction method. The 'manual optimal extraction' was chosen to open and use the AdOpt package, as well as containing the specific routines that allow for the measurement of the PAH emission extent.

2. Running through the extraction process in AdOpt leads to a pixel by pixel weighting of the PSF flux to the source flux, providing the best SNR spectrum than previously possible with Spitzer's IRS instrument. The resultant spectrum is produced and shown along with the source position along the actual CCD slit image (see Figure 3.4 for an example). Using the CCD slit image and scrolling the cursor along the extraction line (where the y position increases in wavelength along the slit from top to bottom) the wavelength range of the PAH emission features within the spectrum is selected. Doing so allows for specific measurements along the dispersion direction to be made relative to the chosen wavelength, and this is done appropriately for each visible PAH feature.
3. Finally, the PAH extent is measured from the instrumental PSF via Gaussian fitting routines in AdOpt, calculating values of the ratio PAH_{FWHM}/PSF_{FWHM} as well as individual component values in both pixels and calculated into arcseconds (see Figure 3.5). These values were noted for each nod, order and module for each object.
4. After the extent measurements had been made using AdOpt's routines, all of the spectral data were then extracted from each object again using the automatic optimal routines. Thus, these were exported for each order and nod as '*.fits*' files, to enable them to be analysed by other routines for further analysis.

The extent measurements that were noted for each object were mean averaged across their respective nods for each order. The measurement data can be found in Table 4. Examples of the data extracted and plotted can be found in Figure 3.6.

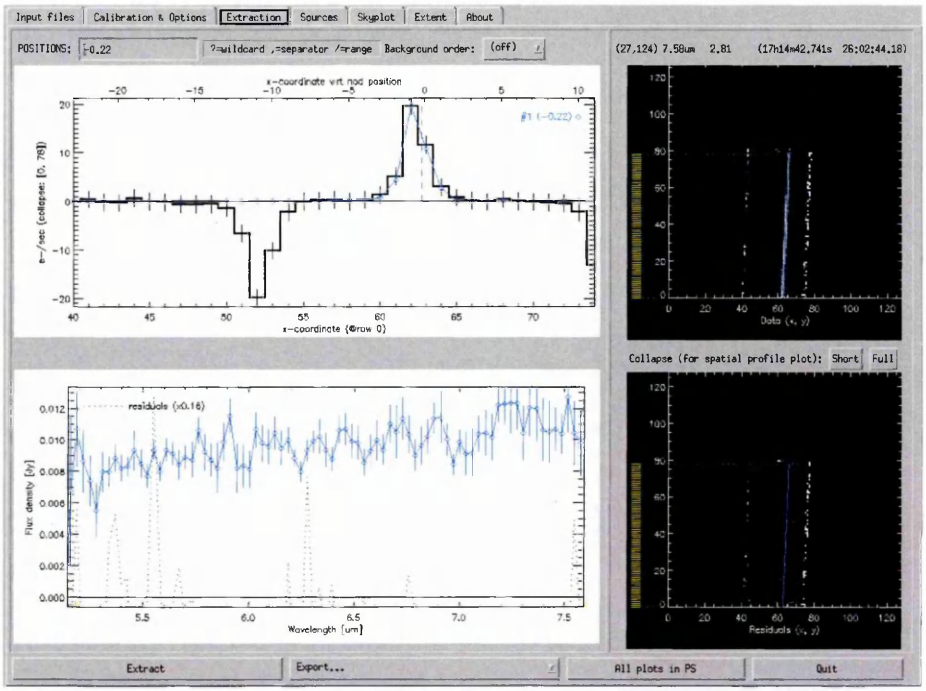

Figure 3.4. This is an example of the AdOpt manual extraction routine: top left is the source detector and shows the nod subtraction between nod 2 and nod 1 from the positive and negative profiles, bottom left is the extracted spectrum, top and bottom right is the CCD image of the slit and source traced by the blue line. The decrease in y pixel position indicates increasing wavelength, where a variance in the dispersion direction (x) weighted against the PSF provides the extent.

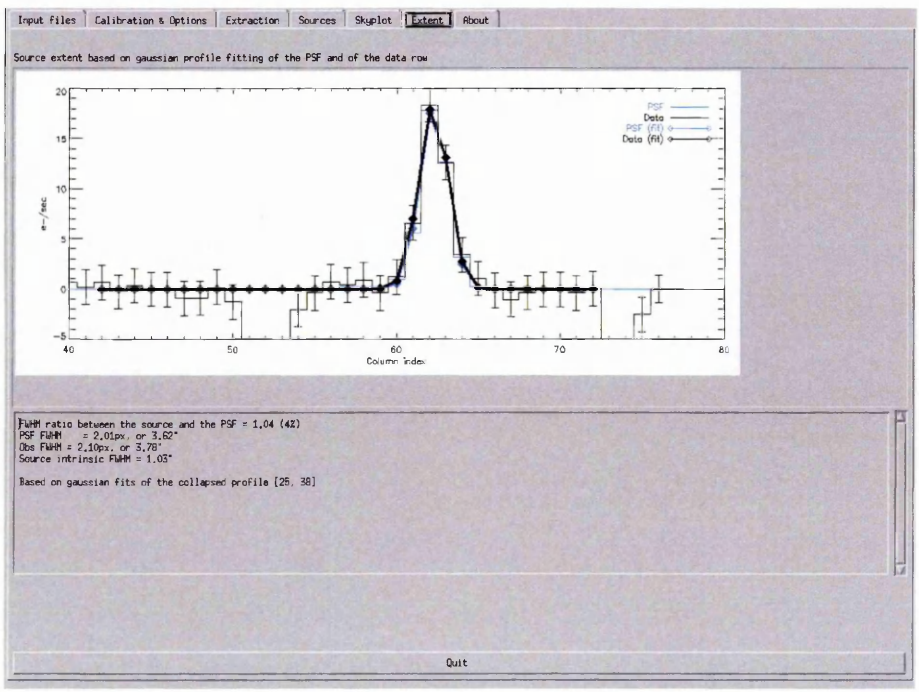

Figure 3.5. This is an example of the extent viewer: at the top the source emission (solid black line) and PSF (solid blue line) profiles are shown; at the bottom the calculated FWHM extent values are shown.

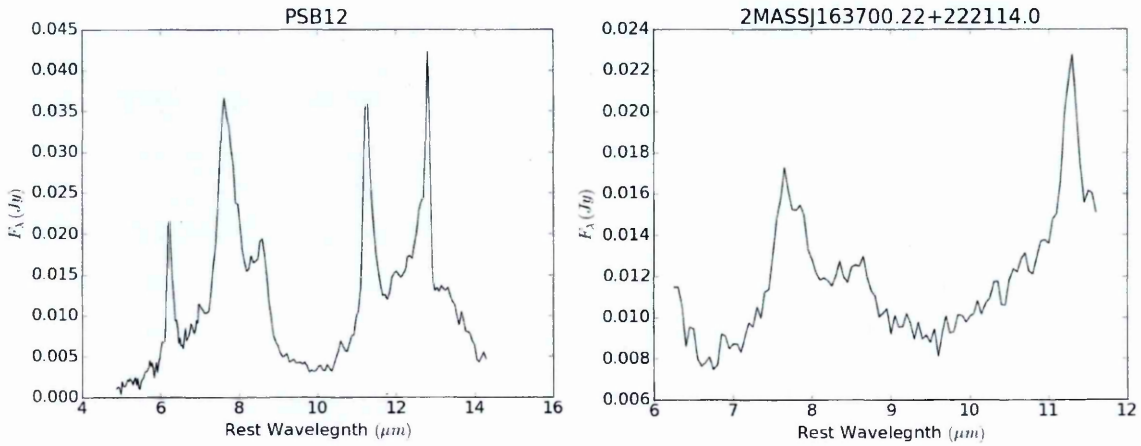

Figure 3.6. Example spectra from the author's python plotting routines.

PID	AOR KEY	Object Name	Distance (Mpc)[bc]	PAH Exention (FWHM/PSF)			
				6.2μm	7.7μm	8.6μm	11.3μm
20083	14014464	[VV2006] J171818.2+584905	1414	-	0.97	-	-
	14015744	FLSVLA J171106.7+590436	1206	-	0.97	-	-
	14016256	[VV2010c] J171324.2+585548	1389	-	0.95	-	-
	14017024	[PCE2006] 1404	1251	-	1.07	-	-
49	4163840	2MASS J00070361+1554238	426	-	1.12	-	1.09
	4164096	2MASS J01203157+2003278	335	-	1.6	-	1.4
	4165632	IRAS F16574+1838	601	-	1.01	-	0.99
	4165888	2MASS J17144277+2602485	578	-	1.18	-	-
	4166400	2MASS J00505570+2933381	497	-	1.06	-	-
	4166656	2MASS J01083516+2148186	886	-	1.02	-	-
	4166912	2MASS J01572105+1712484	715	-	1.04	1.03	-
	4168192	[VV2000] J125807.5+232922	828	-	1.01	-	-
	4168448	2MASS J13070066+2338050	864	-	1.06	0.98	-
	4168960	2MASS J14533151+1353587	506	-	1.05	-	-
	4169472	2MASS J16370022+2221140	709	-	1.03	-	-
	4169984	2MASS J22255425+1958372	530	-	1.05	-	-
30314	18027008	LBQS 0018-0220	1651	-	-	0.91	-
	18027264	[VV2000] J023233.1-211726	1710	1.09	0.97	-	0.87
	18027520	[VV2006] J041327.2+102743	1614	-	1.21	-	-
	18027776	QSO J0812+4028	1741	0.92	0.87	-	-
	18028032	QSO B0908+0603	1621	1.04	1.07	-	-
	18028288	[VV2000] J100517.5+434609	1717	1.05	1.11	-	-
	18028800	LBQS 1230+1627B	1630	0.9	0.88	-	-
	18029312	QSO J1415+1129	1656	1.04	1.04	-	-
	18029568	QSO B1611+4719	1679	1.01	1.02	-	-
	18028544	QSO B1104-181	1692	-	1.24	-	-
20142	14193408	2MASSI J1118302+402553	552	-	1.1	-	1.03
	14194432	2E 2584	584	1.03	1.04	-	-
	14200064	2E 1519.0+2238	496	-	1.02	-	-
	14197504	2MASSI J1417008+445606	425	1.17	1.05	-	1.01
	14196224	2XMM J132349+654148	592	1	1.04	-	1.02
50508	26328320	2MASS J00501008+2806199	869	1.87	1.88	2.11	1.83
	26334720	2MASS J22394602+1929549	664	1.51	1.07		1.3
	26334976	2MASS J23030430+1624406	895	1.5	1.03	1.11	1.16
	26334208	2MASS J17053665+2101380	855	-	1.04	-	-
	26334464	2MASX J22374267+1456143	873	-	1.04	-	-
	26330624	2MASS J10012116+2150112	802	0.96	1.14	0.92	-
	26333440	2MASS J15215105+2251209	891	-	-	-	-
50558	26413568	LEDA 2822178	963	1.54	1.63	1.29	-
	26413824	4C 05.16	988	1.18	1.02	-	-
	26415104	LEDA 2830969	1416	-	1.03	-	1.14
242	13628416	QSO J0920+4531	1112	-	1.02	-	-
	13628672	[VV2010c] J115718.4+600345	1246	-	1.01	1.01	-
3231	10497536	2MASS J01051501-2612466	426	1.31	1.17	1.49	1.39
	10496000	2MASS J22023161-5657577	322	1.47	1.46	1.54	1.49
	10495744	2MASS J21573517+0114331	497	1.34	1.2	1.44	1.27
	10494464	2MASS J15554606+1532218	481	1.72	1.78	1.91	1.86
	10494208	2MASS J02542961+1509122	377	1.82	1.37	1.75	1.77
	10491648	2MASS J03574895-1340458	295	1.21	1.08	1.19	1.09
	10491392	2MASS J23080919+0538305	527	1.4	1.45	1.59	1.48
	10490624	2MASS J22565483-3649515	333	1.87	1.15	1.31	1.34
	10490368	2MASS J00285431-7726146	336	1.65	1.32	1.72	1.4
40330	22929920	2MASX J11182408+5602074	268	1.15	1.04	1.06	1.02
	22930432	LEDA 2600134	256	1.19	1.09	1.09	1.09
	22931968	NVSS J110909+455125	253	1.16	1.21	1.1	1.22
	23509504	NVSS J103228+121037	136	1.16	1.11	1.32	1.2
	23510016	NVSS J15574349+2727530	130	1.2	1.23	1.25	1.12
	23510528	2MASX J22385422+1311404	249	1.08	1.15	1.12	1.13
	23510784	2MASX J08004768+3743435	170	1.11	1.22	1.26	1.12
	23511040	2MASX J09040105+0127294	215	1.12	1.1	1.19	1.16
30715	18852608	[BKD2008] WR 525	87	1.86	1.81	1.31	1.27
	18852864	Mrk 42	102	1.19	1.22	1.07	1.09
	18853120	2MASS J04344153+4014216	86	1.14	1.32	1.12	1.11

Table 4. The PAH_{FWHM}/PSF_{FWHM} ratios of each of the PAH emission peaks. Cells without values are where PAH emission extent couldn't be determined by AdOpt. [bc] See Table 3.

3.2 RESULTS

The relevant PAH emission data obtained and extracted from the objects, was then analysed. The following sections present the results of the obtained FWHM data. The most common/easy way to disentangle PAHs were used to compare any possible variance in the SF regions with cosmological redshift. The calculated physical angular diameters are also presented through the use of the simple geometric relation between the angular size of the PAH emission, and the angular diameter distance.

3.2.1 The FWHM PAH-PSF Ratios

Figures 3.7 and 3.8 are two plots that highlight the PAH_{FWHM}/PSF_{FWHM} ratio against the objects' redshifts for the $6.2\mu m$ and $7.7\mu m$ emission bands respectively. The error bars are estimated using a 'Monte Carlo' method, first measuring the standard deviation of the values that are less than or equal to 1, then multiplying this by the ratio of the standard deviation of a zero-mean Gaussian distribution with the standard deviation of negative values from that same Gaussian distribution. The grey band represents a 15% extent from the PSF as an arbitrary lower limit on what is considered to be an extended source of emission as advised by instrument specialists, which is in rough agreement with the 1σ estimate. Thus, the emission here is only considered to be significantly extended from the PSF if the ratio is $\gtrsim 1.15$. This value has been determined from the instrumental constraints and the limitations from the optimal extraction routines (Lebouteiller et al., 2010).

It should be noted that not all emission bands could have their PAH extents calculated from the PSF, meaning some PAH feature specific population sizes may be smaller/larger than others from the total sample. However, both Figures 3.7 and 3.8 show a similar relationship between the angular sizes and distance of each object, with angular size apparently increasing with decreasing redshift. This result is what is expected from the simple geometry, assuming the objects can be resolved from the PSF.

Figures 3.7 and 3.8 have two clear and distinct populations that can be seen, with one at low redshift $0 < z < 1$, and the other at high redshift $1.5 < z < 2.9$, a gap that could be potentially filled for future missions such as JWST. Regarding the extent, it can be seen that the emission in the brightest PAH feature ($7.7\mu m$) appears to be typically found at smaller scales than the $6.2\mu m$ PAH, despite the apparently large number being extended. Those objects at high redshift show apparent constraint to the PSF in Figure 3.7, whereas Figure 3.8 shows slightly more variation. This most likely signals that the high-z sample's spatial extents cannot be significantly resolved to provide an actual conclusive result. However, it is found from the data presented that only ~20% of the sample is significantly extended, with the remaining ~80% unresolved from the PSF, which appears to suggest that the SF regions are more commonly close to the nucleus. This outcome may indicate that the processes that regulate Black Hole Accretion are closely physically linked to the triggers of the star formation. The extent profile is illustrated further in Figure 3.9 with a histogram of all the measured extents binned to the size of the sample.

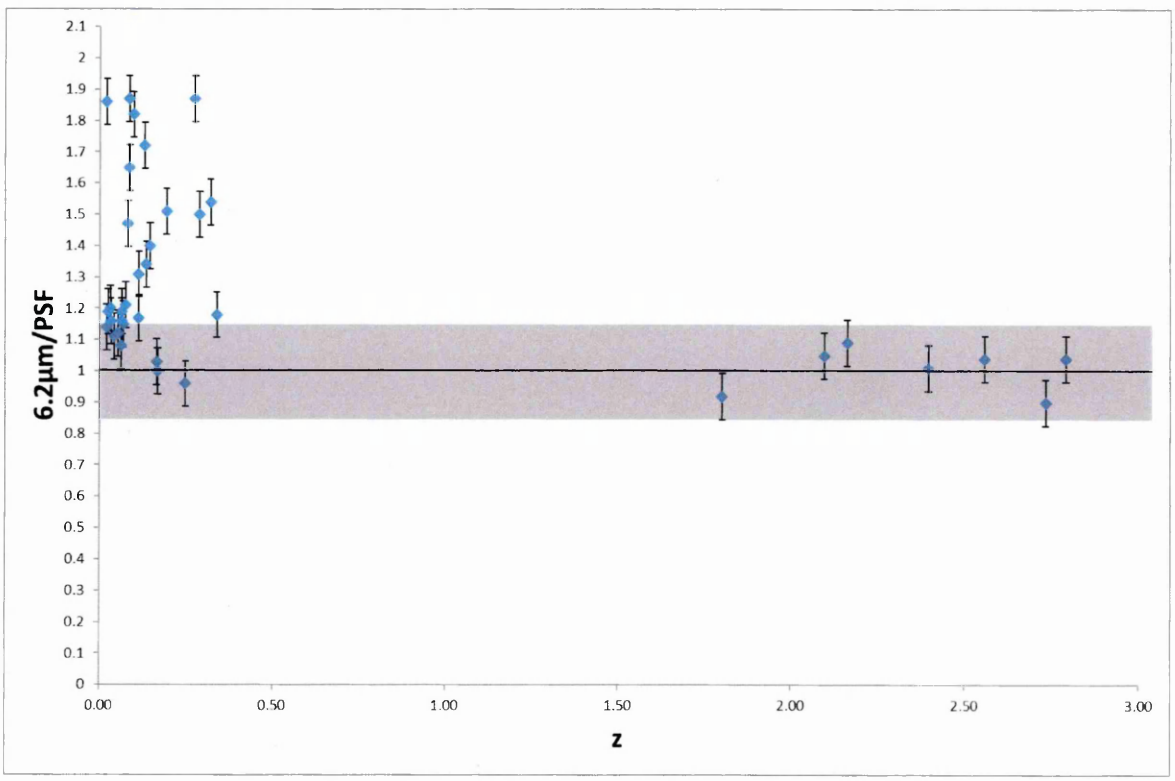

Figure 3.7. The $6.2\mu m_{FWHM}/PSF_{FWHM}$ ratio against redshift. Here you can see the local objects are the main contributors to the population of extended objects, along with the clear population gap between $0.5 < z < 1.5$. The error bars represent a 1σ distribution of those ratio values ≤ 1 in the $6.2\mu m$ population. The grey band represents 15% from unity and the solid black line represents unity.

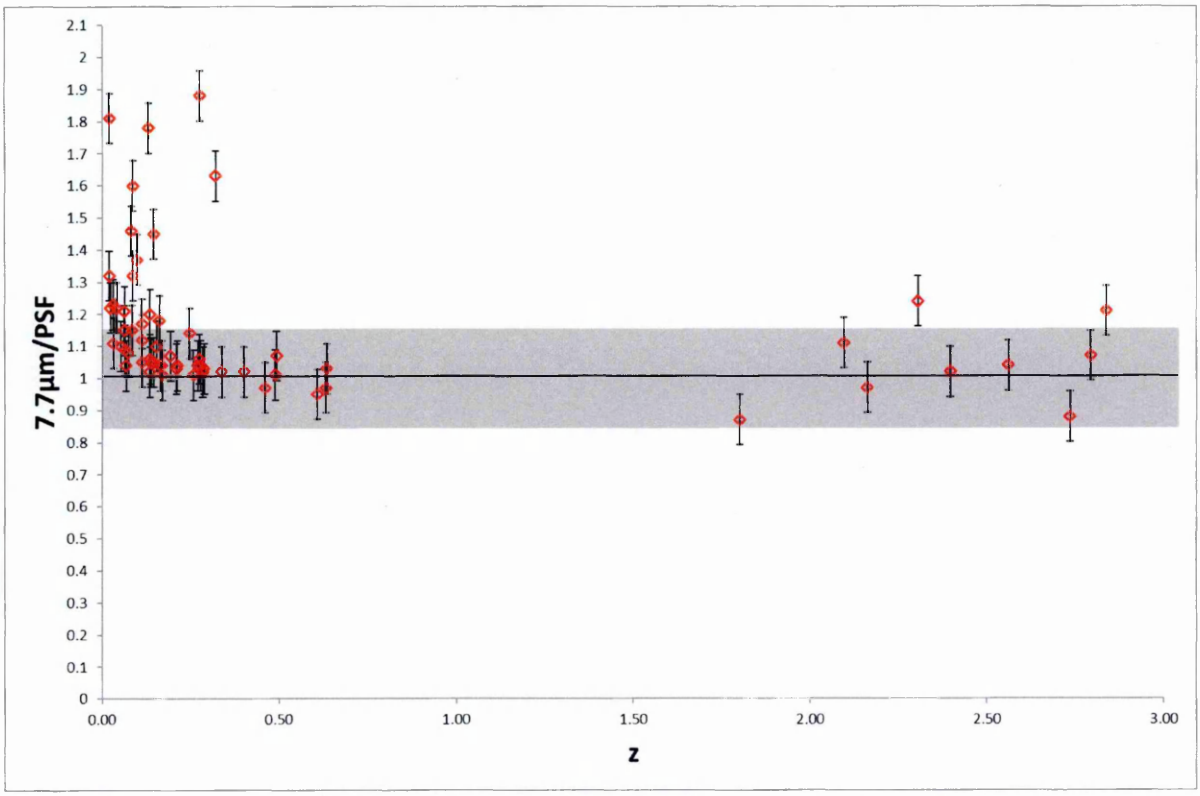

Figure 3.8. The $7.7\mu m_{FWHM}/PSF_{FWHM}$ ratio against redshift. The population is significantly larger than that of Figure 3.7 as well as presenting a similar shape, along with the population gap. The error bars are determined similarly to those of Figure 3.7, but with the $7.7\mu m$ population. The greay band represents 15% from unity and the solid black line represents unity.

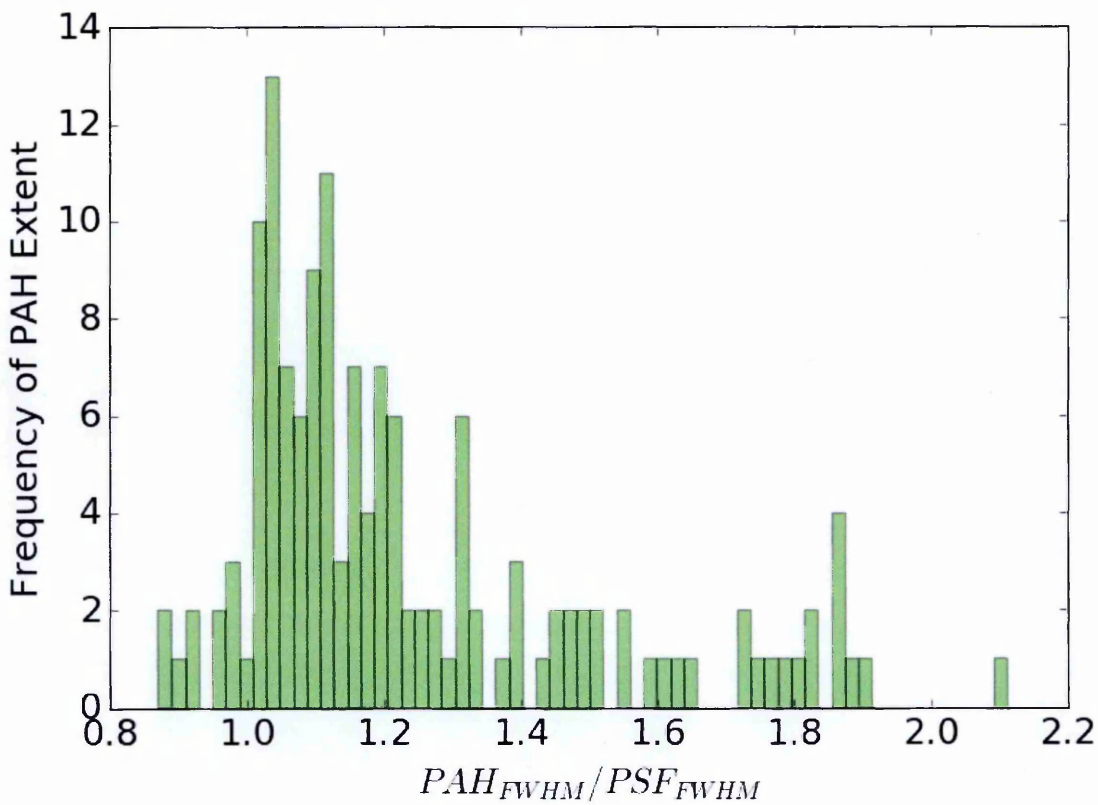

Figure 3.9. A histogram representing the distribution of extents from the entire sample. Most of the sample lies with an extent between 10% and 20% from unity.

3.2.2 Determining the Physical Extent

From the obtained results in Figures 3.7 and 3.8 one can qualitatively make interpretations about the physical extent. However, it does not tell one the physical extent of the PAH emission. Therefore, the physical sizes of these objects will now be calculated assuming a standard, flat cosmology; $\Omega_\Lambda = 0.7, \Omega_m = 0.3$ and $H_0 = 70\ km\ s^{-1} Mpc^{-1}$, representing the density parameters of Dark Energy and Matter, and the Hubble parameter respectively (Komatsu et al., 2008). This cosmology is prescribed for determining the correct cosmological distances of each object with respect to their redshifts. As mentioned in section 3.1.2 the PSF represents the intrinsic profile, and therefore, limitations of the optics of the telescope. However, when obtaining observational data from a target this will produce a profile that will, in effect, contain an entangled product of the PSF profile and that of the source. This is what is known as 'convolution', and means that the source has to be 'deconvolved' from the PSF in order to obtain a truer reflection of the source's profile (See Figure 3.10 for an illustration).

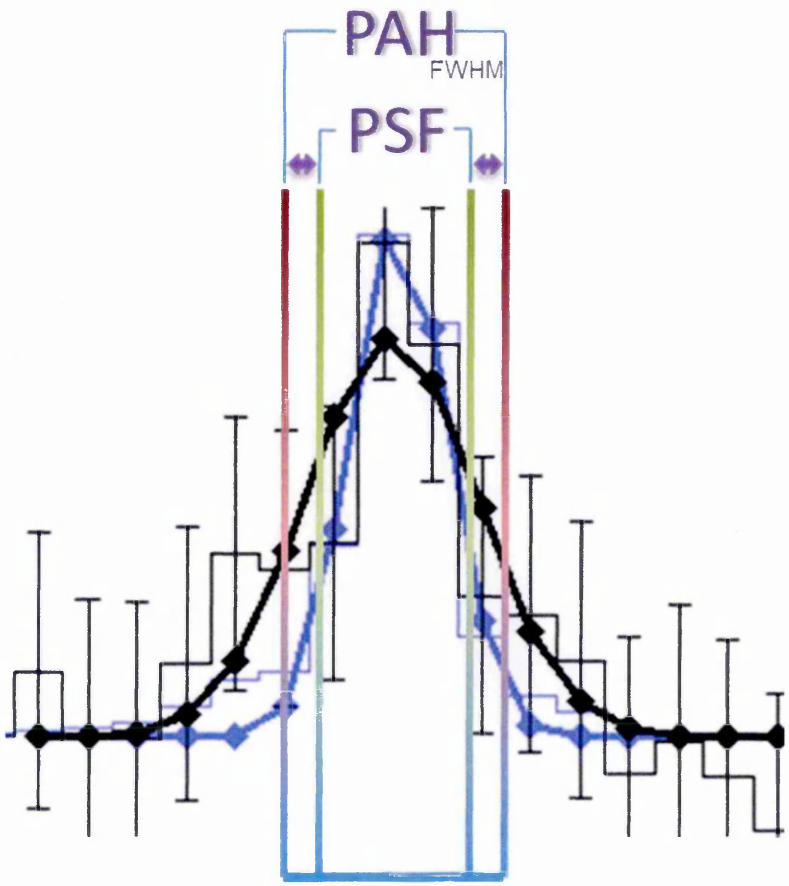

Figure 3.10. Example PAH FWHM (black) and PSF FWHM(blue) profiles. A PAH FWHM that is larger than that of the PSF FWHM means the emission can be spatially resolved, and therefore, deconvolved from the PSF.

Therefore, if it is assumed that the PSF_{FWHM} is perfectly convolved with the source PAH_{FWHM}, as opposed to a convolved function with unknown additional components, then one can deconvolve the source PAH_{FWHM} from the PSF_{FWHM} using the following formula in:

$$D_{dec} = \sqrt{(\sigma_{PAH}^2 - \sigma_{PSF}^2)} \tag{1.5}$$

where σ_{PSF} is the PSF FWHM and σ_{PAH} is the PAH measured FWHM. Thus, with all the recorded values for both of these quantities in arcsecs from the $7.7\mu m$ PAH emission, chosen due to it being the most prominent and strong PAH emission, all of the values were deconvolved with their respective PSF values. It should be noted, that any negative values become zero due to the square root and therefore cannot be deconvolved from the PSF. The resultant, deconvolved, values of all the objects are then converted from arcsecs into a physical size/diameter by utilising the simple angular diameter distance relation:

$$D = d_A \tan\theta$$

Thus, for

$$\theta \ll 1\, radian$$

$$\therefore D \simeq d_A\theta \tag{1.6}$$

where D is the physical diameter of the object, θ is the angular size of the object in radians and d_A is the angular diameter distance.

However, one must first determine the values of d_A for each object before the physical diameter can be calculated. These values have been computed with the standard cosmology as previously outlined utilising the Vardanyan (2015) cosmology calculator (see Figure 3.11). Once the d_A values were determined for all objects, they were then used to determine the physical size with equation 1.6, converting from arcsecs to radians:

$$D(Kpc) = \left[\left(\frac{2\pi}{360}\right)\left(\frac{D_{dec}(")}{3600}\right)\right] \times d_A(Mpc) \times 1000 \qquad (1.7)$$

All of these values, through all of the defined stages, are listed in Table 5.

AOR Key	Object Name	Z	PSF_FWHM "	DeC Extent (")	DeC Extent (kpc)
14014464	[VV2006] J171818.2+584905	0.63	3.53	0	0
14015744	FLSVLA J171106.7+590436	0.46	3.44	0	0
14016256	[VV2010c] J171324.2+585548	0.61	1.00	0	0
14017024	[PCE2006] 1404	0.49	3.30	1.26	7.6
4163840	2MASS J00070361+1554238	0.11	3.60	1.82	3.75
4164096	2MASS J01203157+2003278	0.09	3.26	4.07	6.61
4165632	IRAS F16574+1838	0.17	3.46	0.49	1.43
4165888	2MASS J17144277+2602485	0.16	3.46	2.17	6.07
4166400	2MASS J00505570+2933381	0.14	3.48	1.22	2.95
4166656	2MASS J01083516+2148186	0.29	3.47	0.70	3.00
4166912	2MASS J01572105+1712484	0.21	3.51	1.00	3.48
4168192	[VV2000] J125807.5+232922	0.26	3.54	0.50	2.01
4168448	2MASS J13070066+2338050	0.28	3.25	1.14	4.79
4168960	2MASS J14533151+1353587	0.14	3.3	1.06	2.59
4169472	2MASS J16370022+2221140	0.21	3.52	0.87	2.99
4169984	2MASS J22255425+1958372	0.15	3.34	1.07	2.75
18027008	LBQS 0018-0220	2.60	10.35	0	0
18027264	[VV2000] J023233.1-211726	2.16	10.28	0	0
18027520	[VV2006] J041327.2+102743	2.84	6.48	4.41	34.5
18027776	QSO J0812+4028	1.80	10.58	0	0
18028032	QSO B0908+0603	2.79	8.22	3.13	24.6
18028288	[VV2000] J100517.5+434609	2.10	10.59	5.10	42.5
18028800	LBQS 1230+1627B	2.74	10.72	0	0
18029312	QSO J1415+1129	2.56	10.62	3.03	24.36
18029568	QSO B1611+4719	2.40	10.55	2.12	17.26
18028544	QSO B1104-181	2.31	10.52	7.71	63.27
14193408	2MASSI J1118302+402553	0.15	3.62	1.66	4.44
14194432	2E 2584	0.17	3.34	0.95	2.70
14200064	2E 1519.0+2238	0.14	3.48	0.70	1.68
14197504	2MASSI J1417008+445606	0.11	3.5	1.12	2.31
14196224	2XMM J132349+654148	0.17	3.51	1.00	2.88
26328320	2MASS J00501008+2806199	0.28	3.4	5.41	22.8
26334720	2MASS J22394602+1929549	0.19	3.44	1.31	4.22
26334976	2MASS J23030430+1624406	0.29	3.28	0.81	3.51
26334208	2MASS J17053665+2101380	0.27	3.39	0.97	4.01
26334464	2MASX J22374267+1456143	0.28	3.34	0.95	4.04
26330624	2MASS J10012116+2150112	0.25	3.36	1.84	7.15
26333440	2MASS J15215105+2251209	0.29	3.56	0	0
26413568	LEDA 2822178	0.32	3.5	4.51	21.0
26413824	4C 05.16	0.34	3.5	0.70	3.37
26415104	LEDA 2830969	0.64	3.48	0.86	5.90
13628416	QSO J0920+4531	0.40	3.51	0.71	3.80
13628672	[VV2010c] J115718.4+600345	0.49	3.37	0.48	2.89
10497536	2MASS J01051501-2612466	0.11	3.25	1.97	4.08
10496000	2MASS J22023161-5657577	0.08	3.51	3.73	5.83
10495744	2MASS J21573517+0114331	0.14	3.38	2.24	5.40
10494464	2MASS J15554606+1532218	0.13	3.46	5.10	11.9
10494208	2MASS J02542961+1509122	0.10	1.89	1.77	3.23
10491648	2MASS J03574895-1340458	0.08	3.46	1.41	2.02
10491392	2MASS J23080919+0538305	0.15	3.21	3.37	8.61
10490624	2MASS J22565483-3649515	0.09	3.51	1.99	3.22
10490368	2MASS J00285431-7726146	0.09	3.39	2.92	4.76
22929920	2MASX J11182408+5602074	0.07	3.35	0.96	1.24
22930432	LEDA 2600134	0.06	3.50	1.52	1.88
22931968	NVSS J110909+455125	0.06	3.34	2.28	2.79
23509504	NVSS J103228+121037	0.03	3.50	1.69	1.11
23510016	NVSS J15574349+2727530	0.03	3.64	2.61	1.64
23510528	2MASX J22385422+1311404	0.06	3.49	1.98	2.39
23510784	2MASX J08004768+3743435	0.04	3.51	2.45	2.02
23511040	2MASX J09040105+0127294	0.05	3.57	1.64	1.71
18852608	[BKD2008] WR 525	0.02	3.38	5.10	2.15
18852864	Mrk 42	0.02	3.42	2.39	1.18
18853120	2MASS J04344153+4014216	0.02	3.43	2.96	1.23

Table 5. The calculated deconvolved extent values. Zero values indicate PAH FWHM could not be deconvolved from the PSF FWHM.

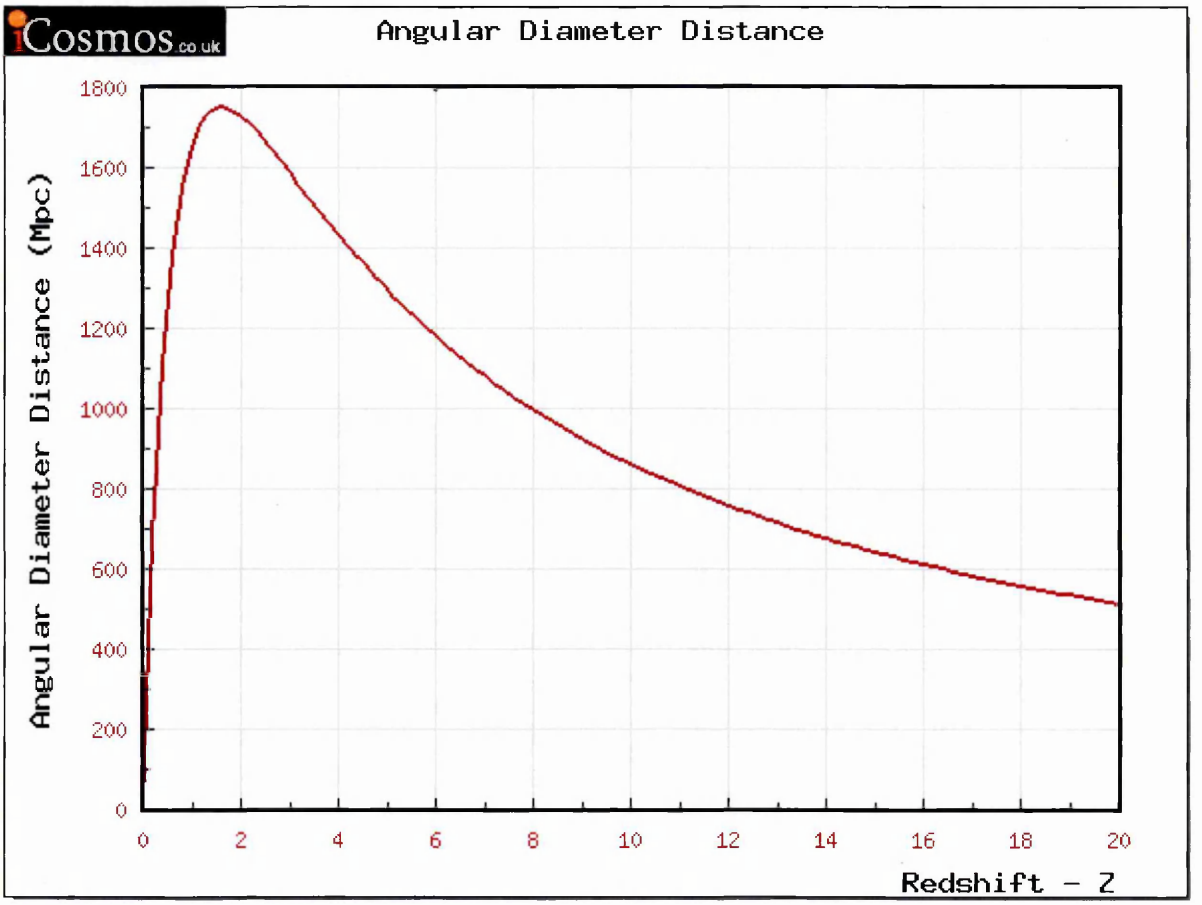

Figure 3.11. The calculated function of the angular diameter distance d_A against redshift z using the pre-stated standard cosmology. Taken from Vardanyan (2015).

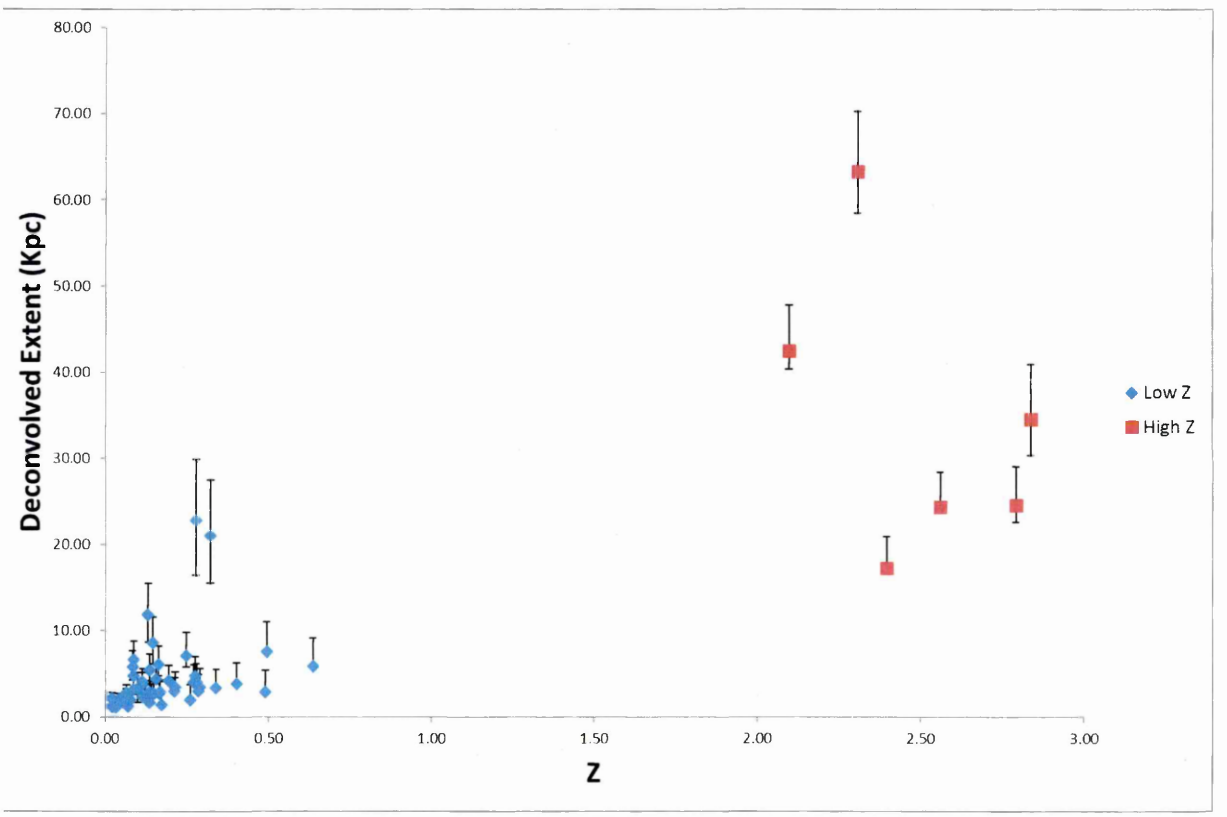

Figure 3.12. The deconvolved extent against redshift of the low-z and high-z objects. The error bars are determined from the half σ distribution in Figures 3.7 and 3.8.

Figure 3.12 is the resultant plot of the deconvolved physical extent/diameter against redshift. Interestingly this plot also highlights the trend for the PAH emission to become more extended and therefore increases in size with the increase in redshift. Considering typical galaxies have diameters of $\sim 30kpc$ the more extreme results indicating diameters of up to $\sim 60kpc$ appear to be more spurious, and therefore, being as a result of the inability to spatially resolve the object significantly. In Figures 3.7 and 3.8 with the PSF, the objects are effectively 'clumping' at diameters $< 15kpc$ at redshifts $z < 0.7$, along with six larger physical extents at high redshifts of $z > 2$. This result could indicate that star formation is present throughout the entire host galaxies on evolutionary scales where this diminishes at low-z. Although, again considering the average diameter of a galaxy as stated, it is possible for the PAH emission cannot be adequately resolved due to instrumentation limitations. From this, however, it is found that the sample of high redshift objects $z > 1.5$ in Figure 3.11 shows apparent marginally extended SF at a mean of $34 \pm 5.3kpc$, where the entire low redshift objects at $z < 1$ present SF with a median extent of $3.2 \pm 1.4kpc$.

3.2.3 Conclusions and Interpretation

From this Chapter, the key conclusive points made from the data are:

- Across the whole sample of the objects with $7.7\mu m$ features, ~80% show the PAH emission constrained to the PSF as seen in Figure 3.8. The ~20% that is extended are the result of the low-z objects that could be adequately resolved from the PSF.
- Comparing Figure 3.8 with Figure 3.12 it can be seen that the deconvolved physical extent of the high-z objects exhibits SF throughout their host galaxies. This conclusion is not final however due to the high-z object's smaller angular size on the plane of the sky making it difficult to resolve the PAH emission from the AGN and host galaxy.
- At low-z the objects in Figure 3.12 do show some constraint to the nucleus in their SF regions ($\leq 1kpc$). However, this is not common, with most of the objects lying outside of the nuclear regions. This indicates there is no conclusive evidence of a close relation between AGN activity and SF via feedback.

- The James Webb Space Telescope will be able to fill the population gap of quasars, as well as re-observe the objects from the sample in this thesis to overcome the spatial resolution and sensitivity issues that are faced with Spitzer, in that the objects were either very local, or had long integration times.

Chapter 4

QSO TEMPLATE IN THE MID-IR

Considering the wealth of spectra on QSOs from this thesis' sample the best SNR composite spectrum was created using bespoke routines; this composite spectrum can be utilised as a template for QSO environments in the Mid-IR. Since there is a low-z and a high-z population, three templates with the total sample, high redshift and low redshift were produced. A qualitative comparison is made between the low-z and high-z composites, along with a comparison of the total sample composite with those of other objects.

This Chapter presents the methodology used for producing the composites, followed by a comparison between the individual component composites, a comparison between composites of other objects and the average PAH ionisation conditions.

4.1 PRODUCING THE COMPOSITES

For the production of the composites, the author's own routines were utilised and written in the Python language. These routines can provide the ability to look at each nod for each order of a given object, as well as co-adding both of the nods of each available order to improve the signal-to-noise ratio. The full low-resolution spectra of each object are then interpolated to a limited IRS wavelength range. The result allows for the building of the composites. This process is as follows:

1. The extracted spectra are imported into bespoke Python routines one by one with both nods. The nods of each object are then co-added together helping to boost the SNR of the data. Finally, the co-added object spectra are then corrected for their respective redshifts to the rest frame. These spectra are then saved for later use.
2. The final step is running the compositing routine, which co-adds the desired object spectra together to form a single combined spectrum. Each nod co-added spectrum is first normalised to the median flux of the sample spectra at $5.5\mu m$ for each sample (i.e. high-z, low-z and total sample), this wavelength was chosen primarily for being the most featureless. The routine then interpolates each of the normalised spectra to the desired wavelength range and interval. The routine then completes the process by co-adding the interpolated and normalised data together, thus forming the composite/template spectrum.

4.1.1 Low-z Composite

In Figure 4.1 the composite that only contains the low redshift objects $z < 1$ co-added together is presented. The low redshift sample is the dominant source of the PAH emission feature's shapes and profiles in the full template. This dominance is due to the objects being closer and brighter with SNRs substantially larger than 10 when compared with the weaker PAH emission shapes and profiles in the high-z sample (see Figure 4.2). The data presented portrays the best extraction of the features as a result of the SMART AdOpt routines. Thus, the large sample size, with the optimal extraction routines helps to produce a composite with a better SNR than could be achieved previously. It also plays host to many atomic lines that are commonly detected, and therefore, would expect from starbursting and AGN environments.

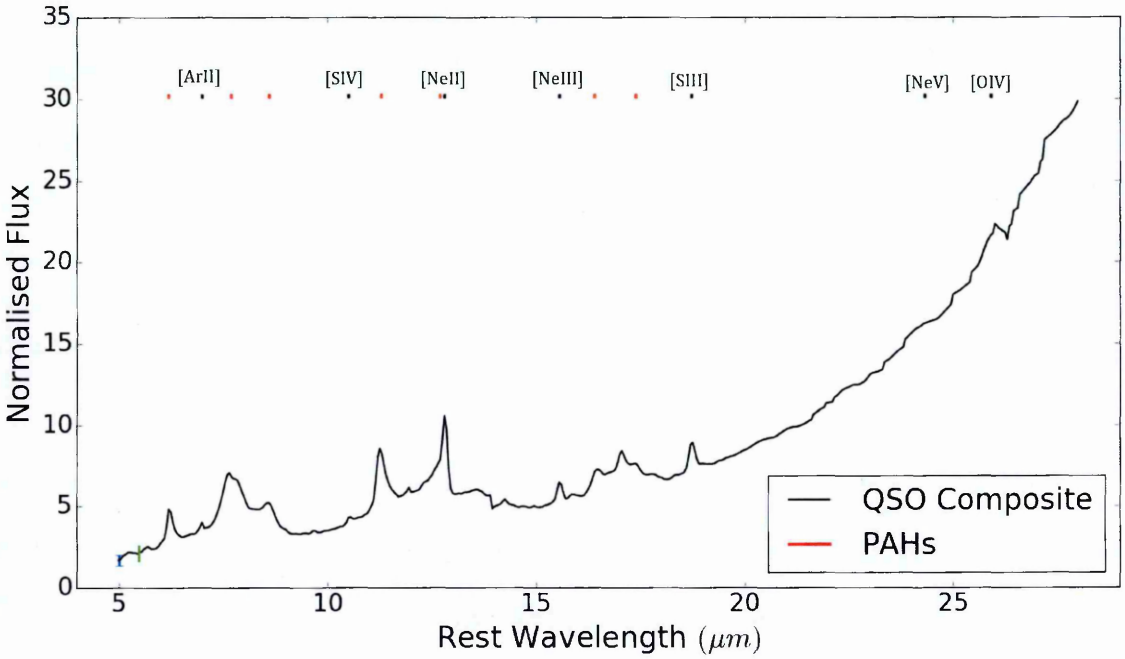

Figure 4.1. Low-z composite spectrum normalised to the median continuum flux of the low-z population at $5.5\mu m$, this point is represented by the green vertical bar. The blue error bar represents the standard error of the mean of the entire template.

4.1.2 High-z Composite

In Figure 4.2 the composite that only contains the high redshift objects $z > 1.5$ co-added together is presented. The object data within the high redshift sample is solely from the observations made by Lutz et al. (2008), where a composite of this data was also produced. However, these data were analysed before the optimal extraction routines were written for SMART. Therefore, the data presented represents the best template available with superior SNR than was achieved previously by Lutz et al. (2008). The number of quasars with PAH emission in the Lutz et al. (2008) that has a total sample of twelve, increased from nine to ten with the addition 'LBQS 0018-0220'. Thus, the combination of the additional object with the optimal extraction routines has helped to boost the PAH feature's profile and shapes significantly to where they are now more pronounced from the continuum.

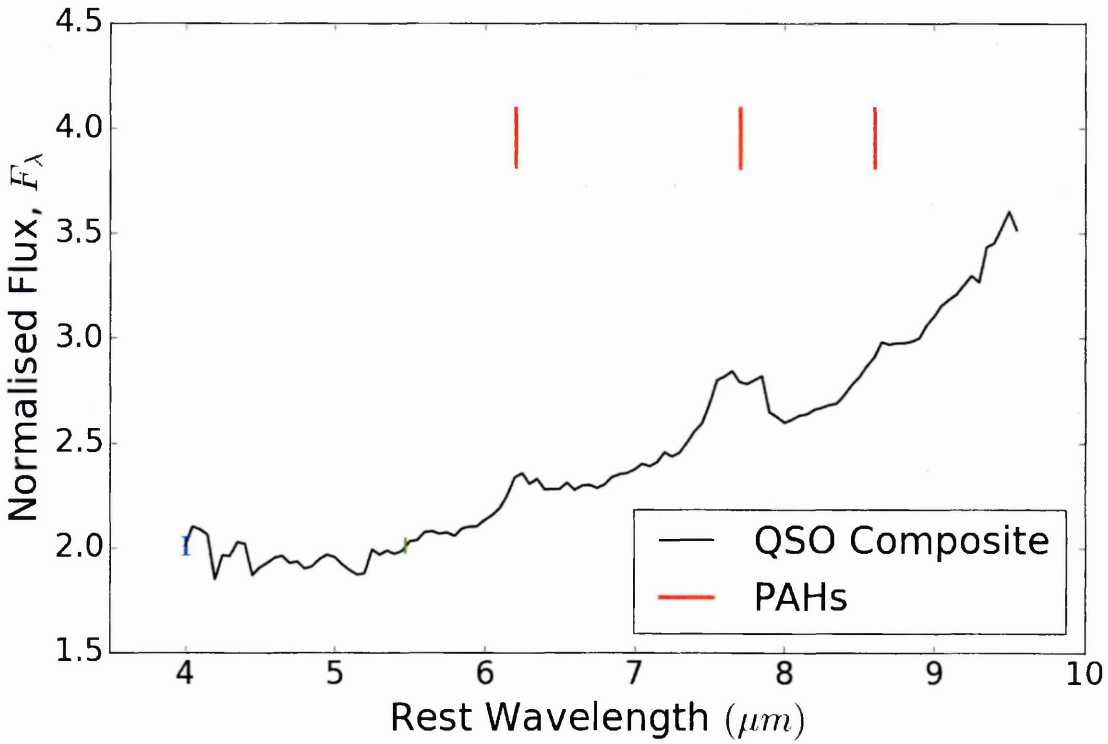

Figure 4.2. High-z composite spectrum normalised to the median continuum flux of the high-z population at 5.5μm, this point is represented by the green vertical bar. The blue error bar is the same as Figure 4.1.

4.1.3 Full-z Composite

In Figure 4.3 the best high SNR full composite of all the objects co-added together is presented. Here the spectra were normalised to the median flux value at 5.5μm; this was chosen because it is devoid of any features in the objects' spectra as well as to avoid the regions where silicates are known to be present. The PAH features in all the spectra are shown to be very prominent, along with the presence of various lines such as [OIV] and [NeV]. Lines which would be expected from the presence of any AGN due to their high ionisation potential and the AGN's ability to produce these lines with its harsh and strong radiation fields. Lines such as [NeII] and [NeIII] indicate the presence of star formation, helping to confirm the presence of star forming regions alongside the PAH features. Although, it should be noted that it is the low redshift objects that predominantly help constitute the shape of the composite's features due to their superior SNR, whereas the weaker SNRs of the high redshift objects do not affect the shape of the composite's features noticeably.

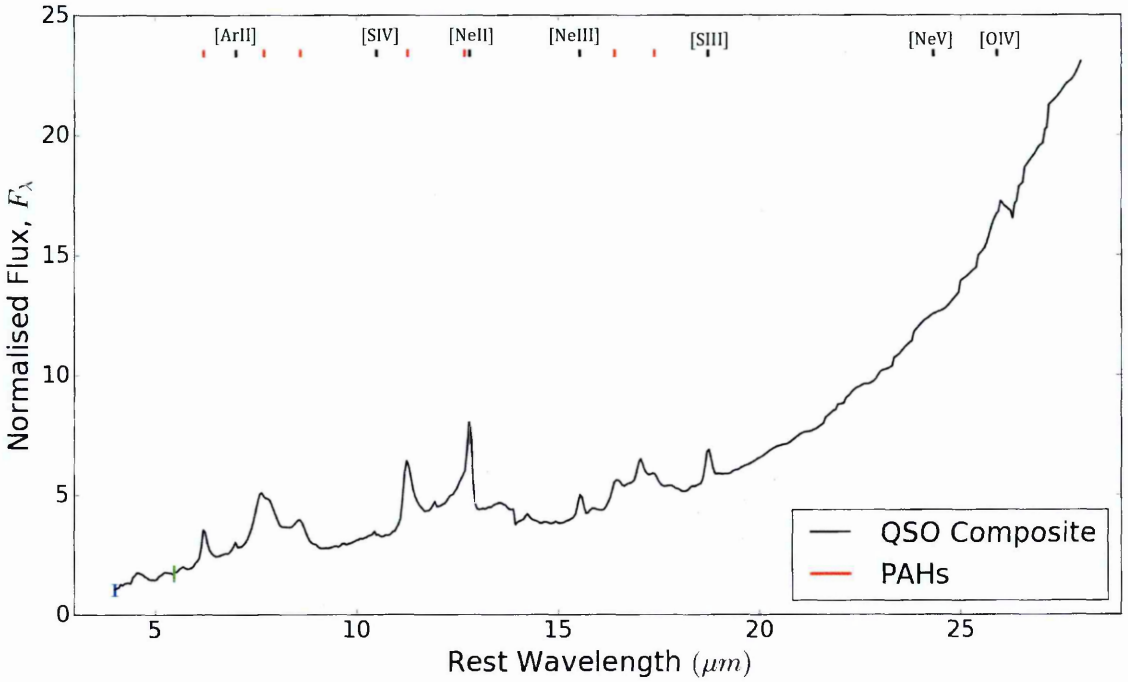

Figure 4.3. Composite spectrum of the total sample normalised to the median continuum flux at 5.5μm, this point is represented by the green vertical bar. The blue error bar is the same as Figure 4.1.

4.2 UTILISING THE TEMPLATES

The template/composite SED spectra from this thesis' quasar sample represents the best SNR averaged spectrum, thereby allowing the observer to determine the average chemical composition as well as the physical mechanisms that can be inferred from the observed chemical makeup. Therefore, a composite spectrum can allow for further science and analysis to be performed on helping to disentangle quasars further from other luminous extragalactic objects. Thus, what follows is a variety of quick analytical methods: SED template comparisons and average PAH strengths.

4.2.1 Comparison with Elbaz et al. (2011) Templates

Elbaz et al. (2011) present two template SEDs from photometric data samples of known so-called 'Main Sequence' and 'Starbursting' galaxies. Both are compared phenomenologically to make inferences to the physical mechanisms to see how their environments are different and, by extension, observing how galaxies evolve at different stages of their 'life'. Therefore, a comparison is made between the full template SED from Figure 4.3 with that of the Elbaz et al. (2011) data below in Figure 4.4.

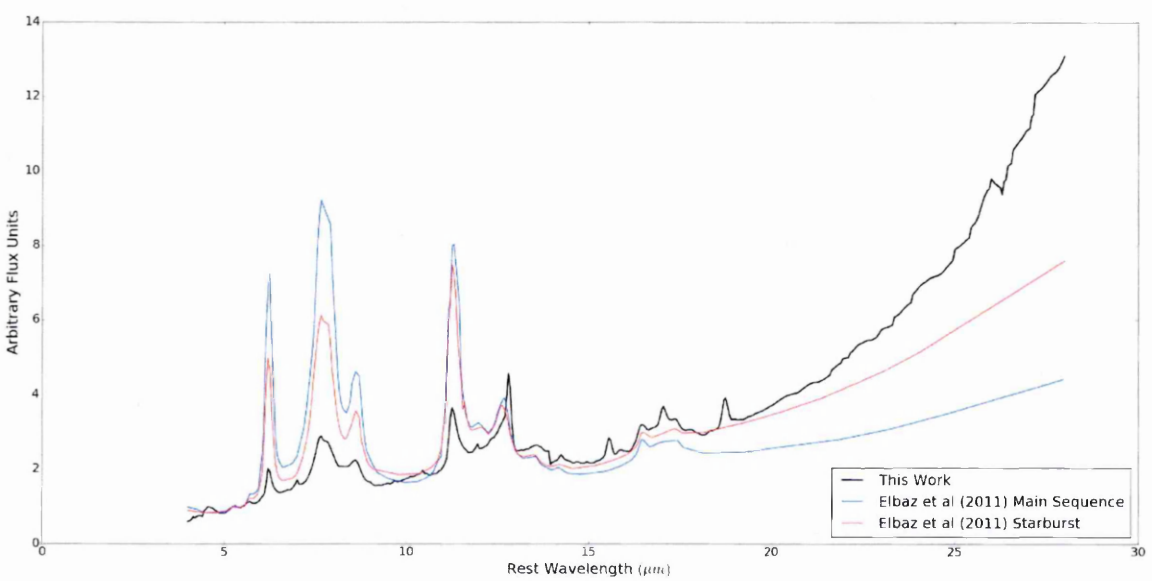

Figure 4.4. Comparison between my QSO composite and that of the Elbaz et al. (2011) photometric SED templates for Starbursting and Main Sequence galaxies. The spectra are normalised to their respective fluxes at $5.5\mu m$. Note the hot dust component at long wavelengths and the supressed PAH emission in the template.

From the first glance of Figure 4.4, it can be clearly seen that there is a hot dust component present at longer wavelengths, also the PAH emission from the QSO template has smaller equivalent widths than that of the Elbaz et al. (2011) sample. In comparison with the main sequence and starbursting templates, there is a marked progressive decrease in the PAH emission strength respectively. Thus, it appears to demonstrate three different stages of galactic evolution based upon varying star formation rates of each of these objects. Following from this idea of evolution, Elbaz et al. (2011) states that the surface brightness of IR emission (Σ_{IR}) increases from the main sequence to the starburst. In other words, the young stellar population is more compact. This apparent compactness could indicate the presence of stronger radiation fields that 'push back' the photo-dissociation region boundaries, where the PAH molecules reside and thereby leading to smaller equivalent widths and a stronger IR continuum due to 'dustier' environments. The compactness corroborates the results in section 3.2 where ~80% of the sample shows apparently spatially constrained star formation. However, concerning kpc scales the sample in this thesis shows the surface brightness of PAH emission is on average determined to the order of $\Sigma_{PAH} \sim \times 10^{8} L_{\odot}\ kpc^{-2}$, where starbursting galaxies with compact star formation should have surface brightness levels of $\Sigma_{PAH} \geq 3 \times 10^{10} L_{\odot}\ kpc^{-2}$, indicating this may not be the cause of the suppression of PAH emission, however determining the high-z physical sizes is difficult given the size of the uncertainty depicted in section 3.2.2.

4.2.2 Average PAH Conditions

One of the advantages of a composite spectrum is that it can represent the average or typical chemistry of a particular type of object. From section 2.1.4 it is known that there are ionised PAHs and neutral PAHs. Therefore, a ratio between ionised and neutral PAHs can be used as a proxy for radiation field strength. Further details can be found in Chapter 5, where it will be discussed. Figures 4.5 and 4.6 demonstrate the Python routines used on the composite to determine the equivalent widths using the 6.2μm PAH as an example.

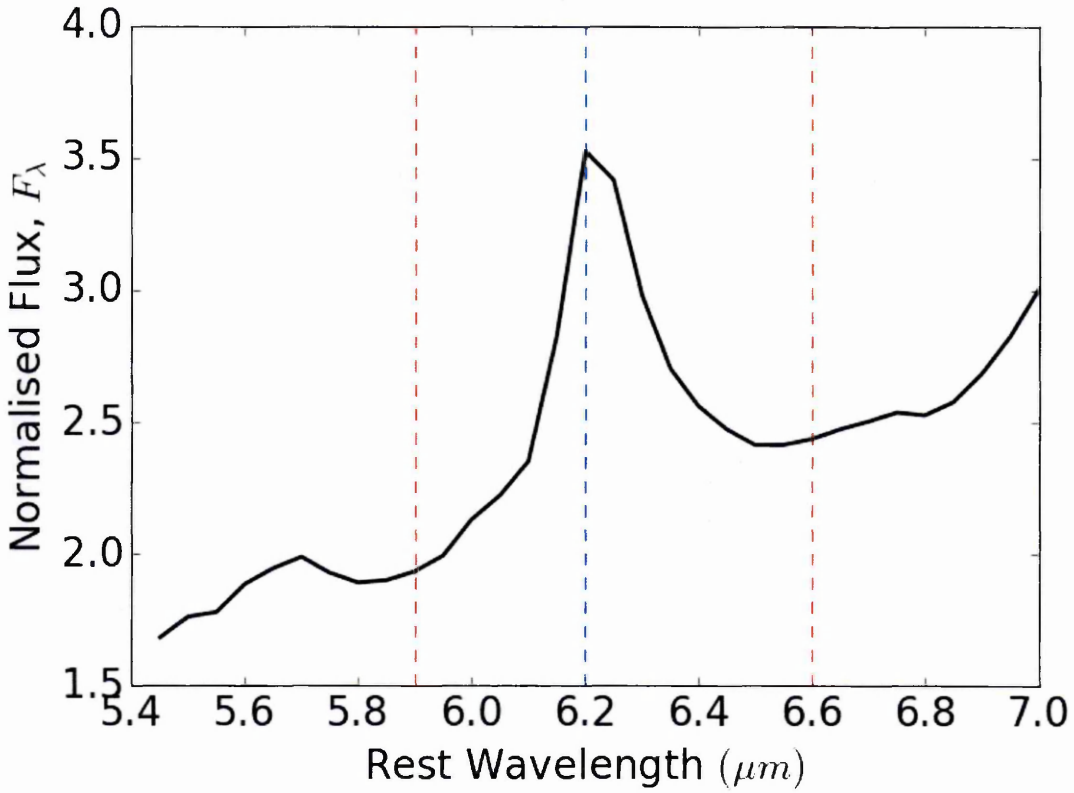

Figure 4.5. The composite focussed onto the wavelength region containing the 6.2μm PAH. The red dashed lines show the integration range, where the blue dashed line indicates the centre of the PAH peak.

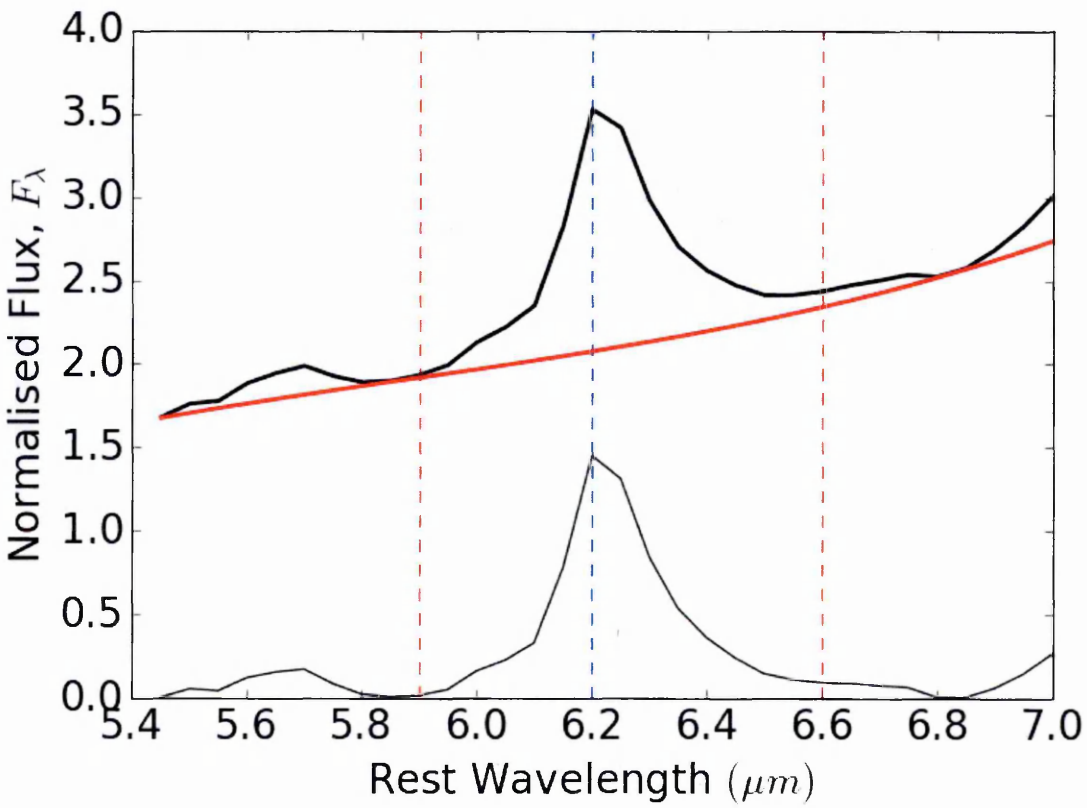

Figure 4.6. The resultant continuum drawn from the python polynomial fitting routines at the top. At the bottom is the continuum subtracted spectrum of the 6.2μm PAH.

The continuum is drawn through a polynomial fitting routine built into python based off user defined points. The continuum is then subtracted to give a 'flat' spectrum as shown in Figure 4.6, which allows for simple integration between the defined regions in red. After the integrated flux has been determined it is then divided through by the continuum at the centre of the PAH to give the equivalent width in units of μm. Table 6 details the resultant calculations of the equivalent width below (see Chapter 5 for a more in-depth methodology).

6.2μm PAH		**7.7μm PAH**		**11.3μm PAH**	
EQW (μm)	Error (μm)	EQW (μm)	Error (μm)	EQW (μm)	Error (μm)
1.65×10^{-1}	1.59×10^{-2}	2.28×10^{-1}	1.35×10^{-2}	2.04×10^{-1}	1.11×10^{-2}

Table 6. Calculated equivalent width values from the composite PAHs.

From Table 6 it is shown that the overall strengths for the ionised PAHs are similar to that of the neutral 11.3μm PAH, with 7.7μm/11.3μm closer to unity at 1.12 ± 0.09 and 6.2μm/ 11.3μm demonstrating suppressed ionisation at 0.81 ± 0.08. The errors are propagated through from the spectra as determined by SMART.

4.2.3 Conclusions and Interpretation

From this Chapter, the key conclusive points made from the data are:

- QSO/AGN PAHs are much weaker than starbursting and the main sequence galaxies, which is seemingly consistent with stronger star formation due to intense stellar radiation fields 'pushing back' the photodissociation region boundaries. However, this is tentative due to uncertainties in determining the *kpc* scales.
- Surprisingly, the QSO/AGN template has more neutral than ionised PAHs. This result would be consistent with the AGN having no contribution to heating the PAH emission, which is also consistent with the physical extents found on *kpc* scales in Chapter 3.

- QSOs/AGN show a component of hot dust not present in the main sequence and starbursting galaxies, consistent with hot dust being heated within the AGN torus.

Chapter 5

QUANTIFYING THE PAHS AND THE CORRESPONDING SFRS

PAHs can be used as tracers of star formation and, by extension, enable us to quantify the rate of star formation. The PAHs, however, must first be quantified by determining the PAH flux of the currently resolvable PAH features in all of the objects in the sample. Focussing on the $6.2, 7.7, 8.6$ and $11.3\mu m$ features, the integral fluxes and equivalent widths (EQW) are calculated where they are present in the spectra using an IDL programme. This data can be used to help determine the strength of the ionisation within the star formation regions around quasars. What follows in the next section is the methodology, results and analysis from quantifying the PAHs, and thereby determining the SFR values.

5.1 MEASURING THE PAH INTEGRAL FLUXES AND EQWS

The measurement of the PAH features was performed by utilising a specialised IDL routine. This routine allows the user to define which PAH feature they want to measure for each FITS file containing a Spitzer/IRS spectrum. As well as the ability to 'draw' a continuum with user defined 'anchor points' for which a spline can be fitted to, this produces continuum flux for each corresponding real/observed data point. From this the integral fluxes can be derived within a defined region, followed by the EQWs. The process by which this happens is as follows:

1. Firstly, the raw object file is loaded, after this the data is then redshift corrected from the values in Table 2. The corrected object data is saved to a permanent file.

2. The object data is restored from the relevant object file. The PAH feature of interest (6.2,7.7,8.6 *and* 11.3μm) can then be selected. Running the routine with the selected PAH feature will plot the spectrum focussed on that particular region. The routine will ask for 'anchor points' (See Figure 5.1) to be defined by using the cursor, after which a spline will be fitted to the anchor point coordinates, defining the continuum (see Figure 5.2).
3. After the continuum is 'drawn' the integration range is selected. The start and end points are determined using the cursor, along with the centre of the PAH feature to determine which flux data points are closest to the PAH peak. This feature will aid to calculating the continuum flux.
4. The outputted integral flux and equivalent width values along with their errors are outputted onto the plot (see Figure 5.3). These results can be then saved as an image file as well as a data file. The calculations for these outputted values will be highlighted in the following section.

It shall be noted that the continuum drawn for the 7.7μm feature was reused for the 8.6μm feature, this is to prevent the human error of plotting anchor points in different places, maintaining consistency with the PAH features that lie within the same region of the spectrum. The above process was repeated for all of the objects in the sample for each PAH feature where applicable.

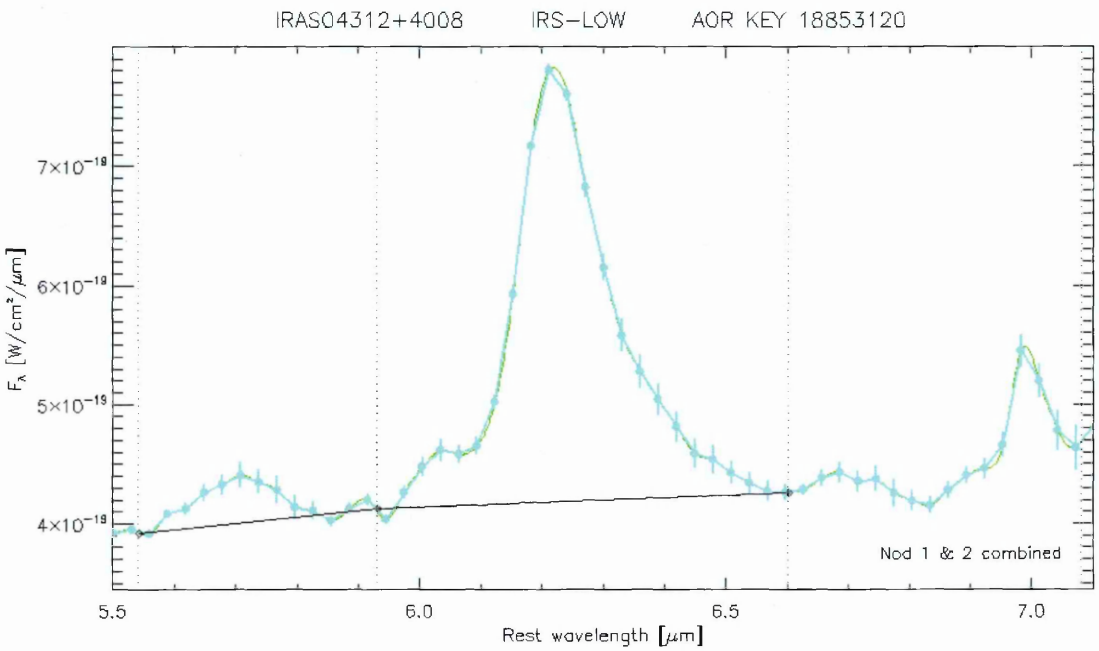

Figure 5.1. Example of determining the continua via the cursor as noted in step 2.

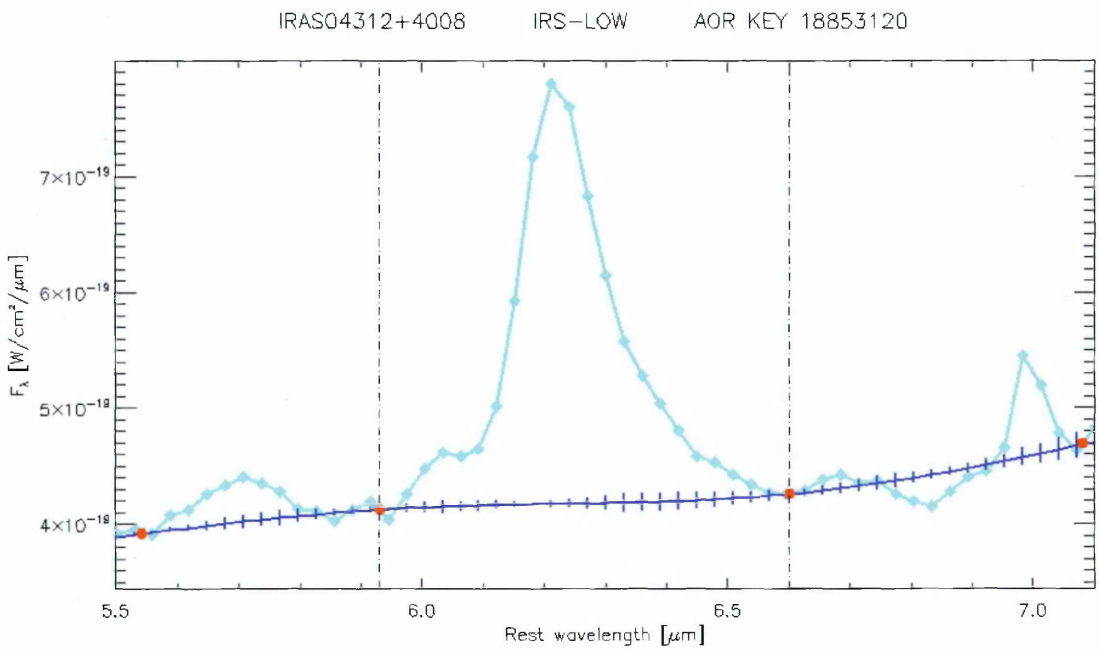

Figure 5.2. The resultant drawn continuum from the 'anchor points' determined by the cursor.

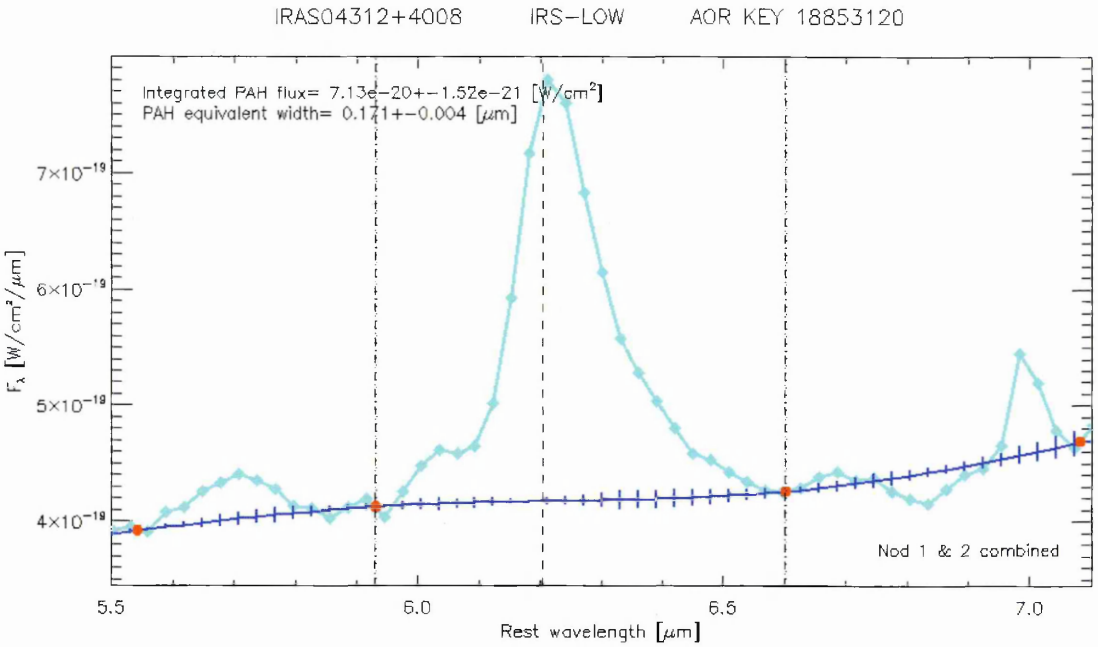

Figure 5.3. The resultant calculated values for the integral flux and equivalent width of the PAH determined from the integration range as defined by the 'start' and 'end' dashed lines. The central line represents the centre of the PAH, and allows for the equivalent width to be determined by dividing the PAH flux with the continuum flux.

5.1.1 Calculating the Integral Fluxes and Equivalent Widths

As it was shown in the introduction to this Chapter, the routines used were useful to enable quick and precise analysis of the PAH features of these relatively faint objects. The following section will detail how the routine calculates the integral fluxes and equivalent widths. Firstly, it shall be noted that the definition of the equivalent width can be expressed mathematically as in equation 1.8:

$$EW_\lambda = \int \frac{F_o(\lambda) - F_c(\lambda)}{F_c(\lambda)} d\lambda \tag{1.8}$$

where EW_λ is the equivalent width in units of length (μm), $F_o(\lambda)$ is the flux above the continuum and $F_c(\lambda)$ is the flux of the continuum.

The flux observed by Spitzer is a function of the wavelength in microns. Therefore, the flux density has dimensions of 'power per unit area per unit wavelength'. The calculation of the integrated flux values by the IDL routines is straight forward and provides a good approximation to the flux values. The limits of the integration for each PAH were set to the following: $6.1 - 6.6\mu m$ for $6.2\mu m$, $7.2 - 8.3$ for $7.7\mu m$, $8.3 - 8.88\mu m$ for $8.6\mu m$ and $11.1 - 11.7\mu m$ for the $11.3\mu m$ PAH. When the desired integration range is selected, the profile is integrated numerically. It shall be noted that the fluxes and equivalent widths were only calculated if present; spectra that were too noisy or were redshifted outside of the instrumental ranges (i.e. the $11.3\mu m$ PAH) were not used. The integral fluxes of each PAH feature from each object, the values for which can be found in Table 7.

AOR	6.2 μm PAH		7.7 μm Flux		8.6 μm Flux		11.3 μm Flux	
	Flux	Error	Flux	Error	Flux	Error	Flux	Error
14014464	6.04	1.09	17.39	1.54	3.64	1.06	8.32	1.75
14015744	10.61	1.10	21.02	0.83	1.48	0.60	10.37	1.57
14016256	4.57	0.78	4.60	1.16			3.72	1.80
14017024	7.50	1.45	17.13	1.25	6.72	0.76	5.99	1.39
14193408	63.48	5.57	99.51	5.69	25.54	4.70	50.25	3.62
14194432	39.95	5.29	45.25	4.17			27.34	2.32
14196224	18.89	3.37	38.48	1.92			18.51	2.79
14197504	35.22	2.73	43.18	5.84	11.21	3.36	45.30	2.25
14200064	31.90	3.40	35.68	7.55			25.62	4.38
13628416	9.53	0.58	17.78	1.61			7.36	1.11
13628672	28.16	1.59	61.04	1.32	10.07	0.71	18.11	2.63
18027008	3.62	1.73	4.83	1.48	2.12	1.00		
18027264	8.75	1.48	14.56	1.21	1.85	0.72	10.33	2.46
18027520	4.14	0.76	6.15	2.26				
18027776	3.77	1.39	11.67	1.18			3.24	1.27
18028032	8.97	1.27	11.48	1.32	4.98	1.04		
18028544	24.82	1.88	19.70	1.59	0.30	1.04	24.10	2.73
18028800	6.42	2.37	2.43	1.74	2.18	1.38		
18029312	23.04	5.99	15.03	5.92	9.65	4.42		
18029568	3.98	1.36	4.12	0.73	0.22	0.39		
18852608	15.28	1.66	44.17	4.09	9.43	0.83	35.23	1.48
18852864	118.14	7.41	119.63	6.62	32.13	3.82	96.54	2.68
18853120	719.57	15.22	908.00	31.69	237.88	7.54	695.26	3.93
10490368	92.56	6.41	203.98	8.07	23.64	2.40	75.09	1.12
10490624	16.31	2.20	38.58	2.02	7.32	0.74	19.18	0.90
10491392	44.90	4.47	64.40	3.60	12.12	1.02	32.08	0.93
10491648	221.00	2.33	402.30	6.44	60.15	1.11	162.56	1.88
10494208	20.44	2.17	46.72	3.82	10.26	0.78	18.88	0.94
10494464	31.61	3.12	53.24	1.68	9.17	1.24	27.40	0.80
10495744	35.37	3.24	91.93	3.47	13.86	0.95	33.88	1.14
10496000	48.59	3.76	75.35	4.43	14.74	1.31	42.63	1.16
10497536	32.96	2.74	43.73	2.22	16.37	0.90	34.29	0.89
22929920	326.49	6.59	629.58	8.24	104.12	3.13	238.01	3.21
22930432	263.70	7.13	495.09	11.27	78.90	2.09	211.17	2.47
22931968	234.85	8.53	424.37	26.79	59.66	2.92	164.27	3.14
23509504	278.60	7.87	522.99	13.30	80.99	6.68	205.51	3.42
23510016	443.36	5.02	860.78	18.01	135.81	5.79	343.11	3.22
23510528	406.39	12.53	721.84	12.23	86.84	4.63	248.24	5.65
23510784	492.45	14.43	913.43	20.16	128.47	5.07	302.11	2.64
23511040	777.68	11.64	1501.16	12.44	195.90	12.51	428.51	7.58
26328320	14.11	5.44	75.90	3.34	15.84	2.15	48.95	3.95
26330624	65.92	11.24	53.49	7.46			71.77	7.76
26333440	56.08	14.43	130.54	14.99	41.90	9.20	55.24	15.76
26334208	13.85	7.99	37.05	4.27	2.16	2.15	32.58	4.37
26334464	45.74	10.83	14.66	4.08	21.60	2.33	43.20	8.18
26334720	32.05	5.45	64.78	4.19	9.41	2.15	26.57	1.78
26334976	38.69	4.01	68.54	2.39	15.05	1.38	40.71	3.08
26413568	1.90	1.59	9.23	1.62	3.78	0.55	10.83	0.87
26413824	15.37	4.40	39.99	3.27	6.55	0.64	13.18	1.42
26415104	16.78	3.00	32.43	0.97	4.99	0.78	19.73	2.55

Table 7. The calculated values for the integral flux of the PAHs where present. Empty cells are where there was no discernible PAH emission. All data is presented in units of $\times 10^{-22}\ Wcm^{-2}$.

5.1.2 Calculating the Luminosities and SFRs

With all of the integral fluxes calculated for each PAH emission feature of each object, where present, attention could now be turned towards determining how the environment of these objects changes over different cosmological redshifts (i.e., the distance and history) for example. While some properties such as ionisation profile ratios are dimensionless and are not affected by distance, all values are first compared to their respective luminosities before being manipulated further to maintain consistency.

Therefore, assuming the same flat cosmology as stated in Chapter 3, the integral flux values of the PAH features of each object are converted to units of luminosity. The calculation for this is demonstrated in equation 1.9 with first determining the luminosity distance from the angular diameter distance:

$$D_L = D_M(1+z) = D_A(1+z)^2 \tag{1.9}$$

where D_L is the luminosity distance, D_M is the comoving distance and D_A is the angular diameter distance.

Converting all of the distances of each object to the luminosity distance with respect to their redshifts allows the fluxes to be therefore calculated with the simple inverse-square law in equation 1.10. However, the distance values had to be first simply converted from parsecs to metres. The flux units also had to be converted to units of Wm^{-2} from Wcm^{-2}:

$$L(W) = F(Wm^{-2})\, 4\pi {D_L}^2 (m^2) \tag{1.10}$$

where $L(W)$ is the output luminosity in watts and $F(Wm^{-2})$ is the input flux in watts per unit area.

It will also provide the ability to determine values easily for the star formation rate using calibrated values similar to ones discussed in Chapters 1 and 2.

The SFR values are determined from the total sum of the luminosities from the 6.2, 7.7 *and* 11.3 μm PAH emission features. The total sum is used to incorporate the total luminosity of the most common PAH emission features that are known to be the result of UV photons from star formation, thereby providing a better approximation for determining the SFR. Shipley et al. (2016) calculated an alternate proportionality constant that has been calibrated for the total sum of the luminosities for high-z galaxies, as shown in equation 1.11:

$$SFR(M_{\odot}\, yr^{-1}) = 1 \times 10^{-42.56 \pm 0.03} L_{(6.2+7.7+11.3)\mu m}\ (erg\ s^{-1})$$

$$\therefore \log SFR\ (M_{\odot}\, yr^{-1}) = (-42.56 \pm 0.03) \log L_{(6.2+7.7+11.3)\mu m}\ (erg\ s^{-1}) \qquad (1.11)$$

5.2 RESULTS

Following on from the previous section outlining the methodology for calculating the PAH integral luminosities and equivalent widths, and these values can be used to help make numerical inferences to the environment of star-forming regions within QSOs/AGN.

The resultant analysis determined from the calculated values is now presented.

5.2.1 PAH Ionisation Fraction

As discussed in section 2.1.4, PAHs exhibit emission profiles in different bands, with the ionised PAHs emanating from the 6.2, 7.7 and 8.6μm as well as the neutral from, in our limited case, the 11.3μm band. The 6.2μm and 7.7μm PAH bands are the most prominent of the ionised PAHs, with the 11.3μm PAH being the strongest of the neutral. Therefore, an 'ionisation fraction' between ionised and neutral PAHs can be useful in indicating how ionised the SF environments around quasars are. This idea is assuming that the PAH ionisation fraction is proportional to the stellar radiation field. This proportionality can be shown in equation 1.12 below (Boersma et al., 2015):

$$\frac{n_{PAH^+}}{n_{PAH^0}} = 3.76 \times 10^{-5} \frac{G_0 T_{gas}^{1/2}}{n_e} \tag{1.12}$$

where n_{PAH^+}/n_{PAH^0} is the ionised-neutral PAH density ratio, G_0 is the Habing radiation field (Habing, 1968), T_{gas} is the temperature of the gas and n_e is the electron number density of the gas. $G_0 T_{gas}^{1/2}/n_e$ collectively is known as the ionisation parameter, and resembles the ionising strength/density of the stellar radiation field, this is shown with the Habing radiation field being a measure of the field's strength/density due to the incident stellar UV photons acting on the material surrounding O and B stars in units of power per unit surface area.

Figure 5.4 shows the ionised-neutral PAH ratios $7.7\mu m/11.3\mu m$ correlating with $6.2\mu m/11.3\mu m$. The greater these ratios, the stronger the ionisation parameter of the PAHs and, by extension, the stronger the radiation field from the star forming regions as per equation 1.12. The correlation between the two ratios produces a line of best fit with a slope of 1.969, the upper and lower limits represent a 1σ separation from the line of best fit. Comparing this with Figure 5.5 from the work of Bernard-Salas et al. (2009a) it can be seen that the ionisation strengths, in general, are not as strong in the quasar sample, following similar ionisation fractions as the *HII* regions. This consequence could further allude to the relative compactness of the PAH emission from section 4.2.1, where a stronger radiation field penetrates more deeply into the surrounding dusty material. Alonso-Herrero et al. (2011) show that the $11.3\mu m$ PAH features seemingly have a more robust survivability than their shorter wavelength counterparts when in closer proximity to an AGN, which have even stronger radiation fields

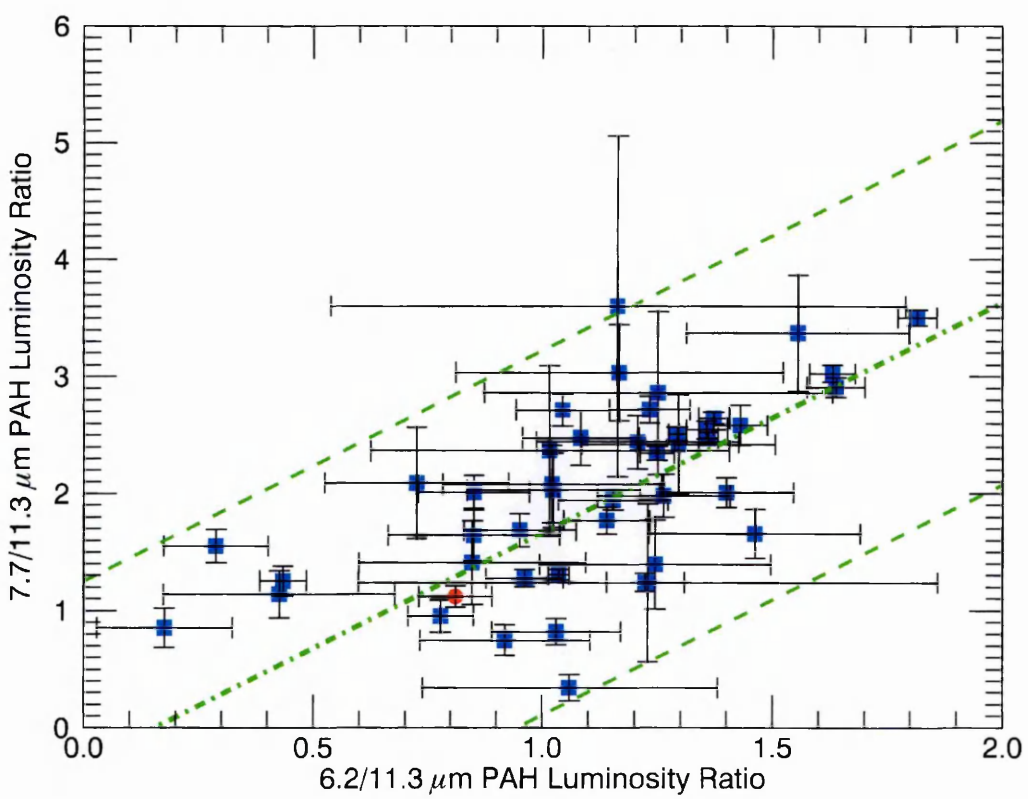

Figure 5.4. The ratios between ionised and neutral PAHs where the 6.2, 7.7 and $11.3\mu m$ are present within the sample. The least squares linear trend (centre green line) has a slope of 1.969. The upper and lower limits from the central linear fit represent a 1σ distribution from this linear trend. The red circle highlights the composite ratios from Chapter 4.

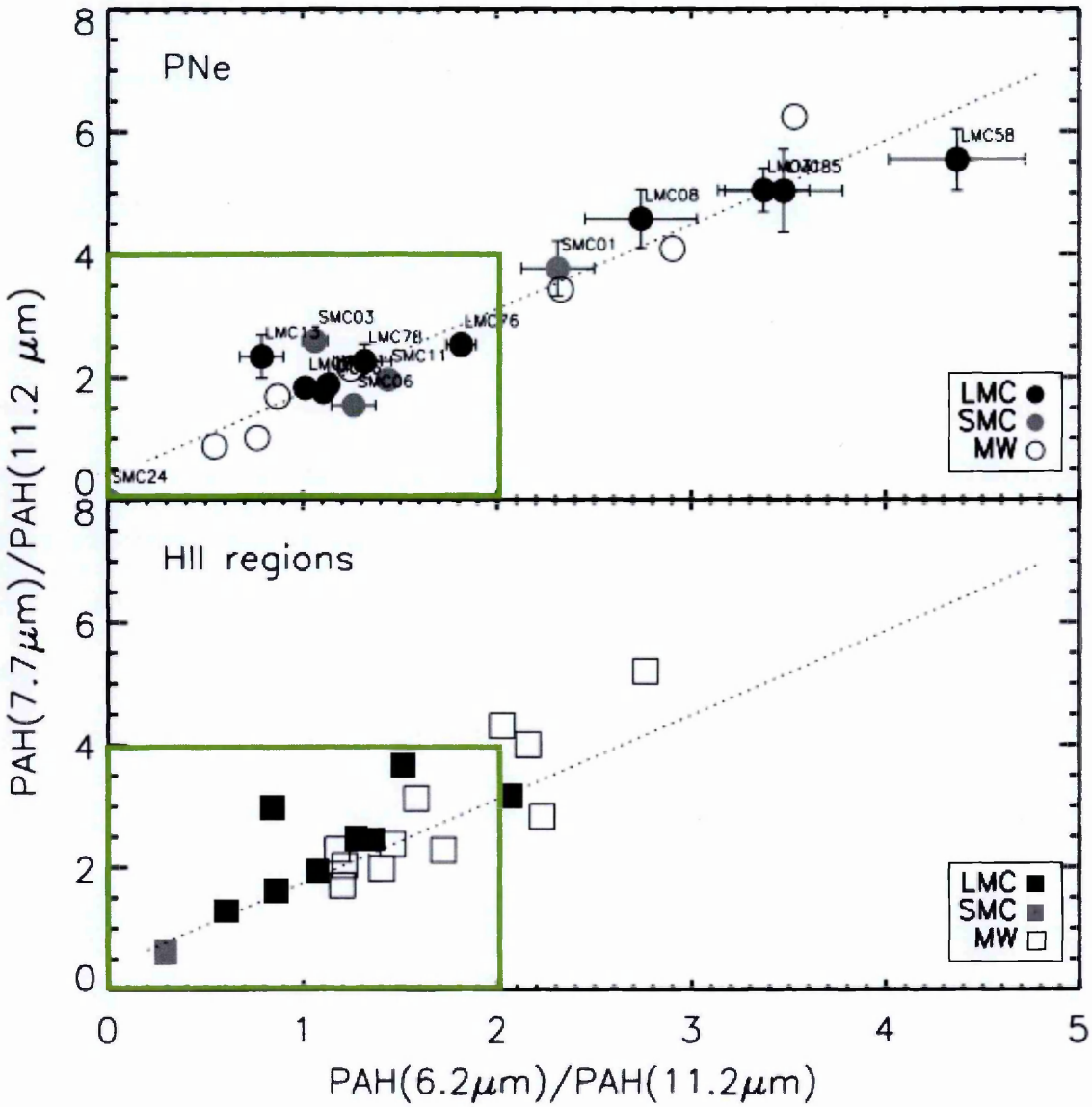

Figure 5.5. Ionised to neutral PAH ratio data from a planetary nebulae sample in comparison with HII regions. The green boxes indicate the region where my sample lies. Taken from Bernard-Salas et al. (2009a).

5.2.2 SFRs Determined from PAH Luminosities

As noted in sections 1.2 and 2.1, star formation processes are known to occur actively within AGN host galaxies. It is, therefore, possible to use PAH emission as a proxy for the total infrared luminosity, which is in itself, very tightly correlated to the Star Formation Rate. Therefore, using the calculated luminosities and SFR values from the relations derived from Shipley et al. (2016) one can compare how the SFR varies over redshift, which can act as a proxy for the star formation history of these objects (Madau et al., 1998).

Figure 5.6 shows all of the available luminosities from the 6.2, 7.7 and 11.3μm PAH features of each object against redshift.

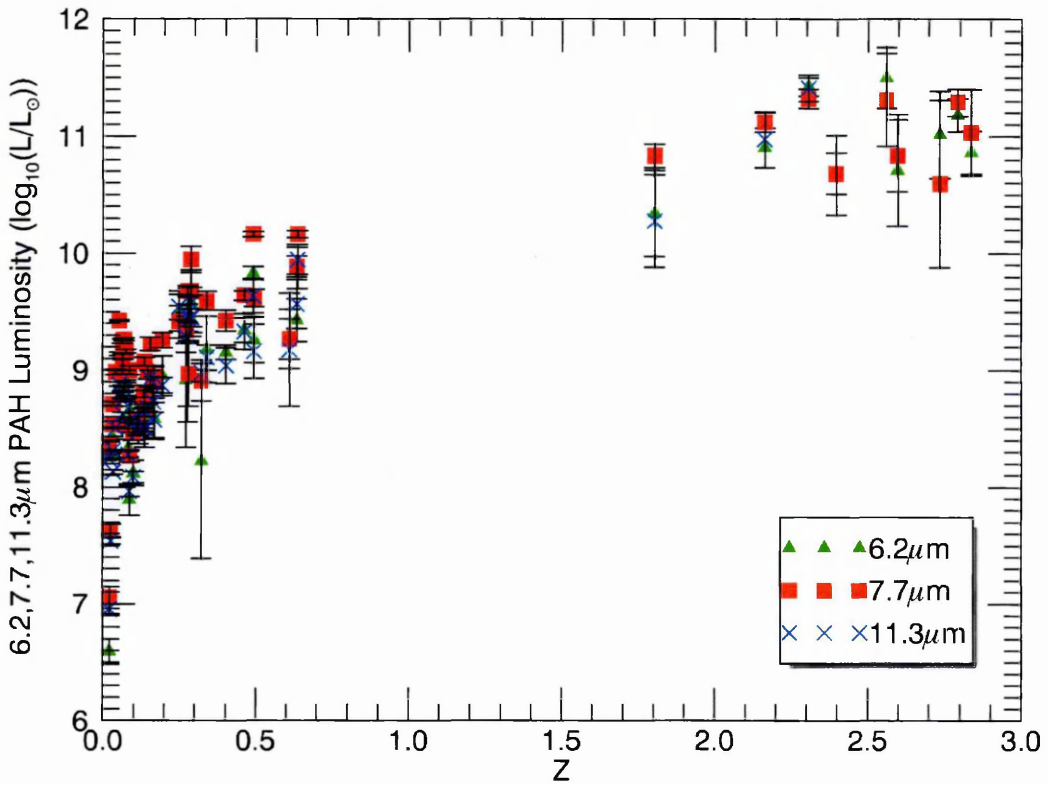

Figure 5.6. The log of the PAH luminosities in units of solar luminosity $L_{\odot}$ against their corresponding redshifts.

Shipley et al. (2016) calibrated SFR values from PAH luminosities for high-z galaxies. As well as the linear calibration fit for the total PAH luminosity demonstrated in equation 1.11, there are also linear trends for each of the individual component PAHs. The calibration plots of each of these can be found in Figure 5.7. The individual calibrated values can also be found in equation 1.13 presented similarly to equation 1.11:

$$\log SFR(M_{\odot}\, yr^{-1}) = (-40.06 \pm 0.09) + \log L_{6.2\mu m}\,(erg\ s^{-1})$$

$$\log SFR\,(M_{\odot}\, yr^{-1}) = (-42.38 \pm 0.06) + \log L_{7.7\mu m}\,(erg\ s^{-1}) \qquad (1.13)$$

$$\log SFR\,(M_{\odot}\, yr^{-1}) = (-44.14 \pm 0.08) + \log L_{11.3\mu m}\,(erg\ s^{-1})$$

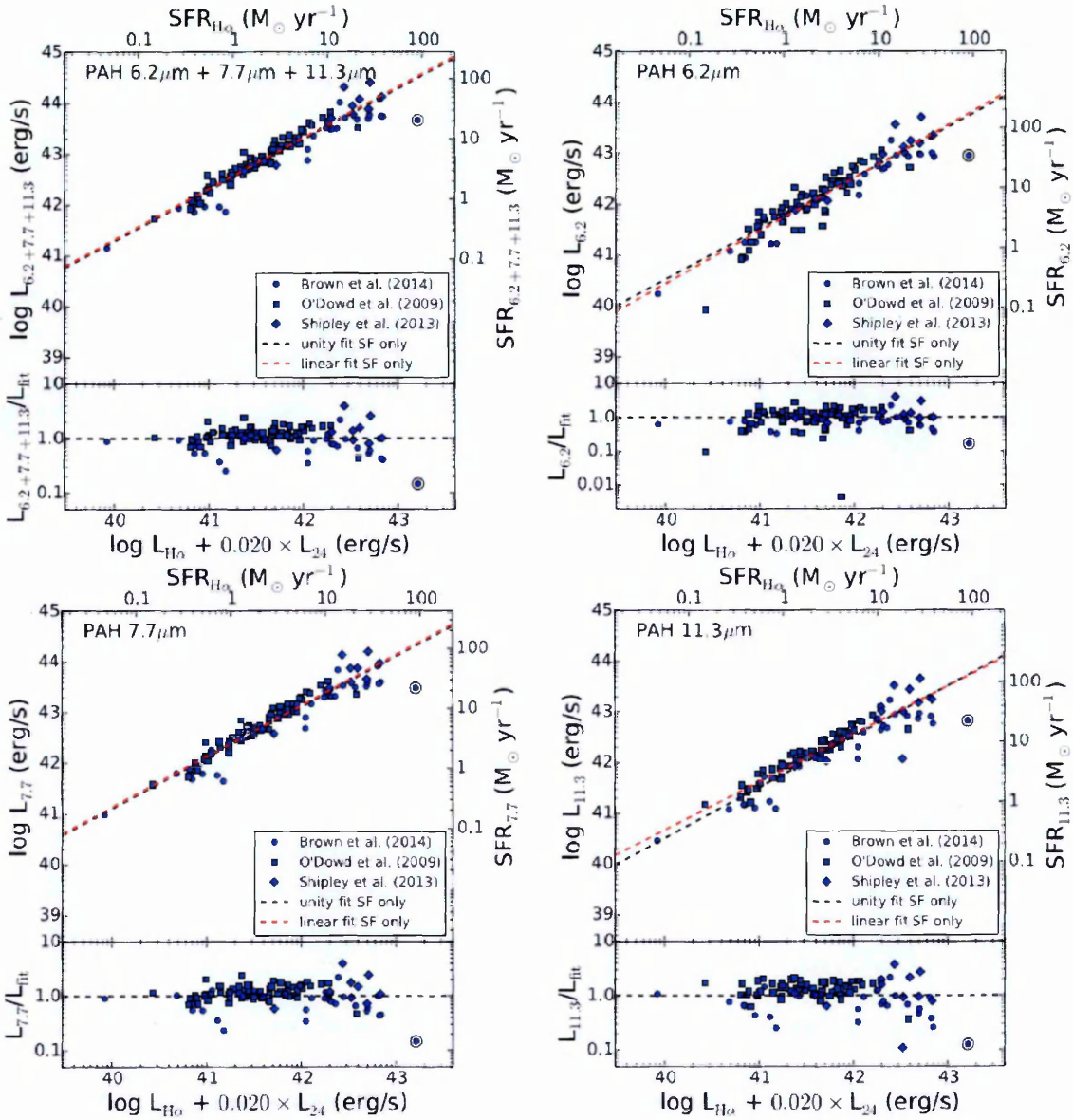

Figure 5.7. The extinction-corrected *Hα* luminosities are plotted against each of the PAH luminosities. A unity relation in the bottom panels of each plot determines how well expected values match to observation. This is used to help calibrate against the SFR. Taken from Shipley et al. (2016).

With equations 1.11 and 1.13 calibrated from the correlations in Figure 5.7, the SFR values have been determined for each of the component PAHs as well as the total combined PAH luminosity. Figure 5.8 shows the resultant SFR values calculated using equations 1.11 and 1.13 that enables a comparison between the different PAHs as SFR determiners.

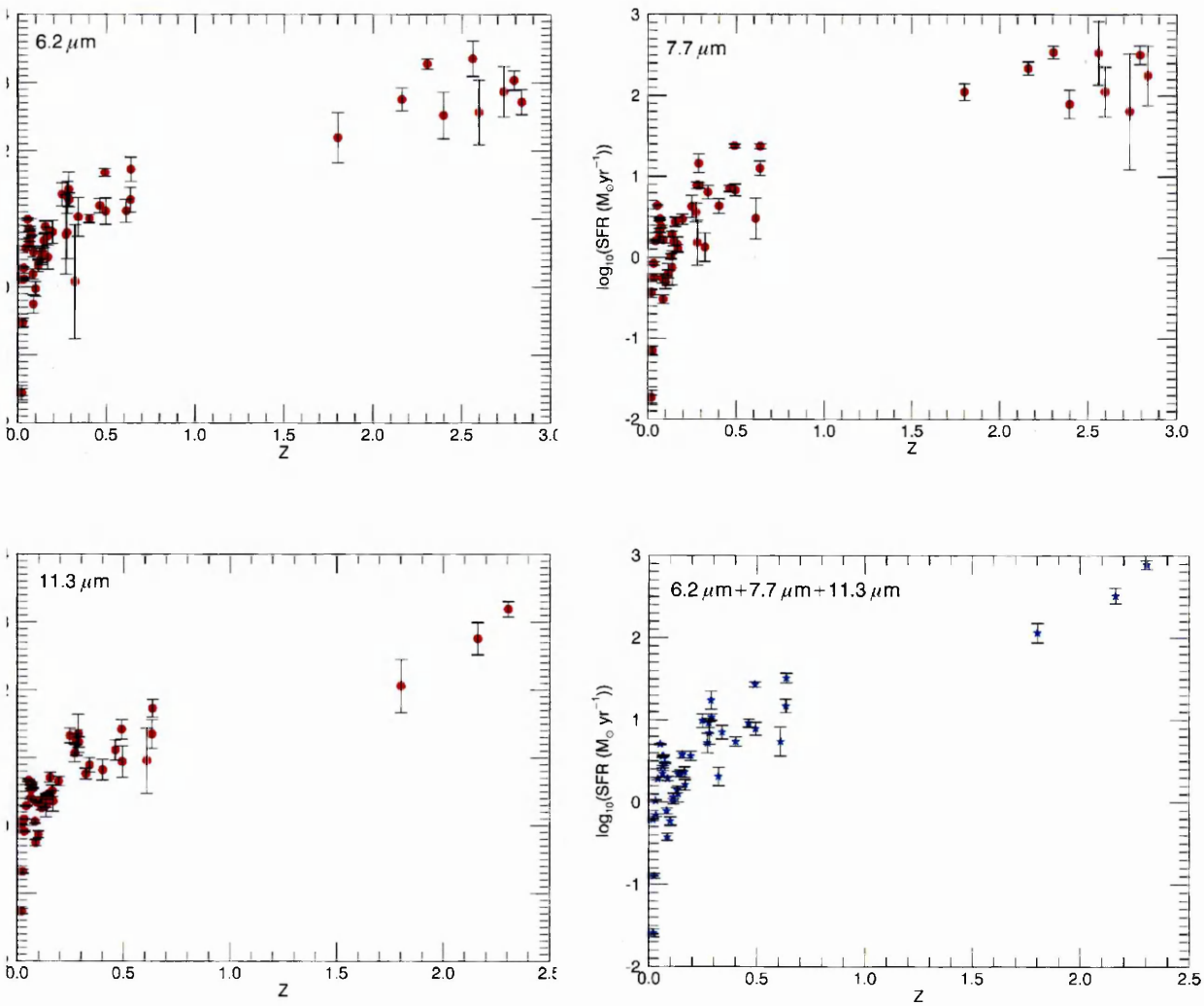

Figure 5.8. The log of the SFR values plotted against redshift for each of the individual PAH luminosities: top left is the SFR determined from the 6.2μm luminosity, top right is from the 7.7μm, bottom left is from the 11.3μm and bottom right is from the combined total where all three of the PAH features were present.

The results from the calculated SFR values in Figure 5.8 show all of the objects where the respective PAH emission features were present. It is noticeable that the individual components either slightly under or overestimate these values with greater margins of error, but allows a greater selection of the sample to be shown considering the slightly fewer values that exist for the 11.3μm PAH. The clear advantages to calculating the SFRs from $L_{6.2\mu m+7.7\mu m+11.3\mu m}$ are the reduced error through propagation, therefore providing a more tightly constrained estimate of the SFRs (see Figure 5.7). Across all of the plots in Figure 5.8 there is also a common shape and pattern of increasing SFR that appears to be consistent with the Madau (1998) plot of cosmic star formation density. These plots do not measure cosmic star formation density as

they do not measure the SFRs per comoving volume of space, but as QSO number density also increases with a similar shape, these results imply a similar SF density epoch to galaxies. It shall be noted there could be a slight dependency that this result is due to the flux limits of Spitzer, although this is considered unlikely with the high SNRs as a result of the optimal extraction routines used. A comparison with the $H\alpha$ line emission to measure SFRs, however, could not be made due to there being very limited pre-existing values for the objects in this sample (only 7 out of 63), and the inevitable contamination from the Broad Line Regions. This drawback resulted in comparisons of SFR with black hole mass being limited as well, either due to being redshifted out of the optical and are not detected, or they have simply not yet been measured.

5.2.3 PAH Profiles

As it was noted in section 2.1.4, PAHs can have a varying profile, shape and peak. Peeters et al. (2002) put these varying peaks into a classification system from class A through to class C increasing in wavelength. An attempt was made to make an observation as to what the common Class of PAHs is represented in the sample. However, this was thwarted by the low-resolution instruments used and the noisy nature of the data. This noisy data makes it difficult to resolve features that have fairly small/finite differences in the wavelength of their peaks. Examples of the 6.2μm and 7.7μm feature can be found in Figure 5.9. Despite these problems, however, it does somewhat look like the 6.2μm sample is mostly made up of Class A PAHs. This result would seemingly make sense since this correlates with hotter, denser and heavily processed environments such as the strong SF radiation fields/ISM/*HII* regions (Bernard-Salas et al., 2009b). Especially compared with Class C PAHs that are considered to be associated with cooler environments of limited UV photon excitation (e.g. Sloan et al., 2007), however, this is by no means conclusive. The 7.7μm PAHs appear to be too noisy to draw meaningful conclusions, but they appear to have a possible association with Class A PAHs. Observations would have to be made with greater spectral resolution to garner a classification, but while maintaining the required sensitivity needed to observe these objects.

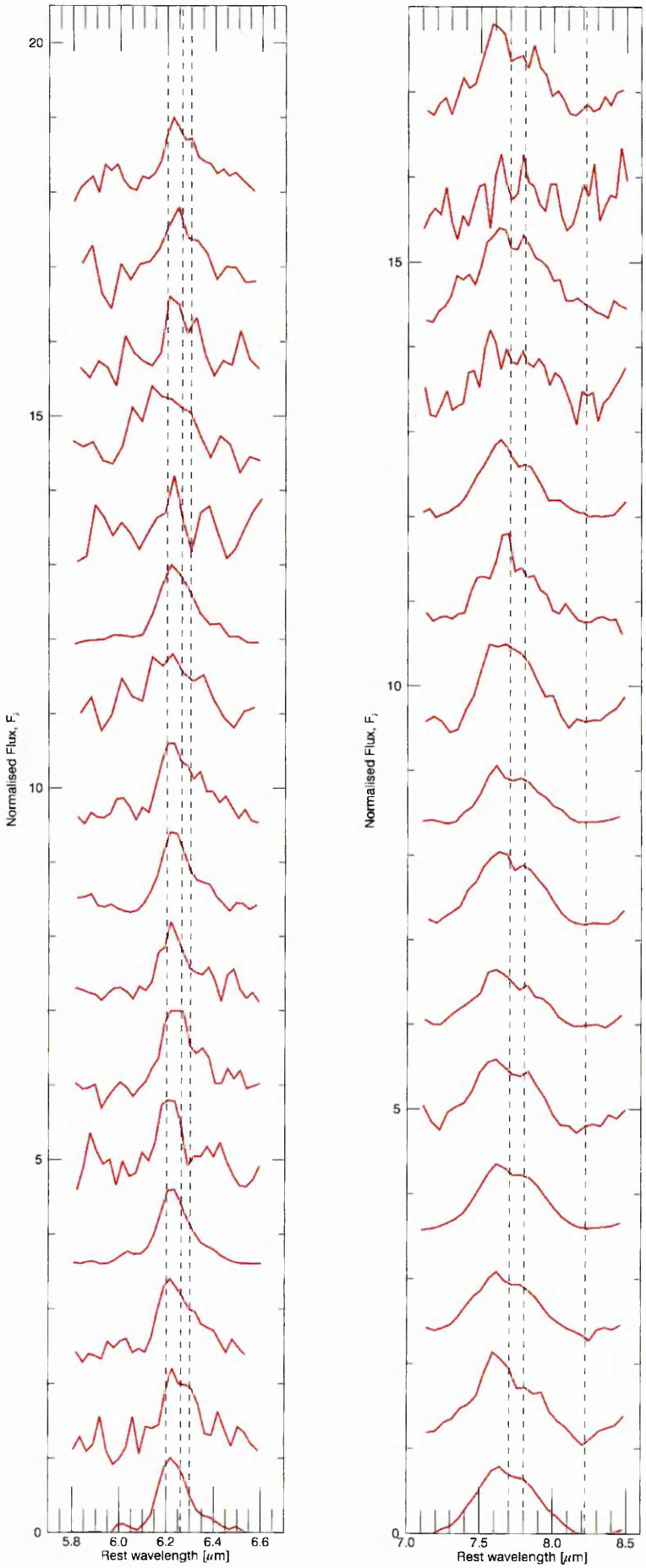

Figure 5.9. Examples of the PAH profiles observed with Class A, B and C marked by the dashed lines. In both it appears as if the sample favours Class A PAHs. This is not conclusive however due to instrumental limitations in resolving these features finitely.

5.2.4 Conclusions and Interpretation

From this Chapter, the key conclusive points made from the data are:

- PAH ionisation fractions of the PAHs in the QSO/AGN sample indicate similar ionisation strengths to *HII* regions; this is most likely due to the strong SF radiation fields creating a large separation between the stars and the photodissociation regions. Weakening the ionisation fractions.
- The SFRs all peak at around $z\sim2.4-2.5$ which is consistent with the Madau et al. (1998) plot of cosmic star formation density for galaxies, implying QSOs/AGN share similar evolutionary tracks in SF that peak at a similar epoch. This result could be down to flux limits, but that is doubtful due to high SNR values provided by the optimal extraction techniques used.
- The PAH profiles cannot be conclusively disentangled with the noise, and therefore, distortion of the PAHs' shapes and profiles. However, it seems they might be mostly Class A PAHs, which is commonly associated with well-processed dust commonly found in the ISM/*HII* regions.

Chapter 6

WATER IN THE EINSTEIN CROSS QUASAR

6.1 A BRIEF INTRODUCTION TO GRAVITATIONAL LENSING

In astronomy there is a multitude of ways to observe the universe where observations can be made in a variety of wavelengths: with either direct imaging, obtaining spectra to determine chemical compositions or time-domain observations. Our ability to observe the universe is however inhibited by its large scale and of the instrumentation used to observe it. One way to combat this problem of resolving distant, and therefore dim, objects is using a 'gravitational lens'. These gravitational lenses were first predicted by Einstein's theory of general relativity over 100 years ago. Einstein stipulated that the presence of mass-energy curves the space-time that contains it. Therefore, this implies that a large concentration of mass-energy (e.g. the sun or a cluster of galaxies) could warp space-time so as to bend the direction of light, thereby altering the apparent position of a light source that happens to pass by the large concentration of mass-energy relative to an observer's line of sight. The geometry for this configuration is shown in Figure 6.1.

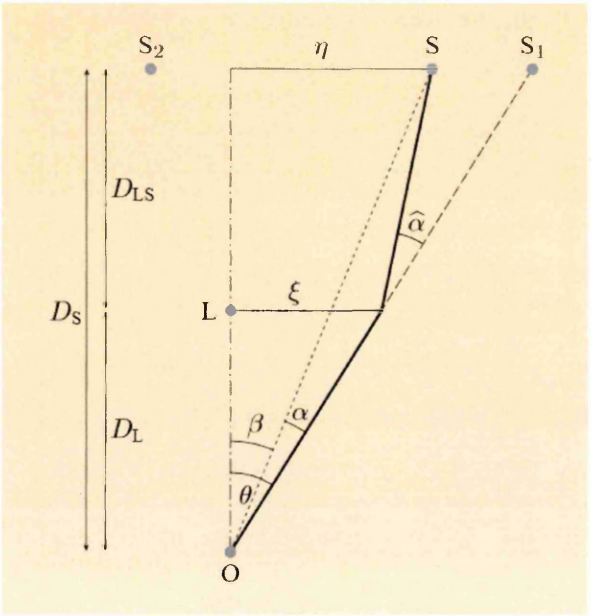

Figure 6.1. The geometry of gravitational lensing of a source S by a lens L, with the apparent positions of the source seen from the Earth S_1 and S_2. ξ is the impact parameter. D_{LS} is the distance to the source as seen from the lens. Taken from Serjeant (2010).

It should be noted that all of the distances in Figure 6.1 (D_S, D_L and D_{LS}) are angular diameter distances, and from Figure 3.10 in Chapter 3 it can be seen that $D_S \neq D_{LS} + D_L$ due to the nature of the cosmology. To better illustrate consider a flat universe with where the comoving distance r is related to the angular diameter distance D by $D(z) = r(z)/(1+z)$, comoving distances can add, but therefore the angular diameter distances cannot. However, assuming this simple geometry the angles depicted in Figure 6.1 can be related by the 'lens equation' in equation 1.14 (Serjeant, 2010):

$$\boldsymbol{\beta = \theta - \alpha(\theta)} \qquad (1.14)$$

where $\boldsymbol{\beta}$ is the angle between the source and the lens, $\boldsymbol{\theta}$ is the angle between the lens and the apparent source location and $\boldsymbol{\alpha}$ is the angle between the actual source location and the apparent source location, and all of these angles are vectors on the plane of the sky.

According to general relativity the deflection angle for a point source from Figure 6.1 is given by:

$$\hat{\alpha} = \frac{4GM}{\xi c^2}$$

where

$$\alpha = \frac{D_{LS}}{D_S}\hat{\alpha}$$

$$\therefore \alpha = \frac{D_{LS}}{D_S}\frac{4GM}{\xi c^2}$$

Therefore, if $\boldsymbol{\beta} = 0$ (i.e. the source is directly behind the lens) the lens equation can be rewritten as a scalar to provide the angular size of the image since $\alpha = \theta = \theta_E$, this is known as the Einstein radius for a point mass lens. Also, from Figure 6.1 it can be seen that $\theta = \xi/D_L$ which therefore leads to the resultant equation 1.15 below:

$$\theta_E = \sqrt{\frac{4GM}{c^2}\frac{D_{LS}}{D_S D_L}} \tag{1.15}$$

where θ_E is the Einstein Radius for a point mass lens, G is Newton's gravitational constant, M is the mass of the lens, c is the speed of light, with D_{LS}, D_S and D_L the angular diameter distances as per Figure 6.1.

With regards to lenses whose mass is extended such as the lens that warps the subject of this Chapter, the Einstein Cross quasar or QSO J2237+0305, the Einstein radius can, instead, be described for a 'singular isothermal sphere'. This particular lens model is 'singular' due to the mass density tending towards infinity as the radius tends to zero, leading to a singularity, and

is 'isothermal' due to treating the lens as an ideal gas of stars/matter at a constant temperature. This is shown in Equation 1.16 (e.g. Li et al., 2011):

$$\theta_{E,SIS} = 4\pi \left(\frac{\sigma_v}{c}\right)^2 \frac{D_{LS}}{D_S} \tag{1.16}$$

where $\theta_{E,SIS}$ is the Einstein radius for a singular isothermal sphere, σ_v is the velocity dispersion of the lens, c is the speed of light, with D_{LS} and D_S being the angular diameter distances as stated before.

The resultant images of such a singular isothermal sphere of extended mass distribution for a perfectly aligned background source would be an Einstein ring, if the lens is elliptical, there are up to 5 distinct images of the background object depending on the location of the background source. In practice, the fifth central image on the image plane cannot be seen since it is demagnified. Therefore, only four images of the background source remain visible producing an 'Einstein Cross' formation. The Einstein Cross configuration is shown in Figure 6.2, where the background caustics (source plane) are in perfect alignment with the foreground lens, this means the resultant critical lines (image plane) have the angular separation from the lens as shown in equation 1.15.

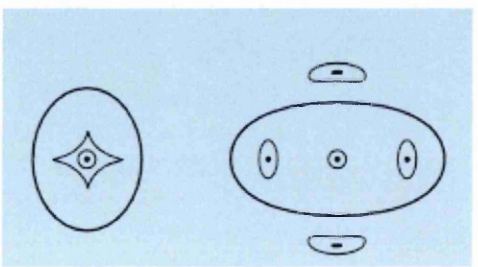

Figure 6.2. The geometry of gravitational lensing of a source directly behind a lensing object. The left diagram is the source plane directly behind the lens. The right diagram is the image plane. This arrangement produces five distinct images in the image plane, however the central image is demagnified meaning only four can be seen. This is also known as an Einstein Cross. Taken from Serjeant (2010).

6.2 THE EINSTEIN CROSS

QSO 2237+0305 was discovered by Huchra et al. (1985) with the 'Multiple Mirror Telescope' (MMT) during the 'Centre for Astrophysics Redshift Survey'. The lens itself (coined Huchra's Lens) consists of a $15mag$ spiral galaxy at redshift $z = 0.0394$, with the quasar almost directly centred onto the lens at a redshift of $z = 1.695$. However, when first discovered only one of the images could be seen due to limitations of the 2" resolution that was available with the MMT at the time of observation and therefore any recorded spectra of the quasar were contaminated by the lensing galaxy. The four images were not resolved until the $3.6m$ 'Canada-France-Hawaii Telescope' managed to disentangle the images spatially with its plate scale of 0.2" per pixel (Yee, 1988). This data turned out to be in agreement on a separate set of observations from the Cerro Tololo $4m$ telescope, which had superior calibration, despite poorer seeing conditions (Schneider et al., 1988). Other observations have also helped to confirm the inferred geometry from the simple lens models used (e.g. Rix et al., 1992; Crane et al., 1991; Racine, 1991).

QSO 2237+0305 was also the first quasar to exhibit gravitational microlensing properties as well (Irwin et al., 1989). This discovery resulted in the ability to analyse the quasar nuclear emission regions in scrupulous detail, magnifying the region to $\leq 1 \times 10^{-6}$" demonstrating sensitive variability in brightness across the region, opening the door to better understanding the quasar emission regions and its mechanisms. However, studies on the quasar emission regions are not yet conclusive and still require theoretical expansion (e.g. Pooley et al., 2007; Kochanek, 2004).

Figure 6.3 shows an image of QSO 2237+0305 taken from the Hubble Space Telescope's Wide Field Camera. Here the four images of the quasar with the lensing galaxy at the centroid can be clearly seen with the images in a cross formation. Leading to the common designation of the 'Einstein Cross', and is a result of the background quasar's perfect alignment with the foreground lensing galaxy with respect to our line of sight as stated in section 6.1.

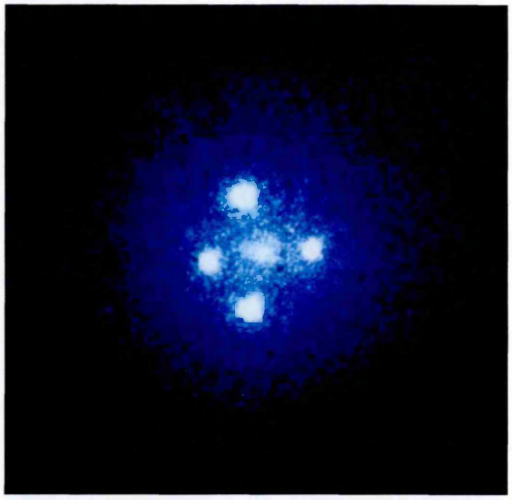

Figure 6.3. QSO J2237+0305 also known as the Einstein Cross. Image taken from Hubble (1990).

6.3 OBSERVATIONS WITH SPITZER IRS

During the process of checking each spectrum in CASSIS to identify whether or not the object possessed PAH emission, the author had initially but incorrectly identified such emission to correspond to that of the $7.7\mu m$ PAH to be present in the QSO J2237+0305 spectrum. It was then discovered that this spectrum possessed an unusual feature at $\sim 6.6\mu m$ that had not been previously reported in the initial observations by Agol et al. (2009), nor does any prominent feature appear to present itself within the previous analysis undertaken. The reasoning for this is most likely due to the optimal extraction routines (Lebouteiller et al., 2010) being unavailable at the time the original analysis was written. However, the object was extracted, exported and analysed by Agol et al. (2009).

In Figure 6.4a this feature can clearly be observed in the rest frame within both nods of the LL2 module and order, the feature becomes even more prominent when both nods are co-added in Figure 6.4b. While investigating the cause of the $6.6\mu m$ feature it was found that there is a close analogue to the emission of water vapour that also peaks at $6.6\mu m$, which could indicate this is the first H_2O vapour emission detected in the mid-IR of quasars. This analogue is detailed by Sargent et al. (2014) from circumstellar discs using Spitzer IRS data, although water vapour emission has been detected before in quasars, up to redshifts of $z = 3.91$ (Lis et al., 2011). A comparison between the work of Sargent et al. (2014) against the tentative and serendipitous water vapour feature is in Figure 6.5, where the spectra are centred at the $6.6\mu m$ peak. The shapes of FS Tau, FZ Tau and GN Tau appear strikingly similar with the emission from the Einstein cross showing a slight blueshift of the order $\sim \times 10^{-3}c$. The blueshift could be the result of the water vapour travelling towards us along our line of sight. If this is the case, the outflow could be representing a moving 'superwind' at $\sim 2000 kms^{-1}$. This matches with other galaxy driven superwinds have been commonly observed with velocities up to $\sim 3000 kms^{-1}$ (e.g. Heckman, 2002).

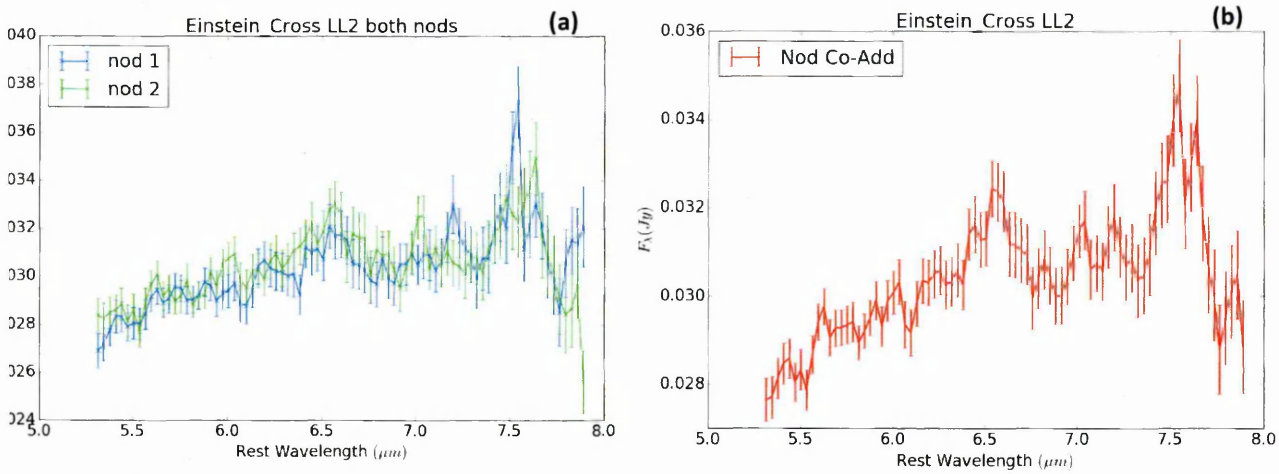

Figure 6.4. QSO J2237+0305 spectral data extracted using SMART and plotted using the Python routines as described in this work. a.) On the left we can see that the 6.6μm feature is present in both nods of order LL2. b.) On the right is the resultant co-adding of both of the nods together and the feature is enhanced. Showing a ~2σ detection from the continuum.

It will be important to note that this apparently broad feature that peaks at 6.6μm is down to the low-resolution modules used in Spitzer. These water vapour molecules usually emit in discrete lines. Therefore, it is believed that this feature is made up of smaller discrete emission lines, however, is made broad by the instrument being unable to resolve each component spectrally. If further investigation is to be made with more powerful instrumentation, consideration will need to be made that this feature may not resemble this particular shape.

It is evident however that further investigation is needed. The amount of IR spectral data available on the Einstein cross is limited, and the development of new instrumentation would be needed in order to gain the sensitivity required to further disentangle the feature from the continuum. This could potentially serve a future observation programme for the upcoming James Webb Space Telescope (JWST), which is discussed further in Chapter 7.

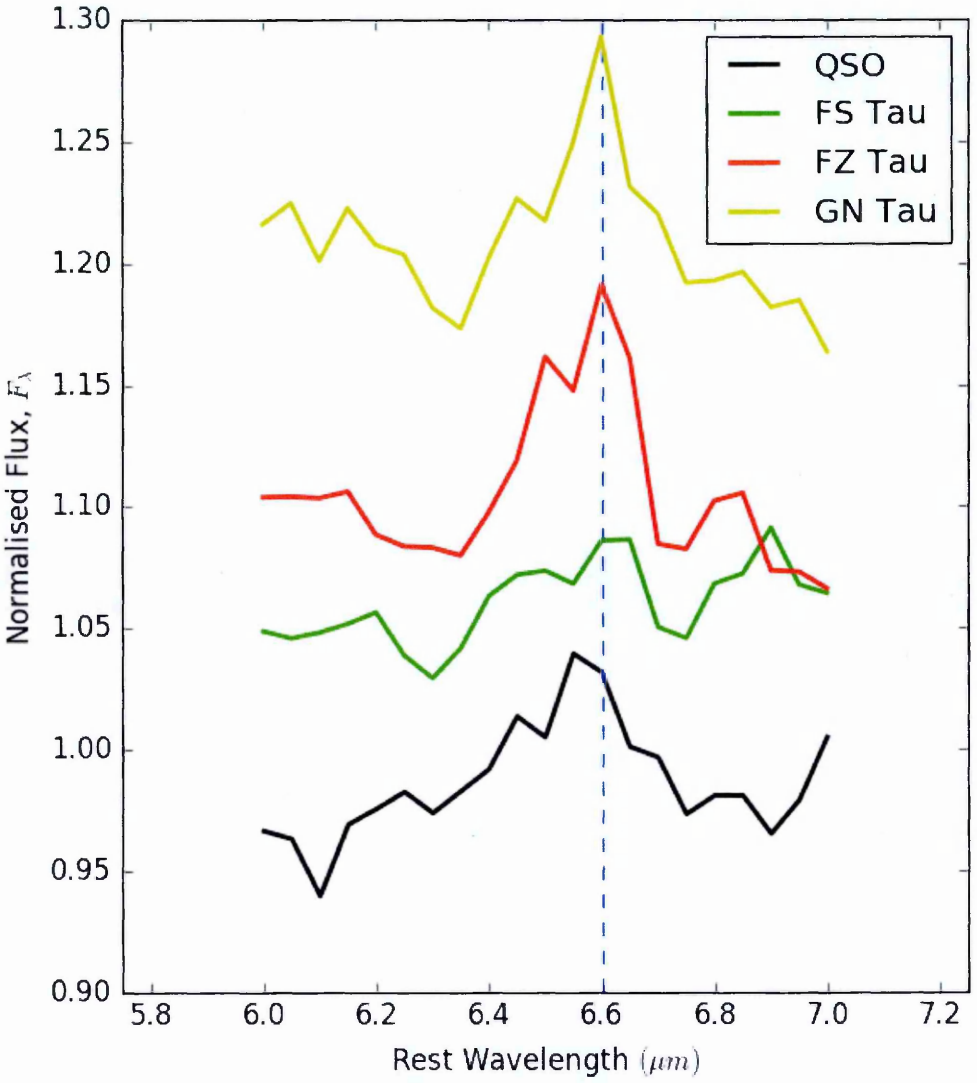

Figure 6.5 QSO J2237+0305 is compared with observations of FS Tau, FZ Tau and GN Tau as used by Sargent et al. (2014) by an arbitrary scale, focusing on the region around the 6.6μm peak (blue dashed line). The fundamental shape appears to be present in QSO J2237+0305, as well as a slight blueshift of the 6.6μm peak.

6.4 Discussion and Conclusions

H_2O outflows have been detected in a variety of different objects aside from the direct analogue of $6.6\mu m$ in circumstellar discs used in section 6.3. For example, Omont et al. (2011) reports water vapour emission from a high-z gravitationally lensed submillimetre galaxy. Also, Omont et al. (2013) find water vapour lines in a high-z gravitationally lensed ULIRG observed in the far infrared where the water vapour luminosity is strongly dependent on the IR luminosity. Omont et al. (2013) also argue this imply infrared radiative excitation of H_2O vapour lines, where high-z galaxies of $L_{IR} \geq \times 10^{13} L_{\odot}$ are strong H_2O vapour emitters, however with no low-z analogue.

Other gravitationally lensed quasars have also been noted to be observed with H_2O vapour emission. Van der Werf et al. (2011) showed QSO APM08279+5255 to emit high excitation lines of water vapour. Similar to Omont et al. (2013) the excitation of these lines are dominated by the local intense IR radiation fields, and since gas coolants are excited via collisional processes, the H_2O vapour cannot be a major coolant. Van der Werf et al. (2011) also argue the QSO contained massive clumps of optically thick SF as well as the SF being Eddington-limited due to radiation pressure exceeding the thermal gas pressure.

From the work done in this Chapter on QSO 2237+0305 there is a suggestion that the transition mechanism responsible for the H_2O vapour emission will most likely be observed by JWST, not only for further observation of the Einstein Cross quasar, but also a potential discovery in other objects. Also, further work will be needed to model the outflow to understand better the physical reasoning for its emission, as well as further work on the effects of differential magnification due to different parts of extended background objects having different magnification (e.g. Serjeant, 2012).

Chapter 7

SUMMARY AND FUTURE WORK

7.1 SUMMARY

This thesis has presented an analysis of the PAH emission that traces SF around AGN/QSOs. Measuring the extents of the PAH emission and deconvolving these from their corresponding empirical PSFs thereby allowing the determination of their physical sizes, as well as producing the best SNR template of QSOs in the mid-IR, analysing the SFRs from AGN/QSOs and finally making a serendipitous yet tentative discovery of water in the Einstein Cross quasar.

Therefore, the following are conclusions from the resultant analysis of the sample data presented in this thesis:

- There are two clear and distinct populations present due to a redshift deficit in the data, meaning that future missions with similar observing programmes/science goals can select their sample targets with an aim to fill this gap in the data thereby improving the understanding of the chemical evolution at different epochs.
- Across the whole sample of the objects with $7.7\mu m$ features, ~80% show the PAH emission constrained to the PSF as seen in Figure 3.8. The ~20% that is extended are the result of the low-z objects that could be adequately resolved from the PSF.
- Comparing Figure 3.8 with Figure 3.12, it can be seen that the deconvolved physical extent of the high-z objects exhibits SF throughout their host galaxies. This conclusion is not final however due to the high-z object's smaller angular size on the plane of the sky making it difficult to resolve the PAH emission from the AGN and host galaxy.

- At low-z the objects in Figure 3.12 do show some constraint to the nucleus in their SF regions ($\leq 1kpc$). However, this is not common with most of the objects in the sample lying outside of the nuclear regions. This result means there is no conclusive evidence of a close relation between AGN activity and SF via feedback.
- The best SNR QSO/AGN template was produced and compared with templates from Elbaz et al. (2011). QSO/AGN PAHs are much weaker than starbursting and the main sequence galaxies, which is seemingly consistent with stronger star formation due to intense stellar radiation fields 'pushing back' the photodissociation region boundaries. However, this is tentative due to uncertainties in determining the *kpc* scales.
- It was surprisingly found that the QSO/AGN template has more neutral than ionised PAHs, consistent with the AGN having no contribution to heating the PAH emission.
- There is also a component of hot dust in the QSO/AGN template that is not present in main sequence and starbursting galaxies, consistent with hot dust being heated within the AGN torus.
- The ionisation fractions were plotted, where a line of best fit can be shown in Figure 5.4. The average ionisation conditions of the PAHs from the composite place them very close to the line of best fit at 1.12 ± 0.09 for $7.7/11.3\mu m$ and 0.81 ± 0.08 for $6.2/11.3\mu m$. This result shows the average ionisation to be confined to the same ratios as those of HII regions.
- The calculated SFRs all increase consistently with plots of cosmic star formation density for galaxies, implying QSOs/AGN share similar evolutionary tracks in SF that follow similar trends at similar epochs.
- It seems the QSO/AGN PAHs might be mostly Class A PAHs, which is commonly associated with well-processed dust commonly found in the ISM/*HII* regions, although it is not conclusive due to the limitations caused by noise.
- A $\sim 2\sigma$ serendipitous detection of a feature that appears to resemble that of water vapour emission was tentatively found with a rest-frame peak at $6.6\mu m$ from the Einstein Cross quasar QSO J2237+0305.

- The transition mechanism responsible for the H_2O vapour emission will most likely be observed by JWST. Further work will be needed to model the outflow to understand better the physical reasoning for its emission, as well as further work on the effects of differential magnification due to different parts of extended background objects having different magnification (e.g. Serjeant, 2012).

7.2 FUTURE WORK

7.2.1 The James Webb Space Telescope

The next viable future mission that could extend the work presented here would be the James Webb Space Telescope (JWST) due for launch in 2018. This telescope and its instruments will operate from the near to mid-Infrared, a wavelength range of $0.6\mu m - 28.5\mu m$.

The instruments that will be able to perform tasks in the wavelengths of interest, as per this thesis, are:

- The Mid-Infrared Instrument (MIRI), MIRI will enable low resolution (R~100) spectroscopy with the range of $5 - 14\mu m$, as well as high resolution (R~2070) spectroscopy with the range of $4.9 - 28.8\mu m$. It can also perform wide-field broadband imagery in the MID-IR.
- The Near-Infrared Spectrograph (NIRSpec), NIRSpec will also have the same resolutions as MIRI. However, the low-resolution spectroscopy will operate between $0.6 - 5.0\mu m$ with the high-resolution spectroscopy operating $1 - 5.0\mu m$. NIRSpec has the unusual ability to obtain 100 spectra simultaneously with thanks to its innovative micro-electromagnetic shutter system. These micro-shutters can also be used to block portions of the sky where any contamination from the background or other sources can be limited.
- The Near-Infrared Camera (NIRCam), NIRCam is JWST's principal on-board imager that operates in bands between $0.6 - 5.0\mu m$. As well as just direct imaging, it has a coronagraph to block out bright sources, such as stars, for the purpose of imaging exoplanets.
- The Fine Guidance Sensor/Near InfraRed Imager and Slitless Spectrograph (FGS/NIRISS). This instrument contains two components: the FGS allows JWST to point precisely at given targets to provide high-quality images; NIRISS is an imager which

can also perform slitless spectroscopy and the whole instrument operates between $0.8 - 5.0\mu m$. Slitless spectroscopy allows for a wide-field image to be dispersed with a grism filter, allowing the spectra to be obtained from multiple sources within the field.

The instrument that can observe the most PAHs is MIRI, especially with regards to redshifted PAH emission considering a redshift limit of $z \rightarrow 3\ for\ \lambda_{rest} = 6.2\mu m$. However, the other spectrographs, such as NIRSpec, will be able to image the $3.3\mu m$ PAH feature, which could not be observed in Spitzer as it lies outside of its window.

The on-board instrumentation will operate at a greater spectral resolution and sensitivity compared to Spitzer (Gardner et al., 2006). These instruments will help to contribute further to the possible detection of PAH features present within quasars that could not be resolved from the continuum previously, for example, where the IR continuum is stronger compared to any weak and broad molecular features. As well as great spectral resolving power, the JWST's $6.5m$ primary mirror will provide the ability to better spatially resolve the PAH emission (~8 times greater than Spitzer). Further analysis of the objects already within the sample analysed in this these can be observed, and more specifically the high-z sample from Lutz et al. (2008), as well as building a larger target list that can fill the gap in objects that lie $0.9 \leq z < 1.8$.

7.2.2 Space Infrared Telescope for Cosmology and Astrophysics (SPICA)

SPICA is currently a proposed mission that is designed to follow on from the AKARI spacecraft, and will bridge the far-infrared gap left by JWST (Goicoechea et al., 2011). With the instrumental coverage operating between $12 - 210\mu m$, it aims to have a superior sensitivity between $12 - 100\mu m$ compared to the Herschel Telescope. The currently proposed launch date is 2025 with the proposed instruments:

- SAFARI: Imaging grating spectrometer that operates between $30-210\mu m$. This device is the main scientific instrument of the proposed mission.
- A Low-resolution imager and spectrograph operating between $12-34\mu m$

The mission objects are similar to JWST's, although the primary mirror is smaller at $2.5m$, which means its spatial resolution and sensitivity will be affected, and therefore not as a high angular resolution as JWST. However, SPICA will be able to cover a larger portion of the IR spectrum compared the very limited window of JWST at very high sensitivities. SPICA will be able to detect PAH emission features up to redshifts of $z \rightarrow 7$.

BIBLIOGRAPHY

AGOL, E., GOGARTEN, S.M., GORJIAN, V. and KIMBALL, A., 2009. Spitzer Observations of a Gravitationally Lensed Quasar, Qso 2237+0305. *Astrophysical Journal,* **697**(2), pp. 1010-1019.

ALLAMANDOLA, L.J., TIELENS, A.G.G.M. and BARKER, J.R., 1985. Polycyclic Aromatic-Hydrocarbons and the Unidentified Infrared-Emission Bands - Auto Exhaust Along the Milky-Way. *Astrophysical Journal,* **290**(1), pp. L25-L28.

ALLAMANDOLA, L., HUDGINS, D. and SANDFORD, S., 1999. Modeling the unidentified infrared emission with combinations of polycyclic aromatic hydrocarbons. *Astrophysical Journal,* **511**(2), pp. L115-L119.

ALONSO-HERRERO, A., RAMOS ALMEIDA, C., ESQUEJ, P., ROCHE, P.F., HERNAN-CABALLERO, A., HONIG, S.F., GONZALEZ-MARTIN, O., ARETXAGA, I., MASON, R.E., PACKHAM, C., LEVENSON, N.A., RODRIGUEZ ESPINOSA, J.M., SIEBENMORGEN, R., PEREIRA-SANTAELLA, M., DIAZ-SANTOS, T., COLINA, L., ALVAREZ, C. and TELESCO, C.M., 2014. Nuclear 11.3 mu m PAH emission in local active galactic nuclei. *Monthly Notices of the Royal Astronomical Society,* **443**(3), pp. 2766-2782.

ALONSO-HERRERO, A., RIEKE, G.H., RIEKE, M.J., COLINA, L., PEREZ-GONZALEZ, P.G. and RYDER, S.D., 2006. Near-infrared and star-forming properties of local luminous infrared galaxies. *Astrophysical Journal,* **650**(2), pp. 835-849.

BAHCALL, J.N., 1991. The Decade of Discovery. *Bulletin of the American Astronomical Society,* **23**, pp. 904.

BEICHMAN, C., NEUGEBAUER, G., HABING, H., CLEGG, P. and CHESTER, T., 22 July 2002, 2002-last update, IRAS Explanatory Supplement [Homepage of NASA], [Online]. Available: http://irsa.ipac.caltech.edu/IRASdocs/exp.sup/toc.html2015].

BERNARD-SALAS, J., 2015. Spectroscopic studies of PAHs with the James Webb Space Telescope. *AstroPAH,* **24**, pp. 4.

BERNARD-SALAS, J., PEETERS, E., SLOAN, G.C., GUTENKUNST, S., MATSUURA, M., TIELENS, A.G.G.M., ZIJLSTRA, A.A. and HOUCK, J.R., 2009a. Unusual Dust Emission from Planetary Nebulae in the Magellanic Clouds. *Astrophysical Journal,* **699**(2), pp. 1541-1552.

BERNARD-SALAS, J., SPOON, H.W.W., CHARMANDARIS, V., LEBOUTEILLER, V., FARRAH, D., DEVOST, D., BRANDL, B.R., WU, Y., ARMUS, L., HAO, L., SLOAN, G.C., WEEDMAN, D. and HOUCK, J.R., 2009b. A Spitzer High-Resolution Mid-Infrared Spectral Atlas of Starburst Galaxies. *Astrophysical Journal Supplement Series,* **184**(2), pp. 230-247.

BOERSMA, C., BREGMAN, J. and ALLAMANDOLA, L.J., 2015. Properties of Polycyclic Aromatic Hydrocarbons in the Northwest Photon Dominated Region of Ngc 7023. Iii. Quantifying the Traditional Proxy for Pah Charge and Assessing its Role. *Astrophysical Journal,* **806**(1), pp. 121-121.

BRANDL, B.R., BERNARD-SALAS, J., SPOON, H.W.W., DEVOST, D., SLOAN, G.C., GUILLES, S., WU, Y., HOUCK, J.R., WEEDMAN, D.W., ARMUS, L., APPLETON, P.N., SOIFER, B.T., CHARMANDARIS, V., HAO, L., MARSHALL, J.A., HIGDON, S.J. and HERTER, T.L., 2006. The mid-infrared properties of starburst galaxies from Spitzer-IRS spectroscopy. *Astrophysical Journal,* **653**(2), pp. 1129-1144.

BROWN, M.J.I., MOUSTAKAS, J., SMITH, J.-.T., DA CUNHA, E., JARRETT, T.H., IMANISHI, M., ARMUS, L., BRANDL, B.R. and PEEK, J.E.G., 2014. An Atlas of Galaxy Spectral Energy Distributions from the Ultraviolet to the Mid-Infrared. *Astrophysical Journal Supplement Series,* **212**(2), pp. 18.

CLEGG, P.E., ADE, P.A.R., ARMAND, C., BALUTEAU, J.P., BARLOW, M.J., BUCKLEY, M.A., BERGES, J.C., BURGDORF, M., CAUX, E., CECCARELLI, C., CERULLI, R., CHURCH, S.E., COTIN, F., COX, P., CRUVELLIER, P., CULHANE, J.L., DAVIS, G.R., DIGIORGIO, A., DIPLOCK, B.R., DRUMMOND, D.L., EMERY, R.J., EWART, J.D., FISCHER, J., FURNISS, I., GLENCROSS, W.M., GREENHOUSE, M.A., GRIFFIN, M.J., GRY, C., HARWOOD, A.S., HAZELL, A.S., JOUBERT, M., KING, K.J., LIM, T., LISEAU, R., LONG, J.A., LORENZETTI, D., MOLINARI, S., MURRAY, A.G., NAYLOR, D.A., NISINI, B., NORMAN, K., OMONT, A., ORFEI, R., PATRICK, T.J., PEQUIGNOT, D., POULIQUEN, D., PRICE, M.C., NGUYENQRIEU, ROGERS, A.J., ROBINSON, F.D., SAISSE, M., SARACENO, P., SERRA, G., SIDHER, S.D., SMITH, A.F., SMITH, H.A., SPINOGLIO, L., SWINYARD, B.M., TEXIER, D., TOWLSON, W.A., TRAMS, N.R., UNGER, S.J. and WHITE, G.J., 1996. The ISO long-wavelength spectrometer. *Astronomy & Astrophysics,* **315**(2), pp. L38-L42.

CLEMENTS, D.L., SUTHERLAND, W.J., MCMAHON, R.G. and SAUNDERS, W., 1996. Optical imaging of ultraluminous IRAS galaxies: How many are mergers? *Monthly Notices of the Royal Astronomical Society,* **279**(2), pp. 477-497.

COMPIEGNE, M., FLAGEY, N., NORIEGA-CRESPO, A., MARTIN, P.G., BERNARD, J.-., PALADINI, R. and MOLINARI, S., 2010. Dust in the Diffuse Emission of the Galactic Plane: the Herschel/spitzer Spectral Energy Distribution Fitting. *Astrophysical Journal Letters,* **724**(1), pp. L44-L47.

CRANE, P., ALBRECHT, R., BARBIERI, C., BLADES, J.C., BOKSENBERG, A., DEHARVENG, J.M., DISNEY, M.J., JAKOBSEN, P., KAMPERMAN, T.M., KING, I.R., MACCHETTO, F., MACKAY, C.D., PARESCE, F., WEIGELT, G., BAXTER, D., GREENFIELD, P., JEDRZEJEWSKI, R., NOTA, A. and SPARKS, W.B., 1991. 1st Results from the Faint Object Camera - Images of the Gravitational Lens System G2237+0305. *Astrophysical Journal,* **369**(2), pp. L59-&.

DASYRA, K.M., TACCONI, L.J., DAVIES, R.I., NAAB, T., GENZEL, R., LUTZ, D., STURM, E., BAKER, A.J., VEILLEUX, S., SANDERS, D.B. and BURKERT, A., 2006. Dynamical properties of ultraluminous infrared galaxies. II. Traces of dynamical evolution and end products of local ultraluminous mergers. *Astrophysical Journal,***651**(2), pp. 835-852.

DE GRAAUW, T., 1997. *First results of the ISO Short-Wavelength Spectrometer.*

DESERT, F., BOULANGER, F. and PUGET, J., 1990. Interstellar Dust Models for Extinction and Emission. *Astronomy & Astrophysics,* **237**(1), pp. 215-236.

DEVEREUX, N.A. and YOUNG, J.S., 1990. The Origin of the Far-Infrared Luminosity from Spiral Galaxies. *Astrophysical Journal,* **350**(2), pp. L25-L28.

DOPITA, M.A., PEREIRA, M., KEWLEY, L.J. and CAPACCIOLI, M., 2002. Star formation rates in interacting starburst galaxies. *Astrophysical Journal Supplement Series,* **143**(1), pp. 47-72.

ELBAZ, D., DICKINSON, M., HWANG, H.S., DIAZ-SANTOS, T., MAGDIS, G., MAGNELLI, B., LE BORGNE, D., GALLIANO, F., PANNELLA, M., CHANIAL, P., ARMUS, L., CHARMANDARIS, V., DADDI, E., AUSSEL, H., POPESSO, P., KARTALTEPE, J., ALTIERI, B., VALTCHANOV, I., COIA, D., DANNERBAUER, H., DASYRA, K., LEITON, R., MAZZARELLA, J., ALEXANDER, D.M., BUAT, V., BURGARELLA, D., CHARY, R., GILLI, R., IVISON, R.J., JUNEAU, S., LE FLOC'H, E., LUTZ, D., MORRISON, G.E., MULLANEY, J.R., MURPHY, E., POPE, A., SCOTT, D., BRODWIN, M., CALZETTI, D., CESARSKY, C., CHARLOT, S., DOLE, H., EISENHARDT, P., FERGUSON, H.C., SCHREIBER, N.F., FRAYER, D., GIAVALISCO, M., HUYNH, M., KOEKEMOER, A.M., PAPOVICH, C., REDDY, N., SURACE, C., TEPLITZ, H., YUN, M.S. and WILSON, G., 2011. GOODS-Herschel: an infrared main sequence for star-forming galaxies. *Astronomy & Astrophysics,* **533**, pp. A119.

FARRAH, D., BERNARD-SALAS, J., SPOON, H.W.W., SOIFER, B.T., ARMUS, L., BRANDL, B., CHARMANDARIS, V., DESAI, V., HIGDON, S., DEVOST, D. and HOUCK, J., 2007. High-resolution mid-infrared spectroscopy of ultraluminous infrared galaxies. *Astrophysical Journal,* **667**(1), pp. 149-169.

FAZIO, G.G., HORA, J.L., ALLEN, L.E., ASHBY, M.L.N., BARMBY, P., DEUTSCH, L.K., HUANG, J.S., KLEINER, S., MARENGO, M., MEGEATH, S.T., MELNICK, G.J., PAHRE, M.A., PATTEN, B.M., POLIZOTTI, J., SMITH, H.A., TAYLOR, R.S., WANG, Z., WILLNER, S.P., HOFFMANN, W.F., PIPHER, J.L., FORREST, W.J., MCMURTY, C.W., MCCREIGHT, C.R., MCKELVEY, M.E., MCMURRAY, R.E., KOCH, D.G., MOSELEY, S.H., ARENDT, R.G., MENTZELL, J.E., MARX, C.T.,

LOSCH, P., MAYMAN, P., EICHHORN, W., KREBS, D., JHABVALA, M., GEZARI, D.Y., FIXSEN, D.J., FLORES, J., SHAKOORZADEH, K., JUNGO, R., HAKUN, C., WORKMAN, L., KARPATI, G., KICHAK, R., WHITLEY, R., MANN, S., TOLLESTRUP, E.V., EISENHARDT, P., STERN, D., GORJIAN, V., BHATTACHARYA, B., CAREY, S., NELSON, B.O., GLACCUM, W.J., LACY, M., LOWRANCE, P.J., LAINE, S., REACH, W.T., STAUFFER, J.A., SURACE, J.A., WILSON, G., WRIGHT, E.L., HOFFMAN, A., DOMINGO, G. and COHEN, M., 2004. The Infrared Array Camera (IRAC) for the Spitzer Space Telescope. *Astrophysical Journal Supplement Series,* **154**(1), pp. 10-17.

FERRARESE, L. and MERRITT, D., 2000. A fundamental relation between supermassive black holes and their host galaxies. *Astrophysical Journal,* **539**(1), pp. L9-L12.

GEBHARDT, K., BENDER, R., BOWER, G., DRESSLER, A., FABER, S., FILIPPENKO, A., GREEN, R., GRILLMAIR, C., HO, L., KORMENDY, J., LAUER, T., MAGORRIAN, J., PINKNEY, J., RICHSTONE, D. and TREMAINE, S., 2000. A relationship between nuclear black hole mass and galaxy velocity dispersion. *Astrophysical Journal,***539**(1), pp. L13-L16.

GOICOECHEA, J.R., NAKAGAWA, T. and SAFARI SPICA TEAMS, 2011. Spica: the Next Generation Infrared Space Telescope. *Conditions and Impact of Star Formation: New Results with Herschel and Beyond,* **52**, pp. 253-258.

HABING, H., 1968. Interstellar Radiation Density between 912 a and 2400 a. *Bulletin of the Astronomical Institutes of the Netherlands,* **19**(6), pp. 421-&.

HARLAND, D.M., 2015, Infrared Astronomical Satellite (IRAS) [Homepage of Encyclopædia Britannica Online], [Online]. Available: http://www.britannica.com/topic/Infrared-Astronomical-Satellite [September 21, 2015].

HECKMAN, T. and BEST, P., 2014. The Coevolution of Galaxies and Supermassive Black Holes: Insights from Surveys of the Contemporary Universe. *Annual Review of Astronomy & Astrophysics,* **52**.

HECKMAN, T.M., 2002. Galactic Superwinds Circa 2001. In: J.S. MULCHAEY and J. STOCKE, eds, *Extragalactic Gas at Low Redshift.* Astronomical Society of the Pacific, pp. 292.

HERNAN-CABALLERO, A., ALONSO-HERRERO, A., HATZIMINAOGLOU, E., SPOON, H.W.W., RAMOS ALMEIDA, C., DIAZ SANTOS, T., HOENIG, S.F., GONZALEZ-MARTIN, O. and ESQUEJ, P., 2015. Resolving the Active Galactic Nucleus and Host Emission in the Mid-Infrared using a Model-Independent Spectral Decomposition. *Astrophysical Journal,* **803**(2), pp. UNSP 109.

HIGDON, S.J.U., DEVOST, D., HIGDON, J.L., BRANDL, B.R., HOUCK, J.R., HALL, P., BARRY, D., CHARMANDARIS, V., SMITH, J.D.T., SLOAN, G.C. and GREEN, J., 2004. The SMART data analysis package for the infrared spectrograph on the Spitzer Space Telescope. *Publications of the Astronomical Society of the Pacific,***116**(824), pp. 975-984.

HIGUERA-G, M. and RAMOS P, A.F., 2013. Pahs as Tracers of Local Agn-Starburst Connection. *Revista Mexicana De Astronomia Y Astrofisica,* **49**(2), pp. 301-309.

HOFFMEISTER, C., 1929. *Astron. Nachr.,* **236**, pp. 233.

HOUCK, J.R., ROELLIG, T.L., VAN CLEVE, J., FORREST, W.J., HERTER, T., LAWRENCE, C.R., MATTHEWS, K., REITSEMA, H.J., SOIFER, B.T., WATSON, D.M., WEEDMAN, D., HUISJEN, M., TROELTZSCH, J., BARRY, D.J., BERNARD-SALAS, J., BLACKEN, C.E., BRANDL, B.R., CHARMANDARIS, V., DEVOST, D., GULL, G.E., HALL, P., HENDERSON, C.P., HIGDON, S.J.U., PIRGER, B.E., SCHOENWALD, J., SLOAN, G.C., UCHIDA, K.I., APPLETON, P.N., ARMUS, L., BURGDORF, M.J., FAJARDO-ACOSTA, S.B., GRILLMAIR, C.J., INGALLS, J.G., MORRIS, P.W. and TEPLITZ, H.I., 2004. The Infrared Spectrograph (IRS) on the Spitzer Space Telescope.*Astrophysical Journal Supplement Series,* **154**(1), pp. 18-24.

HUBBLE SPACE TELESCOPE, 13 September 1990, 1990-last update, Einstein Cross: QSO J2237+0305 [Homepage of NASA], [Online].
Available: http://hubblesite.org/newscenter/archive/releases/1990/20/ [February, 2015].

HUCHRA, J., GORENSTEIN, M., KENT, S., SHAPIRO, I., SMITH, G., HORINE, E. and PERLEY, R., 1985. 2237+0305 - a New and Unusual Gravitational Lens. *Astronomical Journal,* **90**(5), pp. 691-&.

IRWIN, M.J., WEBSTER, R.L., HEWETT, P.C., CORRIGAN, R.T. and JEDRZEJEWSKI, R.I., 1989. Photometric Variations in the Q2237+0305 System - 1st Detection of a Microlensing Event. *Astronomical Journal,* **98**(6), pp. 1989-1994.

JONES, M. and LAMBOURNE, R., 2004. *An Introduction to Galaxies and Cosmology.* First edn. Cambridge: Cambridge University Press & The Open University.

KENNICUTT, R.C., JR. and EVANS,NEAL J.,,II, 2012. Star Formation in the Milky Way and Nearby Galaxies. *Annual Review of Astronomy and Astrophysics, Vol 50,* **50**, pp. 531-608.

KENNICUTT, R.C., 1998a. The global Schmidt law in star-forming galaxies. *Astrophysical Journal,* **498**(2), pp. 541-552.

KENNICUTT, R.C., 1998b. Star formation in galaxies along the Hubble sequence. *Annual Review of Astronomy and Astrophysics,* **36**, pp. 189-231.

KENNICUTT, R.C. and KENT, S.M., 1983. A Survey of H-Alpha Emission in Normal Galaxies. *Astronomical Journal,* **88**(8), pp. 1094-1107.

KESSLER, M.F., STEINZ, J.A., ANDEREGG, M.E., CLAVEL, J., DRECHSEL, G., ESTARIA, P., FAELKER, J., RIEDINGER, J.R., ROBSON, A., TAYLOR, B.G. and DEFERRAN, S.X., 1996. The Infrared Space Observatory (ISO) mission. *Astronomy & Astrophysics,* **315**(2), pp. L27-L31.

KEWLEY, L.J., GELLER, M.J., JANSEN, R.A. and DOPITA, M.A., 2002. The H alpha and infrared star formation rates for the Nearby Field Galaxy Survey. *Astronomical Journal,* **124**(6), pp. 3135-3143.

KIM, H., WAGNER, D. and SAYKALLY, R., 2001. Single photon infrared emission spectroscopy of the gas phase pyrene cation: Support for a polycyclic aromatic hydrocarbon origin of the unidentified infrared emission bands. *Physical Review Letters,* **86**(25), pp. 5691-5694.

KOCHANEK, C.S., 2004. Quantitative interpretation of quasar microlensing light curves. *Astrophysical Journal,* **605**(1), pp. 58-77.

KUTNER, M., 2003. *Astronomy: A Physical Perspective.* Second edn. Cambridge: Cambridge University Press.

LANGHOFF, S.R., 1996. Theoretical infrared spectra for polycyclic aromatic hydrocarbon neutrals, cations, and anions. *Journal of Physical Chemistry,* **100**(8), pp. 2819-2841.

LAURENT, O., MIRABELL, I., CHARMANDARIS, V., GALLAIS, P., MADDEN, S., SAUVAGE, M., VIGROUX, L. and CESARSKY, C., 2000. Mid-infrared diagnostics to distinguish AGNs from starbursts. *Astronomy & Astrophysics,* **359**(3), pp. 887-899.

LEBOUTEILLER, V., BERNARD-SALAS, J., SLOAN, G.C. and BARRY, D.J., 2010. Advanced Optimal Extraction for the Spitzer/IRS. *Publications of the Astronomical Society of the Pacific,* **122**(888), pp. 231-240.

LEGER, A. and PUGET, J.L., 1984. Identification of the Unidentified Ir Emission Features of Interstellar Dust. *Astronomy and Astrophysics,* **137**(1), pp. L5-L8.

LI, A. and DRAINE, B., 2001. Infrared emission from interstellar dust. II. The diffuse interstellar medium. *Astrophysical Journal,* **554**(2), pp. 778-802.

LIS, D.C., NEUFELD, D.A., PHILLIPS, T.G., GERIN, M. and NERI, R., 2011. DISCOVERY OF WATER VAPOR IN THE HIGH-REDSHIFT QUASAR APM 08279+5255 AT z=3.91. *Astrophysical Journal Letters,* **738**(1), pp. L6.

LONSDALE, P. and HELOU, G., 1987. On the origin of the 40 - 120 micron emission of galaxy disks: a comparison with Hα fluxes. *Astrophysical Journal,* **314**, pp. 513-524.

LUTZ, D., STURM, E., TACCONI, L.J., VALIANTE, E., SCHWEITZER, M., NETZER, H., MAIOLINO, R., ANDREANI, P., SHEMMER, O. and VEILLEUX, S., 2008. Star formation in the hosts of high-z QSOs: Evidence from Spitzer PAH detections. *Astrophysical Journal,* **684**(2), pp. 853-861.

MADAU, P., POZZETTI, L. and DICKINSON, M., 1998. The star formation history of field galaxies. *Astrophysical Journal,* **498**(1), pp. 106-116.

MAGORRIAN, J., TREMAINE, S., RICHSTONE, D., BENDER, R., BOWER, G., DRESSLER, A., FABER, S., GEBHARDT, K., GREEN, R., GRILLMAIR, C., KORMENDY, J. and LAUER, T., 1998. The demography of massive dark objects in galaxy centers. *Astronomical Journal,* **115**(6), pp. 2285-2305.

NETZER, H., 2015. Revisiting the Unified Model of Active Galactic Nuclei. *Annual Review of Astronomy & Astrophysics,* **53**.

NETZER, H., 1990. *Saas-Fee Advanced Course of the Swiss Society for Astrophysics and Astronomy: Active galactic nuclei,* **20**.

O'DOWD, M.J., SCHIMINOVICH, D., JOHNSON, B.D., TREYER, M.A., MARTIN, C.D., WYDER, T.K., CHARLOT, S., HECKMAN, T.M., MARTINS, L.P., SEIBERT, M. and VAN DER HULST, J.M., 2009. POLYCYCLIC AROMATIC HYDROCARBONS IN GALAXIES AT z similar to 0.1: THE EFFECT OF STAR FORMATION AND ACTIVE GALACTIC NUCLEI. *Astrophysical Journal,* **705**(1), pp. 885-898.

OKE, J.B. and GUNN, J.E., 1974. Distance of Bl Lacertae. *Astrophysical Journal,* **189**(1), pp. L5-L8.

OMONT, A., NERI, R., COX, P., LUPU, R., GUELIN, M., VAN DER WERF, P., WEISS, A., IVISON, R., NEGRELLO, M., LEEUW, L., LEHNERT, M., SMAIL, I., VERMA, A., BAKER, A.J., BEELEN, A., AGUIRRE, J.E., BAES, M., BERTOLDI, F., CLEMENTS, D.L., COORAY, A., COPPIN, K., DANNERBAUER, H., DE ZOTTI, G., DYE, S., FIOLET, N., FRAYER, D., GAVAZZI, R., HUGHES, D., JARVIS, M., KRIPS, M., MICHALOWSKI, M.J., MURPHY, E.J., RIECHERS, D., SERJEANT, S., SWINBANK, A.M., TEMI, P., VACCARI, M., VIEIRA, J.D., AULD, R., BUTTIGLIONE, B., CAVA, A., DARIUSH, A., DUNNE, L., EALES, S.A., FRITZ, J., GOMEZ, H., IBAR, E., MADDOX, S., PASCALE, E., POHLEN, M., RIGBY, E., SMITH, D.J.B., BOCK, J., BRADFORD, C.M., GLENN, J., SCOTT, K.S. and ZMUIDZINAS, J., 2011. Observation of H2O in a strongly lensed Herschel-ATLAS source at z=2.3. *Astronomy & Astrophysics,* **530**, pp. L3.

OMONT, A., YANG, C., COX, P., NERI, R., BEELEN, A., BUSSMANN, R.S., GAVAZZI, R., VAN DER WERF, P., RIECHERS, D., DOWNES, D., KRIPS, M., DYE, S., IVISON, R., VIEIRA, J.D., WEISS, A., AGUIRRE, J.E., BAES, M., BAKER, A.J., BERTOLDI, F., COORAY, A., DANNERBAUER, H., DE ZOTTI, G., EALES, S.A., FU, H., GAO, Y., GUELIN, M., HARRIS, A.I., JARVIS, M., LEHNERT, M., LEEUW, L., LUPU, R., MENTEN, K., MICHALOWSKI, M.J., NEGRELLO, M., SERJEANT, S., TEMI, P., AULD, R., DARIUSH, A., DUNNE, L., FRITZ, J., HOPWOOD, R., HOYOS, C., IBAR, E., MADDOX, S., SMITH, M.W.L., VALIANTE, E., BOCK, J., BRADFORD, C.M., GLENN, J. and SCOTT, K.S., 2013. H2O emission in high-z ultra-luminous infrared galaxies. *Astronomy & Astrophysics,* **551**, pp. A115.

PEETERS, E., 2002. *Polycyclic Aromatic Hydrocarbons and Dust in Regions of Massive Star Formation*, RIJKSUNIVERSITEIT GRONINGEN.

PEETERS, E., HONY, S., VAN KERCKHOVEN, C., TIELENS, A.G.G.M., ALLAMANDOLA, L.J., HUDGINS, D.M. and BAUSCHLICHER, C.W., 2002. The rich 6 to 9 mu m spectrum of interstellar PAHs. *Astronomy & Astrophysics,* **390**(3), pp. 1089-1113.

PEETERS, E., SPOON, H.W.W. and TIELENS, A.G.G.M., 2004. Polycyclic aromatic hydrocarbons as a tracer of star formation? *Astrophysical Journal,* **613**(2), pp. 986-1003.

PERLEY, R.A., DREHER, J.W. and COWAN, J.J., 1984. The Jet and Filaments in Cygnus-a. *Astrophysical Journal,* **285**(1), pp. L35-&.

PETERSON, B.M., FERRARESE, L., GILBERT, K.M., KASPI, S., MALKAN, M.A., MAOZ, D., MERRITT, D., NETZER, H., ONKEN, C.A., POGGE, R.W., VESTERGAARD, M. and WANDEL, A., 2004. Central masses and broad-line region sizes of active galactic nuclei. II. A homogeneous analysis of a large reverberation-mapping database. *Astrophysical Journal,* **613**(2), pp. 682-699.

PHILLIPPS, S., 2005. *The Structure & Evolution of Galaxies.* First edn. Chichester: John Wiley & Sons.

POOLEY, D., BLACKBURNE, J.A., RAPPAPORT, S. and SCHECHTER, P.L., 2007. X-ray and optical flux ratio anomalies in quadruply lensed quasars. I. Zooming in on quasar emission regions. *Astrophysical Journal,* **661**(1), pp. 19-29.

POUW, A., 1983. The IRAS Spacecraft. *British Interplanetary Society Journal,* **36**, pp. 17-20.

RACINE, R., 1991. 5th Image and Photometric Variability in 2237+0305 (Einstein Cross). *Astronomical Journal,* **102**(2), pp. 454-460.

RIEKE, G.H., YOUNG, E.T., ENGELBRACHT, C.W., KELLY, D.M., LOW, F.J., HALLER, E.E., BEEMAN, J.W., GORDON, K.D., STANSBERRY, J.A., MISSELT, K.A., CADIEN, J., MORRISON, J.E., RIVLIS, G., LATTER, W.B., NORIEGA-CRESPO, A., PADGETT, D.L., STAPELFELDT, K.R., HINES, D.C., EGAMI, E., MUZEROLLE, J., ALONSO-HERRERO, A., BLAYLOCK, M., DOLE, H., HINZ, J.L., LE FLOC'H, E., PAPOVICH, C., PEREZ-GONZALEZ, P.G., SMITH, P.S., SU, K.Y.L., BENNETT, L., FRAYER, D.T., HENDERSON, D., LU, N., MASCI, F., PESENSON, M., REBULL, L., RHO, J., KEENE, J., STOLOVY, S., WACHTER, S., WHEATON, W., WERNER, M.W. and RICHARDS, P.L., 2004. The Multiband Imaging Photometer for Spitzer (MIPS). *Astrophysical Journal Supplement Series,* **154**(1), pp. 25-29.

SALAMA, A., 28 May 2007, 2007-last update, Infrared Space Observatory Mission Overview [Homepage of ESA], [Online]. Available: http://iso.esac.esa.int/Mission_overview.html2015].

RIX, H.W., SCHNEIDER, D.P. and BAHCALL, J.N., 1992. Hubble Space Telescope Wide Field Camera Imaging of the Gravitational Lens 2237+0305. *Astronomical Journal,* **104**(3), pp. 959-967.

SARGENT, B.A., FORREST, W., WATSON, D.M., D'ALESSIO, P., CALVET, N., FURLAN, E., KIM, K.H., GREEN, J., PONTOPPIDAN, K., RICHTER, I. and TAYRIEN, C., 2014. EMISSION FROM WATER VAPOR AND ABSORPTION FROM OTHER GASES AT 5-7.5 mu m IN SPITZER-IRS SPECTRA OF PROTOPLANETARY DISKS.*Astrophysical Journal,* **792**(2), pp. 83.

SCHMIDT, M., 1963. 3C 273 : A Star-Like Object with Large Red-Shift. **197**(4872), pp. 1040.

SCHMIDT, M., 1959. The Rate of Star Formation. *Astrophysical Journal,* **129**(2), pp. 243-258.

SCHMITT, J.O.H.N.L., 1968. BL Lac identified as a Radio Source. **218**(5142), pp. 663.

SCHNEIDER, D.P., TURNER, E.L., GUNN, J.E., HEWITT, J.N., SCHMIDT, M. and LAWRENCE, C.R., 1988. High-Resolution Ccd-Imaging and Derived Gravitational Lens Models of 2237+0305. *Astronomical Journal,* **95**(6), pp. 1619-&.

SCHWEITZER, M., LUTZ, D., STURM, E., CONTURSI, A., TACCONI, L.J., LEHNERT, M.D., DASYRA, K.M., GENZEL, R., VEILLEUX, S., RUPKE, D., KIM, D.-., BAKER, A.J., NETZER, H., STERNBERG, A., MAZZARELLA, J. and LORD, S., 2006. Spitzer Quasar and ULIRG Evolution Study (QUEST). I. The origin of the far-infrared continuum of QSOs. *Astrophysical Journal,* **649**(1), pp. 79-90.

SERJEANT, S. and HATZIMINAOGLOU, E., 2009. The evolution of star formation in quasar host galaxies. *Monthly Notices of the Royal Astronomical Society,* **397**(1), pp. 265-280.

SERJEANT, S., 2010. *Observational Cosmology.* First edn. Cambridge: Cambridge University Press & The Open University.

SERJEANT, S., BERTOLDI, F., BLAIN, A.W., CLEMENTS, D.L., COORAY, A., DANESE, L., DUNLOP, J., DUNNE, L., EALES, S., FALDER, J., HATZIMINAOGLOU, E., HUGHES, D.H., IBAR, E., JARVIS, M.J., LAWRENCE, A., LEE, M.G., MICHALOWSKI, M., NEGRELLO, M., OMONT, A., PAGE, M., PEARSON, C., VAN DER WERF, P.P., WHITE, G., AMBLARD, A., AULD, R., BAES, M., BONFIELD, D.G., BURGARELLA, D., BUTTIGLIONE, S., CAVA, A., DARIUSH, A., DE ZOTTI, G., DYE, S., FRAYER, D., FRITZ, J., GONZALEZ-NUEVO, J., HERRANZ, D., IVISON, R.J., LAGACHE, G., LEEUW, L., LOPEZ-CANIEGO, M., MADDOX, S., PASCALE, E., POHLEN, M., RIGBY, E., RODIGHIERO, G., SAMUI, S., SIBTHORPE, B., SMITH, D.J.B., TEMI, P., THOMPSON, M., VALTCHANOV, I. and VERMA, A., 2010. Herschel ATLAS: The cosmic star formation history of quasar host galaxies. *Astronomy & Astrophysics,* **518**, pp. L7.

SERJEANT, S., 2012. Strong biases in infrared-selected gravitational lenses. *Monthly Notices of the Royal Astronomical Society,* **424**(4), pp. 2429-2441.

SEYFERT, C.K., 1943. Nuclear emission in spiral nebulae. *Astrophysical Journal,* **97**(1).

SHIPLEY, H.V., PAPOVICH, C., RIEKE, G.H., BROWN, M.J.I. and MOUSTAKAS, J., 2016. A New Star Formation Rate Calibration from Polycyclic Aromatic Hydrocarbon Emission Features and Application to High-redshift Galaxies. *Astrophysical Journal,* **818**(1).

SHIPLEY, H.V., PAPOVICH, C., RIEKE, G.H., DEY, A., JANNUZI, B.T., MOUSTAKAS, J. and WEINER, B., 2013. Spitzer Spectroscopy of Infrared-Luminous Galaxies: Diagnostics of Active Galactic Nuclei and Star Formation and Contribution to Total Infrared Luminosity. *Astrophysical Journal,* **769**(1), pp. 75.

SLOAN, G.C., JURA, M., DULEY, W.W., KRAEMER, K.E., BERNARD-SALAS, J., FORREST, W.J., SARGENT, B., LI, A., BARRY, D.J., BOHAC, C.J., WATSON, D.M. and HOUCK, J.R., 2007. The unusual hydrocarbon emission from the early carbon star HD 100764: The connection between aromatics and aliphatics. *Astrophysical Journal,* **664**(2), pp. 1144-1153.

Spitzer Programmes 5 June 2015, 2015-last update [Homepage of Caltech], [Online]. Available: http://irsa.ipac.caltech.edu/data/SPITZER/docs/files/spitzer/spitzer_programs.txt [November, 2015].

TADHUNTER, C., 2008. An introduction to active galactic nuclei: Classification and unification. *New Astronomy Reviews,* **52**(6), pp. 227-239.

The Spitzer Heritage Archive 2015-last update [Homepage of NASA, Caltech], [Online]. Available: http://sha.ipac.caltech.edu/applications/Spitzer/SHA2015].

TIELENS, A., HONY, S., VAN KERCKHOVEN, C. and PEETERS, E., 1999. Interstellar and circumstellar PAHs. *Universe as seen by Iso, Vols i and Ii,* **427**, pp. 579-587.

VAN DER WERF, P.P., ALBA, A.B., SPAANS, M., LOENEN, A.F., MEIJERINK, R., RIECHERS, D.A., COX, P., WEISS, A. and WALTER, F., 2011. WATER VAPOR EMISSION REVEALS A HIGHLY OBSCURED, STAR-FORMING NUCLEAR REGION IN THE QSO HOST GALAXY APM 08279+5255 AT z=3.9. *Astrophysical Journal Letters,* **741**(2), pp. L38.

VARDANYAN, M., , iCosmos Cosmology Calculator.
Available: http://www.icosmos.co.uk/ [February, 2015].

WEINGARTNER, J. and DRAINE, B., 2001. Dust grain-size distributions and extinction in the Milky Way, large magellanic cloud, and small magellanic cloud. *Astrophysical Journal,* **548**(1), pp. 296-309.

WERNER, M.W., ROELLIG, T.L., LOW, F.J., RIEKE, G.H., RIEKE, M., HOFFMANN, W.F., YOUNG, E., HOUCK, J.R., BRANDL, B., FAZIO, G.G., HORA, J.L., GEHRZ, R.D., HELOU, G., SOIFER, B.T., STAUFFER, J., KEENE, J., EISENHARDT, P., GALLAGHER, D., GAUTIER, T.N., IRACE, W., LAWRENCE, C.R., SIMMONS, L., VAN CLEVE, J.E., JURA, M., WRIGHT, E.L. and CRUIKSHANK, D.P., 2004. The Spitzer Space Telescope mission. *Astrophysical Journal Supplement Series,* **154**(1), pp. 1-9.

WIKIPEDIA, 28 June 2016, 2016-last update, M-Sigma relation.
Available: https://upload.wikimedia.org/wikipedia/commons/4/4b/Msigma.jpg [June/1, 2016].

WILMAN, R., GERSSEN, J., BOWER, R., MORRIS, S., BACON, R., DE ZEEUW, P. and DAVIES, R., 2005. The discovery of a galaxy-wide superwind from a young massive galaxy at redshift z approximate to 3. *Nature,* **436**(7048), pp. 227-229.

WITTEBORN, F.C. and YOUNG, L.S., 1976. Spacelab Infrared Telescope Facility (Sirtf). *Journal of Spacecraft and Rockets,* **13**(11), pp. 667-674.

YEE, H.K.C., 1988. High-Resolution Imaging of the Gravitational Lens System Candidate 2237+030. *Astronomical Journal,* **95**(5), pp. 1331-&.

APPENDIX – QSO SAMPLE SPECTRA

Below is a presentation of all of the quasar spectra from the sample used within this thesis. Here it can be seen how the quality of the spectra varies, with some relatively clean and higher SNR spectra where the PAH features are clearly visible (e.g. IRAS 04312+4008). However, other spectra can show a greater amount of noise (lower SNR) between each wavelength bin, where the PAH profile and shape are still distinguishable but are easily hidden (e.g. 2MASS J000703.61). There are also spectra which show an absorption of the continuum due to silicates that can be close to the 7.7μm feature (e.g. 2MASS J130700.66). It will also be noticeable how not all features are present in each spectrum (e.g. 2MASS J010835.16).

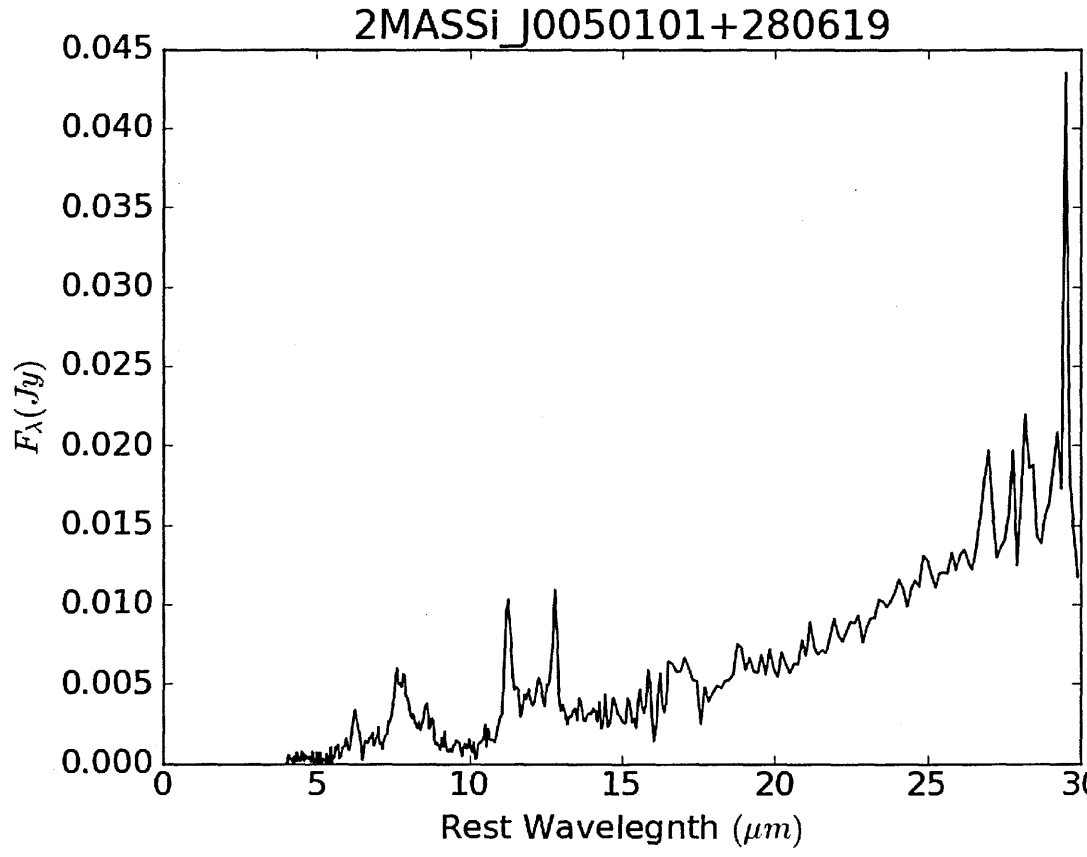

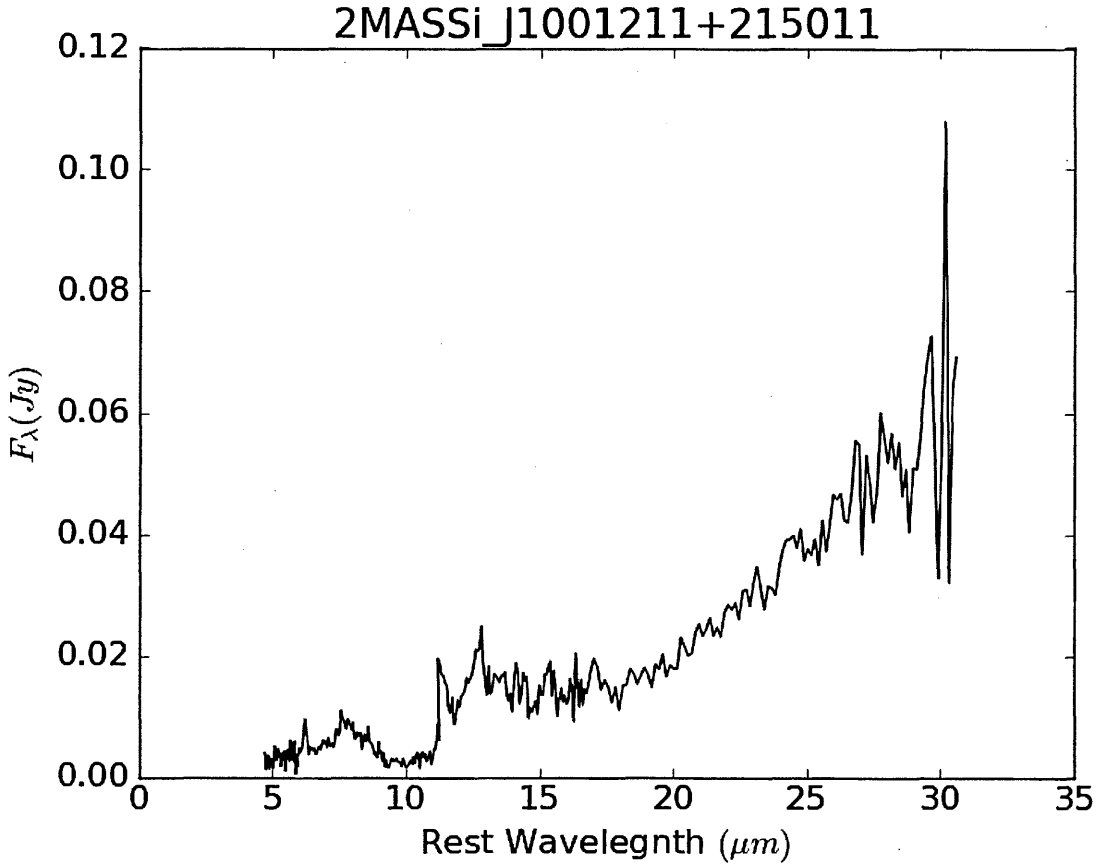
2MASSi_J1001211+215011
0.12
0.10
0.08
0.06
0.04
0.02
0.00
$F_\lambda(Jy)$
0
5
10
15
20
25
30
35
Rest Wavelegnth (μm)

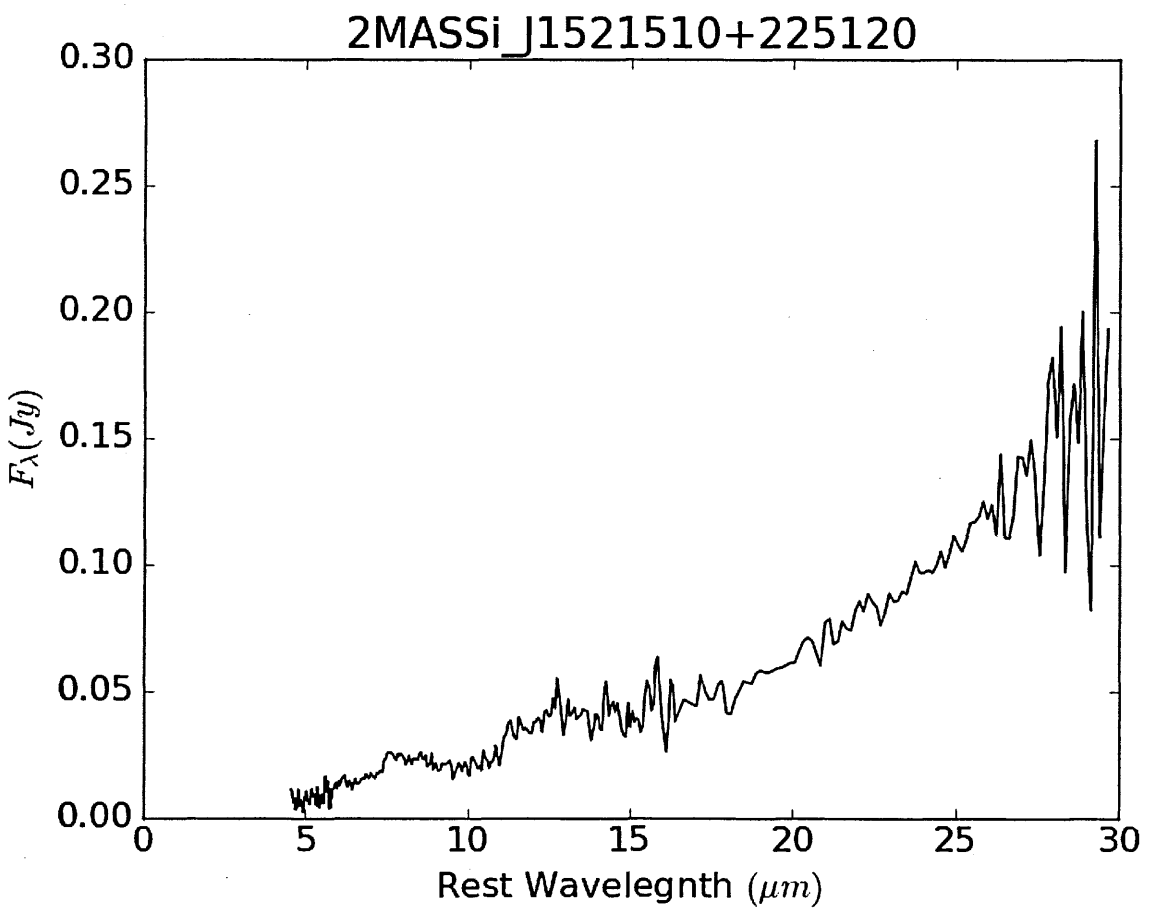
2MASSi_J1521510+225120
0.30
0.25
0.20
0.15
0.10
0.05
0.00
$F_\lambda(Jy)$
0
5
10
15
20
25
30
Rest Wavelegnth (μm)

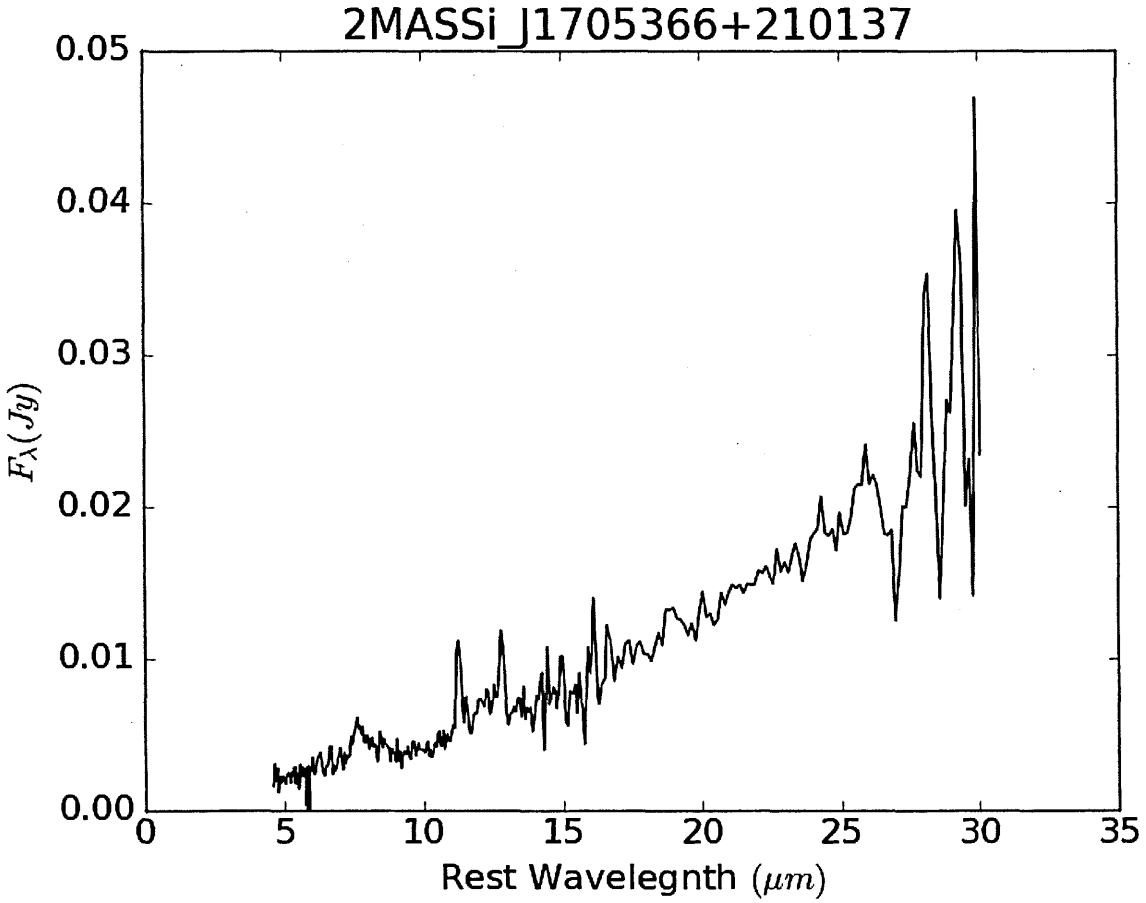
2MASSi_J1705366+210137
0.05
0.04
0.03
0.02
0.01
0.00
$F_\lambda(Jy)$
0
5
10
15
20
25
30
35
Rest Wavelegnth (μm)

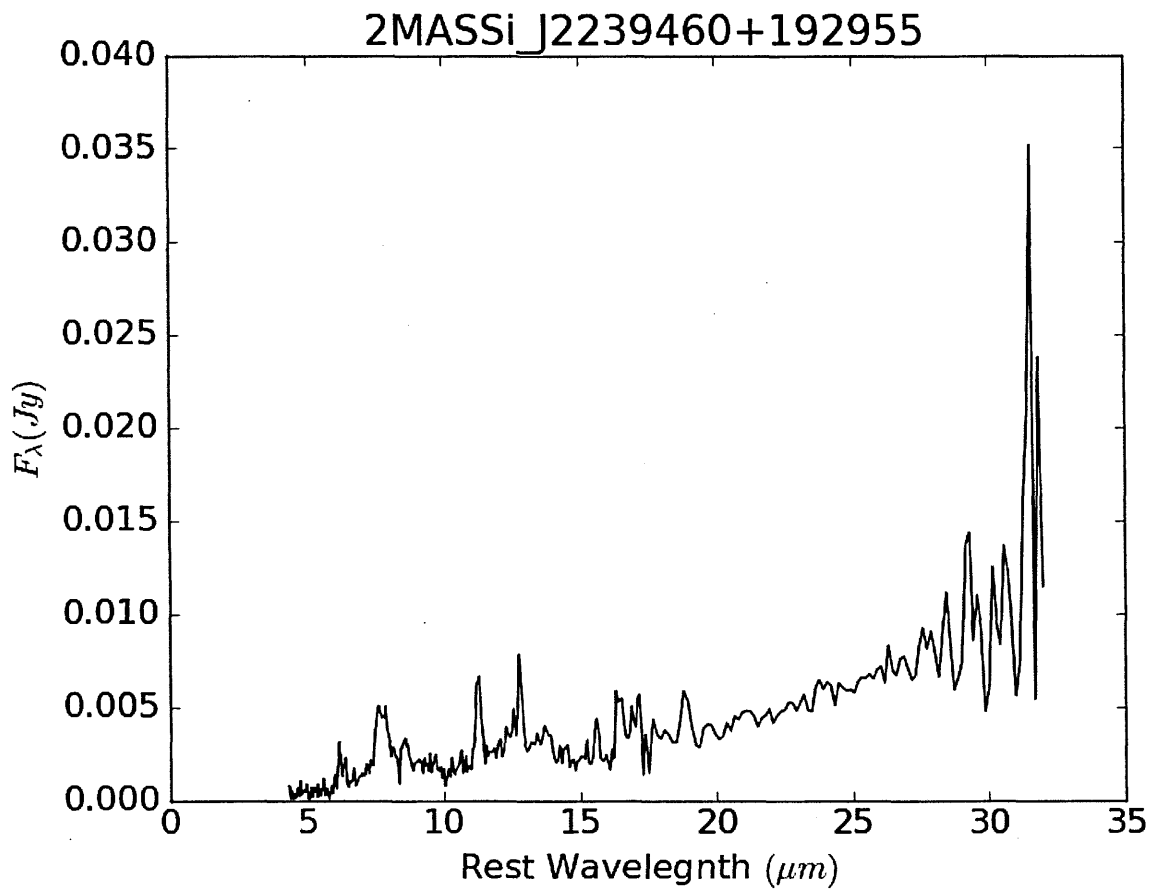
2MASSi_J2239460+192955
0.040
0.035
0.030
0.025
0.020
0.015
0.010
0.005
0.000
$F_\lambda(Jy)$
0
5
10
15
20
25
30
35
Rest Wavelegnth (μm)

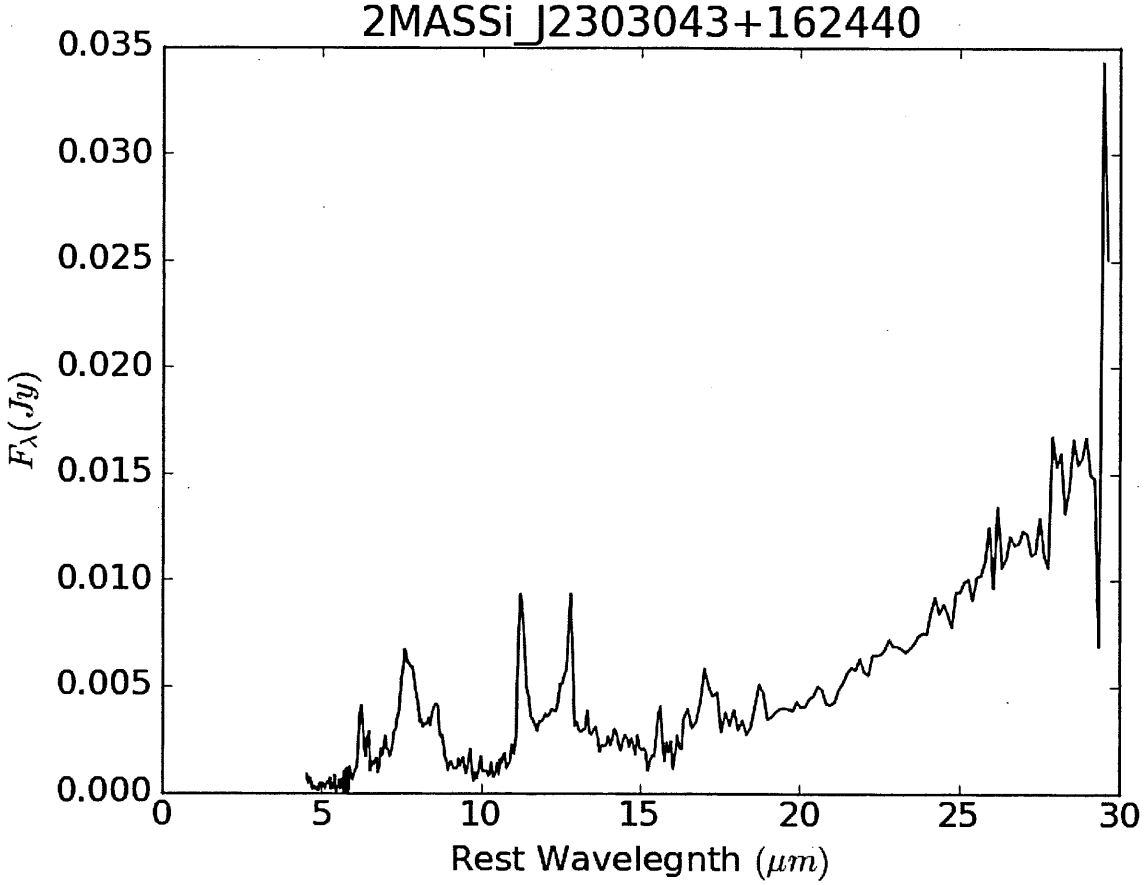
2MASSi_J2303043+162440
0.035
0.030
0.025
0.020
0.015
0.010
0.005
0.000
$F_\lambda(Jy)$
0
5
10
15
20
25
30
Rest Wavelegnth (μm)

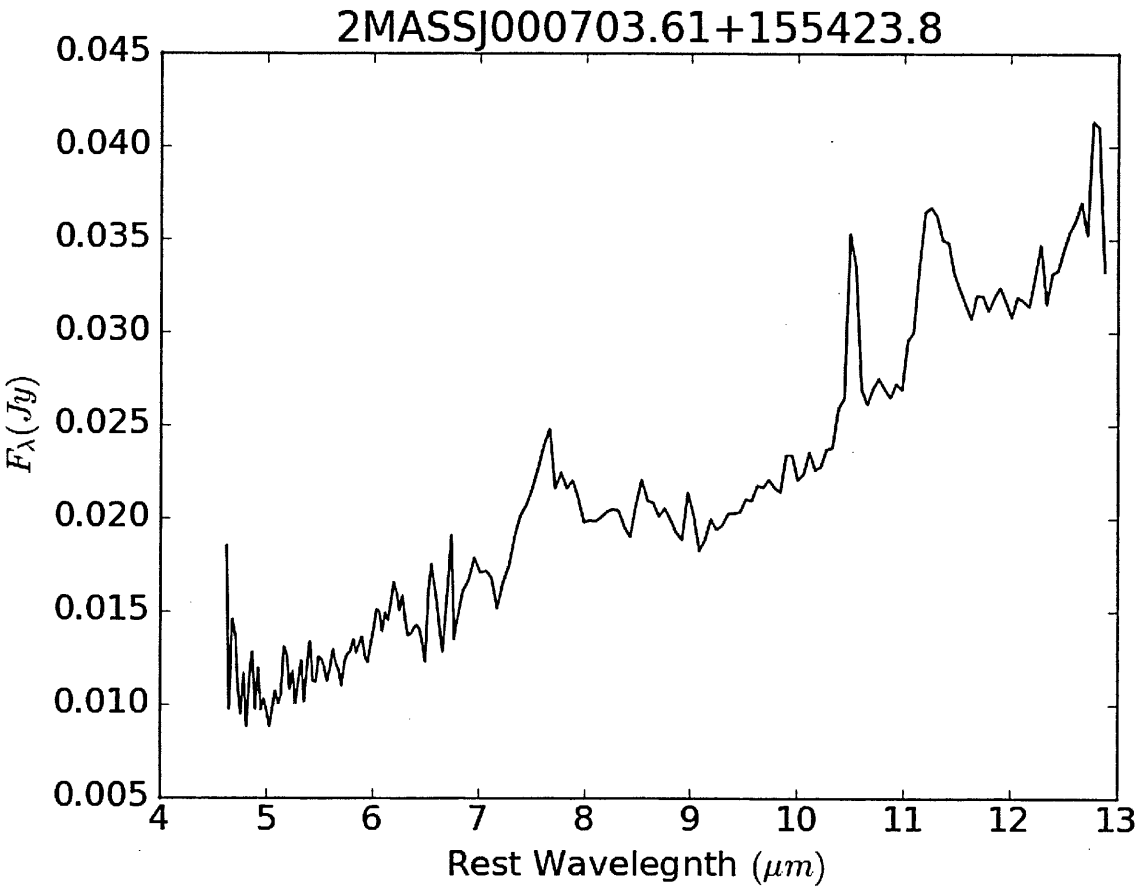
2MASSJ000703.61+155423.8
0.045
0.040
0.035
0.030
0.025
0.020
0.015
0.010
0.005
$F_\lambda(Jy)$
4
5
6
7
8
9
10
11
12
13
Rest Wavelegnth (μm)

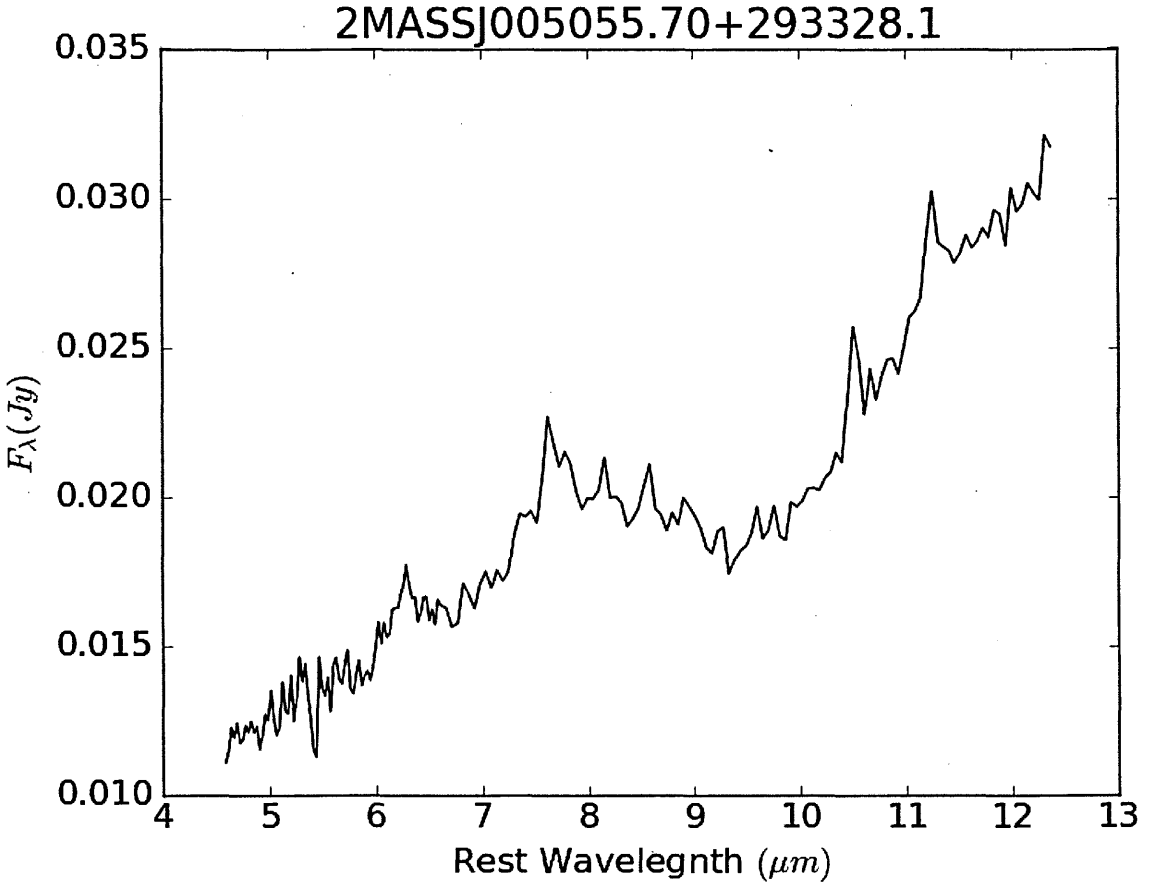
2MASSJ005055.70+293328.1
0.035
0.030
0.025
0.020
0.015
0.010
$F_\lambda(Jy)$
4
5
6
7
8
9
10
11
12
13
Rest Wavelegnth (μm)

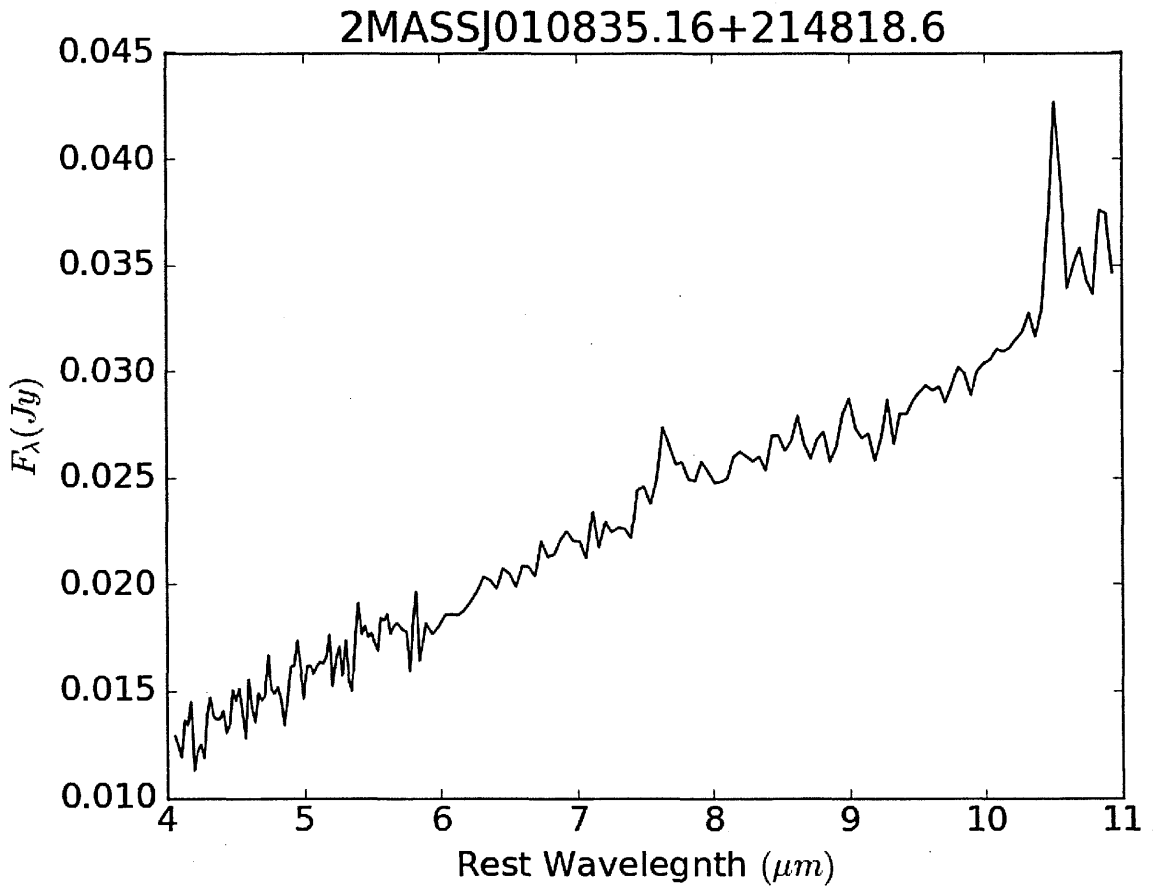
2MASSJ010835.16+214818.6
0.045
0.040
0.035
0.030
0.025
0.020
0.015
0.010
$F_\lambda(Jy)$
4
5
6
7
8
9
10
11
Rest Wavelegnth (μm)

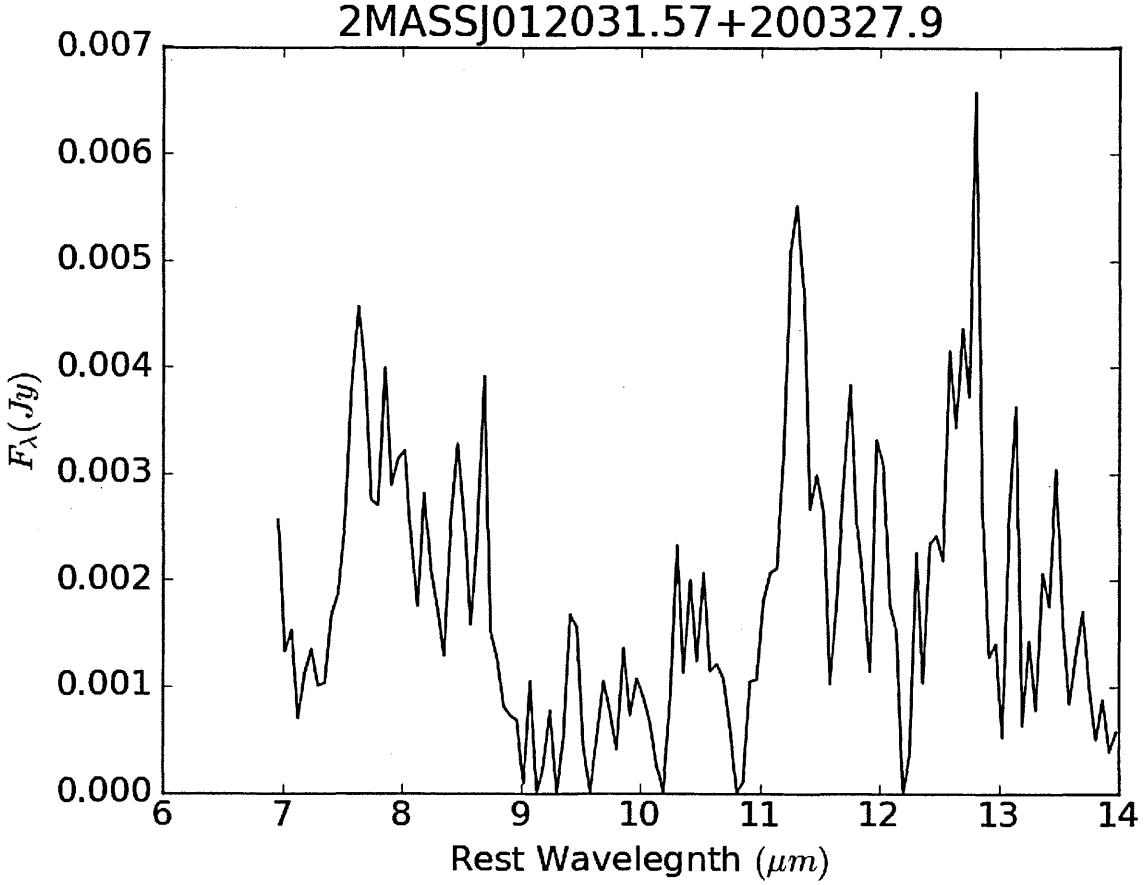
2MASSJ012031.57+200327.9
0.007
0.006
0.005
0.004
0.003
0.002
0.001
0.000
$F_\lambda(Jy)$
6
7
8
9
10
11
12
13
14
Rest Wavelegnth (μm)

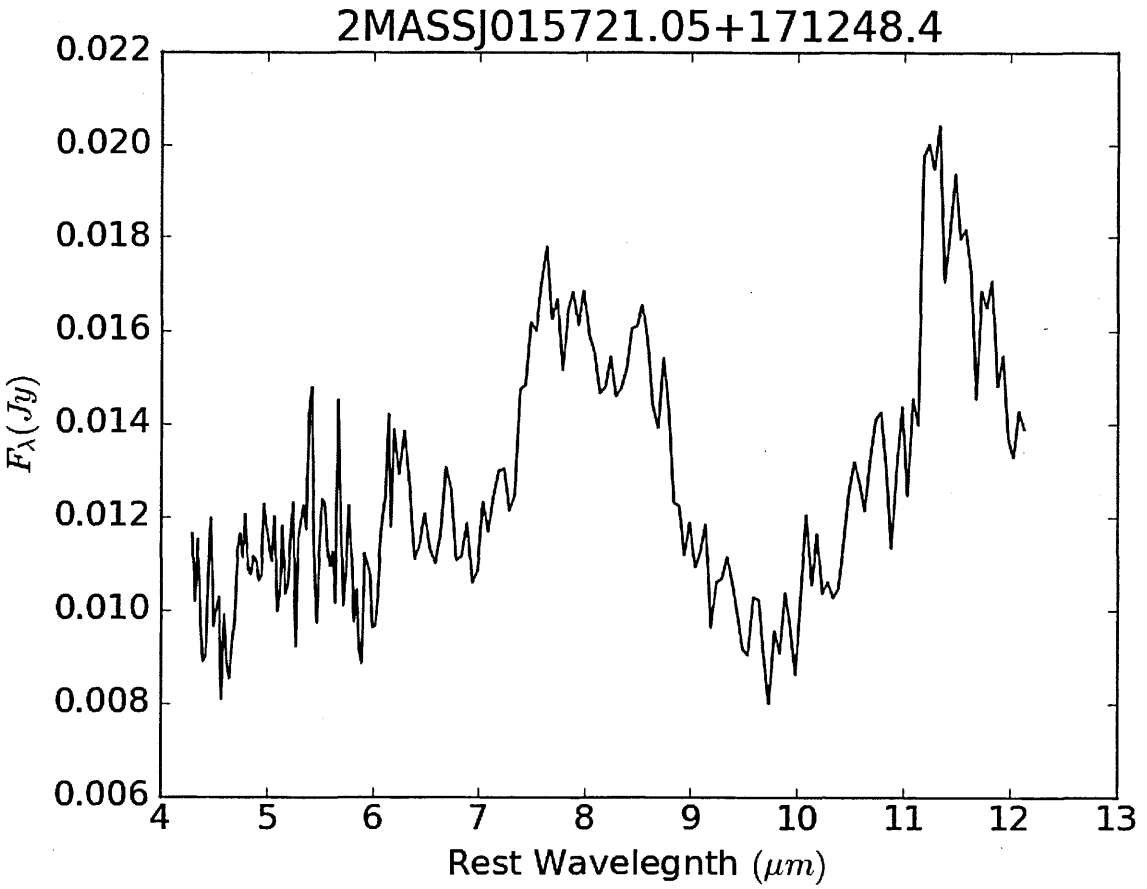
2MASSJ015721.05+171248.4
0.022
0.020
0.018
0.016
0.014
0.012
0.010
0.008
0.006
$F_\lambda(Jy)$
4
5
6
7
8
9
10
11
12
13
Rest Wavelegnth (μm)

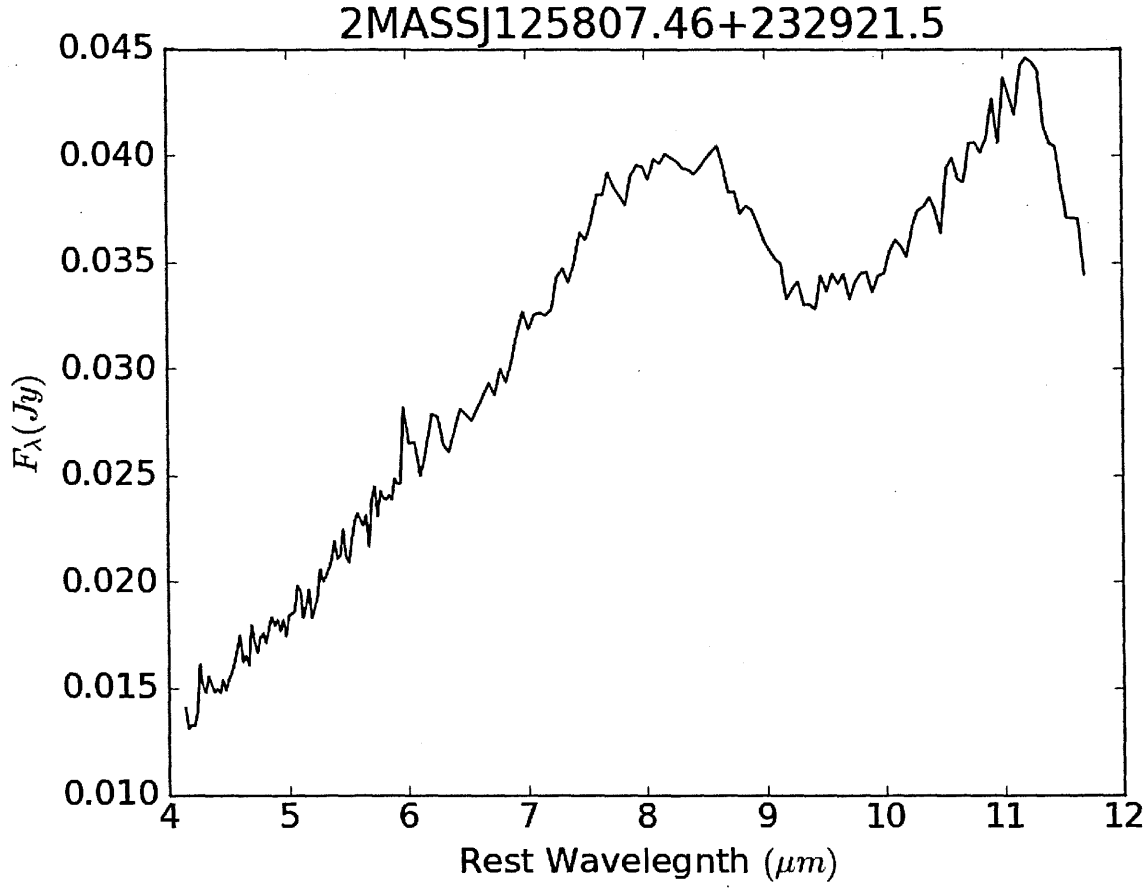
2MASSJ125807.46+232921.5
0.045
0.040
0.035
0.030
0.025
0.020
0.015
0.010
$F_\lambda(Jy)$
4
5
6
7
8
9
10
11
12
Rest Wavelegnth (μm)

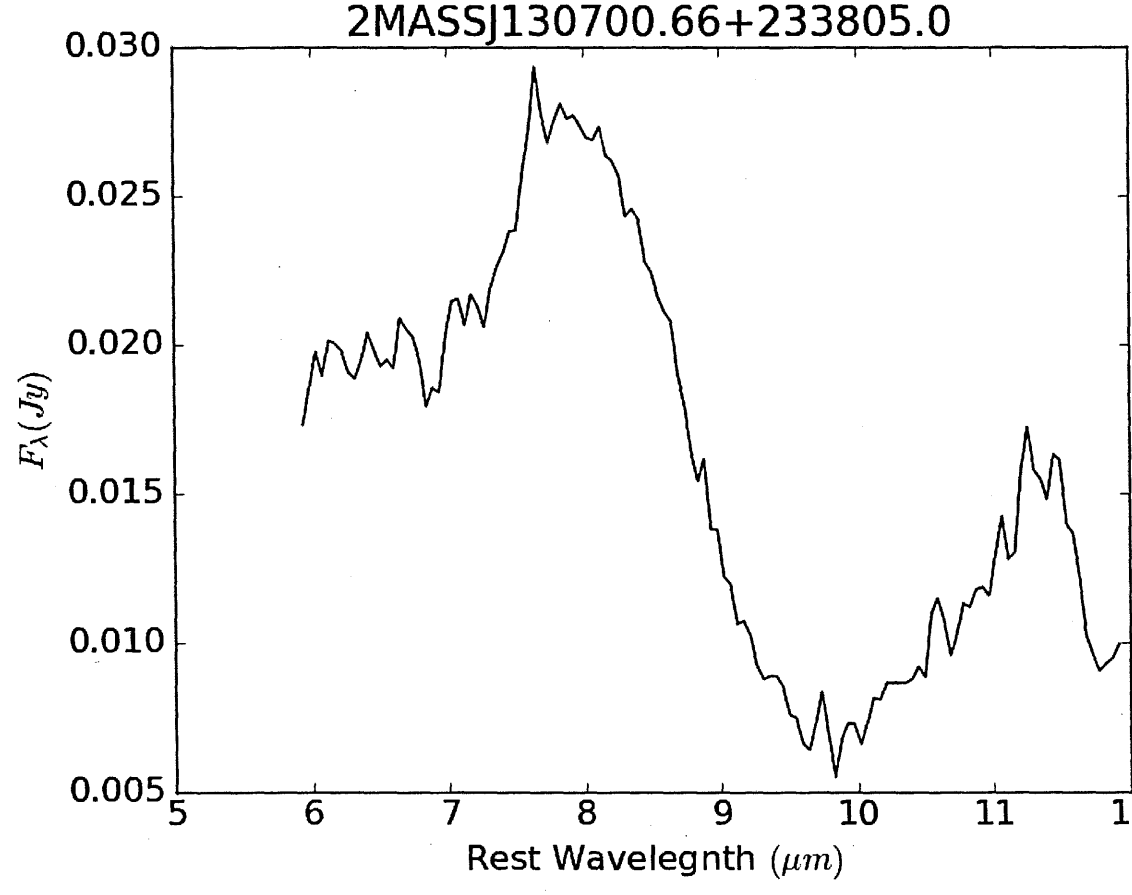
2MASSJ130700.66+233805.0
0.030
0.025
0.020
0.015
0.010
0.005
$F_\lambda(Jy)$
5
6
7
8
9
10
11
12
Rest Wavelegnth (μm)

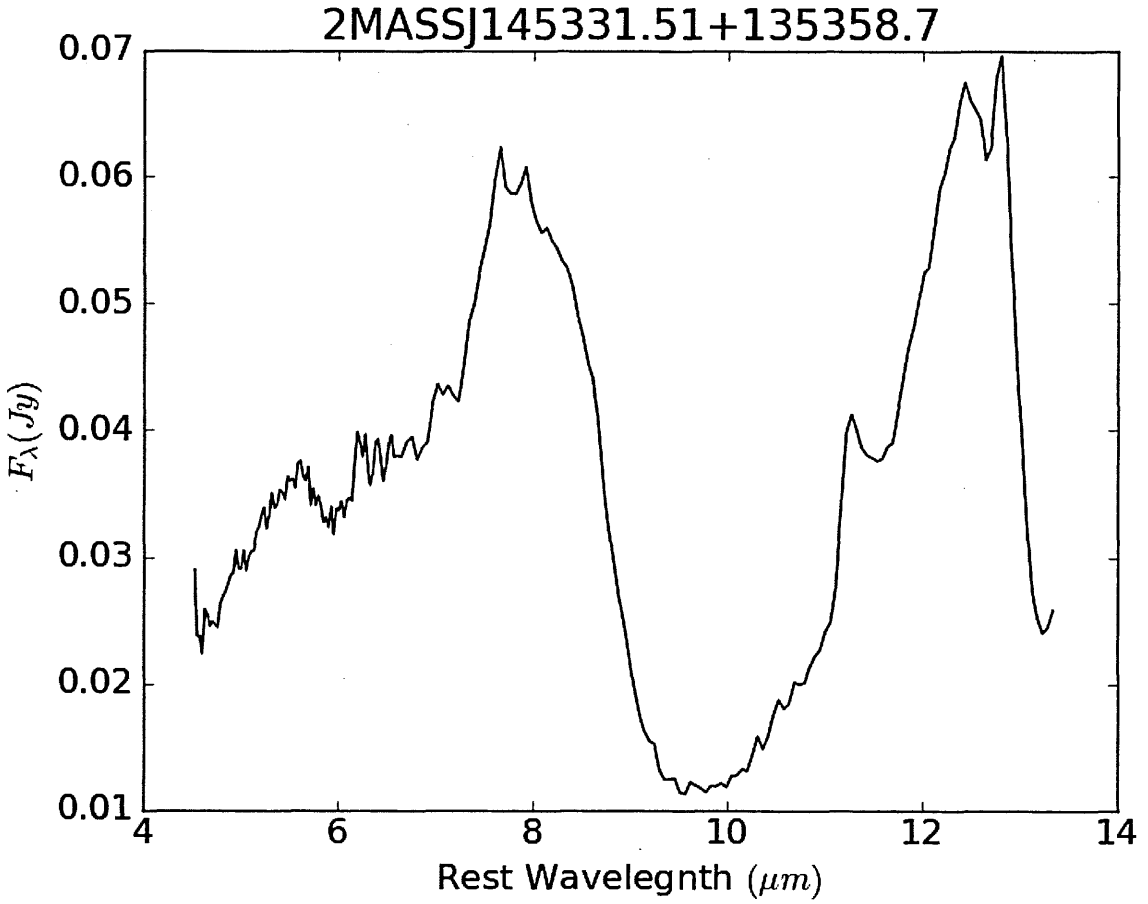
2MASSJ145331.51+135358.7
0.07
0.06
0.05
0.04
0.03
0.02
0.01
$F_\lambda(Jy)$
4
6
8
10
12
14
Rest Wavelegnth (μm)

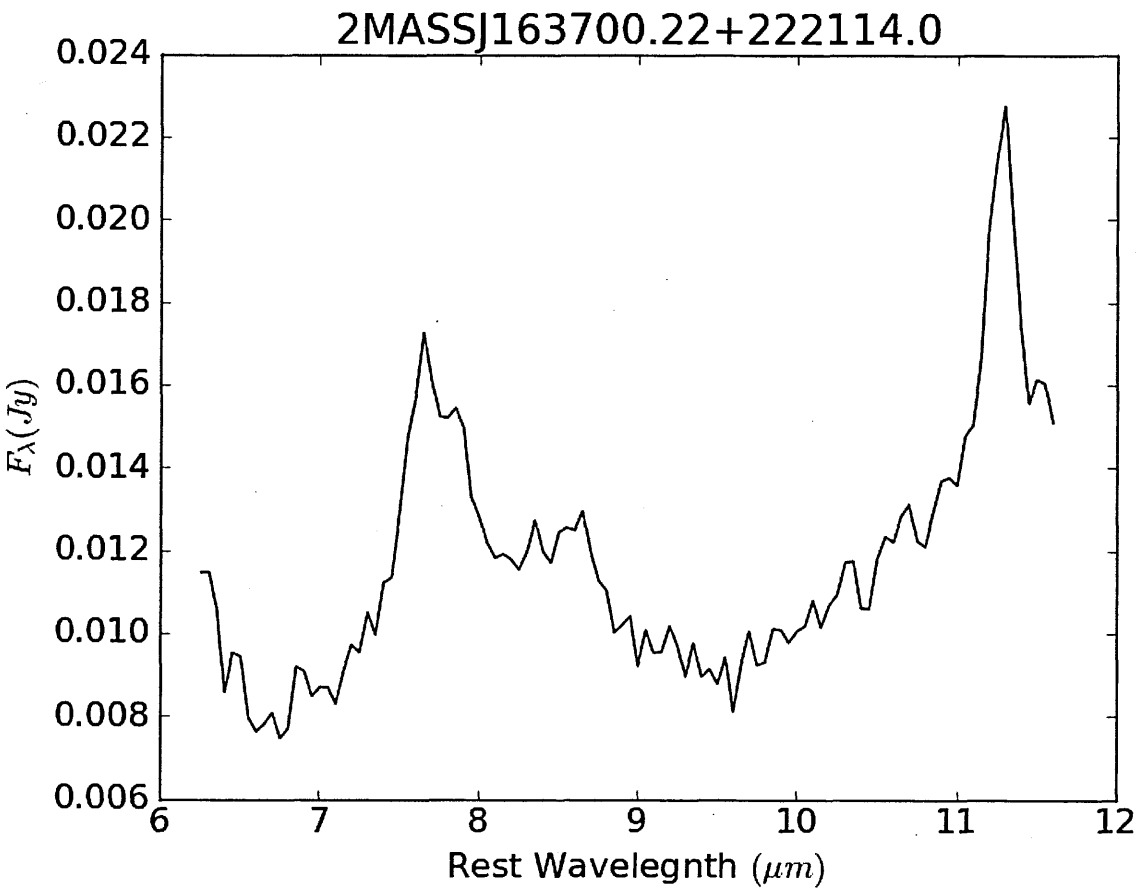
2MASSJ163700.22+222114.0
0.024
0.022
0.020
0.018
0.016
0.014
0.012
0.010
0.008
0.006
$F_\lambda(Jy)$
6
7
8
9
10
11
12
Rest Wavelegnth (μm)

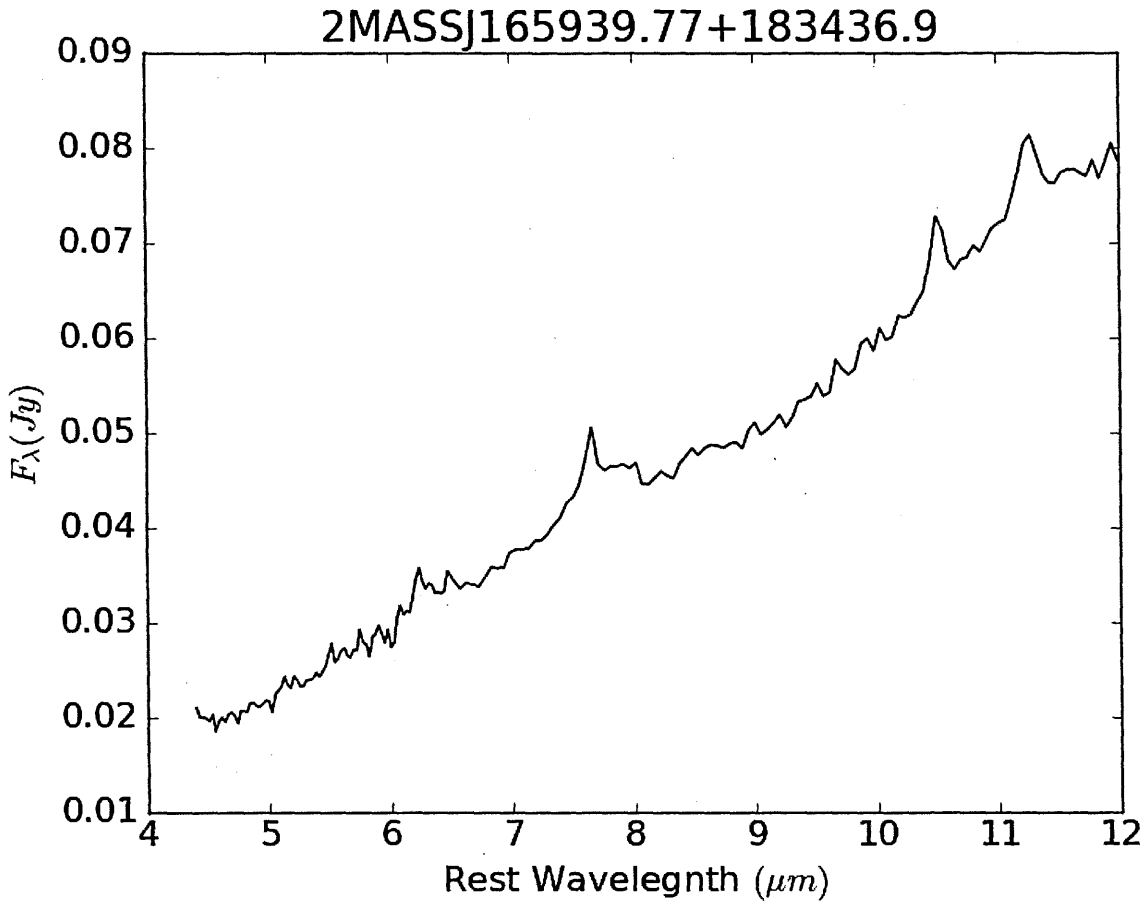
2MASSJ165939.77+183436.9
0.09
0.08
0.07
0.06
0.05
0.04
0.03
0.02
0.01
$F_\lambda(Jy)$
4
5
6
7
8
9
10
11
12
Rest Wavelegnth (μm)

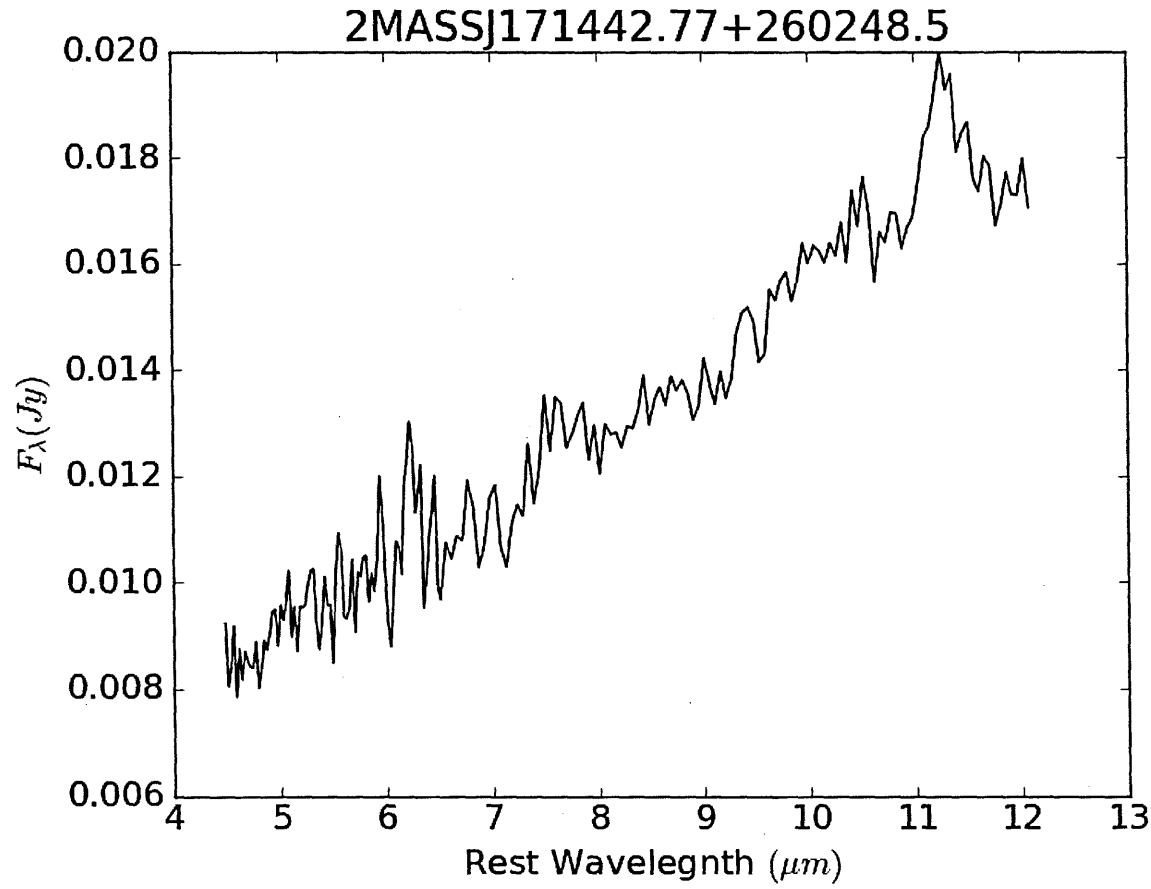
2MASSJ171442.77+260248.5
0.020
0.018
0.016
0.014
0.012
0.010
0.008
0.006
$F_\lambda(Jy)$
4
5
6
7
8
9
10
11
12
13
Rest Wavelegnth (μm)

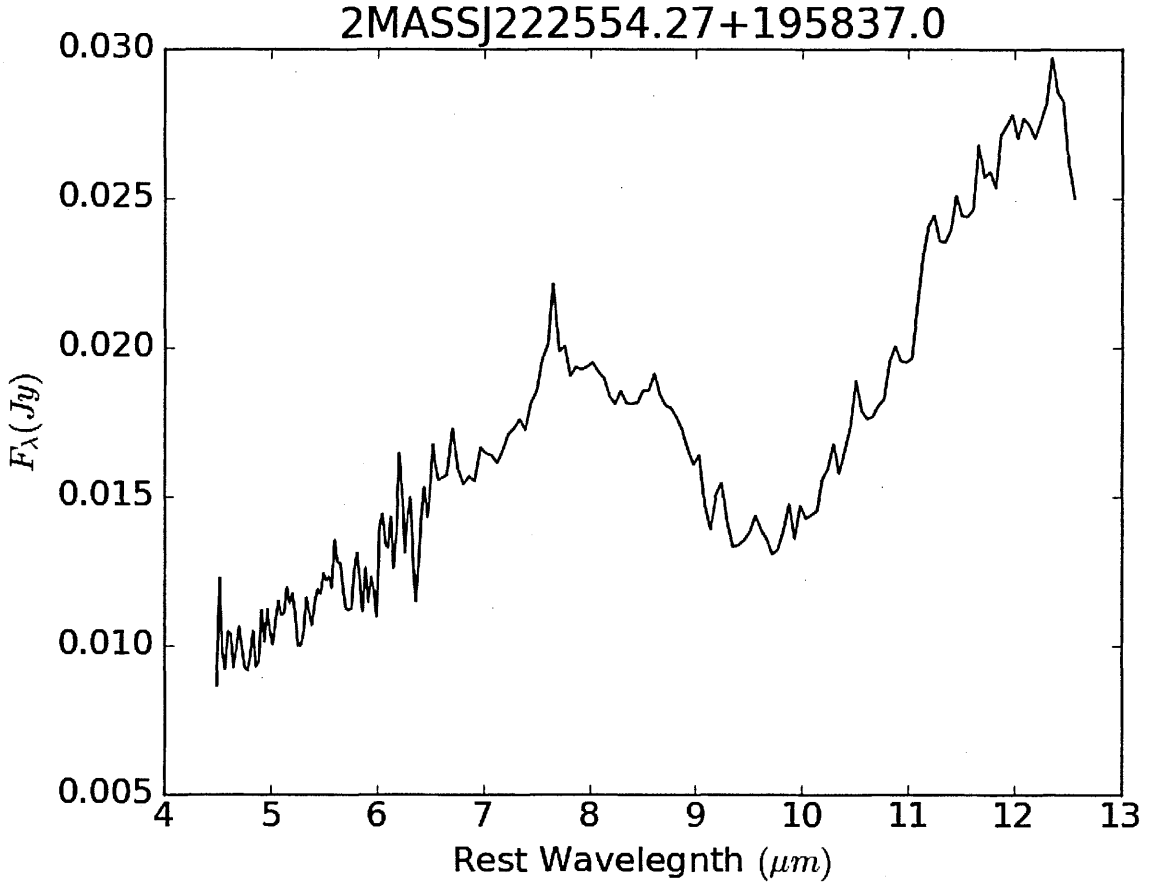
2MASSJ222554.27+195837.0
0.030
0.025
0.020
0.015
0.010
0.005
$F_\lambda(Jy)$
4
5
6
7
8
9
10
11
12
13
Rest Wavelegnth (μm)

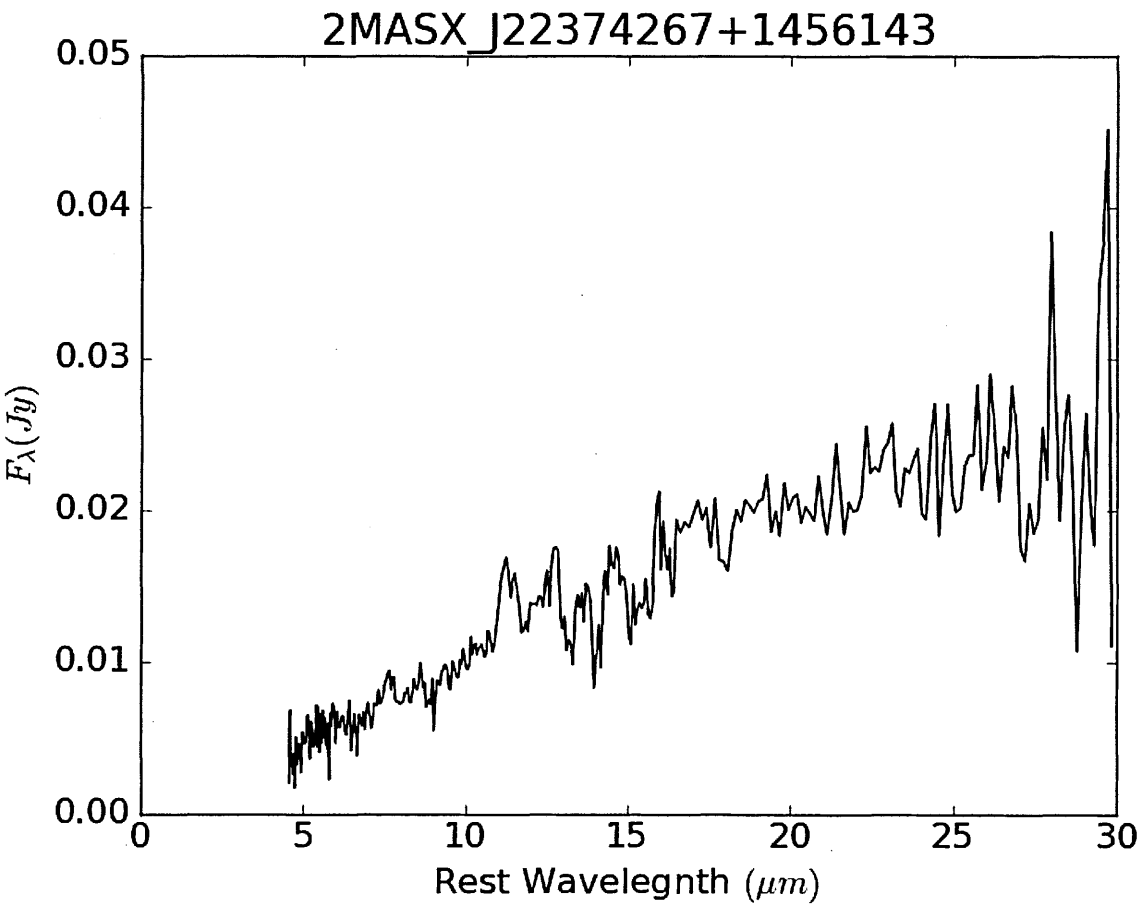
2MASX_J22374267+1456143
0.05
0.04
0.03
0.02
0.01
0.00
$F_\lambda(Jy)$
0
5
10
15
20
25
30
Rest Wavelegnth (μm)

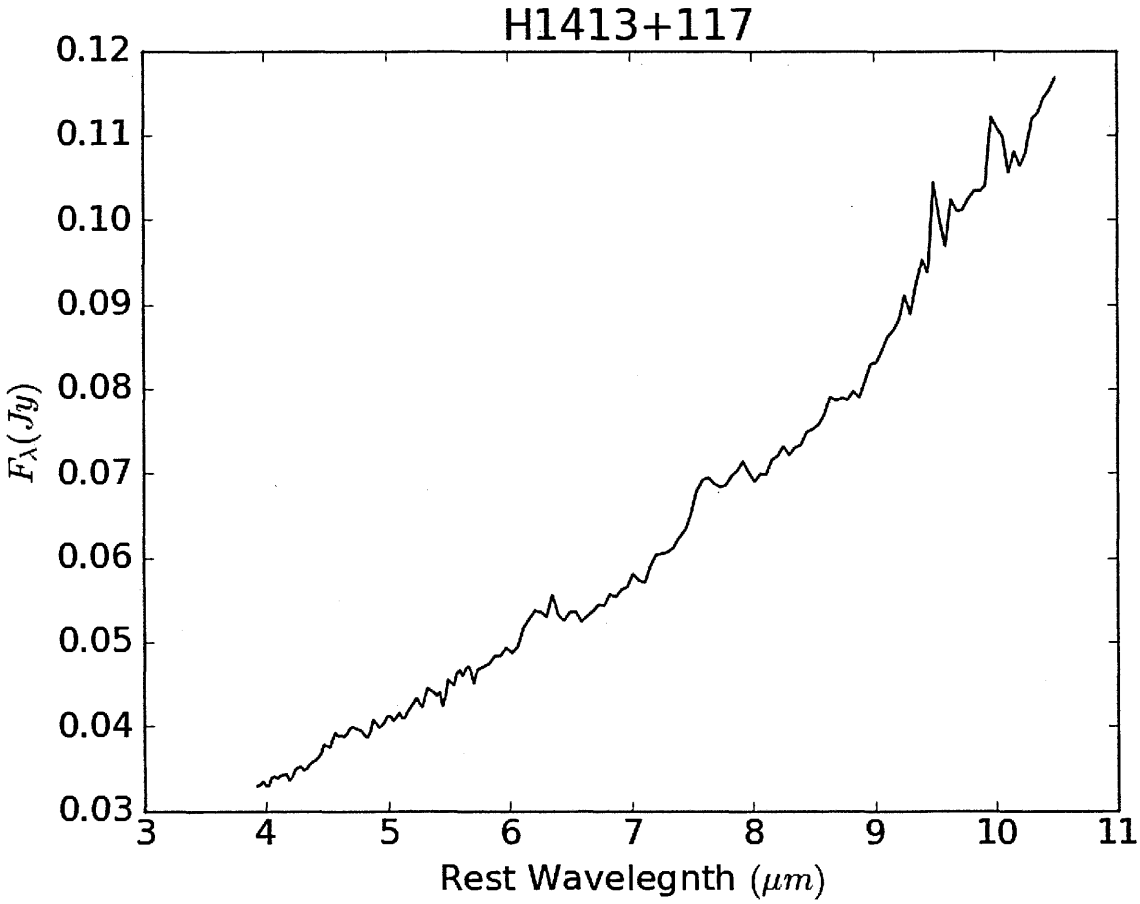
H1413+117
0.12
0.11
0.10
0.09
0.08
0.07
0.06
0.05
0.04
0.03
$F_\lambda(Jy)$
3
4
5
6
7
8
9
10
11
Rest Wavelegnth (μm)

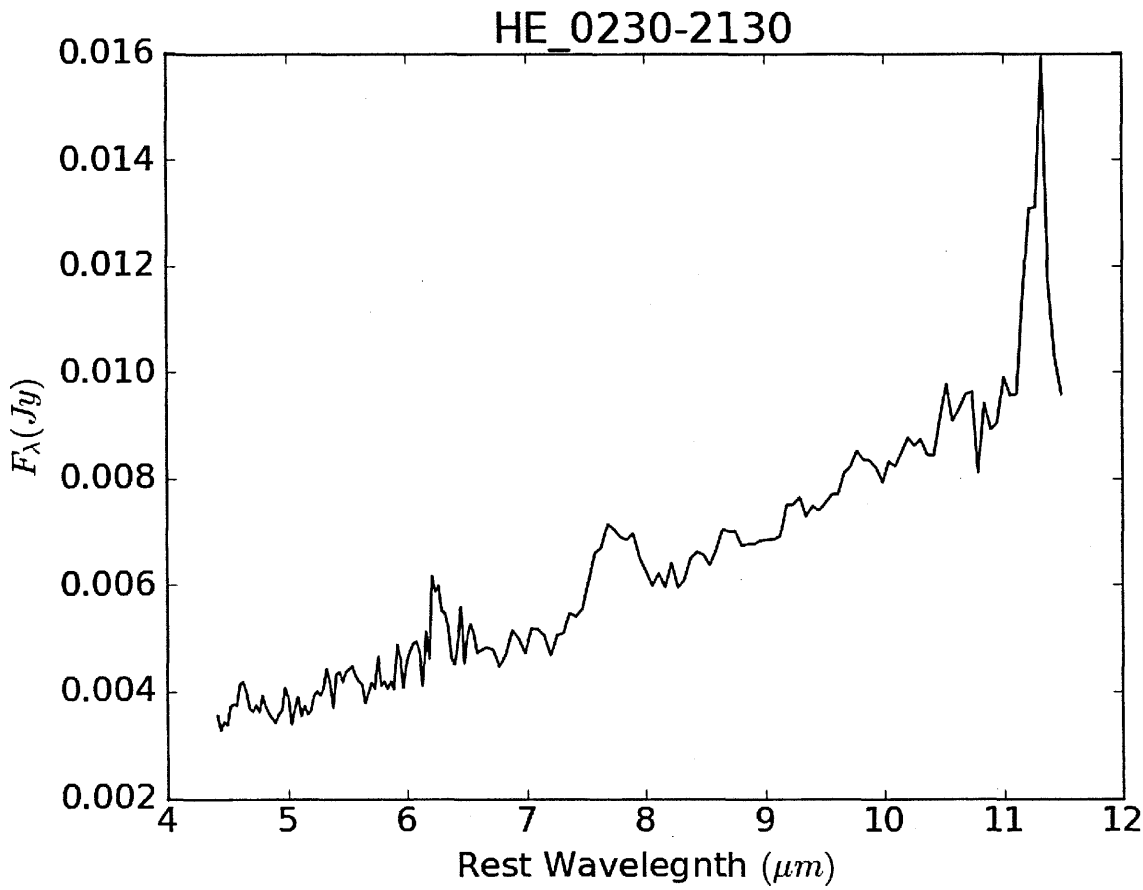
HE_0230-2130
0.016
0.014
0.012
0.010
0.008
0.006
0.004
0.002
$F_\lambda(Jy)$
4
5
6
7
8
9
10
11
12
Rest Wavelegnth (μm)

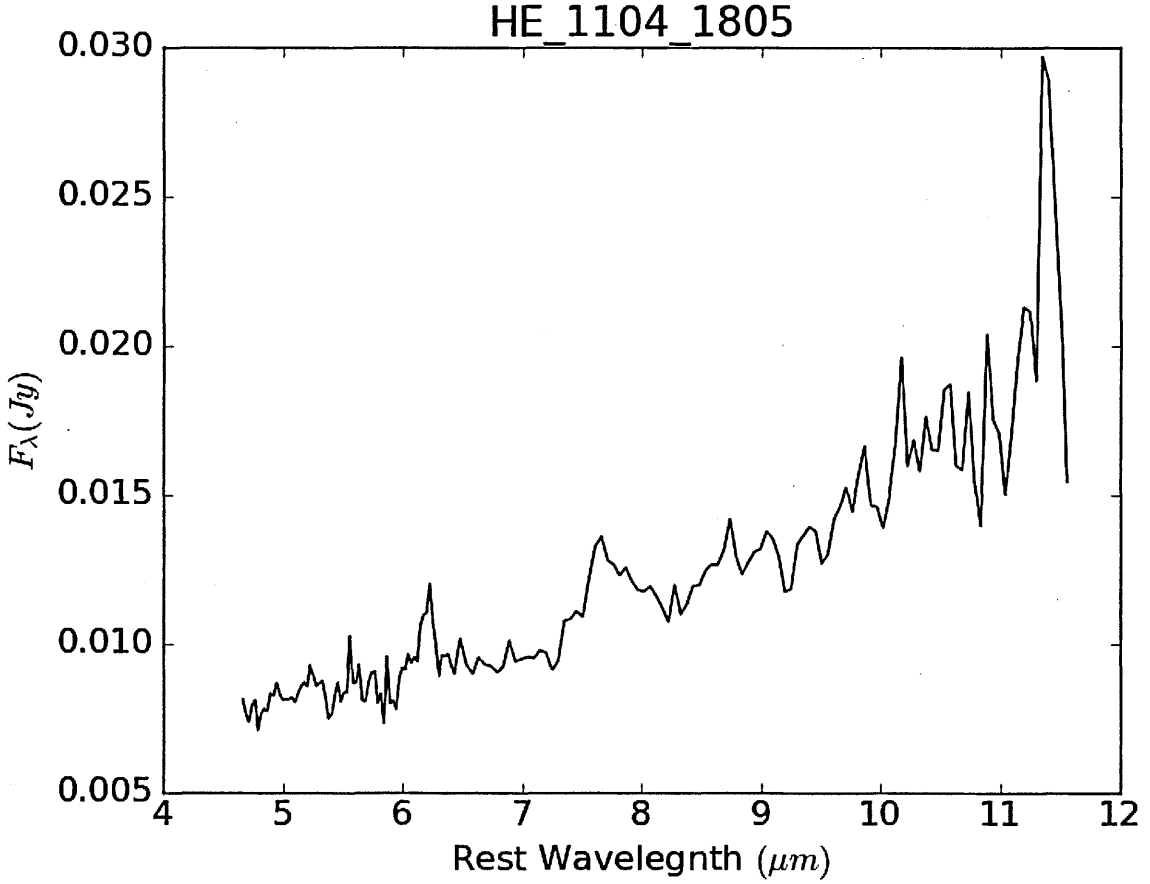
HE_1104_1805
0.030
0.025
0.020
0.015
0.010
0.005
$F_\lambda(Jy)$
4
5
6
7
8
9
10
11
12
Rest Wavelegnth (μm)

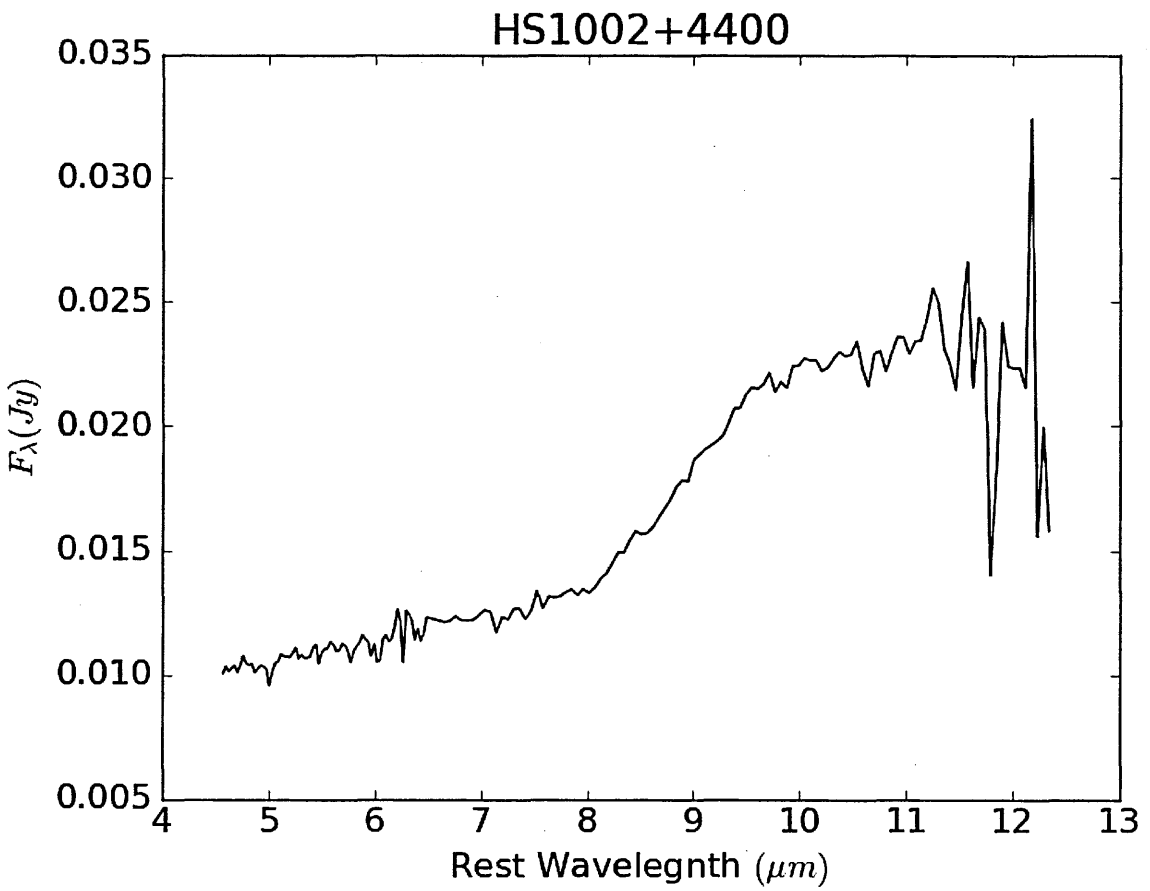
HS1002+4400
0.035
0.030
0.025
0.020
0.015
0.010
0.005
$F_\lambda(Jy)$
4
5
6
7
8
9
10
11
12
13
Rest Wavelegnth (μm)

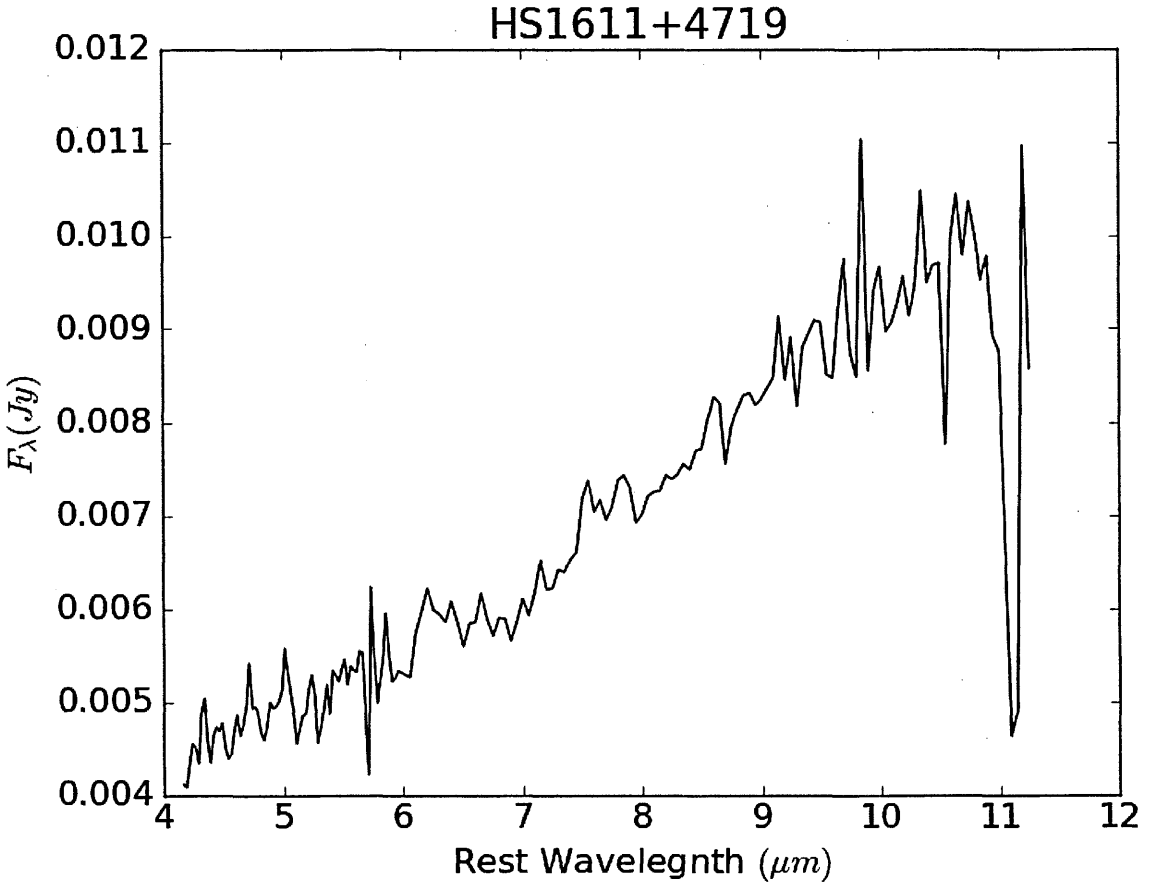
HS1611+4719
0.012
0.011
0.010
0.009
0.008
0.007
0.006
0.005
0.004
$F_\lambda(Jy)$
4
5
6
7
8
9
10
11
12
Rest Wavelegnth (μm)

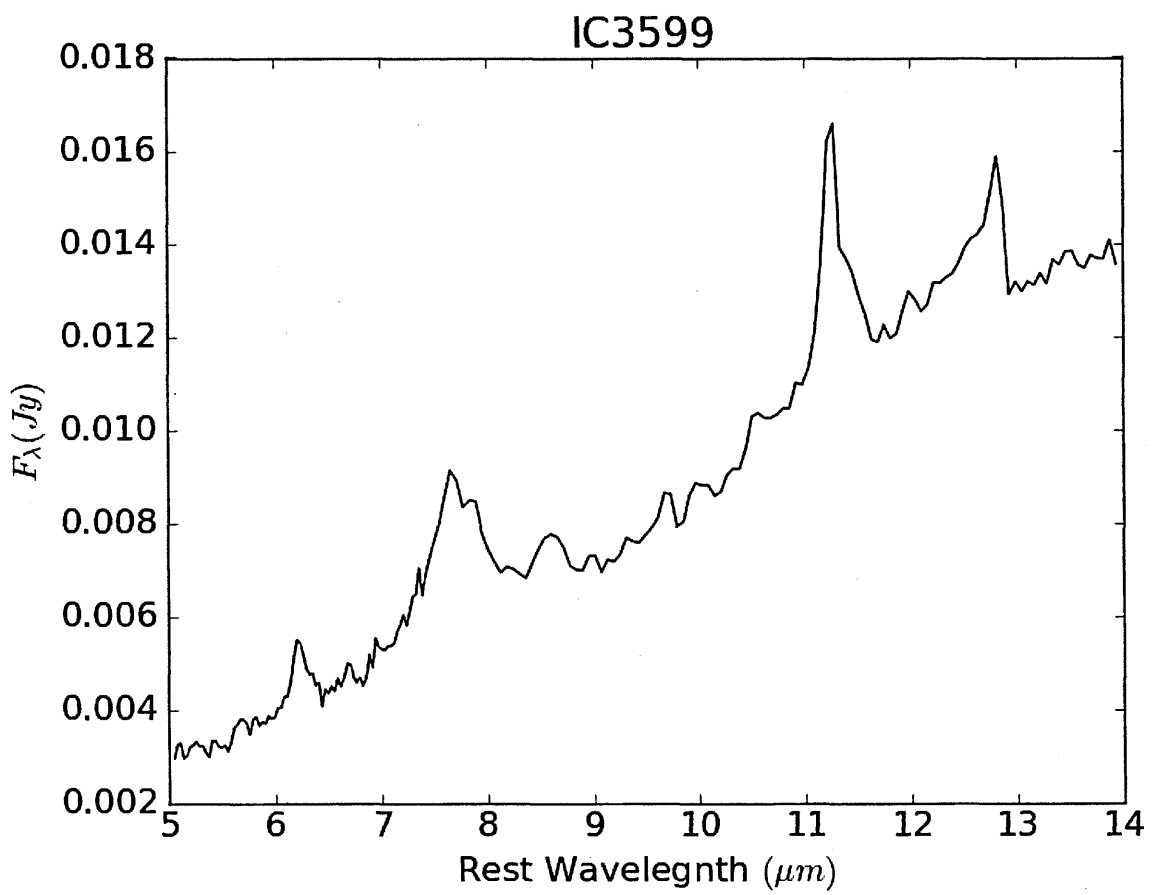
IC3599
0.018
0.016
0.014
0.012
0.010
0.008
0.006
0.004
0.002
$F_\lambda(Jy)$
5
6
7
8
9
10
11
12
13
14
Rest Wavelegnth (μm)

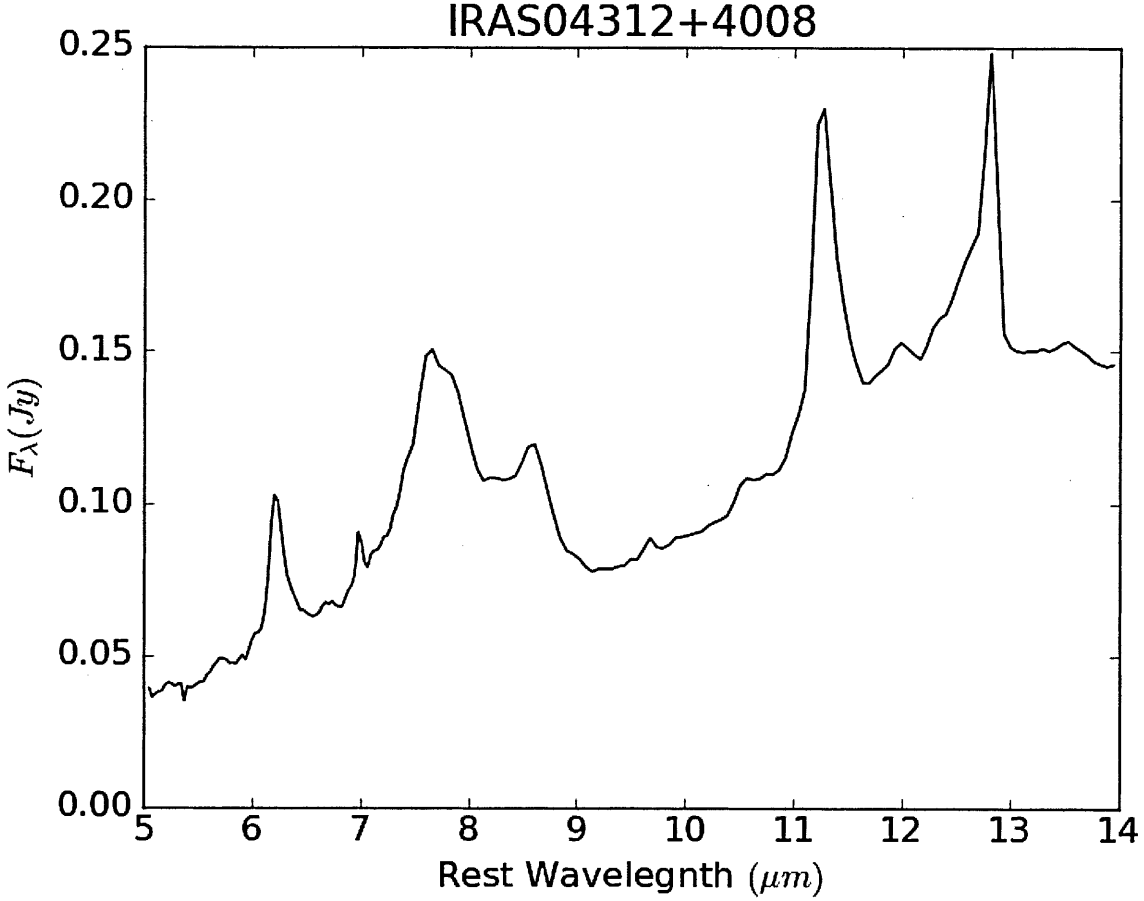
IRAS04312+4008
0.25
0.20
0.15
0.10
0.05
0.00
$F_\lambda(Jy)$
5
6
7
8
9
10
11
12
13
14
Rest Wavelegnth (μm)

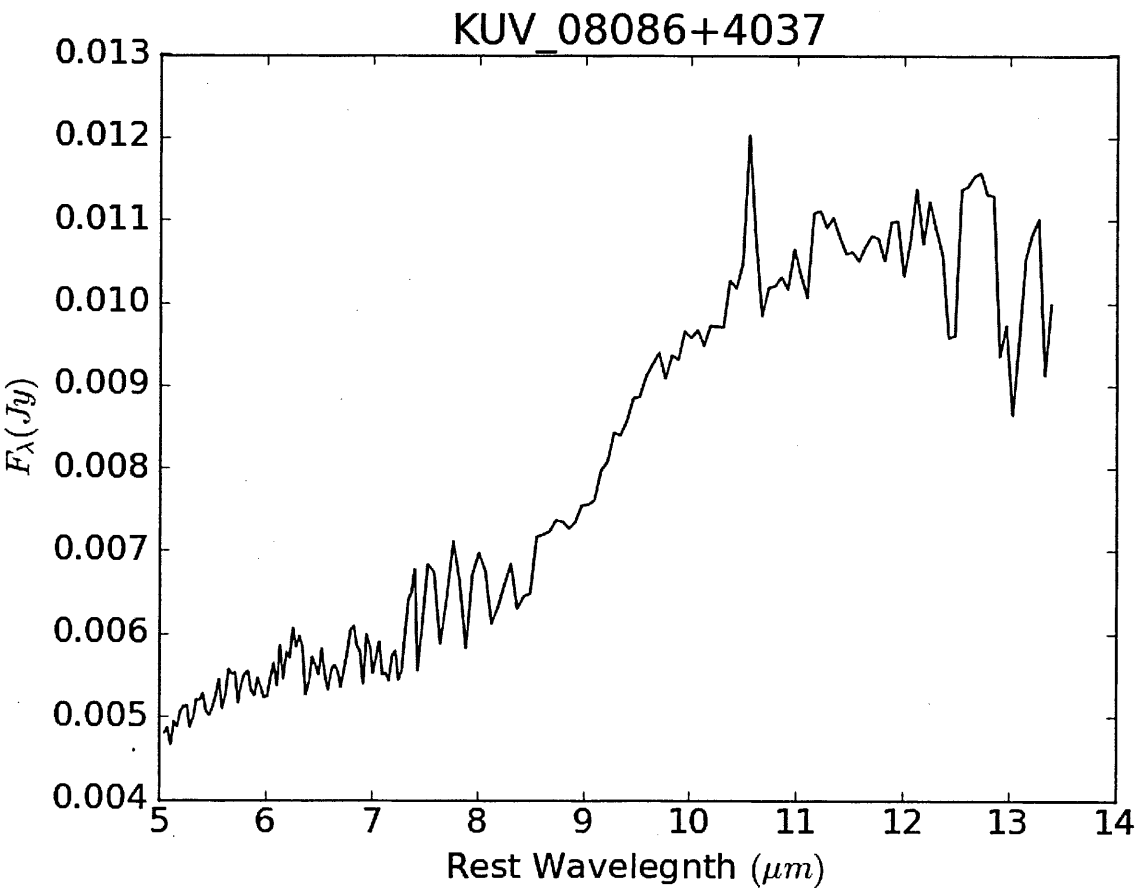
KUV_08086+4037
0.013
0.012
0.011
0.010
0.009
0.008
0.007
0.006
0.005
0.004
$F_\lambda(Jy)$
5
6
7
8
9
10
11
12
13
14
Rest Wavelegnth (μm)

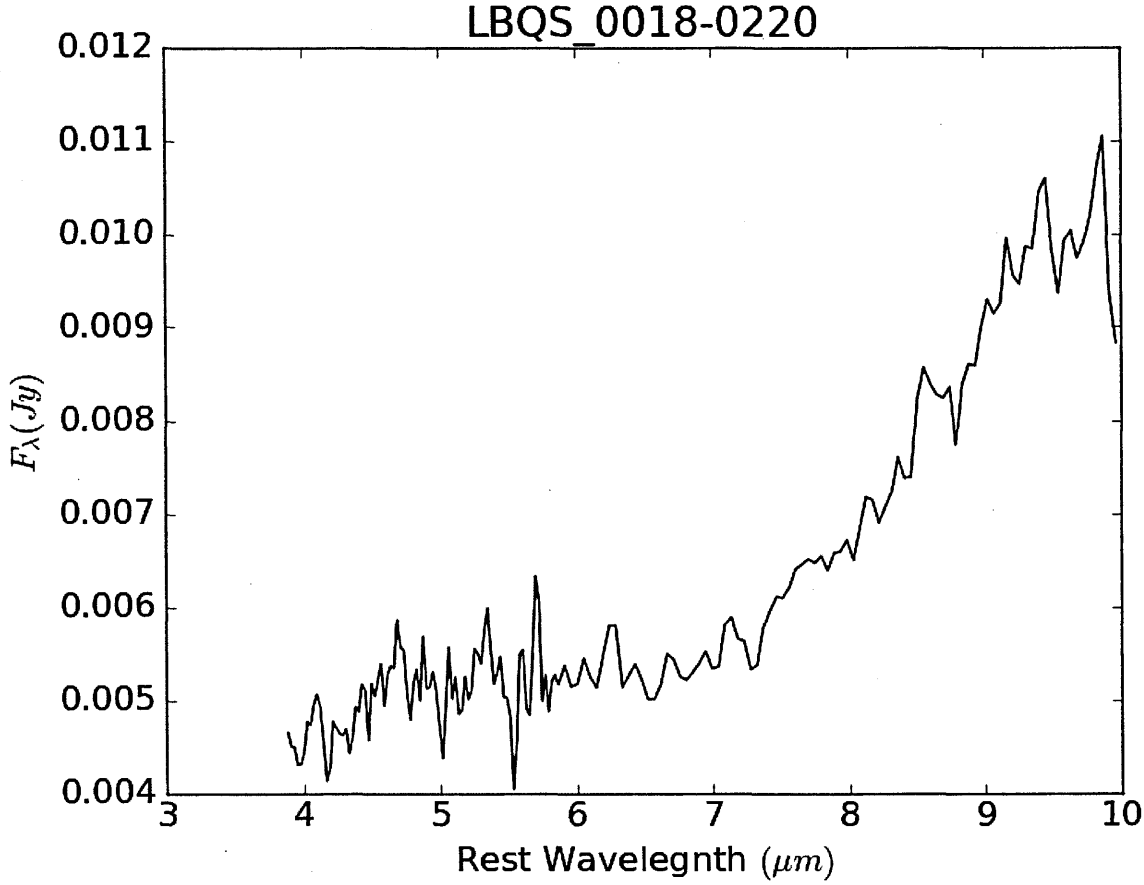
LBQS_0018-0220
0.012
0.011
0.010
0.009
0.008
0.007
0.006
0.005
0.004
$F_\lambda(Jy)$
3
4
5
6
7
8
9
10
Rest Wavelegnth (μm)

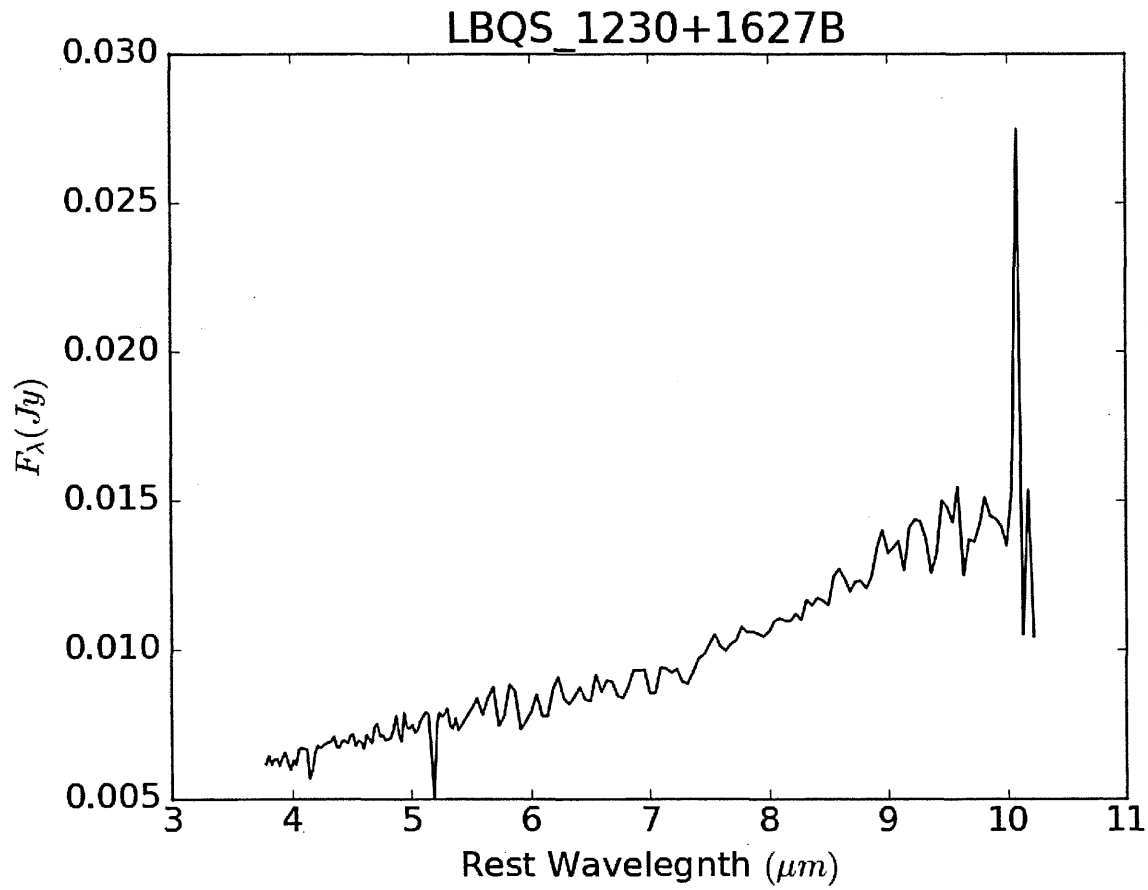
LBQS_1230+1627B
0.030
0.025
0.020
0.015
0.010
0.005
$F_\lambda(Jy)$
3
4
5
6
7
8
9
10
11
Rest Wavelegnth (μm)

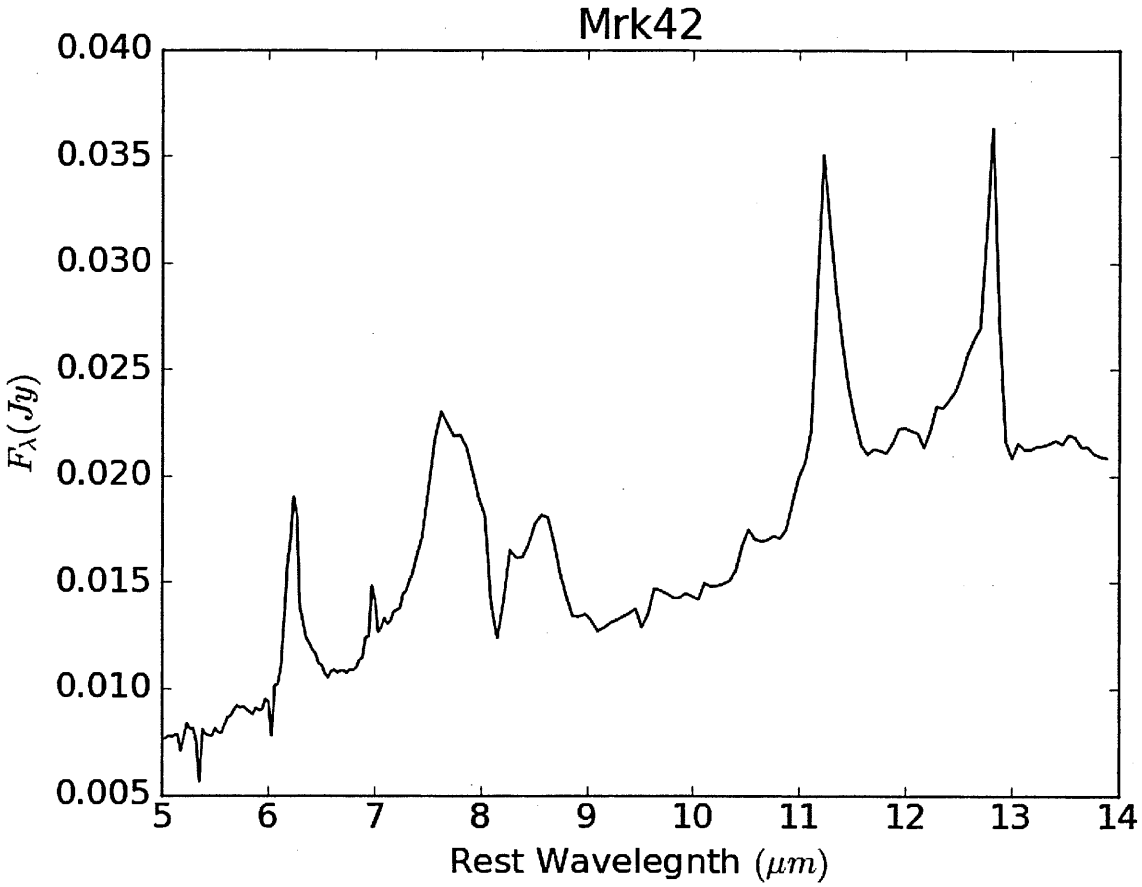
Mrk42
0.040
0.035
0.030
0.025
0.020
0.015
0.010
0.005
$F_\lambda(Jy)$
5
6
7
8
9
10
11
12
13
14
Rest Wavelegnth (μm)

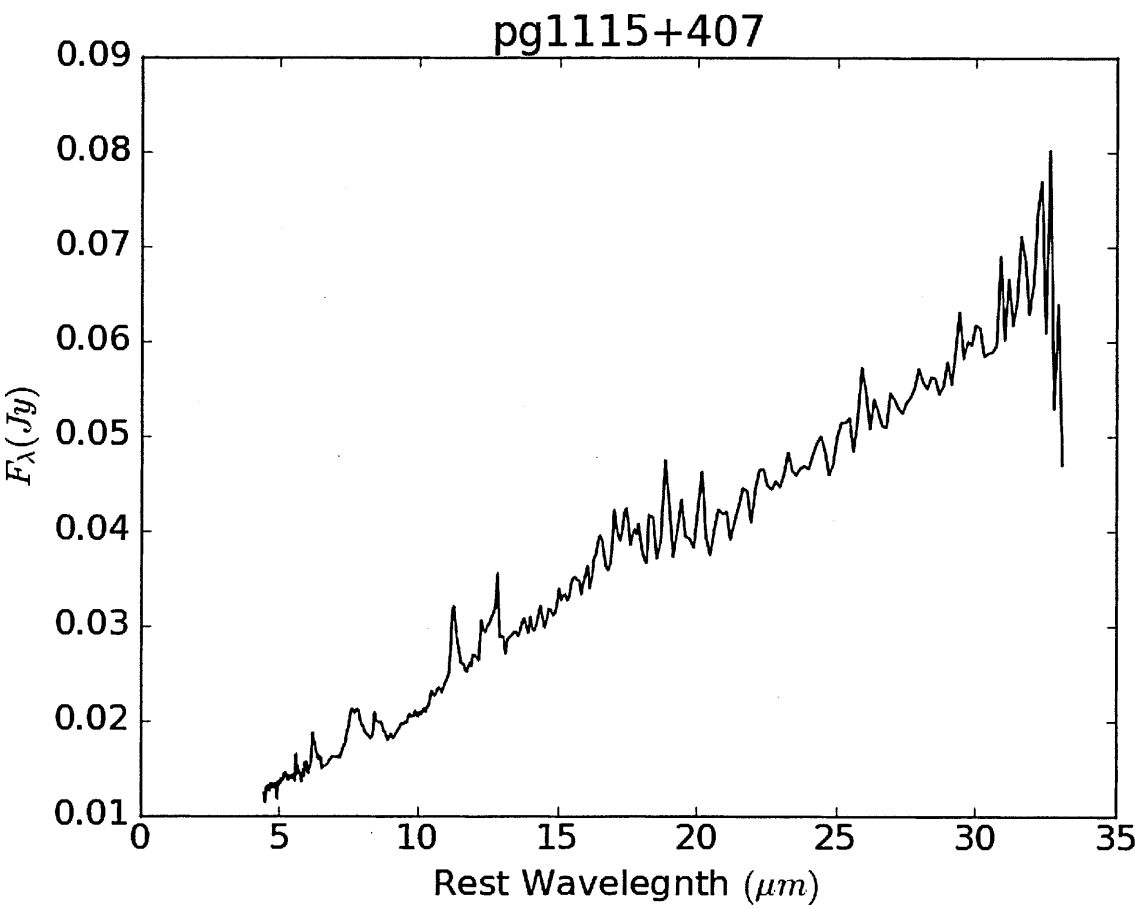
pg1115+407
0.09
0.08
0.07
0.06
0.05
0.04
0.03
0.02
0.01
$F_\lambda(Jy)$
0
5
10
15
20
25
30
35
Rest Wavelegnth (μm)

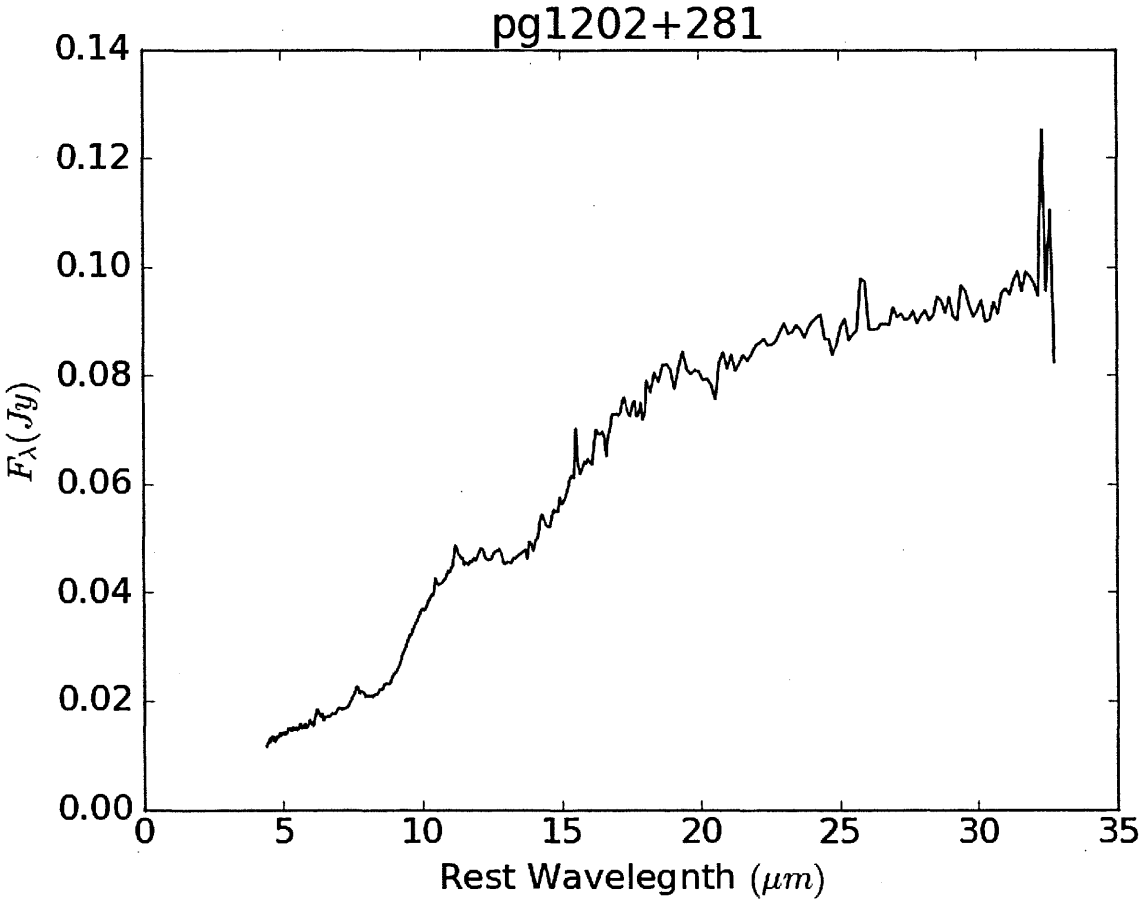
pg1202+281
0.14
0.12
0.10
0.08
0.06
0.04
0.02
0.00
$F_\lambda(Jy)$
0
5
10
15
20
25
30
35
Rest Wavelegnth (μm)

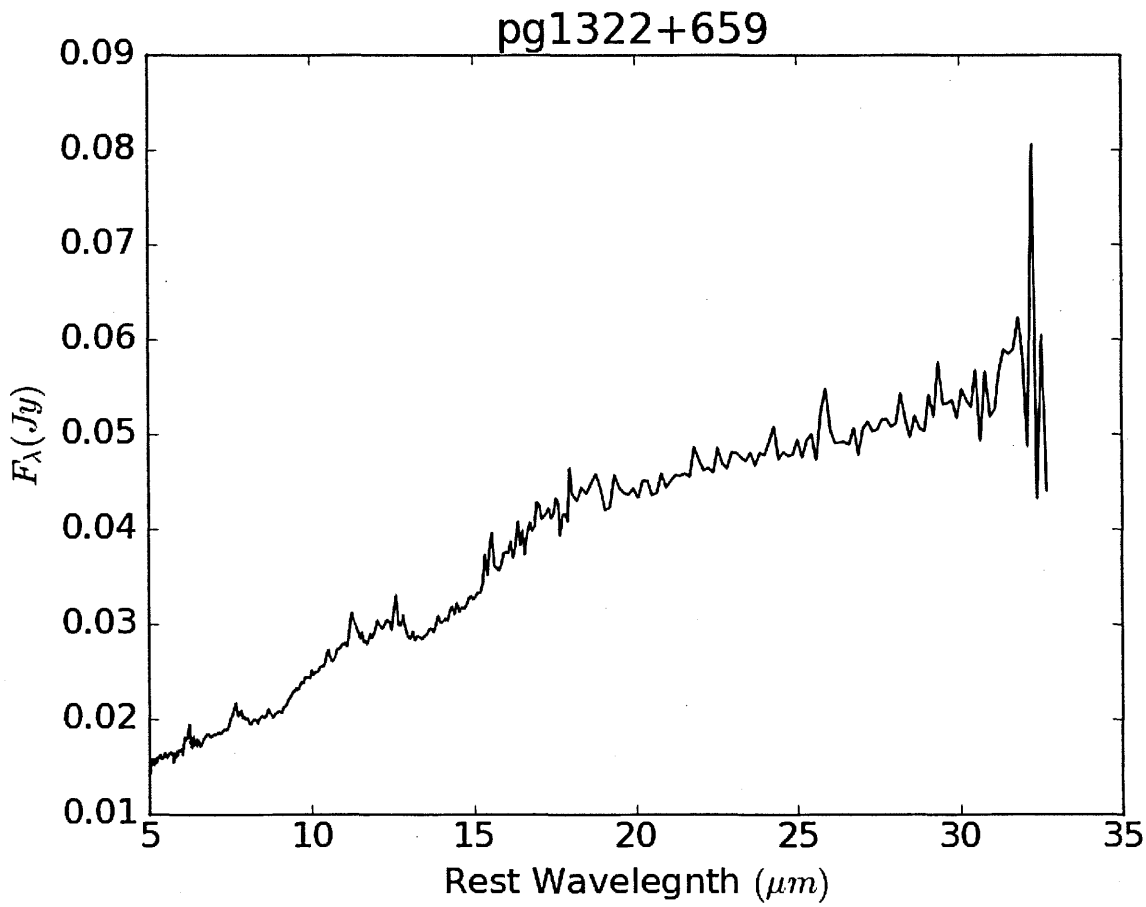
pg1322+659
0.09
0.08
0.07
0.06
0.05
0.04
0.03
0.02
0.01
$F_\lambda(Jy)$
5
10
15
20
25
30
35
Rest Wavelegnth (μm)

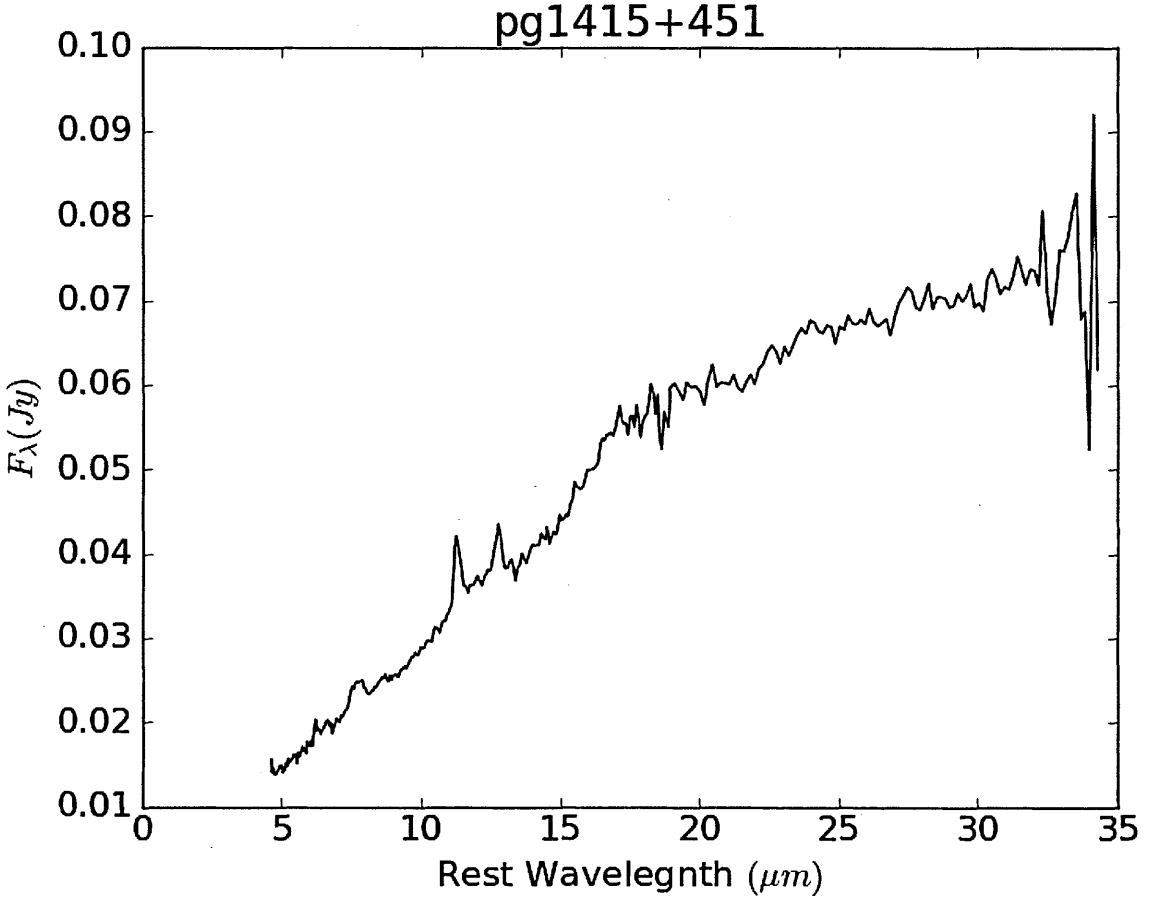
pg1415+451
0.10
0.09
0.08
0.07
0.06
0.05
0.04
0.03
0.02
0.01
$F_\lambda(Jy)$
0
5
10
15
20
25
30
35
Rest Wavelegnth (μm)

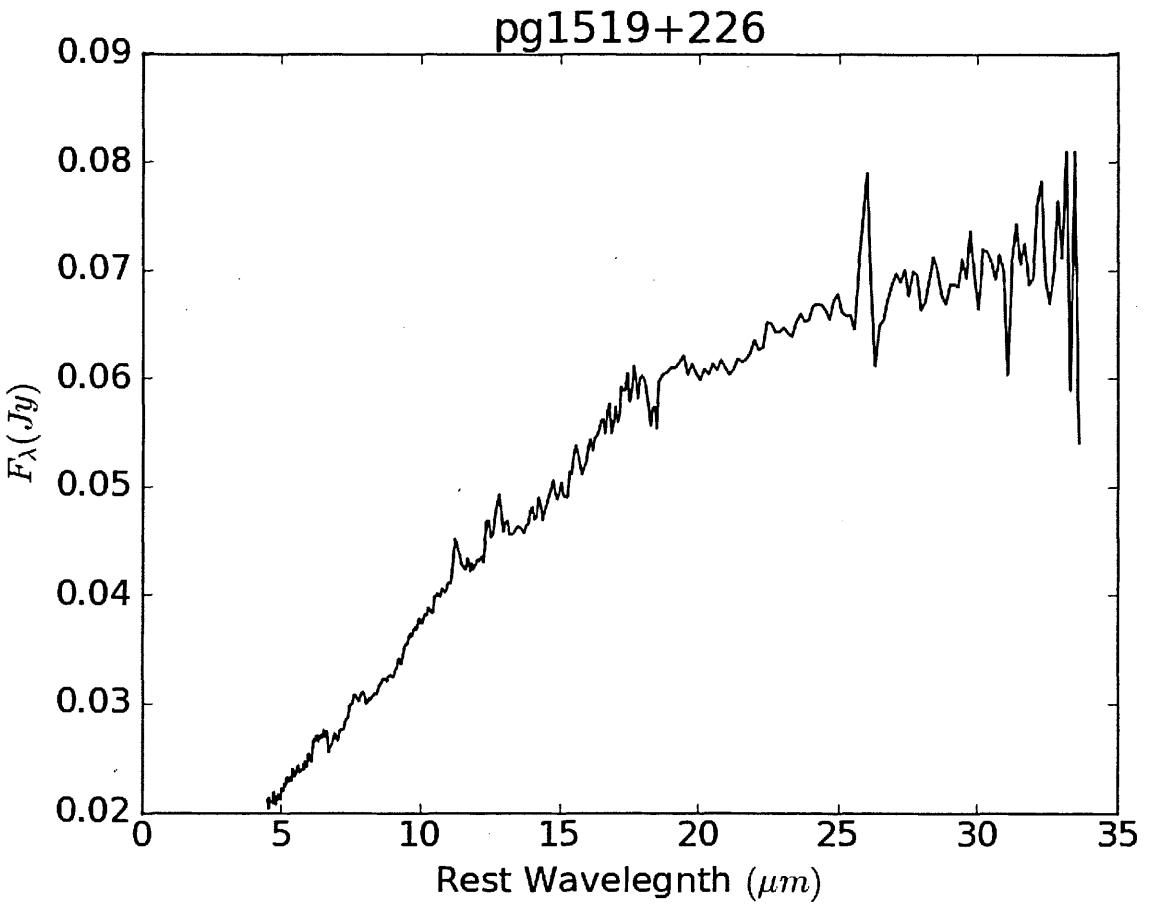
pg1519+226
0.09
0.08
0.07
0.06
0.05
0.04
0.03
0.02
$F_\lambda(Jy)$
0
5
10
15
20
25
30
35
Rest Wavelegnth (μm)

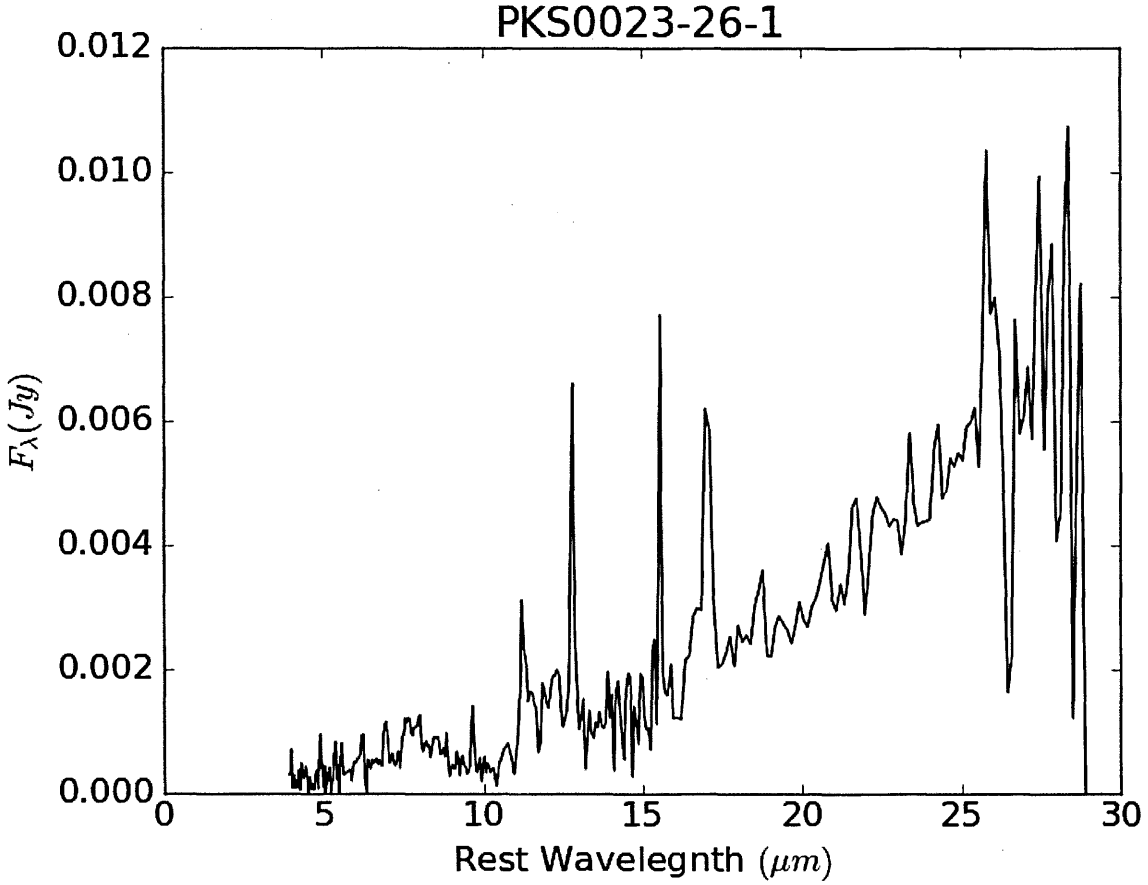
PKS0023-26-1
0.012
0.010
0.008
0.006
0.004
0.002
0.000
$F_\lambda(Jy)$
0
5
10
15
20
25
30
Rest Wavelegnth (μm)

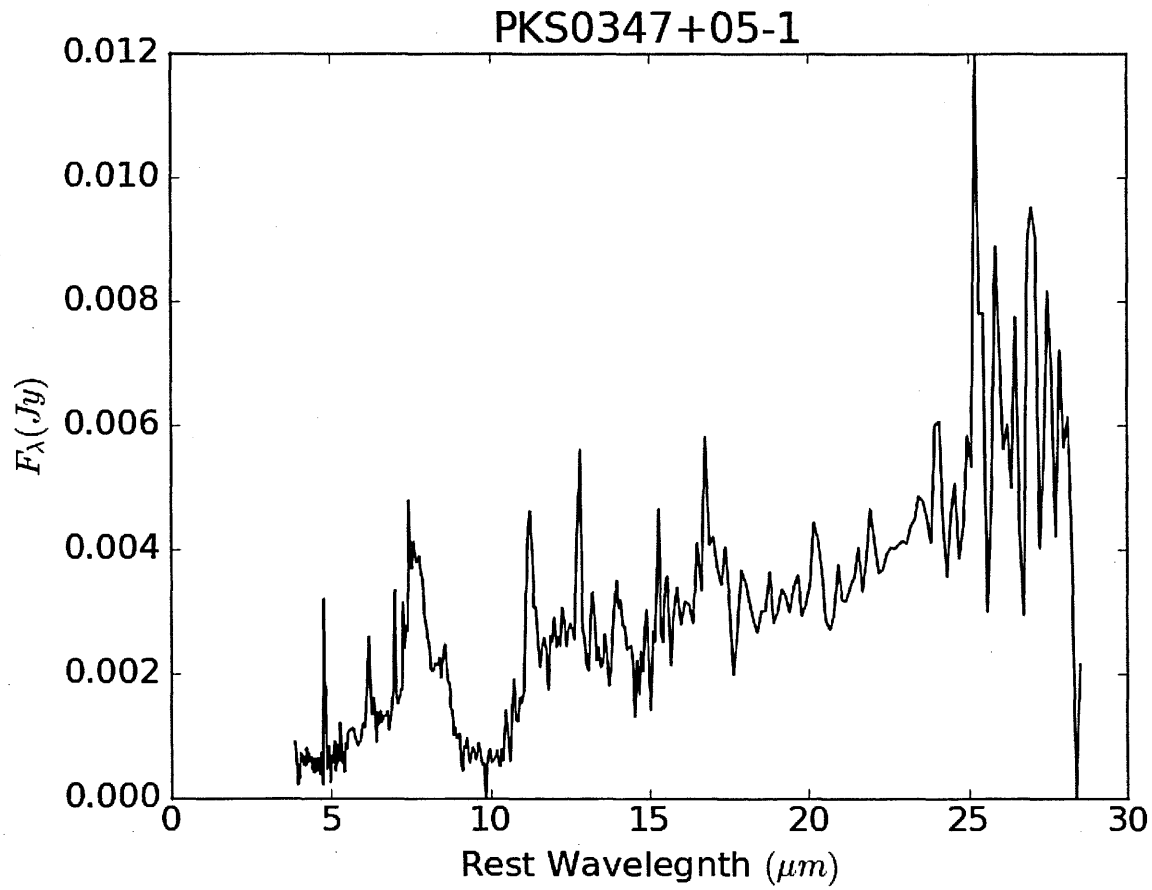
PKS0347+05-1
0.012
0.010
0.008
0.006
0.004
0.002
0.000
$F_\lambda(Jy)$
0
5
10
15
20
25
30
Rest Wavelegnth (μm)

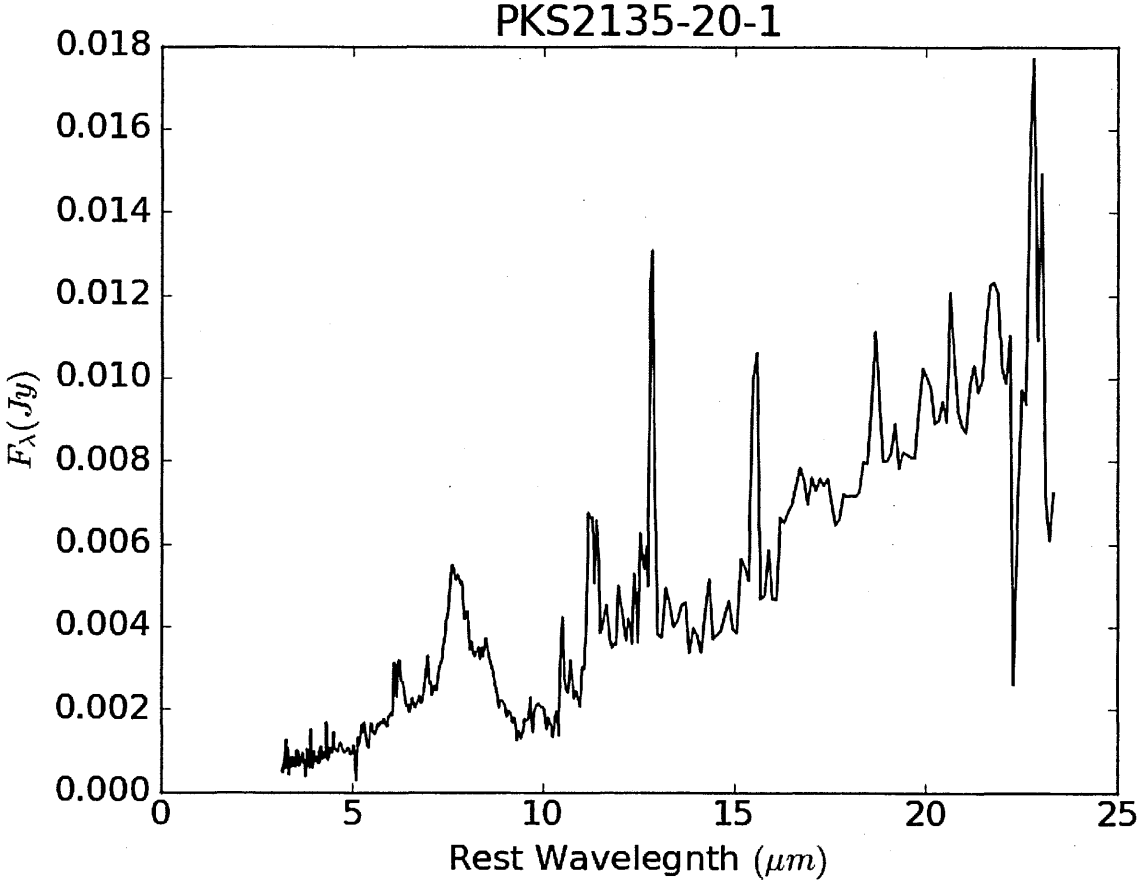
PKS2135-20-1
0.018
0.016
0.014
0.012
0.010
0.008
0.006
0.004
0.002
0.000
$F_\lambda(Jy)$
0
5
10
15
20
25
Rest Wavelegnth (μm)

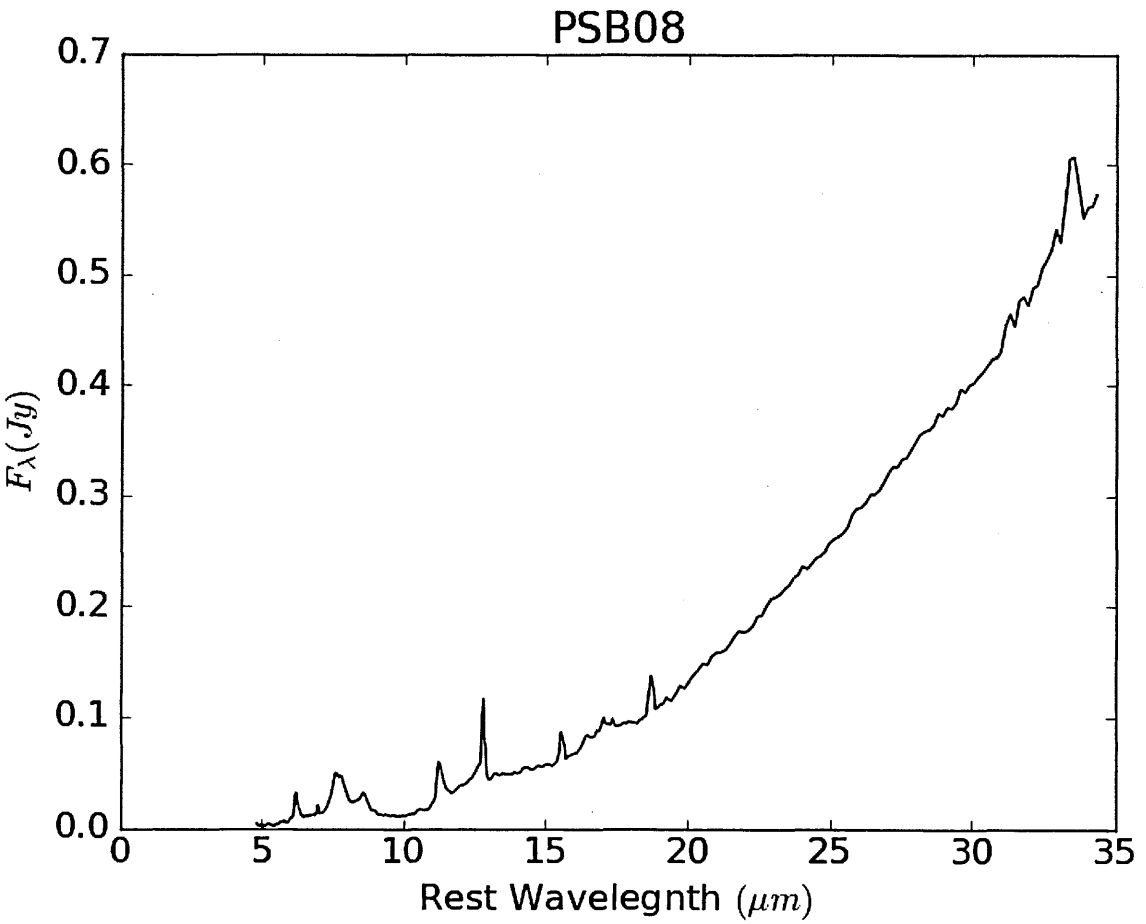
PSB08
0.7
0.6
0.5
0.4
0.3
0.2
0.1
0.0
$F_\lambda(Jy)$
0
5
10
15
20
25
30
35
Rest Wavelegnth (μm)

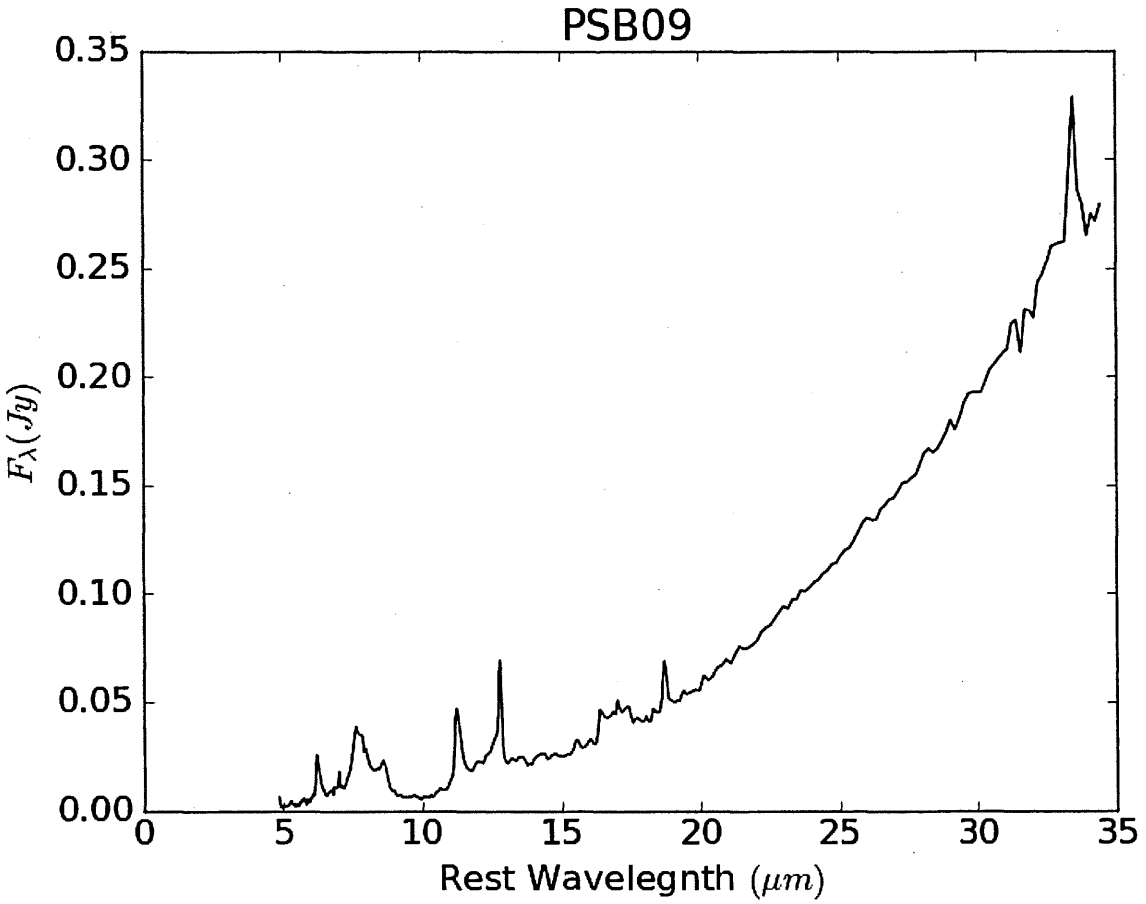
PSB09
0.35
0.30
0.25
0.20
0.15
0.10
0.05
0.00
$F_\lambda(Jy)$
0
5
10
15
20
25
30
35
Rest Wavelegnth (μm)

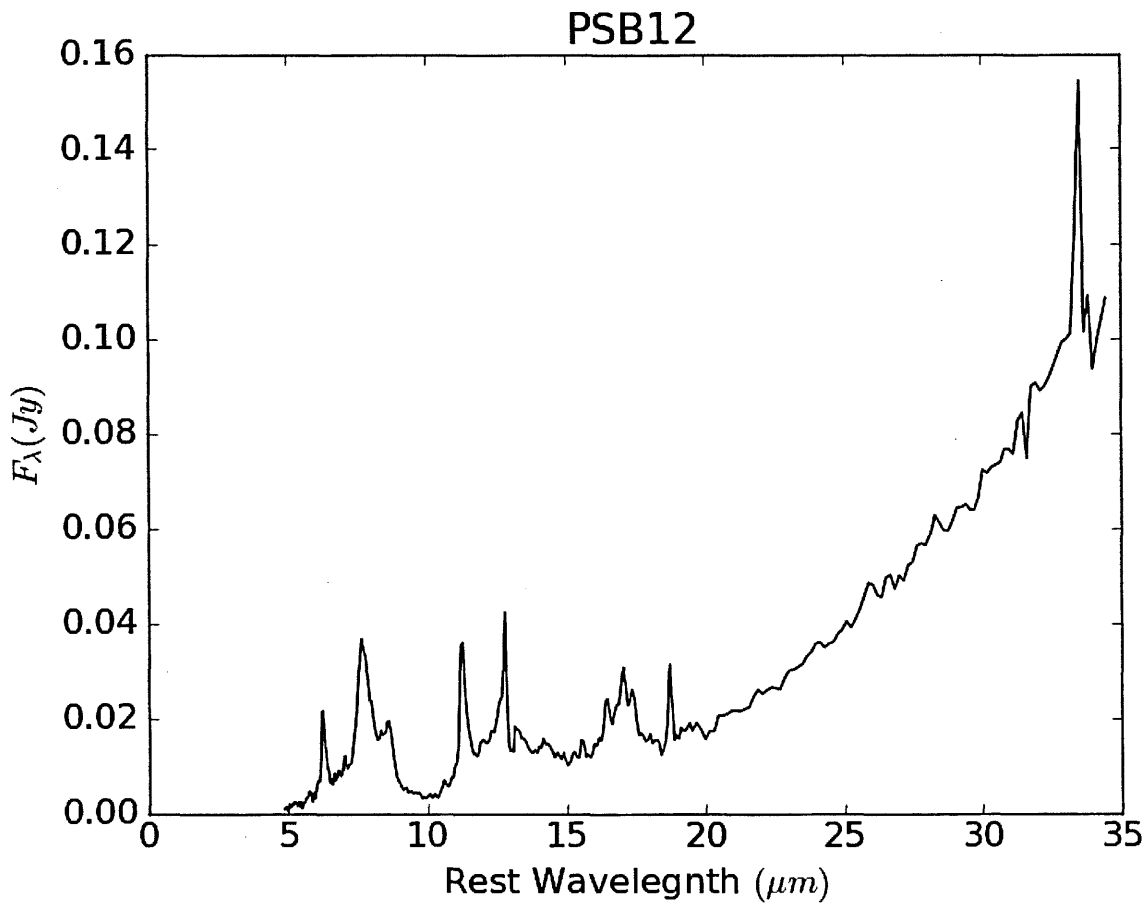
PSB12
0.16
0.14
0.12
0.10
0.08
0.06
0.04
0.02
0.00
$F_\lambda(Jy)$
0
5
10
15
20
25
30
35
Rest Wavelegnth (μm)

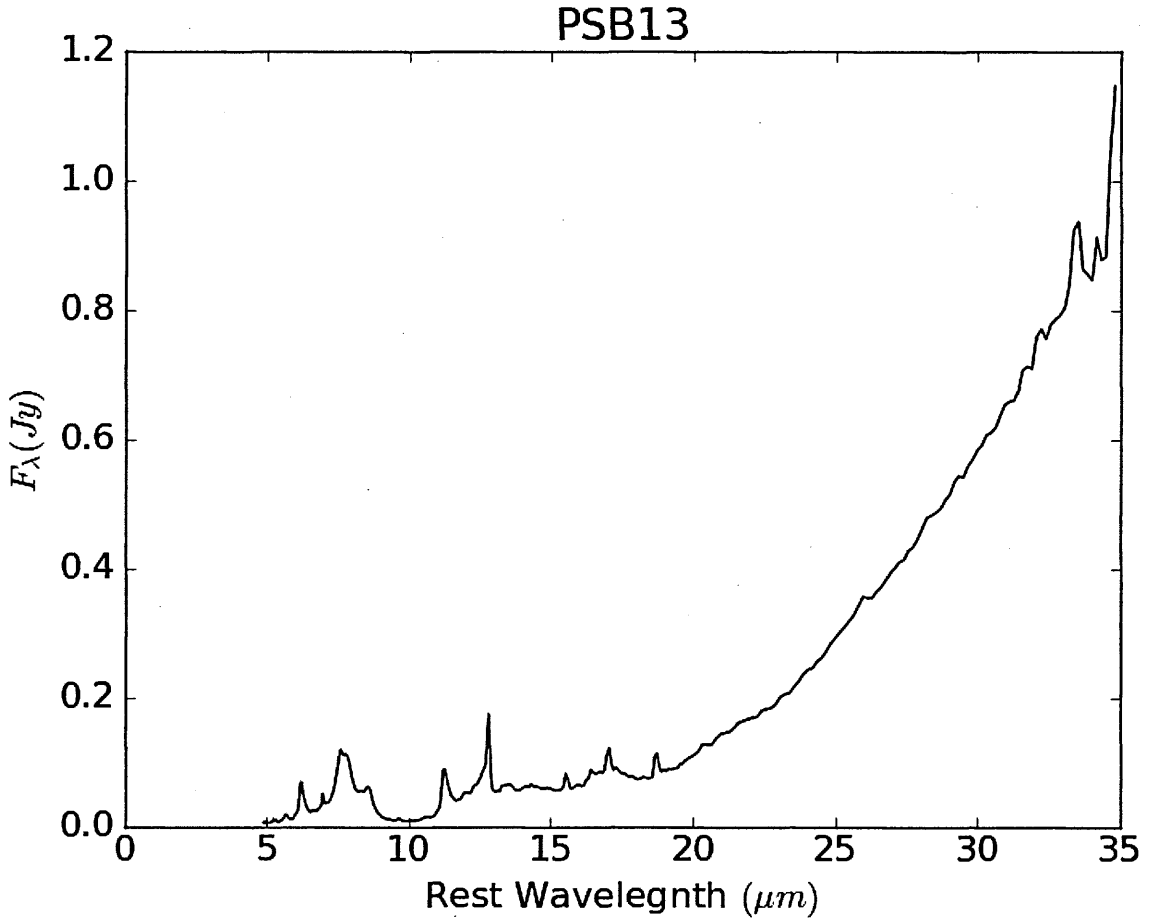
PSB13
1.2
1.0
0.8
0.6
0.4
0.2
0.0
$F_\lambda(Jy)$
0
5
10
15
20
25
30
35
Rest Wavelegnth (μm)

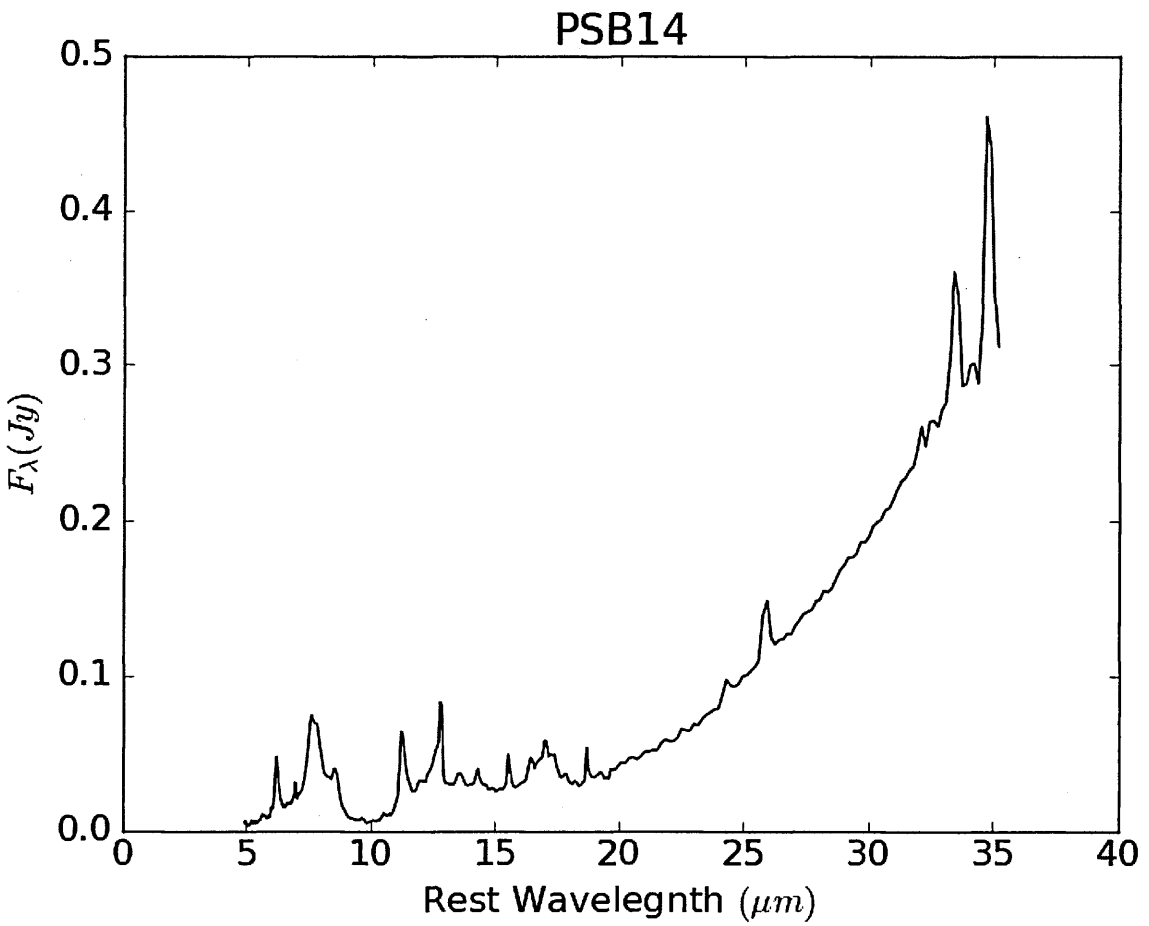
PSB14
0.5
0.4
0.3
0.2
0.1
0.0
$F_\lambda(Jy)$
0
5
10
15
20
25
30
35
40
Rest Wavelegnth (μm)

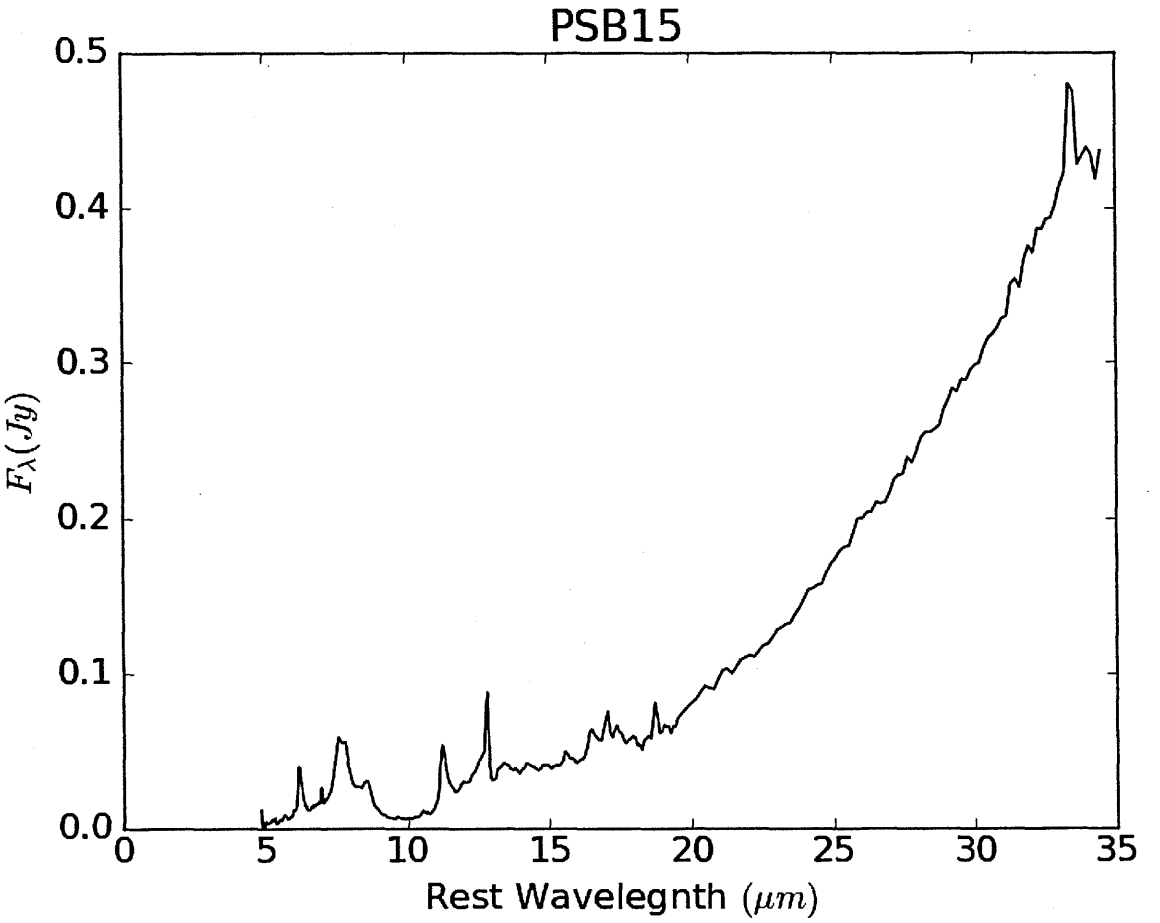
PSB15
0.5
0.4
0.3
0.2
0.1
0.0
$F_\lambda(Jy)$
0
5
10
15
20
25
30
35
Rest Wavelegnth (μm)

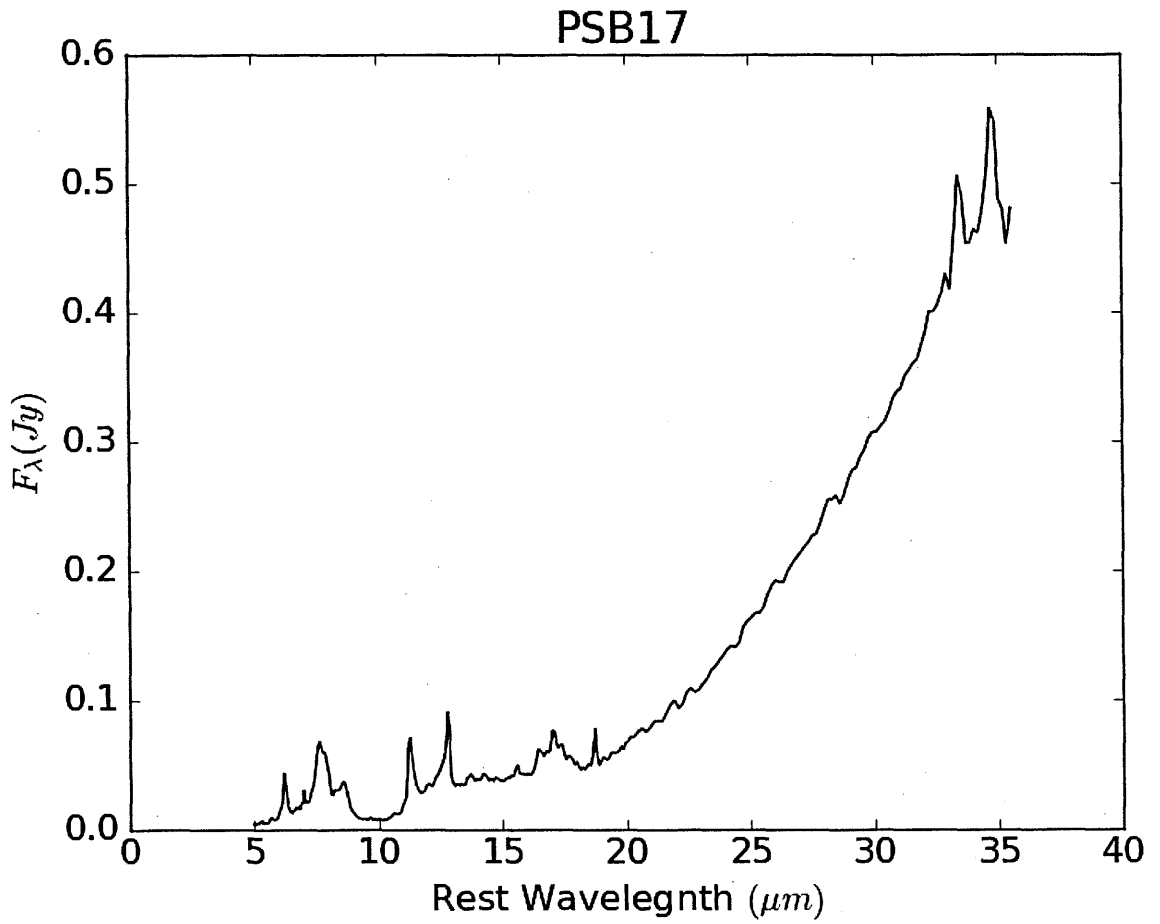
PSB17
0.6
0.5
0.4
0.3
0.2
0.1
0.0
$F_\lambda(Jy)$
0
5
10
15
20
25
30
35
40
Rest Wavelegnth (μm)

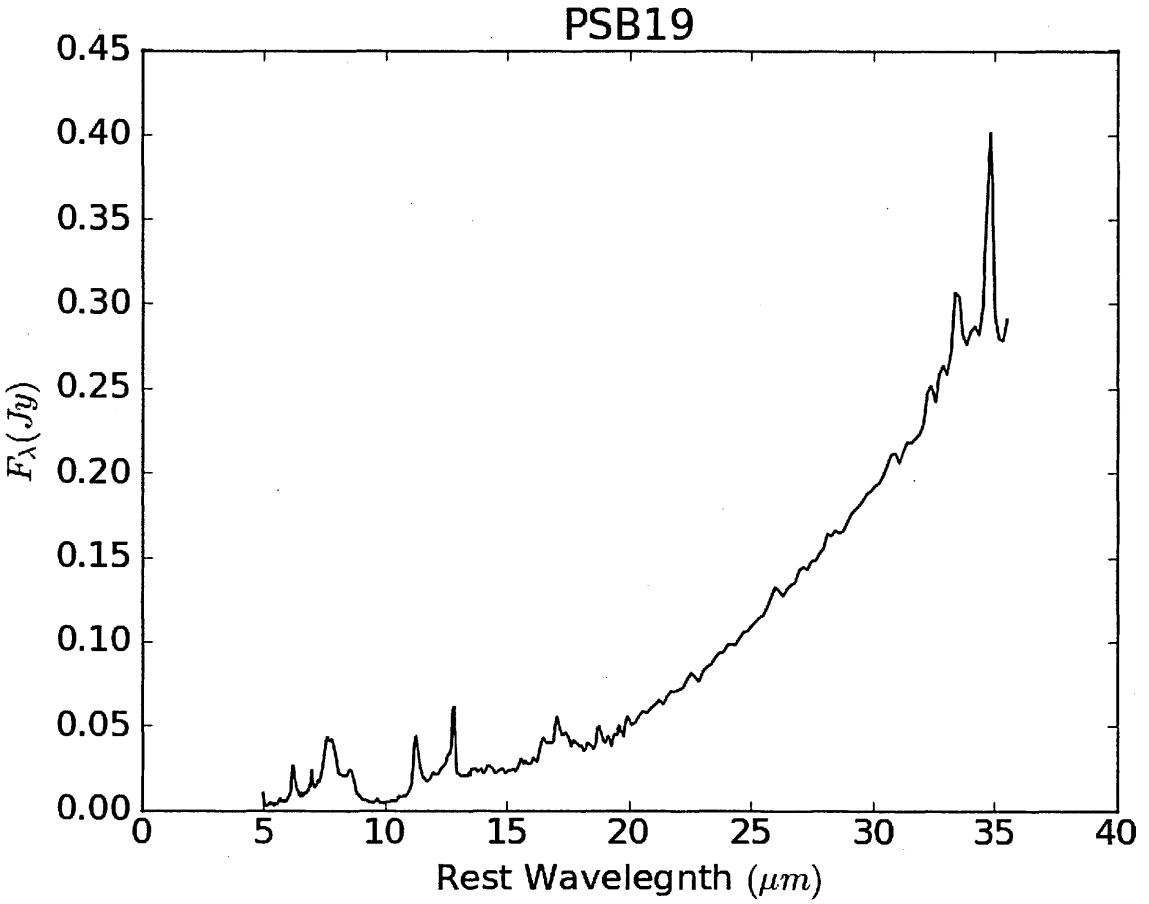
PSB19
0.45
0.40
0.35
0.30
0.25
0.20
0.15
0.10
0.05
0.00
$F_\lambda(Jy)$
0
5
10
15
20
25
30
35
40
Rest Wavelegnth (μm)

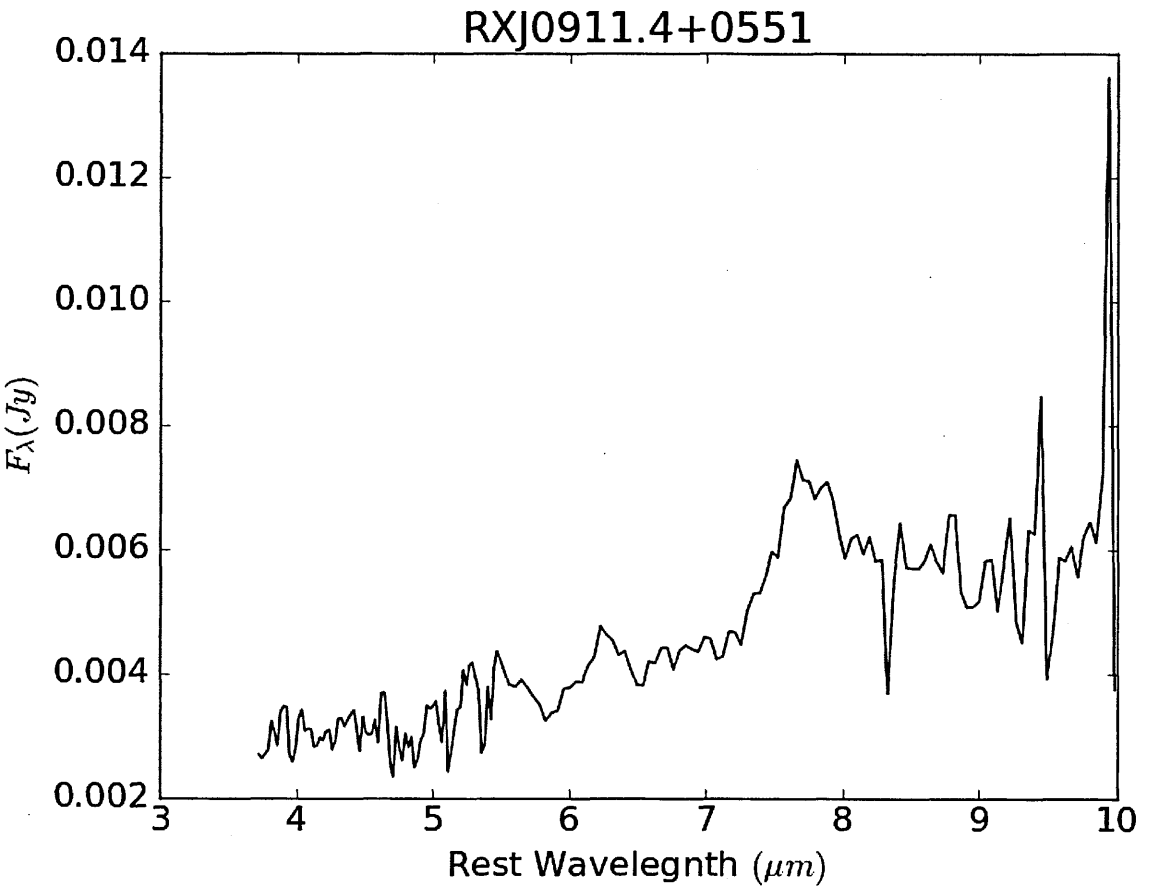
RXJ0911.4+0551
0.014
0.012
0.010
0.008
0.006
0.004
0.002
$F_\lambda(Jy)$
3
4
5
6
7
8
9
10
Rest Wavelegnth (μm)

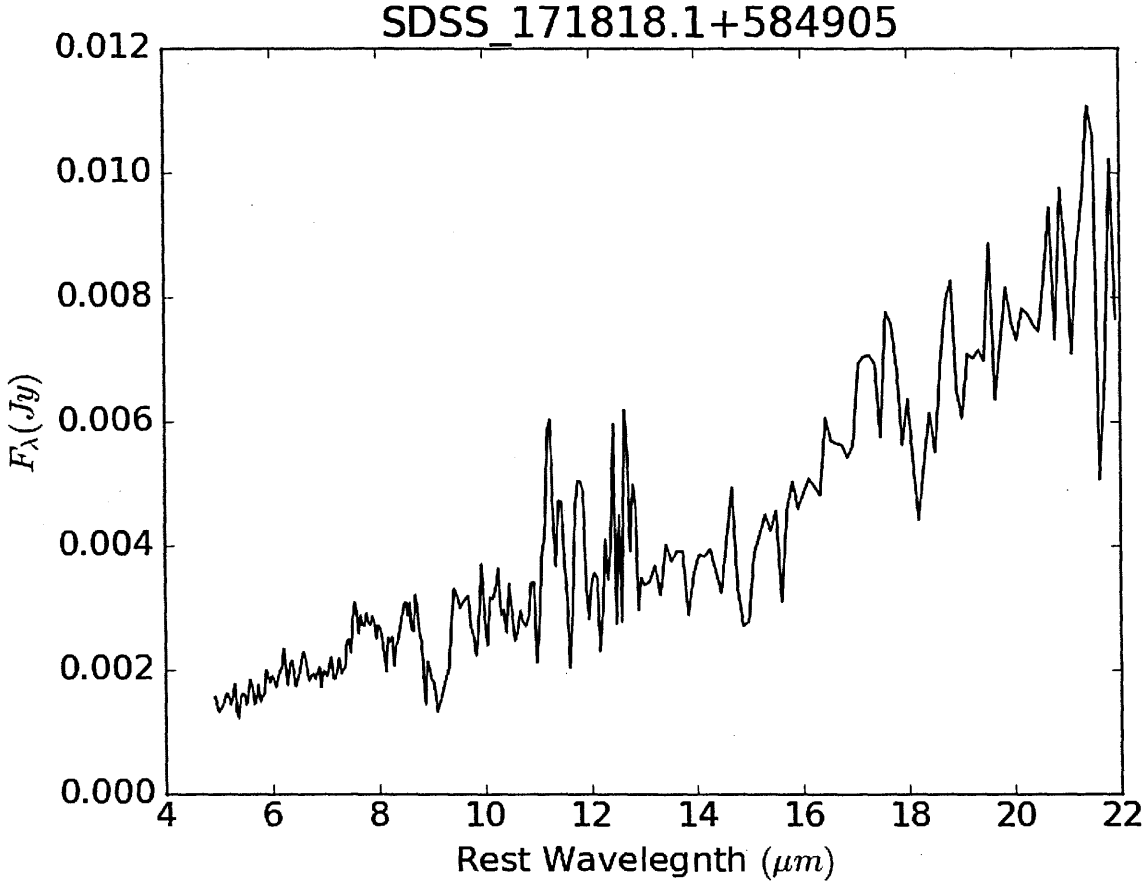
SDSS_171818.1+584905
0.012
0.010
0.008
0.006
0.004
0.002
0.000
$F_\lambda(Jy)$
4
6
8
10
12
14
16
18
20
22
Rest Wavelegnth (μm)

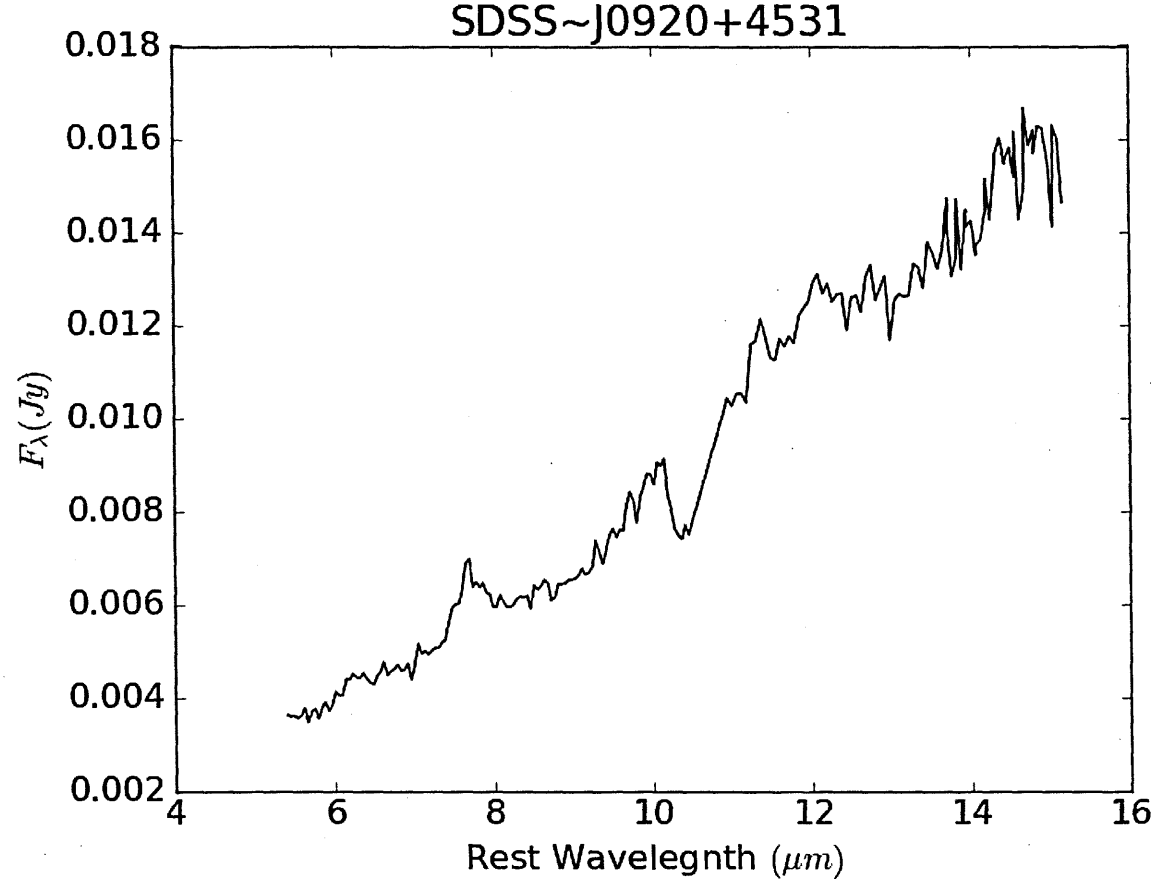
SDSS~J0920+4531
0.018
0.016
0.014
0.012
0.010
0.008
0.006
0.004
0.002
$F_\lambda(Jy)$
4
6
8
10
12
14
16
Rest Wavelegnth (μm)

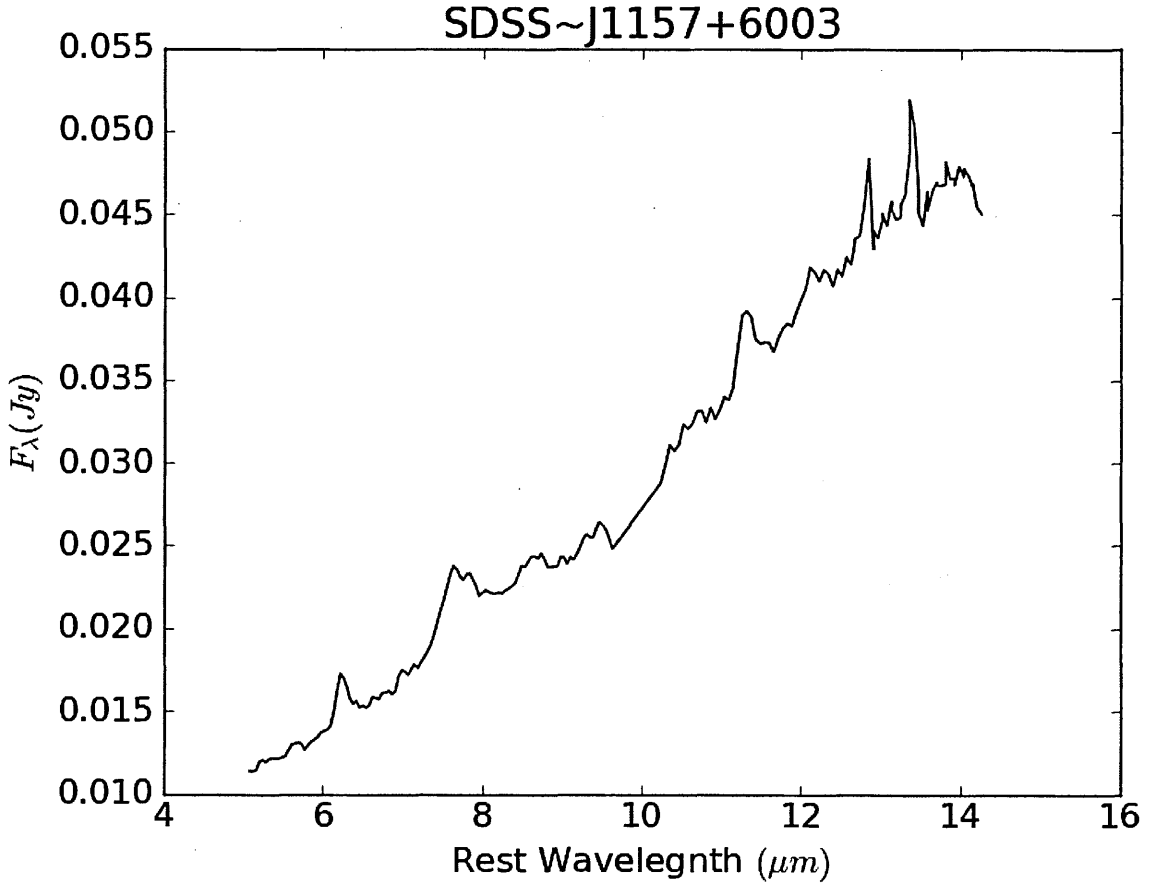
SDSS~J1157+6003
0.055
0.050
0.045
0.040
0.035
0.030
0.025
0.020
0.015
0.010
$F_\lambda(Jy)$
4
6
8
10
12
14
16
Rest Wavelegnth (μm)

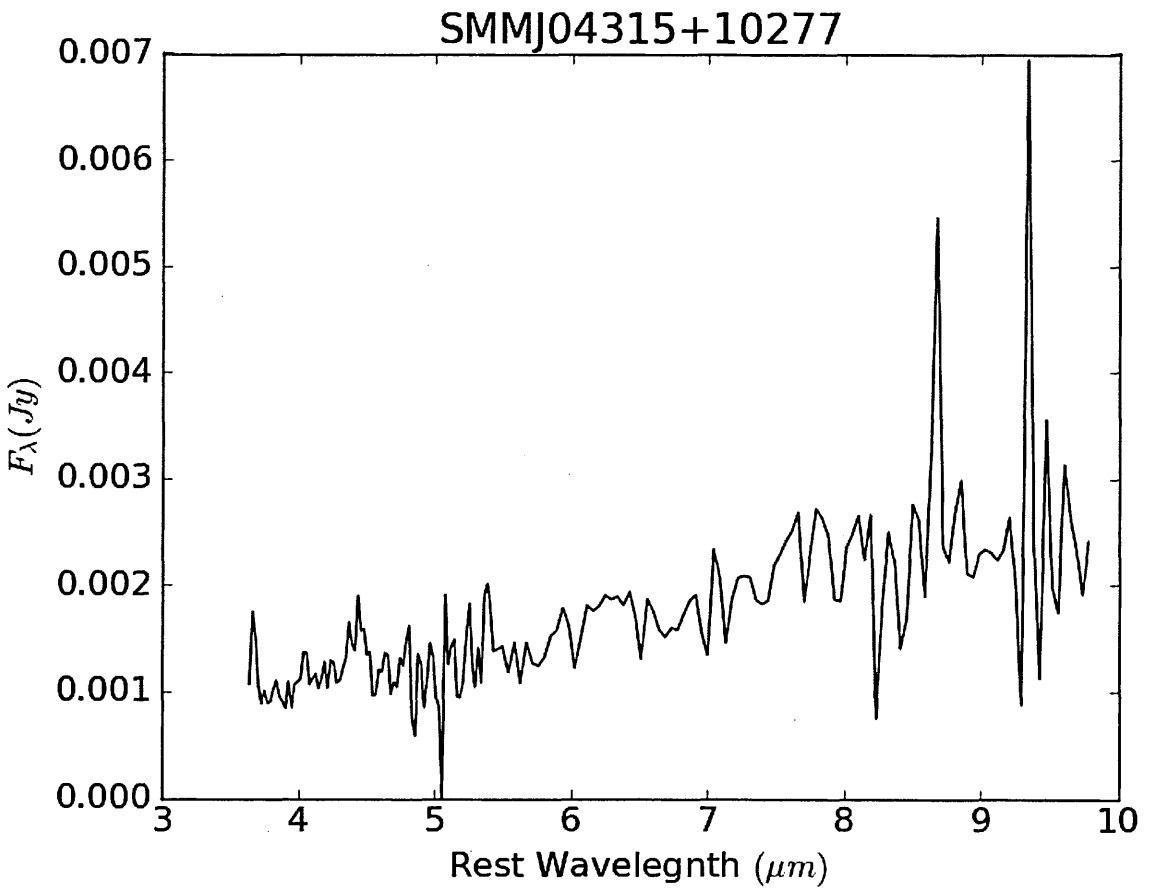
SMMJ04315+10277
0.007
0.006
0.005
0.004
0.003
0.002
0.001
0.000
$F_\lambda(Jy)$
3
4
5
6
7
8
9
10
Rest Wavelegnth (μm)

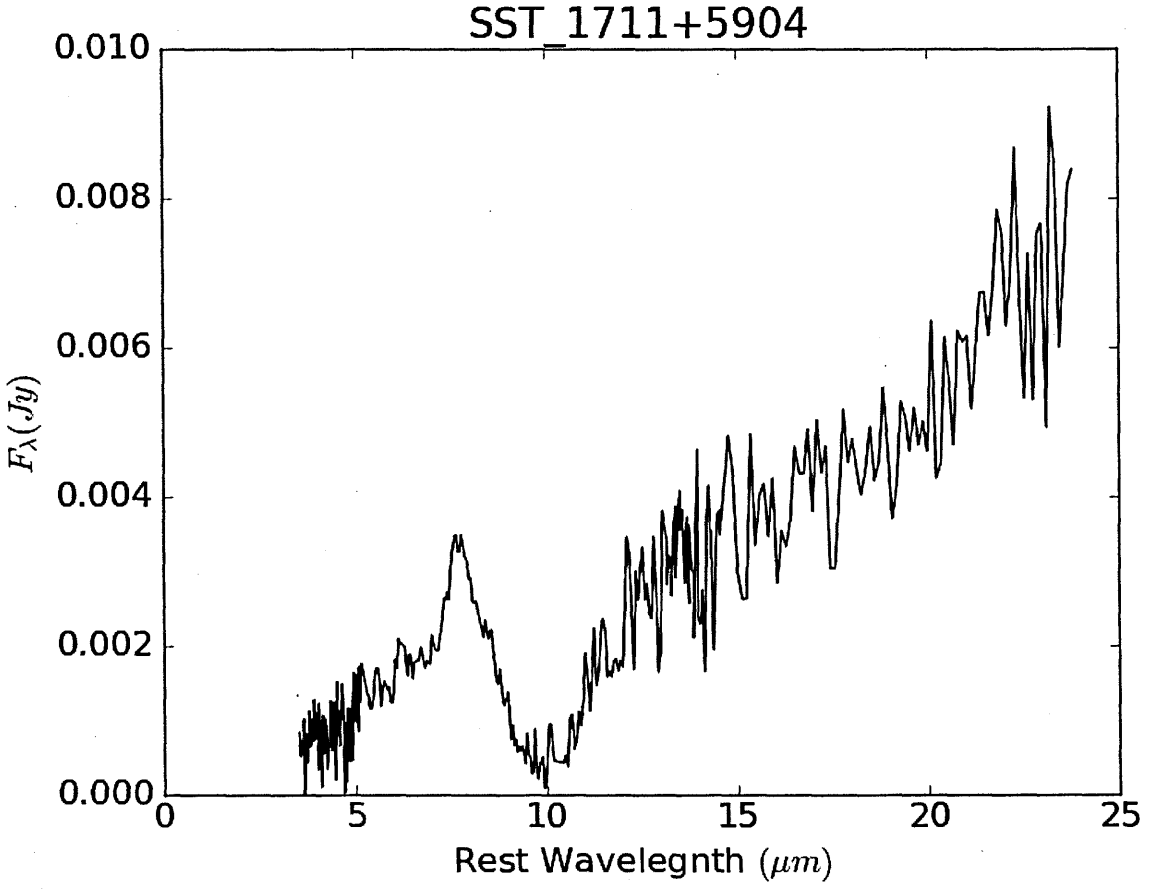
SST_1711+5904
0.010
0.008
0.006
0.004
0.002
0.000
$F_\lambda(Jy)$
0
5
10
15
20
25
Rest Wavelegnth (μm)

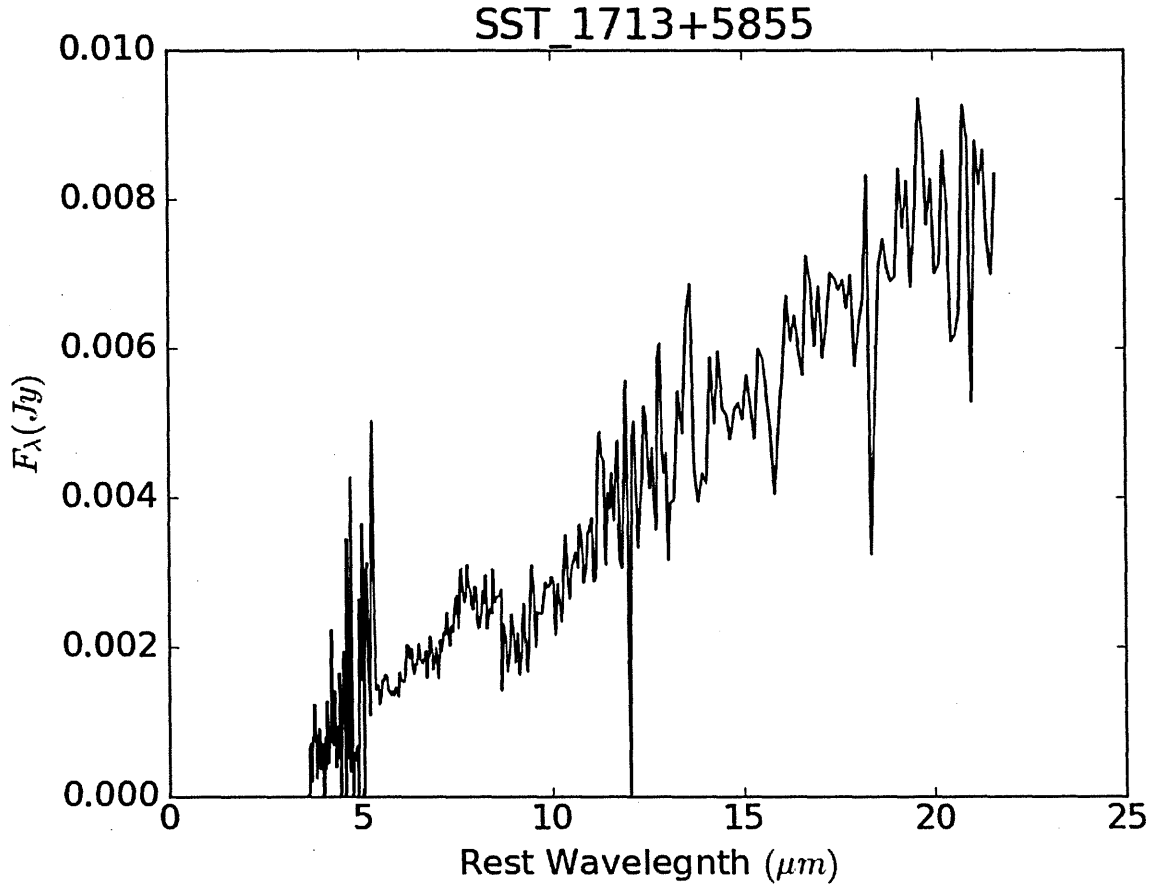
SST_1713+5855
0.010
0.008
0.006
0.004
0.002
0.000
$F_\lambda(Jy)$
0
5
10
15
20
25
Rest Wavelegnth (μm)

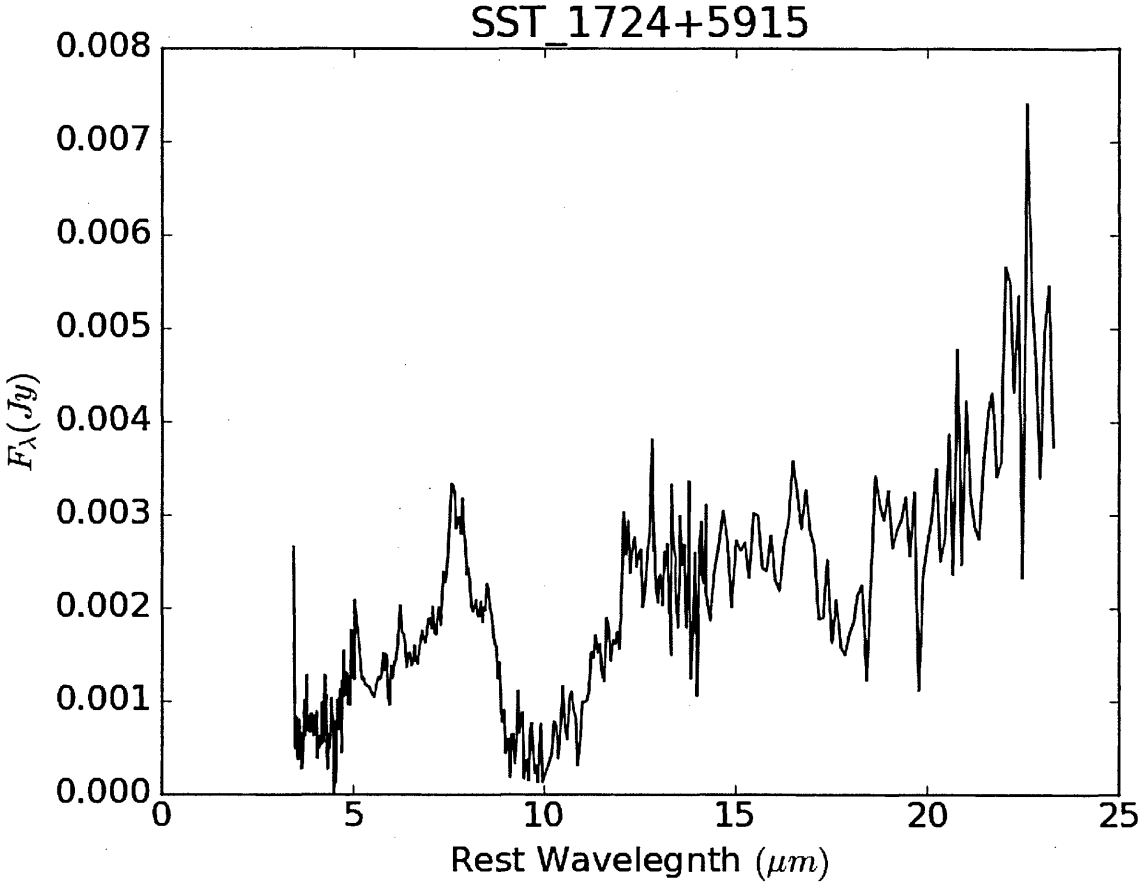
SST_1724+5915
0.008
0.007
0.006
0.005
0.004
0.003
0.002
0.001
0.000
$F_\lambda(Jy)$
0
5
10
15
20
25
Rest Wavelegnth (μm)

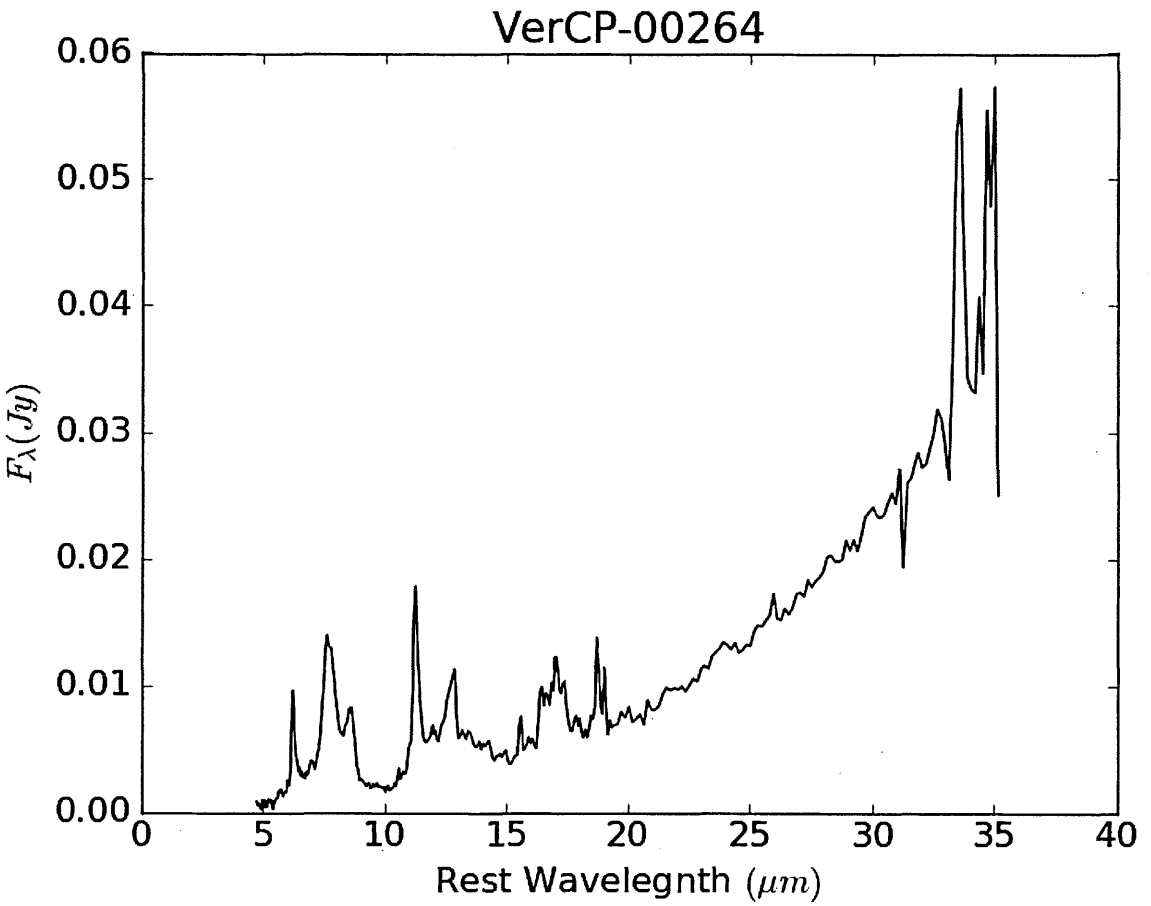
VerCP-00264
0.06
0.05
0.04
0.03
0.02
0.01
0.00
$F_\lambda(Jy)$
0
5
10
15
20
25
30
35
40
Rest Wavelegnth (μm)

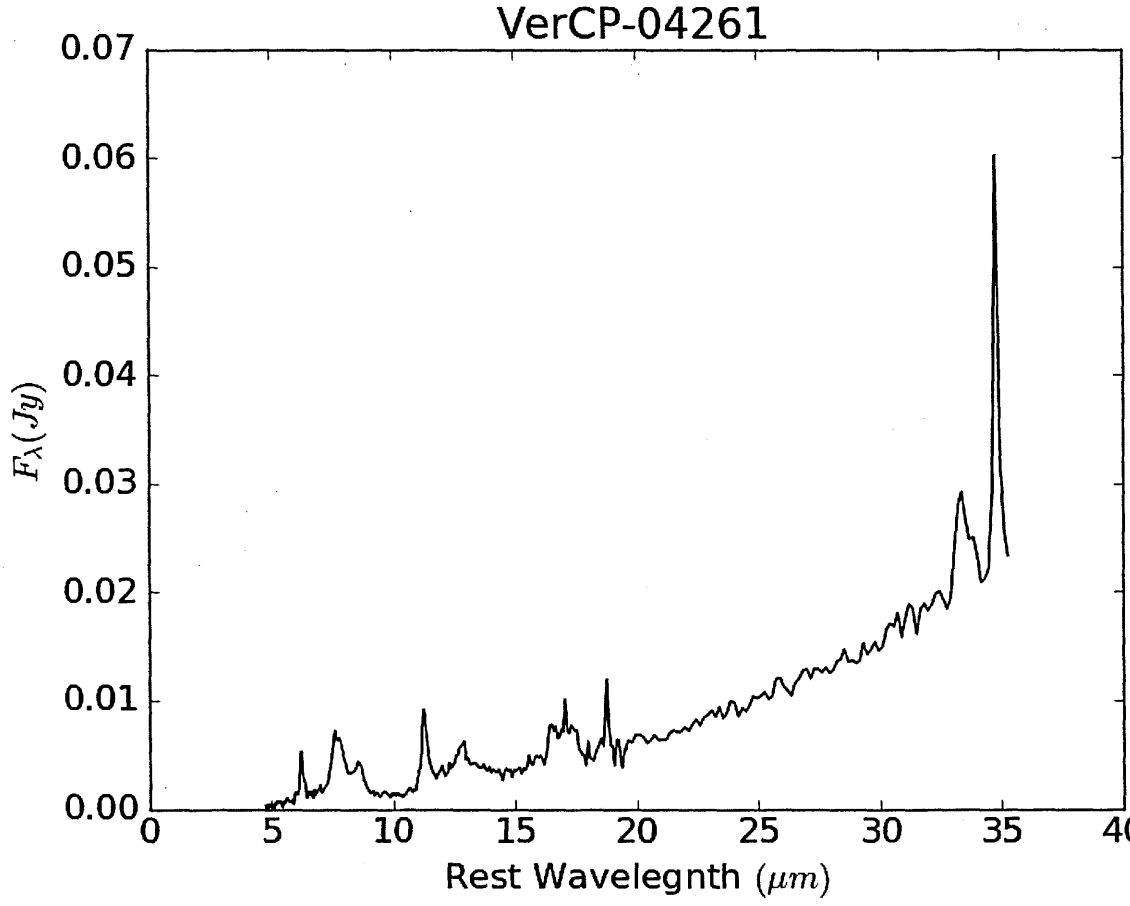
VerCP-04261
0.07
0.06
0.05
0.04
0.03
0.02
0.01
0.00
$F_\lambda(Jy)$
0
5
10
15
20
25
30
35
40
Rest Wavelegnth (μm)

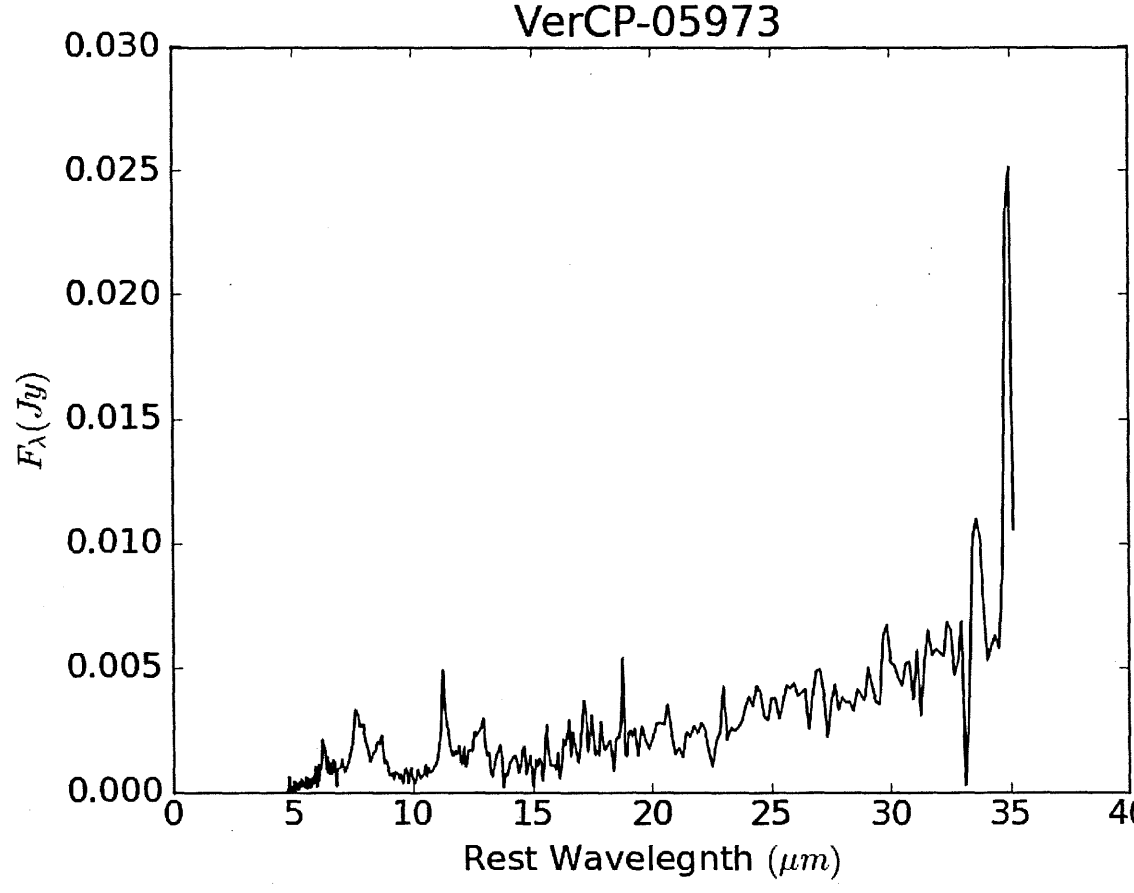
VerCP-05973
0.030
0.025
0.020
0.015
0.010
0.005
0.000
$F_\lambda(Jy)$
0
5
10
15
20
25
30
35
40
Rest Wavelegnth (μm)

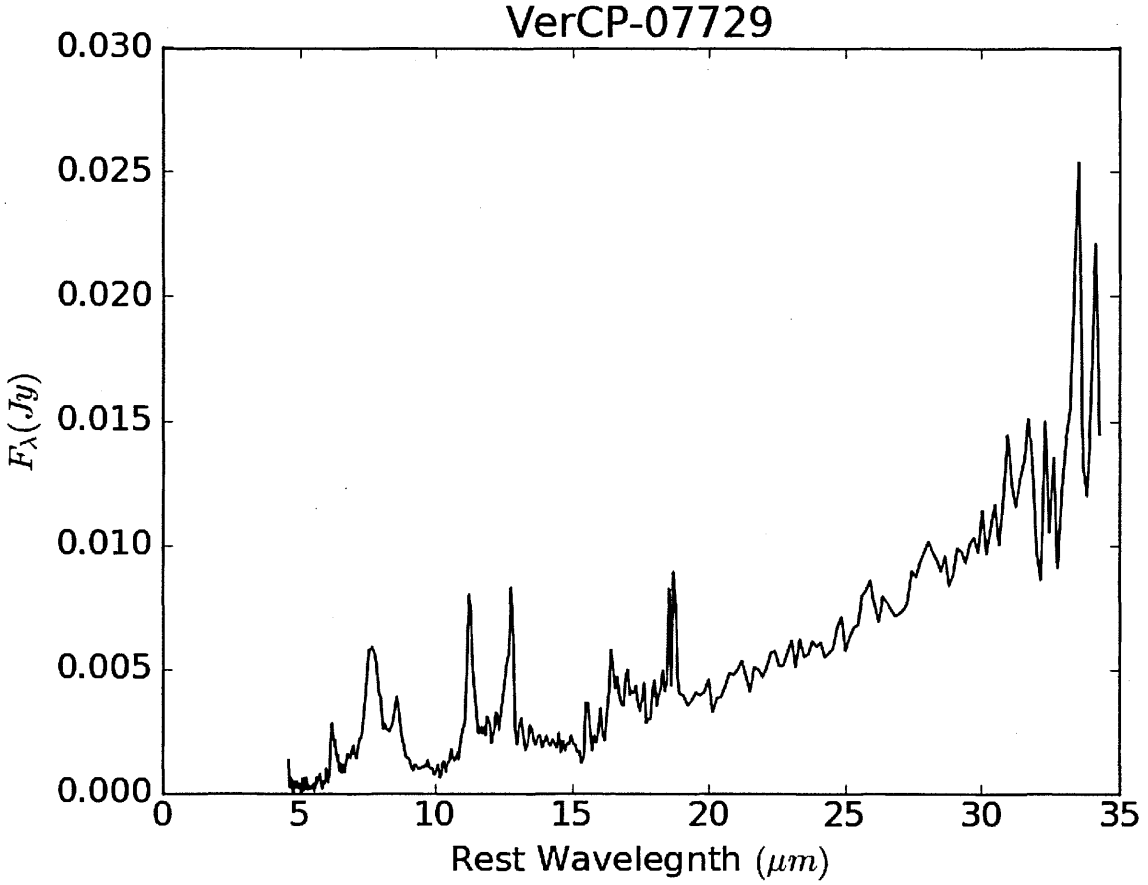
VerCP-07729
0.030
0.025
0.020
0.015
0.010
0.005
0.000
$F_\lambda(Jy)$
0
5
10
15
20
25
30
35
Rest Wavelegnth (μm)

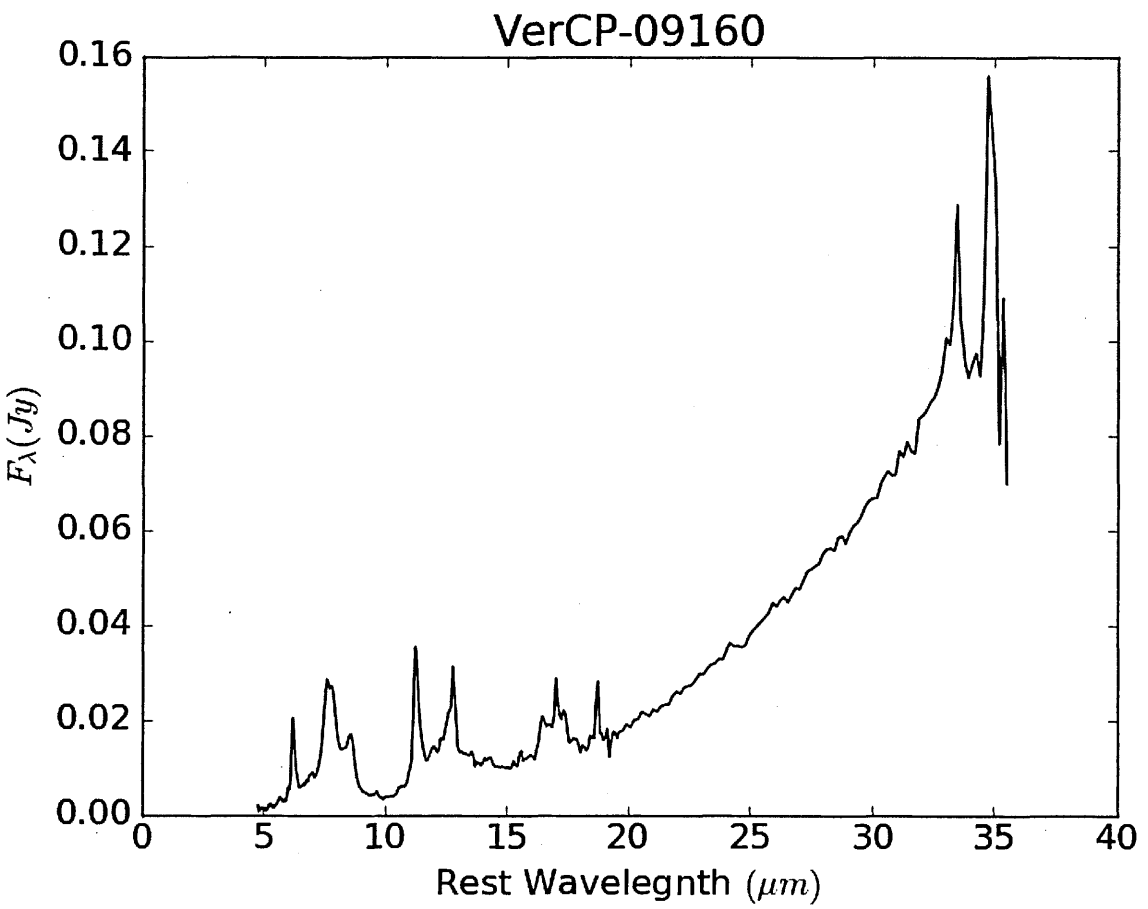
VerCP-09160
0.16
0.14
0.12
0.10
0.08
0.06
0.04
0.02
0.00
$F_\lambda(Jy)$
0
5
10
15
20
25
30
35
40
Rest Wavelegnth (μm)

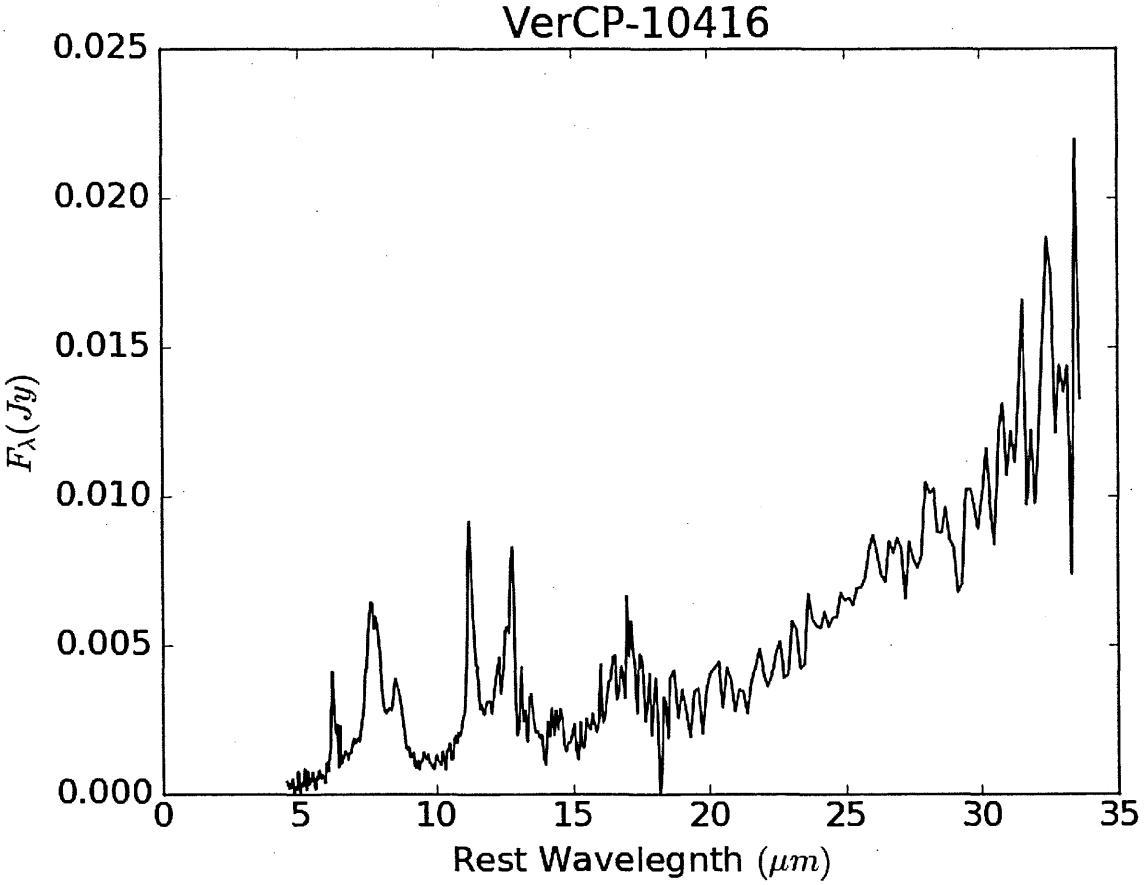
VerCP-10416
0.025
0.020
0.015
0.010
0.005
0.000
$F_\lambda(Jy)$
0
5
10
15
20
25
30
35
Rest Wavelegnth (μm)

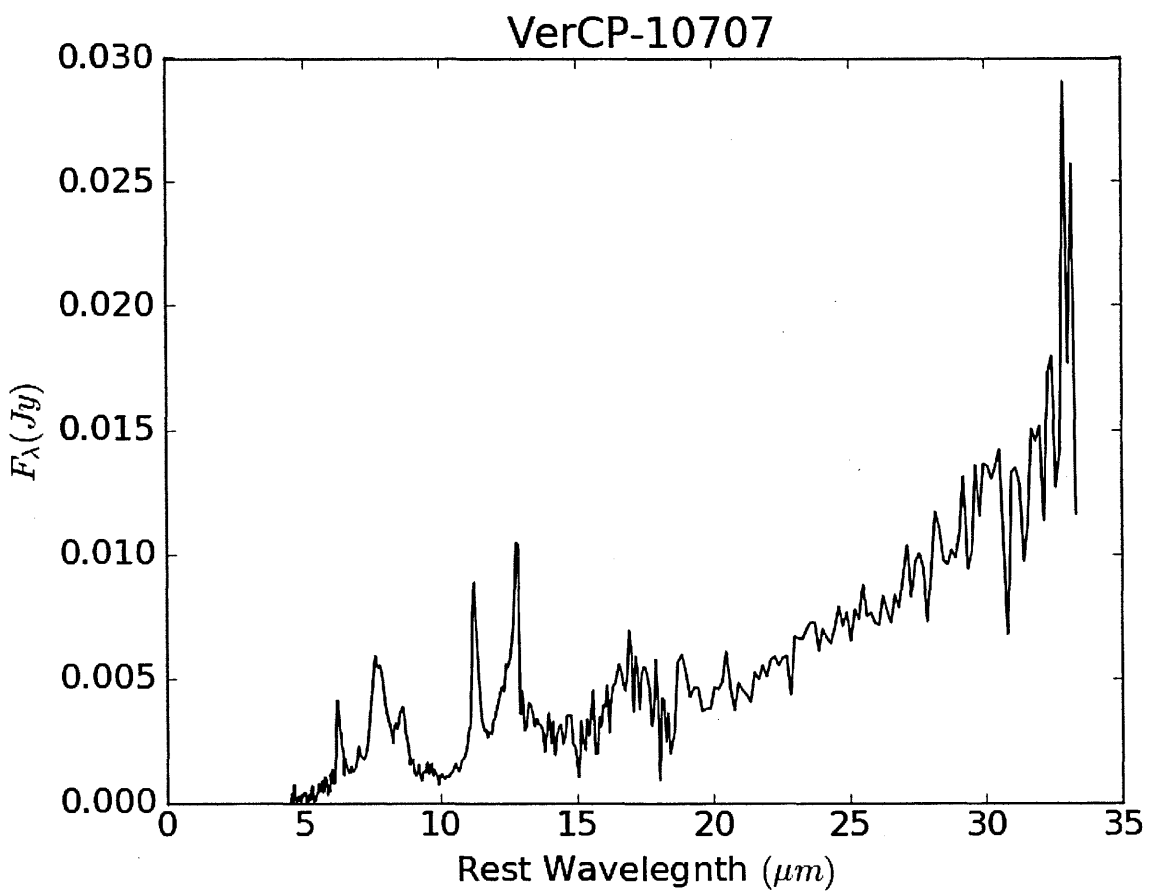
VerCP-10707
0.030
0.025
0.020
0.015
0.010
0.005
0.000
$F_\lambda(Jy)$
0
5
10
15
20
25
30
35
Rest Wavelegnth (μm)

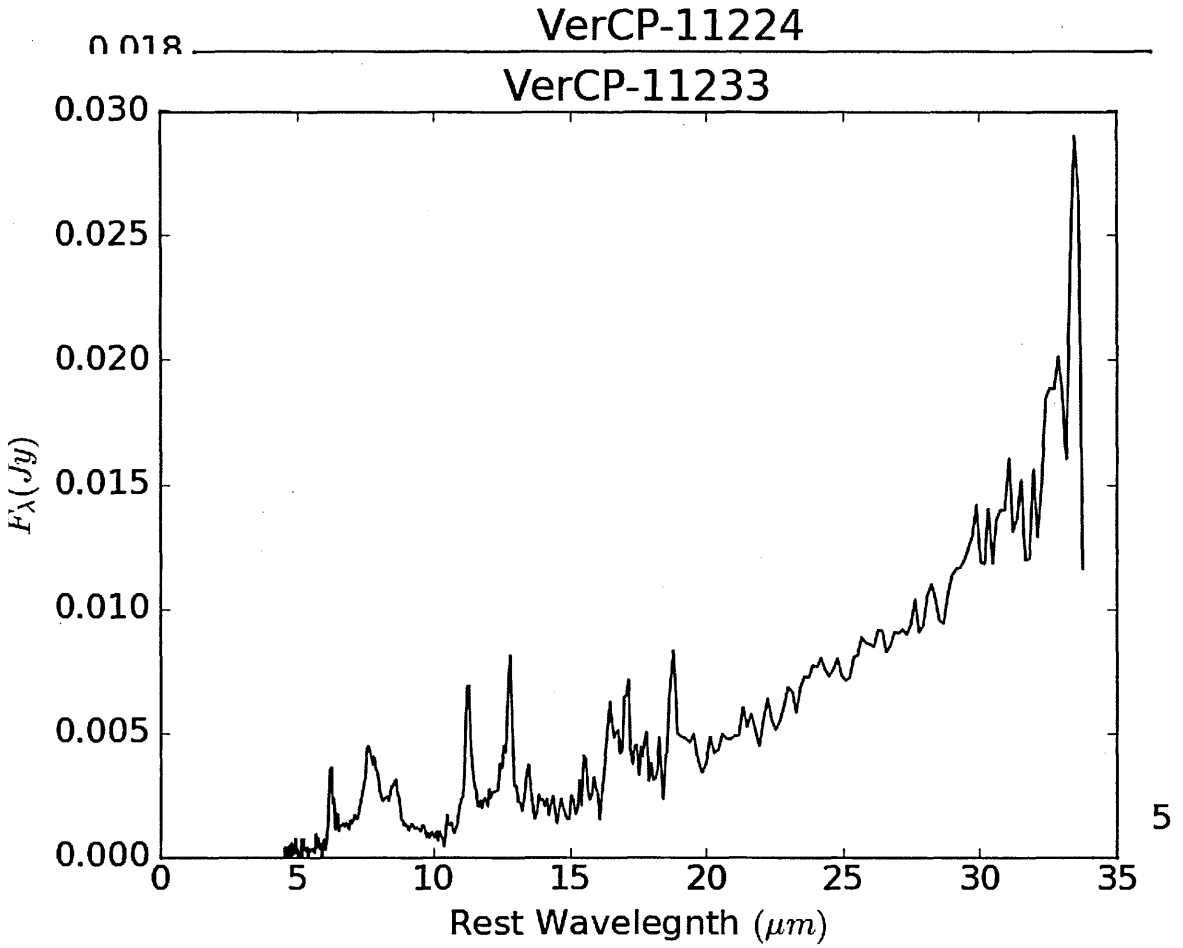
VerCP-11224
VerCP-11233
0.030
0.025
0.020
0.015
0.010
0.005
0.000
$F_\lambda(Jy)$
0
5
10
15
20
25
30
35
Rest Wavelegnth (μm)